TECHNISCHE UNIVERSITÄT MÜNCHEN
Lehrstuhl für Baumechanik

A Coupled Integral Transform Method - Finite Element Method Approach to Model the Soil-Structure-Interaction

Manuela Helene Hackenberg

Vollständiger Abdruck der von der Ingenieurfakultät Bau Geo Umwelt der Technischen Universität München zur Erlangung des akademischen Grades eines

Doktor-Ingenieurs

genehmigten Dissertation.

Vorsitzender: Univ.-Prof. Dr.-Ing. Roberto Cudmani

Prüfer der Dissertation:

1. Univ.-Prof. Dr.-Ing. habil. Gerhard H. Müller
2. Ass. Prof. Dr. ir. Karel N. van Dalen

Die Dissertation wurde am 16.06.2016 bei der Technischen Universität München eingereicht und durch die Ingenieurfakultät Bau Geo Umwelt am 13.10.2016 angenommen.

Abstract

Harmonic or moving forces on the surface of a soil or inside an underground tunnel can lead to vibrations of the medium which can be perceived at the surface of the soil. This often leads to discomfort or problems if the oscillations are beyond the acceptance limit of machines or individuals. If either changes are planned, that influence the excitation force, or new buildings are designed in the vicinity of existing emission systems, it is important to model the complete system appropriately. This does not only include the emission system, which can be for example a tunnel or a building site, and the immission system of the building of interest, but also the soil as transmission medium for the vibrations.

The emission and immission systems can be successfully modeled with the Finite Element Method as they usually consist of different materials arranged in complex geometries and the Finite Element Method is best suited for systems with such characteristics. The transmission medium can be modeled, in contrast to the emission and immission systems, with a rather simple geometry and material behavior, if homogeneous, linear elastic material is assumed for low-frequent vibrations. The complexity of the transmission system lies in its infinite extension, which the model has to be able to reproduce. The Integral Transform Method leads to an analytical solution for the soil for several simple geometries. With this approach, it is possible to model infinite media with horizontal, cylindrical or spherical surfaces.

In this thesis the Integral Transform Method is used to model the infinite extension of the soil with analytically correct solutions of the Lamé differential equation. The complex geometry and material distribution of the emission system of an exemplary tunnel are described by the Finite Element Method. At the interaction surface both subsystems are coupled using the substructure technique. Thus, the advantages of both methods can be combined to model the total system as accurate as possible.

Kurzfassung

Harmonische oder bewegte Lasten, die in einem Tunnel oder an der Oberfläche des Bodens aufgebracht werden, können Vibrationen verursachen, die von Menschen oder empfindlichen Geräten wahrgenommen werden können. Dies kann bei Personen zu Unwohlsein oder ernsthaften gesundheitlichen Problemen führen. Sensitive Maschinen können durch Schwingungen des Untergrundes in ihrer Funktionsweise beeinträchtigt werden oder schlimmstenfalls vollständig funktionsunfähig werden. Daher ist es erforderlich, das ganze System, das an der Schwingungsausbreitung beteiligt ist, wirklichkeitsgetreu zu modellieren. Dies gilt vor allem dann, wenn an bestehenden Systemen Veränderungen vorgenommen werden oder neue Gebäude in der Nähe bekannter bestehender Emissionsorte geplant werden. Dazu müssen sowohl das Emissionssystem, z. B. ein Tunnel oder eine Baustelle, und das Immissionsystem des zu untersuchenden Gebäudes als auch der Boden als Transmissionssystem im Modell erfasst werden.

Emissions- und Immissionssysteme sind geometrisch häufig sehr komplex und setzen sich in der Regel aus Komponenten unterschiedlicher Materialien zusammen. Die Finite Element Methode ist gut geeignet, solche Systeme detailgetreu zu modellieren. Wenn der Boden betrachtet werden soll, so kann dieser in guter Näherung durch einfache geometrische Formen beschrieben werden und für tieffrequente Anregungen über eine homogene, linear elastische Materialverteilung. Die Schwierigkeit bei der Modellierung des Bodens liegt daher nicht in komplexen Geometrien oder Materialverteilungen, sondern in einer realitätsnahen Abbildung seiner unendlichen Ausdehnung. Diese kann mit Hilfe der Integraltransformationsmethode auf der Grundlage analytischer Lösungen für geometrisch einfache Systeme (horizontale, zylindrische oder sphärische Oberflächen) abgebildet werden.

In dieser Arbeit sollen die Vorteile der beiden Methoden kombiniert werden. Die unendliche Ausdehnung des Bodens wird mit der Integraltransformationsmethode erfasst, während die komplexen Geometrien und Materialverteilungen eines Tunnels als beispielhafes Emissionssystem mit der Finiten Element Methode beschrieben werden. Diese beiden Subsysteme werden an einer gemeinsamen Kopplungsfläche mit Hilfe der Substrukturtechnik gekoppelt, so dass das gesamte System realitätsnah modelliert werden kann.

Acknowledgments

An erster Stelle möchte ich mich bei Prof. Gerhard Müller bedanken für die Möglichkeit, am Lehrstuhl für Baumechanik arbeiten zu dürfen und diese Arbeit unter seiner Führung erstellen zu können. Prof. Müller hat mich durch seine fachlichen und inhaltlichen Anmerkungen immer wieder auf neue Ideen gebracht, mir aber dennoch die wissenschaftliche Freiheit gelassen, diese Arbeit nach meiner Vorstellung zu gestalten.

Tevens bedank ik Prof. Karel van Dalen voor zijn bereidwilligheid om mijn proefschrift als tweede promotor te beoordelen en voor zijn waardevolle inhoudelijke aanwijzingen. Danke ebenso an Prof. Roberto Cudmani für die Übernahme des Vorsitzes der Prüfungskommission und die Organisation des Promotionsverfahrens.

Dr.-Ing. Georg Frühe hat mich seit meiner Masterarbeit und weiter in seiner Funktion als Mentor für die TUM Graduate School betreut. Ich möchte mich ganz herzlich für seine Zeit, seine Motivation und sein Engagement bedanken. Dr.-Ing. Martin Buchschmid war als stellvertretender Lehrstuhlleiter ebenfalls jederzeit bereit, offene Fragen mit mir zu diskutieren oder meinen Gedankengängen zuzuhören. Auch dafür herzlichen Dank.

Insgesamt war die Zeit am Lehrstuhl ein sehr schöner Lebensabschnitt, was sicher an unserer angenehmen Arbeitsatmosphäre lag. Dafür möchte ich mich bei allen Kollegen bedanken, die dazu beigetragen haben. Namentlich möchte ich Martin Dengler und Christoph Winter nennen, mit denen ich in vielen Diskussionen und Gesprächen immer wieder neue Erkenntnisse erlangt habe.

Der größte Dank gebührt jedoch meiner Familie, die mich Zeit meines Lebens unterstützt, gefördert, beraten, gefordert, begleitet, gelehrt, beruhigt und unterhalten hat. Danke.

Contents

List of symbols

Latin Symbols

$\mathbf{a}$, $\mathbf{b}$	Exemplary vectors
A	Cross sectional area
A_1, A_2	Measure for the amplitude of the compressional wave in Cartesian coordinates
A_{01}, A_{02}	Measure for the amplitude of the compressional wave in Cartesian coordinates for the static case
$\underline{A}_1$	Modified measure for the amplitude of the compressional wave in Cartesian coordinates for a spatially limited layer
A_r	Amplitude reduction factor
A_t, A_0	Amplitudes of the displacement on the halfspace surface of a system with trench and without trench
b_x, b_y	Widths of the load in x- and y-direction
B_{i1}, B_{i2}	Measure for the amplitudes of the shear waves in Cartesian coordinates with $i = x, y$
B_{0i1}, B_{0i2}	Measure for the amplitudes of the shear waves in Cartesian coordinates for the static case with $i = x, y$
$\underline{B}_{i1}$	Modified measure for the amplitudes of the shear waves in Cartesian coordinates for a spatially limited layer with $i = x, y$
B_x, B_y	Repetition lengths in x- and y-direction
$[B]$	Matrix containing the derivatives of the form functions
c_p, c_s, c_r	Velocities of the compressional wave (P-wave), shear wave (S-wave) and Rayleigh wave
C_{ilm}	Measure for the amplitudes of the compressional and shear waves in spherical coordinates with $i = 1, 2, ..., 6$
C_{in}	Measure for the amplitudes of the compressional and shear waves in cylindrical coordinates with $i = 1, 2, ..., 6$

$\mathbf{C}$	Vector containing the amplitudes of the unit stress states on the halfspace surface Λ and the cylindrical coupling surface Γ
$\mathbf{C_s}$	Vector containing the amplitudes of the unit stress states on the halfspace surface Λ and the spherical coupling surface Γ_s
C_{iz}	Amplitudes of the unit stress states on the halfspace surface Λ with $i = z, y, x$
C_{jr}	Amplitudes of the unit stress states on the cylindrical coupling surface Γ with $j = r, x, \varphi$
C_{rj}	Amplitudes of the unit stress states on the spherical coupling surface Γ_s with $j = r, \vartheta, \varphi$
d	Depth of the covering of an underground tunnel
d_1	City-Block metric
$d_{1,av}$	Average City-Block metric
d_{cos}	Cosine coefficient
d_{Dice}	Dice coefficient
d_{MAC}	Modal Assurance Criterion
$d_{Pearson}$	Pearson correlation coefficient (Q correlation coefficient)
d_r	Minkowski metric
d_s	Element length of the circular Finite Element mesh along the circumference
d_t	Depth of a trench on the halfspace surface
d_ϑ, d_φ	Element lengths of the spherical Finite Element mesh along the longitude and the latitude
$[D]$	Elasticity tensor
E	Young's modulus
$\underline{\mathrm{E}}$	Complex Young's modulus
f	Frequency
F, G	Auxiliary parameters for the calculation of the shear stresses in spherical coordinates
G	Shear modulus
$[G]$	Matrix relating the strain and displacement fields
h	Distance between the center of the cylinder or sphere and the halfspace surface
h_i	Thickness of a spatially limited layer in Cartesian coordinates
k_1, k_2	Coefficients to determine the scalar and vector potential in cylindrical coordinates

k_p, k_s	Wavenumbers of the compressional and shear wave
k_r	Radial wavenumber
k_x, k_y	Wavenumbers in x- and y-direction
K_x, K_y	Wavenumbers of specific excitations in each x- and y-direction
$[K]$	Matrix relating the stresses and unknowns in the Cartesian coordinate system
$[K_{hs}]$	Matrix relating the stresses and unknowns of a halfspace in the Cartesian coordinate system
$[K_{ITM}]$	Stiffness matrix of the system halfspace with cylindrical cavity with $[K_{\Lambda\Lambda_{ITM}}]$, $[K_{\Gamma\Lambda_{ITM}}]$, $[K_{\Lambda\Gamma_{ITM}}]$, $[K_{\Gamma\Gamma_{ITM}}]$
$[K_{s\,ITM}]$	Stiffness matrix of the system halfspace with spherical cavity with $[K_{\Lambda\Lambda_{ITM}}]$, $[K_{\Gamma_s\Lambda_{ITM}}]$, $[K_{\Lambda\Gamma_{sITM}}]$, $[K_{\Gamma_s\Gamma_{sITM}}]$
$[K_{FE}]$	Stiffness matrix of the cylindrical Finite Element structure with $[K_{\Gamma\Gamma_{FE}}]$, $[K_{\Gamma\Omega_{FE}}]$, $[K_{\Omega\Gamma_{FE}}]$, $[K_{\Omega\Omega_{FE}}]$ for 2.5-dimensional finite elements
$[K_{FE}]$	Stiffness matrix of the spherical Finite Element structure with $[K_{\Gamma_s\Gamma_{sFE}}]$, $[K_{\Gamma_s\Omega_{FE}}]$, $[K_{\Omega\Gamma_{sFE}}]$, $[K_{\Omega\Omega_{FE}}]$ for three-dimensional finite elements
l_i	Counter of a spatially limited layer in Cartesian coordinates
L	Basic quantity length
m, l	Degree and order of the spherical harmonics
M	Basic quantity mass
M	Maximum degree of the spherical harmonics
$[M]$	Mass matrix of the Finite Element structure
n	Fourier series member in circumferential direction in cylindrical coordinates
n_{GP}	Number of Gauß points
N_t	Number of samples in the time domain
N_x, N_y	Number of samples on the halfspace surface in x- and y-direction
N_ϑ	Maximum number of points on the longitude of a sphere
N_φ	Maximum number of points on the latitude of a sphere
N_φ	Maximum number of points along the circumference of a cylinder
$[N]$	Matrix containing the form functions
$\mathbf{p}$	Load vector
p_{mov}	Function of a moving load
p_{sta}	Function of a stationary load

p_r, p_x, p_φ	Components of the load vector in cylindrical coordinates
p_r, p_ϑ, p_φ	Components of the load vector in spherical coordinates
p_z, p_y, p_x	Components of the load vector in Cartesian coordinates
P_z	Vertical, harmonic load on the halfspace surface or inside the soil
P_{0z}	Amplitude of the load
$\mathbf{P_{ITM}}$	Load vector containing the loads on the halfspace surface Λ and the cylindrical coupling surface Γ
$\mathbf{P_{\Lambda_{ITM}}}$	Load vector containing the load on the halfspace surface Λ
$\mathbf{P_{\Gamma_{ITM}}}$	Load vector containing the load on the cylindrical coupling surface Γ
$\mathbf{P_{\Gamma_{s\,ITM}}}$	Load vector containing the load on the spherical coupling surface Γ_s
$\mathbf{P_{\Lambda_{1L}}}$, $\mathbf{P_{\Lambda_{2L}}}$	Load vector containing the loads on the surfaces Λ_1 and Λ_2 of a layered halfspace
$\mathbf{P_{\Lambda_{2HC}}}$, $\mathbf{P_{\Gamma_{HC}}}$	Load vector containing the loads on the surfaces Λ_2 and Γ of a halfspace with cylindrical cavity
$p_{i,\Lambda}$	Components of the load vector on the halfspace surface Λ with $i = z, y, x$
$p_{j,\Gamma}$	Components of the load vector on the cylindrical coupling surface Γ with $j = r, x, \varphi$
p_{j,Γ_s}	Components of the load vector on the spherical coupling surface Γ_s with $j = r, \vartheta, \varphi$
Q	General, dimensional quantity
Q^i	Components of the vector of the volume force
r, ϑ, φ	Spherical coordinates
R	Radius of the cylinder or the sphere
R	Insertion Loss
$[S_{ITM}]$	Matrix containing the stress components of the superposed system halfspace with cylindrical cavity with $[S_{\Lambda\Lambda_{ITM}}]$, $[S_{\Gamma\Lambda_{ITM}}]$, $[S_{\Lambda\Gamma_{ITM}}]$, $[S_{\Gamma\Gamma_{ITM}}]$
$[S_{s\,ITM}]$	Matrix containing the stress components of the superposed system halfspace with spherical cavity with $[S_{\Lambda\Lambda_{ITM}}]$, $[S_{\Gamma_s\Lambda_{ITM}}]$, $[S_{\Lambda\Gamma_{s\,ITM}}]$, $[S_{\Gamma_s\Gamma_{s\,ITM}}]$
t	Time coordinate
t_{max}	Time of the maximum displacement
T	Basic quantity time
T	Tanimoto coefficient

$[T]$	Transformation matrix combining $[T_1]$ and $[T_2]$
$[T_1]$	Transformation matrix for the transformation from polar into Cartesian coordinates
$[T_2]$	Transformation matrix containing the Fourier series expansion
$[T_s]$	Transformation matrix combining $[T_{s\,1}]$ and $[T_{s\,2}]$
$[T_{s\,1}]$	Transformation matrix for the transformation from spherical into Cartesian coordinates
$[T_{s\,2}]$	Transformation matrix containing the development into spherical harmonics
$u_{i,\Lambda}$	Components of the displacement vector on the halfspace surface Λ with $i = z, y, x$
$u_{j,\Gamma}$	Components of the displacement vector on the cylindrical coupling surface Γ with $j = r, x, \varphi$
u_{j,Γ_s}	Components of the displacement vector on the spherical coupling surface Γ_s with $j = r, \vartheta, \varphi$
$u_k^{(iz,s)}(s)$	Resulting displacements on the halfspace surface Λ due to $\sigma_{iz}(s)$ with $k = z, y, x$
$u_k^{(jr,n)}(s)$	Resulting displacements on the halfspace surface Λ due to $\sigma_{jr}(n)$ with $k = z, y, x$
$u_l^{(iz,s)}(n)$	Resulting displacements on the cylindrical coupling surface Γ due to $\sigma_{iz}(s)$ with $l = r, x, \varphi$
$u_l^{(jr,n)}(n)$	Resulting displacements on the cylindrical coupling surface Γ due to $\sigma_{jr}(n)$ with $l = r, x, \varphi$
u_{mov}	Displacement of a system due to a moving load
$\mathbf{u}$	Vector of the displacements
u^i	Components of the vector of the displacements
$\mathbf{u_n}$	Vector of the nodal displacements
$\mathbf{u}_{\boldsymbol{\Lambda}_{\mathbf{ITM}}}$	Vector containing the displacement components on the halfspace surface Λ
$\mathbf{u}_{\boldsymbol{\Gamma}_{\mathbf{ITM}}}$	Vector containing the displacement components on the cylindrical coupling surface Γ
$\mathbf{u}_{\boldsymbol{\Gamma}_{\mathbf{s\,ITM}}}$	Vector containing the displacement components on the spherical coupling surface Γ_s
$\mathbf{u}_{\boldsymbol{\Lambda}_{\mathbf{1L}}}$, $\mathbf{u}_{\boldsymbol{\Lambda}_{\mathbf{2L}}}$	Vector containing the displacement components on the surfaces Λ_1 and Λ_2 of a layered halfspace
$\mathbf{u}_{\boldsymbol{\Lambda}_{\mathbf{2HC}}}$, $\mathbf{u}_{\boldsymbol{\Gamma}_{\mathbf{HC}}}$	Vector containing the displacement components on the surfaces Λ_2 and Γ of a halfspace with cylindrical cavity

$\mathbf{u}_{\mathbf{\Gamma_{FE}}}$	Vector containing the displacement components of the Finite Element structure on the cylindrical coupling surface Γ
$\mathbf{u}_{\mathbf{\Gamma_{s\,FE}}}$	Vector containing the displacement components of the Finite Element structure on the spherical coupling surface Γ_s
$[U_{ITM}]$	Matrix containing the displacement components of the superposed system halfspace with cylindrical cavity with $[U_{\Lambda\Lambda_{ITM}}]$, $[U_{\Gamma\Lambda_{ITM}}]$, $[U_{\Lambda\Gamma_{ITM}}]$, $[U_{\Gamma\Gamma_{ITM}}]$
$[U_{s\,ITM}]$	Matrix containing the displacement components of the superposed system halfspace with spherical cavity with $[U_{\Lambda\Lambda_{ITM}}]$, $[U_{\Gamma_s\Lambda_{ITM}}]$, $[U_{\Lambda\Gamma_{sITM}}]$, $[U_{\Gamma_s\Gamma_{sITM}}]$
v	Velocity of a moving load
w_k	Weighting factor of the Gauß points
x, r, φ	Cylindrical coordinates
x, y, z	Cartesian coordinates
y_{c1}, y_{c2}, y_{c3}	Comparison functions

Greek Symbols

Γ	Cylindrical coupling surface
Γ_s	Spherical coupling surface
δW	Total virtual work
δW_e	Virtual work of the external forces
δW_i	Virtual work of the internal forces
δW_I	Virtual work of the inertia forces
ε^{ij}	Components of the strain tensor
ζ	Hysteretic damping ratio
ζ_k, η_k	Coordinates of the Gauß points
λ	Lamé constant
λ_1, λ_2	Coefficients to determine the scalar and vector potential in Cartesian coordinates
λ_p, λ_s, λ_r	Wavelengths of the compressional wave, shear wave and Rayleigh wave
Λ	Halfspace surface
Λ_1, Λ_2	Halfspace surfaces of a layered halfspace
μ	Lamé constant
ν	Poisson ratio
π	Dimensionless quantity

π_d	Dimensionless depth of the covering of the tunnel
π_f	Dimensionless frequency
π_h	Dimensionless depth of the top layer of a layered halfspace
π_P	Dimensionless load
π_R	Dimensionless radius of the tunnel
π_u	Dimensionless displacement
π_y	Dimensionless width of the load in y-direction
ρ	Density
$\sigma_{iz,\Lambda}$	Components of the stress tensor on the halfspace surface Λ with $i = z, y, x$
$\sigma_{iz}\left(s\right)$	Unit stress state on the halfspace surface Λ with $i = z, y, x$ in dependency on the wavenumber $k_y = s\ \Delta k_y$
$\sigma_{iz}\left(s, o\right)$	Unit stress state on the halfspace surface Λ with $i = z, y, x$ in dependency on the wavenumbers $k_x = o\ \Delta k_x$ and $k_y = s\ \Delta k_y$
$\sigma_{iz}^{(jr,n)}\left(s\right)$	Resulting stresses on the halfspace surface Λ due to $\sigma_{jr}\left(n\right)$ with $i = z, y, x$
$\sigma_{jr,\Gamma}$	Components of the stresses on the cylindrical coupling surface Γ with $j = r, x, \varphi$
$\sigma_{jr}\left(n\right)$	Unit stress state on the cylindrical coupling surface Γ with $j = r, x, \varphi$ in dependency on the Fourier series member in circumferential direction n
$\sigma_{jr}^{(iz,s)}\left(n\right)$	Resulting stresses on the cylindrical coupling surface Γ due to $\sigma_{iz}\left(s\right)$ with $j = r, x, \varphi$
σ_{rj,Γ_s}	Components of the stresses on the spherical coupling surface Γ_s with $j = r, \vartheta, \varphi$
$\sigma_{rj}\left(m, l\right)$	Unit stress state on the spherical coupling surface Γ_s with $j = r, x, \varphi$ in dependency on the series members m and l
$\sigma_{rj}^{(iz,os)}\left(m, l\right)$	Resulting stresses on the spherical coupling surface Γ_s due to $\sigma_{iz}\left(o, s\right)$ with $j = r, x, \varphi$
$\boldsymbol{\sigma}$	Vector containing the Cartesian components of the stress tensor σ^{xx}, σ^{yy}, σ^{zz}, σ^{xy}, σ^{yz}, σ^{xz}
$\boldsymbol{\sigma}_\mathbf{c}$	Vector containing the cylindrical components of the stress tensor σ^{xx}, σ^{rr}, $\sigma^{\varphi\varphi}$, σ^{xr}, $\sigma^{\varphi r}$, $\sigma^{x\varphi}$
$\boldsymbol{\sigma}_\mathbf{s}$	Vector containing the spherical components of the stress tensor σ^{rr}, $\sigma^{\vartheta\vartheta}$, $\sigma^{\varphi\varphi}$, $\sigma^{r\vartheta}$, $\sigma^{r\varphi}$, $\sigma^{\vartheta\varphi}$
$[\sigma]$	Stress tensor in Cartesian coordinates
σ^{ij}	Components of the stress tensor
Φ	Scalar Helmholtz potential
χ_0, χ_α	Papkovitch-Neuber potentials

$\boldsymbol{\Psi}$	Vector Helmholtz potential
Ψ_i	Components of the vector Helmholtz potential
Ψ, χ	Scalar potentials in the cylindrical and spherical coordinate systems
ω	Angular frequency
Ω	Angular frequency of one specific excitation

Mathematical Symbols

○—●	Fourier transformation
●—○	Inverse Fourier transformation
δa	Virtual quantity a
i	Imaginary unit
$\lvert\mathrm{a}\rvert$	Absolute value of a parameter a
$\mathbf{a}$	Indication of a vector a
a^i, a_i	Contravariant and covariant components of a vector $\mathbf{a}$
$[A]$	Indication of a matrix A
A^{ij}, A_{ij}	Contravariant and covariant components of a matrix $[A]$
$[I]$	Identity matrix
$\det{[A]}$	Determinant of a matrix $[A]$
$\operatorname{rank}{[A]}$	Rank of a matrix $[A]$
$[A]^T$	Transpose of a matrix $[A]$
$[A]^H$	Adjugate of a matrix $[A]$
$[A]^+$	Moore-Penrose-pseudoinverse of a matrix $[A]$
sign	Signum function
δ_{ij}	Kronecker delta function
$h_m^{(1)}(x)$, $h_m^{(2)}(x)$	Spherical Hankel functions of the first and second kind
$H_n^{(1)}(x)$, $H_n^{(2)}(x)$	Hankel functions of the first and second kind
$j_m(x)$	Spherical Bessel function
$J_n(x)$	Bessel function
$P_m\left(x\right)$	Legendre polynomial
$P_m^l\left(x\right)$	Associated Legendre polynomial
$\check{P}_m^l\left(x\right)$	Normalized associated Legendre polynomial
$y_m(x)$	Spherical Neumann function
$Y_n(x)$	Neumann function (Bessel function of the second kind)
$Y_m^l(\vartheta,\varphi)$	Spherical harmonic of degree m and order l
$\Phi_l(\varphi)$	Azimuthal-dependent part of the spherical harmonics

$\Theta_m^l(\vartheta)$	Polar angle-dependent part of the spherical harmonics
$\in_{ikl}$	Permutation symbol
$\dot{a}$	Partial derivative of a function a with respect to time
$\frac{\partial a}{\partial x}$	Partial derivative of a function a with respect to the coordinate x
$a\|_x$	Covariant derivative of a function a with respect to the coordinate x
$a_{,x}$	Partial derivative of a with respect to x

Diacritical Signs

$\bar{a}$	Value in the singly Fourier transformed domain
$\tilde{a}$	Value in the twofold Fourier transformed domain
$\hat{a}$	Value in the threefold transformed domain
a^*	Conjugate complex value to a value a

Acronyms

ABC	Absorbing Boundary Condition
ARF	Amplitude Reduction Factor
BEM	Boundary Element Method
FC	Fullspace with Cylindrical Cavity
FEM	Finite Element Method
GP	Gauß Point
HC	Halfspace with Cylindrical Cavity
HS	Halfspace
ITM	Integral Transform Method
L	System of Layers
MAC	Modal Assurance Criterion
PiP	Pipe-in-Pipe Method
PML	Perfectly Matched Layer Method
SBFEM	Scaled Boundary Finite Element Method
TLM	Thin Layer Method

1 Introduction

1.1 Motivation

Forces which are applied inside the soil or at its surface lead to displacements of the medium. If dynamic or moving forces are considered, the energy that is introduced into the soil leads to oscillations of the system. These oscillations can be perceived at the surface of the soil and lead to problems or discomfort depending on the amplitude and phase of the vibrations and on the sensitivity of the immission system.

On the one hand the excitation forces can be due to uninfluenceable natural phenomena, on the other hand human-induced actions can also lead to an excitation of the soil. During the last decades the proportion of human-induced forces on the soil has continuously increased. Heavy manufacturing or construction machines are more commonly developed and used. Concerning railway traffic, the velocity as well as the weight of the trains was considerably raised. Also, due to the denser building development, railways are more probable to be situated in cultivated areas. All these developments lead to increased vibrations of the soil.

Examining the development of the immission systems, vibrations of the soil usually affect the buildings itself as well as machines or individuals inside the building. As modern buildings are often built from light-weight material, the root-point excitation of the building by the vibration of the soil can lead to higher vibrations of building components compared to massive constructions. Moreover, the range of application of modern machines and thus their sensitivity concerning vibrations is also increasing. Finally, also humans are more and more aware of noise and oscillations in buildings and suffer discomfort or health problems if their personal limit of acceptance is exceeded.

Resulting out of the increased excitation of the soil and increased sensitivity of the immission system, the necessity to reliably predict the oscillations that will be generated by specific forces is also raised. With accurate models the effect of new railway lines or other excitations on existing buildings can be assessed and possible mitigation measures can be modeled if the vibrations are found to be unacceptable. The modeling of structures is usually done with the Finite Element Method as it is appropriate to model the detailed and complex geometry of structures by discretizing them by finite elements. The modeling of the soil, however, requires more specific methods due to the infinite extension of the medium which has to be adequately represented in the model. Analytical solutions exist in the scope of the Integral Transform Method that describe the behavior of the medium exact, but they are only applicable for rather simple geometries and material descriptions. Independent of the difficulty of modeling an infinite medium, for some applications it is also necessary that the model does not only describe the soil but also structures that are positioned inside the soil. This is not possible in the scope of a pure Integral Transform Method approach.

In this work, a coupled approach of the Integral Transform Method and the Finite Element Method shall be derived in order to model a system of a half-infinite soil with a horizontal surface and various types of structural elements that are positioned inside the soil.

1.2 Literature review

The problem of computing an infinite system is not a new one. There are different methodologies existing that deal with wave propagation in a semi-infinite or infinite medium.

Finite Element Method

An appropriate description of detailed and complex geometries can be achieved by using the Finite Element Method (FEM). The limitations of this approach lie in the lacking boundaries of semi-infinite or infinite systems. As the Finite Element mesh is limited, artificial reflections from the boundaries of the mesh arise which create errors compared to the real, infinite system.

There are several modifications of the FEM possible in order to reduce the disturbing effects of these artificial boundary conditions. Based on a Finite Element discretization the Thin Layer Method (TLM) as a special form of the FEM has been developed to describe the system of a layered soil with horizontally infinite layers of material. As one of the first [Lysmer 1970] used the TLM for his analysis of Rayleigh waves in an isotropic, layered halfspace derived from a limiting process to the Finite Element mesh. [Waas 1972] split up the complete medium into an irregular part that is modeled with finite elements flanked by two layered regions at both sides of the Finite Element mesh. These irregular regions are in horizontal direction infinitely extended. [Waas 1972] discretized the material layers in vertical direction with degrees of freedom only at the upper and lower boundary of each layer assuming linear shape functions in vertical direction and solved the problem in the frequency domain with analytical approaches in the horizontal direction. In contrast to [Lysmer 1970] he derived the characteristic equations directly from the principle of virtual work. The boundary conditions beneath the Finite Element mesh as well as the thin layers are described as a fixed support. Therefore, physically non-existing reflections from this boundary are possible but they are assumed to be negligible if the distance between the surface and the boundary is big enough. [Rücker and Said 1994] modeled a system consisting of a tunnel-soil-building-interaction problem by describing the tunnel, the building and the soil between with two-dimensional finite elements of a certain width. The regions left and right of the Finite Element mesh are modeled using the TLM. The part underneath the Finite Element mesh is described with frequency-dependent, viscous dampers in contrast to the fixed support of [Waas 1972]. [Kausel 1994] derived the TLM in the time domain thus avoiding complex valued eigenvalues. Later, [Kausel 1999] developed Green's functions to describe dynamic point sources on laminated media with the help of the TLM. [Park 2002] expanded the TLM for semi-infinite and finite media using the substructure method for a time domain formulation and paraxial approximation for calculations in the frequency domain. He also developed a formulation of the TLM for cylindrical and spherical coordinate systems and analyzed the phenomenon of numerical dispersion, which occurs in the TLM due to the fact that the medium is discretized in vertical direction. This discretization leads to frequency-dependent differences concerning the results for the calculated wave speed between the TLM method and a continuous, analytical calculation. [Park and Kausel 2003] derived ”tuning factors” which can be used to adapt the dynamic stiffness matrix in order to minimize this effect of numerical dispersion. [De Oliveira Barbosa et al 2012] combined the TLM with the Perfectly Matched Layer Method (PML). By this method they are able to model an infinite system consisting of different layers of material. The different layers are described with the TLM, the infinite extension is modeled with the PML.

In the PML the finite system, which can be solved numerically, is surrounded by a layer of absorbing material in which the waves are attenuated by scaling functions and thus decreasing exponentially. Therefore, reflections from the boundaries are prevented in the model. This approach was developed in the 90's. [Berenger 1994] described the methodology for the first time thus being able to model a situation where an incident wave is not reflected at a given boundary at all but completely absorbed independent of its frequency or the angle of incidence at the boundary. Since then the PML has been adapted to different fields of dynamic behavior. [Basu and Chopra 2003] modified it for time-harmonic elastodynamics in Cartesian coordinates. [Bécache et al 2003] mentioned unstable behavior of the PML and devised two conditions which have to be fulfilled in order to get numerically stable results. [Wu et al 1997] presented an uniaxial PML using anisotropic material as a model of the boundary of the Finite Element mesh. [Johnson 2007] stated that both the method of Berenger as well as the approach presented by Wu can be derived in a general way as the result of a complex coordinate stretching, which is based on an analytical continuation of Maxwells equations into spatially complex coordinates referred to which the fields are decaying exponentially. This complex coordinate stretching is also used in the work of [Rammerstorfer 2008]. [Hastings et al 1996] compared the results of a PML analysis with those they could achieve with Absorbing Boundary Conditions (ABC). For compressional and shear waves they achieved more accurate results with the PML than with absorbing boundaries. The difference between these methods consists in the way the boundary is treated. In the PML the considered finite system is surrounded by an additional, artificial layer of material which avoids reflections at the boundary between the system itself and the artificial layer but models an absorption of the energy of wave propagation inside the artificial layer. By working with ABCs there is no additional layer but the waves that are arriving at the limits of the system are not reflected, but absorbed directly at the boundary.

Also the ABC method has a long tradition. The basic idea is to use boundary conditions at the limits of the Finite Element mesh that only allow wave propagation out of the modeled region and absorb waves which are propagating into the Finite Element mesh as described in [Grote 2000]. For a two-dimensional medium the separation of the waves propagating from or into the Finite Element mesh is complex. [Clayton and Engquist 1977] developed an approach in order to separate the two wave types based on paraxial approximations of the dispersion relation. [Givoli 1991] summarized the information of different fields of mechanics (Hydrodynamics, Electrical Engineering, Civil Engineering, Plasma Physics etc.) concerning the problem of absorbing boundaries. He stated that though there are several publications about local absorbing boundary conditions which perform quite accurately for different situations they usually show reflections if the situation, e. g. the angle of incidence or the frequency range, is modified. Using high-order ABCs is a possibility to cope with the problem of a lacking trackability of local ABCs. But most of the ABCs, which have been developed during the first years of ABCs are only theoretically enabling an arbitrary high-order, because also high-order derivatives of the ABC would be necessary. [Collino 1993] derived ABCs which could be used without the necessity for high derivatives in space and time. Since then more high-order ABCs have been developed, mainly covering the field of the acoustic wave equation. Those treating ABCs for elastodynamics as in [Rabinovich et al 2011] showed unstable behavior for long times. A first stable formulation of high-order local

ABCs is presented in [Baffet et al 2012].

Another adaptation of the FEM for the calculation of infinite or semi-infinite systems is the use of infinite elements. In general, there are two possible approaches to model the infinite extension of the elements. The first approach is based on the use of decay functions which describe the necessary characteristics of the displacement for an infinite extension using suitable form functions. [Bettess 1977] presented a method where the infinite system is modeled in an inner region with finite elements, but the outer layer of elements is described with infinite, exponentially decaying Lagrange polynomials as shape functions. Based on this work, the method of infinite elements was derived for static ([Bettess and Bettess 1984]) and dynamic problems ([Bettess and Bettess 1991]). [Yang 1996] presented a frequency-dependent infinite element. A frequency-independent infinite element is used in [Maharan 2004]. The second approach for the method of infinite elements is based on a mapping of the geometry of the infinite element, which extends the geometry from a finite to an infinite range while the form functions are still regular polynomial functions. [Zienkiewicz et al 1983] described the infinite element by mapping semi-infinite stripes of material on finite elements using appropriate transformation functions. [Abdel-Fattah et al 2000] transformed the infinite, global coordinates to local, finite coordinates using different functions to describe the decay of the field variables (reciprocal, exponential, logarithmic).

Scaled Boundary Finite Element Method

Alternatively to a Finite Element formulation, the Scaled Boundary Finite Element Method (SBFEM) is an additional possibility to model infinite media. [Wolf and Song 2000] presented the possibility to describe finite or infinite media by dividing the medium into several subdomains starting from a scaling center. After transforming the respective partial differential equation into the new coordinates, the surface of the medium is discretized with finite elements thus leading to an ordinary differential equation which can be solved approximately in dependency on the coordinate of the radial direction. In [Wolf 2003] wave propagation in an infinite medium is modeled using the SBFEM.

Boundary Element Method

Instead of discretizing the domain with finite elements, in the Boundary Element Method (BEM) only the boundaries of the domain are discretized. According to a short overview over the historical development by [Gaul et al 2003], [Jaswon 1963] and [Symm 1963] have been the first scientists to develop Boundary Element Methods to solve potential problems using Green's third identity. Subsequently, applications for elastostatic (for example [Rizzo

1967]) and elastodynamic problems (for example [Cruse and Rizzo 1968] or [Cruse 1968]) were presented.

For an infinite medium, the respective differential equation is transformed into a boundary formulation using Green's functions and the reciprocity theorem, as described e. g. in [Gaul et al 2003]. If the domain to be modeled is infinite in one direction, it is possible to discretize only the two-dimensional surface and to take into account the infinite extension in the third direction by fulfilling the Sommerfeld condition of radiation within the fundamental solutions. Nevertheless, if also the surface possesses an infinite extension, the numerically necessary truncation of the infinite surface leads to an error in the calculations. As [Manolis and Beskos 1988] or [Beer and Watson 1989] stated infinite boundary elements can be coupled to the regular domain to model the infinite extension of a continuum. Using a decay function, the behavior of the displacements in an infinite extension is modeled in dependency on the distance between an arbitrary, considered point and the center of the decay function. Also [Zhang and Song 1991] presented an approach for the modeling of a three-dimensional, semi-infinite halfspace. The amplitudes of all wave types are reduced by the same decay function in this method. As the real behavior is different, [Arias and Achenbach 2004] presented a method where only the Rayleigh waves are considered. The amplitudes of the compressional and shear waves are neglected as they are stronger diminished by geometrical damping than the surface Rayleigh waves. Correction coefficients are calculated that are added to the system matrices at the positions of the end nodes between the finite and infinite regions.

The response of a halfspace due to a moving load was calculated by [Andersen and Nielsen 2003] with a three-dimensional model. A time domain BEM for two-dimensional scalar wave propagation problems was presented by [Mansur and Brebbia 1982b] and [Mansur and Brebbia 1982a]. As [Israil and Banerjee 1990] stated, the derivations were pioneering, but led to a formulation with a rather complicated and implicit kernel. Therefore, [Israil and Banerjee 1990] presented alternative kernels for the two-dimensional transient scalar wave propagation and [Israil et al 1992] extended it for axisymmetric and three-dimensional scalar wave propagation while [Carrer and Mansur 1996] included initial conditions for the two-dimensional case. The computational effort of the BEM calculations was reduced by [Bonnet et al 1998] who transformed the unsymmetric, full matrices without band structure into symmetric matrices using the Galerkin-method. [Messner and Schanz 2010] presented a Fast Boundary Element Method where the Convolution Quadrature Method is used in the time domain in order to reduce the computational effort. In another step, the Fast Multipole Boundary Element Method, [Fischer 2004] split the boundary integral operators into near-field and far field contributions and calculated the response of the total system using the multipole-approach.

Besides developments for the improvement of the pure BEM concerning computational costs or the range of application, another advancement was the coupling of BEM and FEM approaches. One of the first publications concerning the coupling of boundary solution techniques to Finite Element solutions was published by [Zienkiewicz et al 1977]. The motivation was to combine the advantages of both approaches. [Brebbia and Georgiou 1979] examined two approaches to solve two-dimensional elastostatic problems with a coupled FEM-BEM approach presenting the result that treating the boundary element region as finite element seems to be an interesting possibility to be implemented in Finite Element codes. [von Estorff and Prabucki 1990] used the coupled approach for a general two-dimensional elastodynamic problem to calculate the response of an elastic halfspace to transient loads. An overview over the application of a coupled FEM-BEM approach for three-dimensional soil-structure-interactions can be found in [Savidis and Bode 2002]. This approach was also compared to field investigations as published by [Savidis and Bergmann 2005]. [Schepers and Savidis 2009] analyzed the behavior of earth-fill dams with the coupled approach and compared it to the efficiency of trenches as measures for the reduction of vibrations. Also for the calculation of a system where elements like diaphragm or quay walls are surrounded by soil, [Clouteau et al 2000] used a periodical approach for the coupling of finite elements and boundary elements. Assuming periodicity of the structures in one direction, a Floquet decomposition is applied to reduce the extension of the discretized domain. A limited reference cell is discretized and the infinite extension is introduced into the system using the periodicity conditions. Subsequently, a number of publications present applications and extensions of this method of a periodic FEM-BEM coupling. In 2005 [Clouteau et al 2005] extended the method to a horizontally layered soil using Green-Floquet functions which are defined as the infinite sum of Green's functions at a certain point for sources that are periodically repeated in space. [Clouteau et al 2006] applied the method for the calculation of the response of an underground tunnel in a layered soil to dynamic loads inside the tunnel. Two examples of real existing tunnels in Paris and London are calculated. The numerical validation of the method is presented in [Lombaert et al 2006] where experiments were carried out at a new high-speed train line between Brussels and Cologne. The dynamic soil and track characteristics are determined experimentally and the transfer functions of soil and the coupled track-soil-system are measured and used for the validation of the numerical results. The effects of a floating slab track are predicted with a periodic FEM-BEM approach in [Gupta and Degrande 2010]. The vibration isolation of continuous and discontinuous floating slab tracks are analyzed and found to be similar for excitation frequencies above the isolation frequencies of the track. At low frequencies, however, continuous floating slab tracks show a better efficiency. The effects of different mitigation measures on the transmission path between the point of load application and a receiving structure were analyzed with a 2.5-dimensional FEM-BEM approach as part of the RIVAS project (Railway Induced Vibration Abatement Solutions) by [Coulier et al 2011]. [Lombaert and Degrande 2009] concentrated on the different excitation mechanisms of railway-induced vibrations and analyzed the response of the system to quasi-static and dynamic excitation due to random track unevenness, which is represented by its power spectral density. [Clouteau et al 2013] wrote a review presenting a general framework that describes the different solution procedures for a soil-environment-system in a general way such that it is valid for different chosen methods (e. g. FEM, BEM).

[Gupta et al 2009] published the results of a parametric study which was performed to analyze the influence of different system parameters on the response of the coupled system. Shear modulus and material damping are identified as main influence parameters for the propagation of waves inside the soil. The geometry of the tunnel is found to influence mainly the response near the tunnel and a larger tunnel leads to less vibrations on the surface of the soil due to energy radiation. The parametric study is performed using the periodic FEM-BEM coupling and compared to the results of a Pipe-in-Pipe model.

Pipe-in-Pipe Method

The Pipe-in-Pipe Method (PiP) also uses the invariance of the system in lengthwise direction and solves the 2.5-dimensional system. [Forrest and Hunt 2006] developed this semi-analytical solution of the differential equation of a system where a circular tunnel cross section is loaded whereas the longitudinal direction is transformed into the wavenumber domain. Based on the cylindrical shell equations, the displacements of the circular tunnel shell are calculated with respect to the circular loads on the shell in the Fourier transformed domain. The halfspace is described, starting with the Lamé differential equation, also in the Fourier transformed domain. Both systems can be coupled and the response of an arbitrary point in the halfspace due to a load on the cylindrical shell can be determined. As presented in [Gupta et al 2007] the results show a good accordance to those of a coupled FEM-BEM approach. A horizontal surface representing the halfspace surface can be introduced according to [Hussein et al 2006]. In a first step, the displacements at the transition between tunnel surface and infinite medium are calculated with the PiP assuming that the near field displacement of the tunnel is not influenced by the halfspace surface. In a next step, loads are calculated in a fullspace model that are necessary to generate the same displacements at a virtual cylinder surface in the fullspace. With these loads, the displacements on the halfspace surface can be computed. In [Hussein et al 2008] this procedure is extended for a layered halfspace, using the assumption that only the layer in which the tunnel is positioned influences the near field of the displacements and stresses. The effect of inclined layers in the halfspace was considered in [Jones and Hunt 2009]. [Jones et al 2010] determined the effect of a free surface on the oscillations inside the medium. The existence of two cylindrical tunnels inside the medium is implemented in [Kuo et al 2011].

Integral Transform Method

Another possibility to solve the differential equation describing the elastodynamic behavior in semi-infinite or infinite media, is used in the Integral Transform Method (ITM). [Wolf 1985] described the methodology to transform a given load from an original domain to a Fourier transformed domain. After the transformation, the response of the system to this load can be evaluated and the response in the original domain is obtained after an inverse Fourier transformation. Several applications of the ITM which can be used for the calculation of soil-structure problems are presented.

[Konrad 1985] used Fourier Transformation Methods to devise the solution of a fullspace with cylindrical excavation in cylindrical coordinates. Later, [Grundmann and Müller 1988] presented the solution of the system of a layered halfspace solved with the ITM. An evaluation of the method was calculated for the system of a layer of soil mounted on a solid rock, which was excited by a plane air wave. [Müller 1989] expanded the method for the calculation of soil-structure-interaction by using mixed boundary conditions for the description of the free surface of the soil as well as for the spatially limited structure. As the inverse Fourier transformation has a high numerical effort, [Lieb 1997] developed an implementation of a Wavelet Transformation Algorithm in order to reduce the computational costs of the ITM. [Lenz 2003] extended the method of Lieb for a three-dimensional system.

With the mentioned modifications, ITM approaches are apt for the calculation of two- or three-dimensional systems with regular geometry. The analytical solution is also used by [van Dalen and Metrikine 2008] and [van Dalen et al 2015] for example to assess the transition radiation that arises if two elastic half-planes or two elastic layers with different parameters are coupled at a boundary and a load is moving on a straight line across this boundary. If there are singular elements existing, ITM calculations cannot be applied without further modifications. The description of complex geometries is advantageous with other approaches as FEM or BEM. A coupling of ITM with FEM or BEM enables the user to combine the positive elements of different methods. [Müller 1993] developed a boundary element formulation based on fundamental solutions of the halfspace which can be calculated with the ITM. A coupling between ITM and FEM was presented by [Zirwas 1996]. He modeled a two-dimensional, finite structure with finite elements and coupled it with a halfspace described by ITM with the substructure technique. [Rastandi 2003] extended Zirwas' solution for a three-dimensional system.

In order to be able to describe complex geometric inclusions which are lying at an arbitrary position in the soil, [Müller et al 2008] developed a fundamental solution for the system of a halfspace with infinite, cylindrical excavation, based on the work of [Buchschmid 2002], who derived fundamental solutions for a two-dimensional halfslice with a hole. [Frühe 2010] devised a fundamental solution for the system of an infinite halfspace with spherical excavation. Thus, not only infinite elements can be modeled but also spatially limited inclusions.

1.3 Outline of the thesis

In this thesis, a coupled ITM-FEM approach is derived to model wave propagation processes in the soil. Using the substructure technique the stiffness matrices of substructures can be coupled. Therefore, as a first step the stiffness matrices of the ITM substructure and the FEM substructure are derived separately.

In chapter 2 the Integral Transform Method is presented. The Lamé differential equation is decoupled using the Helmholtz approach and transformed from partial into ordinary differential equations by a threefold Fourier transformation. The ordinary differential equations can be solved with the boundary conditions of the system. In dependency on the coordinate system the solutions of different fundamental systems can be derived. In this thesis the solutions of a halfspace with a horizontal surface, a fullspace with a cylindrical cavity and a fullspace with spherical cavity are presented.

These fundamental solutions are superposed in chapter 3 in order to be able to model a system with two free surfaces. This solution of a system with two surfaces is obtained by superposing two fundamental systems with one surface each. The surface of each system is loaded with unit loads and the stresses at the surface itself are calculated as well as the stresses at those positions where the second surface shall be introduced. Using the information that the superposition of the stresses has to fulfill the boundary conditions at both surfaces, the flexibility matrix or the stiffness matrix of the superposed system can be calculated. Thus, the solutions of a halfspace with cylindrical cavity and of a halfspace with spherical cavity are derived. These systems can serve as the ITM substructure that shall be coupled to the FEM substructure. The method can analogously be extended to model systems with more than two free surfaces.

Chapter 4 contains the derivation of the stiffness matrix of the Finite Element domain as the second substructure. In case of the spherical Finite Element mesh that can be coupled to the halfspace with spherical cavity, three-dimensional elements are used. However, the Finite Element domain that shall be coupled to the halfspace with cylindrical cavity is formulated with 2.5-dimensional elements. Thus, a formulation of these elements is presented in this chapter. The use of 2.5-dimensional elements is possible because the solution of the ITM substructure halfspace with cylindrical cavity is performed in the wavenumber-frequency domain in dependency on each combination of the wavenumber k_x in longitudinal direction x of the tunnel and the frequency ω. Thus, the spatial direction x can be replaced by the wavenumber k_x also in the Finite Element substructure. The three-dimensional Finite Element mesh of the cylinder is replaced by a superposition of the solutions of a two-dimensional circular mesh in dependency on the y- and z-coordinates for all wavenumbers k_x and ω. Thus, a reduction of the computational cost is obtained while the solution is still able to model the three-dimensional behavior of the structure. The derivation of the stiffness matrix of the 2.5-dimensional elements is presented in this chapter.

After deriving the stiffness matrices of the ITM substructure and the FEM substructure, they are coupled in chapter 5. The equilibrium of forces on the cylindrical or spherical coupling surface as well as the compatibility of the displacements lead to the coupled systems of a halfspace with cylindrical Finite Element mesh or a halfspace with spherical Finite Element mesh.

Some results of the verification of the presented coupled approach are contained in chapter 6. For the first presented coupled structure halfspace with cylindrical Finite Element mesh, dimensionless parameters are introduced to perform a full verification.

In chapter 7 the applicability of the coupled approach for moving loads is mentioned. As examples for possible applications, the effects of mitigation measures are predicted. The insertion loss of a mass-spring system in an underground tunnel is computed for different configurations. Finally, the effect of an open trench as mitigation measure for the reduction of the transmission of vibrations between the point of load application and a point of observation is presented.

2 Fundamental Solutions in Continuum Dynamics

2.1 Preliminary remark

In order to derive the solutions for the ITM substructure of a halfspace with a cylindrical cavity or a halfspace with a spherical cavity, the respective fundamental systems are required. The fundamental systems halfspace, fullspace with cylindrical cavity and fullspace with spherical cavity are presented in this chapter in the sections 2.3, 2.4 and 2.5. The solutions of these systems are based on the fundamental equations in continuum dynamics which are introduced in section 2.2. The superposition of the fundamental systems itself is contained in the following chapter 3.

2.2 Fundamental equations in continuum dynamics

The equilibrium of an infinitesimal small volume element in a three-dimensional continuum is described by the following equation

$$\sigma^{ij}|_j + Q^i - \rho \ddot{u}^i = 0 \tag{2.1}$$

with the Cauchy stress tensor σ^{ij}, the vector of the internal forces inside the volume Q^i and the vector of the inertia forces $\rho \ddot{u}^i$. In equation (2.1) linear elastic behavior of a homogeneous, isotropic material of the continuum is assumed.

If internal forces inside the volume are disregarded and only forces applied at the boundaries of the volume element are taken into account, the relationship between stresses and accelerations can be obtained.

$$\sigma^{ij}|_j - \rho \ddot{u}^i = 0 \tag{2.2}$$

The stress tensor σ^{ij} can be derived from the Green-Lagrange-strain tensor ε^{ij} for a linear elastic, homogeneous, isotropic material according to Hooke's law as

$$\sigma^{ij} = 2\mu\varepsilon^{ij} + \lambda\varepsilon_m^m g^{ij} \tag{2.3}$$

The Lamé constants λ and μ can be further derived from the more common parameters Young's modulus E and Poisson ratio ν by

$$\mu = G = \frac{E}{2\,(1+\nu)} \tag{2.4}$$

$$\lambda = \frac{E\nu}{(1+\nu)\,(1-2\nu)} \tag{2.5}$$

It should be noted that the Lamé constant μ can also be replaced by the shear modulus $G = \mu$.

If it is required to model material damping inside the volume element, hysteretic damping is an adequate approximation for describing the material behavior. According to the correspondence principle mentioned for example in [Wolf 1985] or in [Krämer 1987], hysteretic damping can be modeled by a complex Young's modulus

$$\underline{E} = E\,(1 + i\,\mathrm{sign}\,(\omega)\ \zeta) \tag{2.6}$$

where ζ represents the hysteretic damping ratio of the material. In equation (2.6), a frequency-independent hysteretic damping is used according to [Wolf 1985] or [Gaul 1976]. Measurements presented by [Hardin and Drnevich 1972] also confirmed the applicability of a model assuming frequency independence of material damping for soil material.

The Green-Lagrange-strain tensor ε^{ij} in equation (2.3) can be expressed by the displacement field u^i for small deformations by

$$\varepsilon^{ij} = \frac{1}{2}\left(u^i|^j + u^j|^i\right) \tag{2.7}$$

Introducing equation (2.7) in equation (2.3) and subsequently equation (2.3) in equation (2.2) the Lamé differential equation can be formulated as

$$\mu u^i|_j^j + (\lambda + \mu)\,u^j|_j^i - \rho\ddot{u}^i = 0 \tag{2.8}$$

Every displacement field inside a linear elastic, homogeneous, isotropic continuum has to fulfill the Lamé differential equation. It represents a system of three coupled, partial differential equations. In order to solve this system of equations for the unknown displacements, a decoupling of the equations is advantageous as a direct integration is difficult. The decoupling is done using Helmholtz' principle. This principle states according to e. g. [Eringen and Suhubi 1975] or [Arfken and Weber 1995] that every possible vector field can be replaced by the sum of an irrotational field and a solenoidal field. As the gradient of a scalar field Φ is irrotational and the rotation of a vector field $\boldsymbol{\Psi}$ is solenoidal as stated e. g. in [Meinhold and Miltzlaff 1978], the components of the displacement field u^i can be replaced by

$$u^i = \Phi|^i + \Psi_l|_k \in^{ikl} \tag{2.9}$$

Therefore, for a three-dimensional Cartesian coordinate system the displacements u^i can be calculated as

$$u^1 = \Phi|^1 + \Psi_3|_2 - \Psi_2|_3 \tag{2.10a}$$

$$u^2 = \Phi|^2 + \Psi_1|_3 - \Psi_3|_1 \tag{2.10b}$$

$$u^3 = \Phi|^3 + \Psi_2|_1 - \Psi_1|_2 \tag{2.10c}$$

The introduction of equation (2.9) into the Lamé differential equation (2.8) leads to decoupled partial differential equations for the scalar field Φ and the components of the vector field Ψ_i.

$$\Phi|_j^j - \frac{1}{{c_p}^2}\ddot{\Phi} \quad = 0 \tag{2.11a}$$

$$\Psi_i|_j^j - \frac{1}{{c_s}^2}\ddot{\Psi}_i = 0 \tag{2.11b}$$

In the equations (2.11) c_p and c_s denote the velocities of the compressional waves (P-waves) and the shear waves (S-waves) in the medium in dependency on the material parameters.

$$c_p = \sqrt{\frac{\lambda + 2\mu}{\rho}} \tag{2.12}$$

$$c_s = \sqrt{\frac{\mu}{\rho}} \tag{2.13}$$

Thus, applying Helmholtz' principle, the three coupled partial differential equations of the Lamé differential equation are replaced by four decoupled partial differential equations. The completeness of Helmholtz' principle was first correctly proven by [Somigliana 1892]. This proof was based on the gauge condition that the vector potential $\boldsymbol{\Psi}$ is solenoidal itself.

$$\Psi_i|^i = 0 \tag{2.14}$$

Using this additional requirement, the vector field $\boldsymbol{\Psi}$ contains two independent components and the equations (2.11) describe only three decoupled partial differential equations.

Later, [Long 1967] proved that one component of the vector potential $\boldsymbol{\Psi}$ can be chosen arbitrarily and therefore also three decoupled partial differential equations can be obtained. Both approaches will be used in order to derive the solutions for the system of a halfspace with cylindrical or spherical cavity.

2.3 Fundamental solution for a semi-infinite halfspace

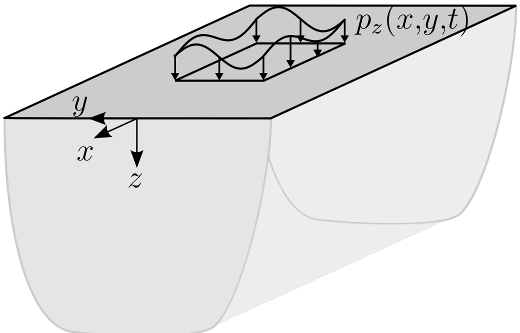

Figure 2.1: Schematic sketch of the halfspace model with an exemplary load

In order to determine the solution for the system of a halfspace as depicted in figure 2.1, the partial differential equations (2.11) can be formulated for the Cartesian coordinate system.

$$\left[\frac{\partial^2}{\partial x^2}+\frac{\partial^2}{\partial y^2}+\frac{\partial^2}{\partial z^2}-\frac{1}{{c_p}^2}\frac{\partial^2}{\partial t^2}\right]\Phi\left(x,y,z,t\right) \quad = 0 \tag{2.15a}$$

$$\left[\frac{\partial^2}{\partial x^2}+\frac{\partial^2}{\partial y^2}+\frac{\partial^2}{\partial z^2}-\frac{1}{{c_s}^2}\frac{\partial^2}{\partial t^2}\right]\Psi_x\left(x,y,z,t\right) = 0 \tag{2.15b}$$

$$\left[\frac{\partial^2}{\partial x^2}+\frac{\partial^2}{\partial y^2}+\frac{\partial^2}{\partial z^2}-\frac{1}{{c_s}^2}\frac{\partial^2}{\partial t^2}\right]\Psi_y\left(x,y,z,t\right) = 0 \tag{2.15c}$$

The component Ψ_z of the vector potential $\boldsymbol{\Psi}$ is set to zero for the given system as mentioned in section 2.2 without any loss of information for the system of a halfspace.

2.3.1 Solution of the system of partial differential equations

A transformation into ordinary differential equations is possible for the given system using a threefold Fourier transformation (see appendix A.1). One of the four partial derivatives remains untransformed, usually the z-coordinate. Regarding the x-, y- and t-coordinates, Fourier transformations are applied from the spatial into the wavenumber domain $x \circ\!\!-\!\!\!-\!\!\bullet\, k_x$, $y \circ\!\!-\!\!\!-\!\!\bullet\, k_y$ and from the time domain into the frequency domain $t \circ\!\!-\!\!\!-\!\!\bullet\, \omega$. Due to the Fourier transformation, the second derivatives with respect to x, y and t in equations (2.15) are replaced by multiplications with the negative wavenumbers respectively frequency squared as also expressed in appendix A.1

$$\left[-{k_x}^2 - {k_y}^2 + {k_p}^2 + \frac{\partial^2}{\partial z^2}\right] \hat{\Phi}\left(k_x, k_y, z, \omega\right) \; = 0 \tag{2.16a}$$

$$\left[-{k_x}^2 - {k_y}^2 + {k_s}^2 + \frac{\partial^2}{\partial z^2}\right] \hat{\Psi}_x\left(k_x, k_y, z, \omega\right) = 0 \tag{2.16b}$$

$$\left[-{k_x}^2 - {k_y}^2 + {k_s}^2 + \frac{\partial^2}{\partial z^2}\right] \hat{\Psi}_y\left(k_x, k_y, z, \omega\right) = 0 \tag{2.16c}$$

with the wavenumbers of the P- and S-waves for a given frequency ω.

$$k_p = \frac{\omega}{c_p} \tag{2.17}$$

$$k_s = \frac{\omega}{c_s} \tag{2.18}$$

The ˆ symbol denotes parameters in the threefold transformed domain.

A solution of the ordinary differential equations (2.16) is possible using an exponential approach for the scalar field $\hat{\Phi}$ and the components of the vector field $\hat{\Psi}_i$ with $i = x, y$

$$\hat{\Phi} \; = A_1\, e^{\lambda_1 z} + A_2\, e^{-\lambda_1 z} \tag{2.19a}$$

$$\hat{\Psi}_i = B_{i1}\, e^{\lambda_2 z} + B_{i2}\, e^{-\lambda_2 z} \tag{2.19b}$$

with

$$\lambda_1 = \sqrt{{k_x}^2 + {k_y}^2 - {k_p}^2} \tag{2.20}$$

$$\lambda_2 = \sqrt{{k_x}^2 + {k_y}^2 - {k_s}^2} \tag{2.21}$$

The unknown coefficients A_1, A_2, B_{i1} and B_{i2} are evaluated using the boundary conditions of the system.

2.3.2 Local and non-local boundary conditions

The solution characteristics strongly depend on the relationship between k_x, k_y and k_p respectively k_s. If λ_1 takes imaginary values (${k_x}^2 + {k_y}^2 < {k_p}^2$), the equations (2.19) describe spatially propagating compressional waves that lead to a far field in the medium. In dependency on the sign of λ_1 the waves are propagating in negative or positive z-direction. If λ_1 has real values (${k_x}^2 + {k_y}^2 > {k_p}^2$), the solution consists of surface waves. A near field is described that is exponentially increasing or decaying with the depth z in dependency on the sign of λ_1. Analogously, λ_2 can be related to spatially propagating shear waves (${k_x}^2 + {k_y}^2 < {k_s}^2$) or to exponentially increasing or decaying surface waves (${k_x}^2 + {k_y}^2 > {k_s}^2$).

As loads shall only be applied on the surface of the halfspace, some of the solution contributions can be excluded. According to the Sommerfeld condition of radiation mentioned in [Sommerfeld 1949], "the energy which is radiated from the sources must scatter to infinity; no energy may be radiated from infinity into the prescribed singularities of the field." Thus, in negative z-direction spatially propagating waves are not possible as well as surface waves with amplitudes that are increasing with the z-coordinate. Using these non-local boundary conditions, the coefficients A_1, A_2, B_{i1} or B_{i2} can be set to zero in dependency on the signs of the wavenumbers and frequencies of the response. [Müller 1989] showed that for negative frequencies the parameters A_1 and B_{i1} describe waves that are physically not possible for both spatially propagating and surface waves and therefore can be set to zero in case of a semi-infinite halfspace.

If the calculations were carried out for positive frequencies, also three of the parameters A_1, A_2, B_{i1} and B_{i2} could be set to zero. However, an additional differentiation would be necessary. For spatially propagating waves A_2 and B_{i2} could be set to zero, for surface waves A_1 and B_{i1}. In order to avoid this case-by-case analysis, all calculations and derivations are carried out for negative frequencies. The results for positive frequencies are complemented using the condition that, as the parameters in the original domain are real, the parameters in the Fourier transformed domain have to be conjugate complex. Therefore, a general, complex parameter $\hat{z}$ in the Fourier transformed domain that has been calculated for a given combination of wavenumbers and frequency ($k_x = \pm K_x$, $k_y = \pm K_y$, $\omega = -\Omega$) can be supplemented for positive frequencies with

$$\hat{z}(K_x, K_y, \Omega) = \hat{z}^*(-K_x, -K_y, -\Omega) \tag{2.22a}$$

$$\hat{z}(K_x, -K_y, \Omega) = \hat{z}^*(-K_x, K_y, -\Omega) \tag{2.22b}$$

$$\hat{z}(-K_x, K_y, \Omega) = \hat{z}^*(K_x, -K_y, -\Omega) \tag{2.22c}$$

$$\hat{z}(-K_x, -K_y, \Omega) = \hat{z}^*(K_x, K_y, -\Omega) \tag{2.22d}$$

with the symbol * indicating the conjugate complex parameter.

After excluding three of the six unknowns using the information about the non-local boundary conditions, the remaining three constants A_2, B_{x2} and B_{y2} can be determined with the help of the local boundary conditions on the surface of the halfspace.

$$\hat{\sigma}_{zz}\left(k_x, k_y, z = 0, \omega\right) = -\hat{p}_z\left(k_x, k_y, \omega\right) \tag{2.23a}$$

$$\hat{\sigma}_{yz}\left(k_x, k_y, z = 0, \omega\right) = -\hat{p}_y\left(k_x, k_y, \omega\right) \tag{2.23b}$$

$$\hat{\sigma}_{xz}\left(k_x, k_y, z = 0, \omega\right) = -\hat{p}_x\left(k_x, k_y, \omega\right) \tag{2.23c}$$

To obtain the unknowns, the dependency of the stresses on the unknowns A_2, B_{x2} and B_{y2} is required and shall be derived in the following section.

2.3.3 Stresses in the Cartesian coordinate system

The relationship between the unknowns and the stresses on the halfspace surface is derived using the material law and the kinematic relations. This is carried out for the general situation with the initial six unknowns A_1, A_2, B_{x1}, B_{x2}, B_{y1} and B_{y2}. Thus, a general solution is presented that can also be adapted to the system of a layered halfspace or a single layer of material on a fixed boundary where the Sommerfeld condition of radiation cannot be applied in the spatially limited layer as will be presented in section 2.3.4.

The components of the stress tensor $\hat{\sigma}_{ij}$ can be expressed according to equation (2.3) in dependency on the Green-Lagrange-strain tensor $\hat{\varepsilon}_{ij}$ for the Cartesian coordinate system as

$$\hat{\sigma}_{ij} = 2\mu\hat{\varepsilon}_{ij} + \lambda\hat{\varepsilon}_{mm}\delta_{ij} \tag{2.24}$$

In matrix notation equation (2.24) can be expressed as

$$\begin{aligned}\begin{pmatrix}\hat{\sigma}_{xx}\\ \hat{\sigma}_{yy}\\ \hat{\sigma}_{zz}\\ \hat{\sigma}_{xy}\\ \hat{\sigma}_{yz}\\ \hat{\sigma}_{xz}\end{pmatrix} &= \begin{bmatrix}\lambda+2\mu & \lambda & \lambda & 0 & 0 & 0\\ \lambda & \lambda+2\mu & \lambda & 0 & 0 & 0\\ \lambda & \lambda & \lambda+2\mu & 0 & 0 & 0\\ 0 & 0 & 0 & 2\mu & 0 & 0\\ 0 & 0 & 0 & 0 & 2\mu & 0\\ 0 & 0 & 0 & 0 & 0 & 2\mu\end{bmatrix} \begin{pmatrix}\hat{\varepsilon}_{xx}\\ \hat{\varepsilon}_{yy}\\ \hat{\varepsilon}_{zz}\\ \hat{\varepsilon}_{xy}\\ \hat{\varepsilon}_{yz}\\ \hat{\varepsilon}_{xz}\end{pmatrix} \\ \hat{\boldsymbol{\sigma}} &= [D] \; \hat{\boldsymbol{\varepsilon}}\end{aligned} \tag{2.25}$$

The linearized strain tensor $\hat{\varepsilon}_{ij}$ is derived from the displacements in Cartesian coordinates as

$$\hat{\varepsilon}_{ij} = \frac{1}{2}\left(\hat{u}_{i,j} + \hat{u}_{j,i}\right) \tag{2.26}$$

In the Fourier transformed domain (k_x, k_y, z, ω), equation (2.26) can be written as

$$\begin{aligned}\begin{pmatrix}\hat{\varepsilon}_{xx}\\ \hat{\varepsilon}_{yy}\\ \hat{\varepsilon}_{zz}\\ \hat{\varepsilon}_{xy}\\ \hat{\varepsilon}_{yz}\\ \hat{\varepsilon}_{xz}\end{pmatrix} &= \begin{bmatrix} ik_x & 0 & 0\\ 0 & ik_y & 0\\ 0 & 0 & \frac{\partial}{\partial z}\\ \frac{1}{2}ik_y & \frac{1}{2}ik_x & 0\\ 0 & \frac{1}{2}\frac{\partial}{\partial z} & \frac{1}{2}ik_y\\ \frac{1}{2}\frac{\partial}{\partial z} & 0 & \frac{1}{2}ik_x\end{bmatrix} \begin{pmatrix}\hat{u}_x\\ \hat{u}_y\\ \hat{u}_z\end{pmatrix} \\ \hat{\boldsymbol{\varepsilon}} &= \left[\hat{G}\right] \; \hat{\mathbf{u}}\end{aligned} \tag{2.27}$$

Introducing equation (2.27) in equation (2.25), a relationship between stresses and displacements is obtained.

$$\begin{pmatrix}\hat{\sigma}_{xx}\\ \hat{\sigma}_{yy}\\ \hat{\sigma}_{zz}\\ \hat{\sigma}_{xy}\\ \hat{\sigma}_{yz}\\ \hat{\sigma}_{xz}\end{pmatrix} = \begin{bmatrix} ik_x(\lambda+2\mu) & ik_y\lambda & \lambda\,\frac{\partial}{\partial z}\\ ik_x\lambda & ik_y(\lambda+2\mu) & \lambda\,\frac{\partial}{\partial z}\\ ik_x\lambda & ik_y\lambda & (\lambda+2\mu)\,\frac{\partial}{\partial z}\\ ik_y\mu & ik_x\mu & 0\\ 0 & \mu\,\frac{\partial}{\partial z} & ik_y\mu\\ \mu\,\frac{\partial}{\partial z} & 0 & ik_x\mu\end{bmatrix} \begin{pmatrix}\hat{u}_x\\ \hat{u}_y\\ \hat{u}_z\end{pmatrix} \tag{2.28}$$

The components of the displacement field u_i are expressed by the scalar and vector potential in the Cartesian coordinate system by

$$u_i = \Phi_{,i} + \Psi_{l,k} \in_{ikl} \tag{2.29}$$

In the transformed domain, equation (2.29) is formulated for the displacements $\hat{u}_i$ as

$$\begin{pmatrix} \hat{u}_x \\ \hat{u}_y \\ \hat{u}_z \end{pmatrix} = \begin{bmatrix} ik_x & 0 & -\frac{\partial}{\partial z} \\ ik_y & \frac{\partial}{\partial z} & 0 \\ \frac{\partial}{\partial z} & -ik_y & ik_x \end{bmatrix} \begin{pmatrix} \hat{\Phi} \\ \hat{\Psi}_x \\ \hat{\Psi}_y \end{pmatrix} \tag{2.30}$$

Therefore, the relationship between stresses and the scalar potential $\hat{\Phi}$ and the components of the vector potential $\hat{\Psi}_x$ and $\hat{\Psi}_y$ can be described by

$$\begin{pmatrix} \hat{\sigma}_{xx} \\ \hat{\sigma}_{yy} \\ \hat{\sigma}_{zz} \\ \hat{\sigma}_{xy} \\ \hat{\sigma}_{yz} \\ \hat{\sigma}_{xz} \end{pmatrix} = \begin{bmatrix} -{k_x}^2 (\lambda + 2\mu) - {k_y}^2\lambda + \lambda\frac{\partial^2}{\partial z^2} & 0 & -2ik_x\mu\frac{\partial}{\partial z} \\ -{k_x}^2\lambda - {k_y}^2 (\lambda + 2\mu) + \lambda\frac{\partial^2}{\partial z^2} & 2ik_y\mu\frac{\partial}{\partial z} & 0 \\ -{k_x}^2\lambda - {k_y}^2\lambda + (\lambda + 2\mu)\frac{\partial^2}{\partial z^2} & -2ik_y\mu\frac{\partial}{\partial z} & 2ik_x\mu\frac{\partial}{\partial z} \\ -2k_xk_y\mu & ik_x\mu\frac{\partial}{\partial z} & -ik_y\mu\frac{\partial}{\partial z} \\ 2ik_y\mu\frac{\partial}{\partial z} & \mu\frac{\partial^2}{\partial z^2} + {k_y}^2\mu & -k_xk_y\mu \\ 2ik_x\mu\frac{\partial}{\partial z} & k_xk_y\mu & -\mu\frac{\partial^2}{\partial z^2} - {k_x}^2\mu \end{bmatrix} \begin{pmatrix} \hat{\Phi} \\ \hat{\Psi}_x \\ \hat{\Psi}_y \end{pmatrix} \tag{2.31}$$

Introducing the ansatz functions (2.19)

$$\begin{pmatrix} \hat{\Phi} \\ \hat{\Psi}_x \\ \hat{\Psi}_y \end{pmatrix} = \begin{bmatrix} e^{\lambda_1 z} & e^{-\lambda_1 z} & 0 & 0 & 0 & 0 \\ 0 & 0 & e^{\lambda_2 z} & e^{-\lambda_2 z} & 0 & 0 \\ 0 & 0 & 0 & 0 & e^{\lambda_2 z} & e^{-\lambda_2 z} \end{bmatrix} \begin{pmatrix} A_1 \\ A_2 \\ B_{x1} \\ B_{x2} \\ B_{y1} \\ B_{y2} \end{pmatrix} \tag{2.32}$$

a relationship between the stresses $\hat{\sigma}_{ij}$ and the unknowns A_1, A_2, B_{x1}, B_{x2}, B_{y1} and B_{y2} can be deduced.

$$\begin{pmatrix} \hat{\sigma}_{xx} \\ \hat{\sigma}_{yy} \\ \hat{\sigma}_{zz} \\ \hat{\sigma}_{xy} \\ \hat{\sigma}_{yz} \\ \hat{\sigma}_{xz} \end{pmatrix} = \mu \begin{bmatrix} -2{k_x}^2 - \frac{\lambda}{\mu}{k_p}^2 & -2{k_x}^2 - \frac{\lambda}{\mu}{k_p}^2 & 0 & 0 & -2ik_x\lambda_2 & 2ik_x\lambda_2 \\ -2{k_y}^2 - \frac{\lambda}{\mu}{k_p}^2 & -2{k_y}^2 - \frac{\lambda}{\mu}{k_p}^2 & 2ik_y\lambda_2 & -2ik_y\lambda_2 & 0 & 0 \\ 2{\lambda_1}^2 - \frac{\lambda}{\mu}{k_p}^2 & 2{\lambda_1}^2 - \frac{\lambda}{\mu}{k_p}^2 & -2ik_y\lambda_2 & 2ik_y\lambda_2 & 2ik_x\lambda_2 & -2ik_x\lambda_2 \\ -2k_xk_y & -2k_xk_y & ik_x\lambda_2 & -ik_x\lambda_2 & -ik_y\lambda_2 & ik_y\lambda_2 \\ 2ik_y\lambda_1 & -2ik_y\lambda_1 & {\lambda_2}^2 + {k_y}^2 & {\lambda_2}^2 + {k_y}^2 & -k_xk_y & -k_xk_y \\ 2ik_x\lambda_1 & -2ik_x\lambda_1 & k_xk_y & k_xk_y & -{\lambda_2}^2 - {k_x}^2 & -{\lambda_2}^2 - {k_x}^2 \end{bmatrix} \begin{pmatrix} A_1e^{\lambda_1 z} \\ A_2e^{-\lambda_1 z} \\ B_{x1}e^{\lambda_2 z} \\ B_{x2}e^{-\lambda_2 z} \\ B_{y1}e^{\lambda_2 z} \\ B_{y2}e^{-\lambda_2 z} \end{pmatrix} \tag{2.33}$$

With the help of the above equation (2.33), the boundary conditions (2.23) on the surface of the halfspace ($z = 0$) can be formulated in dependency on the unknowns A_2, B_{x2} and B_{y2} and the unknowns can be determined.

$$\begin{pmatrix} \hat{\sigma}_{zz} \\ \hat{\sigma}_{yz} \\ \hat{\sigma}_{xz} \end{pmatrix} = \mu \underbrace{\begin{bmatrix} 2\lambda_1^2 - \frac{\lambda}{\mu}k_p^2 & 2ik_y\lambda_2 & -2ik_x\lambda_2 \\ -2ik_y\lambda_1 & \lambda_2^2 + k_y^2 & -k_xk_y \\ -2ik_x\lambda_1 & k_xk_y & -\lambda_2^2 - k_x^2 \end{bmatrix}}_{\left[\hat{K}_{hs}\right]} \begin{pmatrix} A_2 \\ B_{x2} \\ B_{y2} \end{pmatrix} = \begin{pmatrix} -\hat{p}_z \\ -\hat{p}_y \\ -\hat{p}_x \end{pmatrix} \tag{2.34}$$

In a general formulation, the unknowns can be computed using Cramer's rule. With the determinant of matrix $\left[\hat{K}_{hs}\right]$

$$\det\left(\mu\left[\hat{K}_{hs}\right]\right) = \mu^3 \det\left[\hat{K}_{hs}\right] = \mu^3\lambda_2^2\left[-\left(2\lambda_1^2 - \frac{\lambda}{\mu}k_p^2\right)^2 + 4\left(k_x^2 + k_y^2\right)\lambda_1\lambda_2\right] \tag{2.35}$$

the unknowns can be calculated by

$$A_2 = \frac{\frac{\hat{p}_z}{\mu}\lambda_2^2\left(2\lambda_1^2 - \frac{\lambda}{\mu}k_p^2\right) - 2i\frac{\hat{p}_y}{\mu}k_y\lambda_2^3 - 2i\frac{\hat{p}_x}{\mu}k_x\lambda_2^3}{\det\left[\hat{K}_{hs}\right]} \tag{2.36a}$$

$$\begin{aligned} B_{x2} = & \frac{2i\frac{\hat{p}_z}{\mu}k_y\lambda_1\lambda_2^2 + \frac{\hat{p}_y}{\mu}\left(\left(\lambda_2^2 + k_x^2\right)\left(2\lambda_1^2 - \frac{\lambda}{\mu}k_p^2\right) - 4k_x^2\lambda_1\lambda_2\right)}{\det\left[\hat{K}_{hs}\right]} + \\ & + \frac{\frac{\hat{p}_x}{\mu}k_xk_y\left(4\lambda_1\lambda_2 - 2\lambda_1^2 + \frac{\lambda}{\mu}k_p^2\right)}{\det\left[\hat{K}_{hs}\right]} \end{aligned} \tag{2.36b}$$

$$\begin{aligned} B_{y2} = & \frac{-2i\frac{\hat{p}_z}{\mu}k_x\lambda_1\lambda_2^2 - \frac{\hat{p}_y}{\mu}k_xk_y\left(4\lambda_1\lambda_2 - 2\lambda_1^2 + \frac{\lambda}{\mu}k_p^2\right)}{\det\left[\hat{K}_{hs}\right]} - \\ & - \frac{\frac{\hat{p}_x}{\mu}\left(\left(\lambda_2^2 + k_y^2\right)\left(2\lambda_1^2 - \frac{\lambda}{\mu}k_p^2\right) - 4k_y^2\lambda_1\lambda_2\right)}{\det\left[\hat{K}_{hs}\right]} \end{aligned} \tag{2.36c}$$

After calculating the unknowns, the stresses and displacements inside the halfspace can be computed in a post-processing step in the transformed domain in dependency on (k_x, k_y, z, ω). The stresses are calculated using equation (2.33). The relationship between the unknowns and the displacements can be derived using the equations (2.30) and (2.32).

$$\begin{pmatrix} \hat{u}_x \\ \hat{u}_y \\ \hat{u}_z \end{pmatrix} = \begin{bmatrix} ik_x & ik_x & 0 & 0 & -\lambda_2 & \lambda_2 \\ ik_y & ik_y & \lambda_2 & -\lambda_2 & 0 & 0 \\ \lambda_1 & -\lambda_1 & -ik_y & -ik_y & ik_x & ik_x \end{bmatrix} \begin{pmatrix} A_1 e^{\lambda_1 z} \\ A_2 e^{-\lambda_1 z} \\ B_{x1} e^{\lambda_2 z} \\ B_{x2} e^{-\lambda_2 z} \\ B_{y1} e^{\lambda_2 z} \\ B_{y2} e^{-\lambda_2 z} \end{pmatrix} \tag{2.37}$$

The parameters in the original domain are obtained in dependency on (x, y, z, t) after a threefold inverse Fourier transformation.

2.3.4 Fundamental solution for a layered halfspace

If the solution of a horizontally layered halfspace as exemplarily depicted in figure 2.2 has to be determined, the boundary conditions have to be adapted. The Sommerfeld condition of radiation is only valid for an infinitely extended medium, which is, in the case of a layered halfspace the infinite layer at the bottom of the system. Thus, for the given system, the unknowns of layer l_2 with the z-coordinate z_2 are $A_{2,l_2}, B_{x2,l_2}, B_{y2,l_2}$. The depicted layer l_1 with the z-coordinate z_1 is described with six unknowns $A_{1,l_1}, A_{2,l_1}, B_{x1,l_1}, B_{x2,l_1}, B_{y1,l_1}, B_{y2,l_1}$ as in the spatially limited layer the Sommerfeld condition of radiation cannot be applied. Due to the geometry of the system, it has to be possible to model waves that are reflected at the boundary and thus spatially propagating waves in negative z-direction or surface waves that are exponentially increasing with the z-coordinate. Therefore, in a layered halfspace six unknowns per spatially limited layer and three unknowns for the infinite system have to be determined. This is done by applying the boundary and transition conditions.

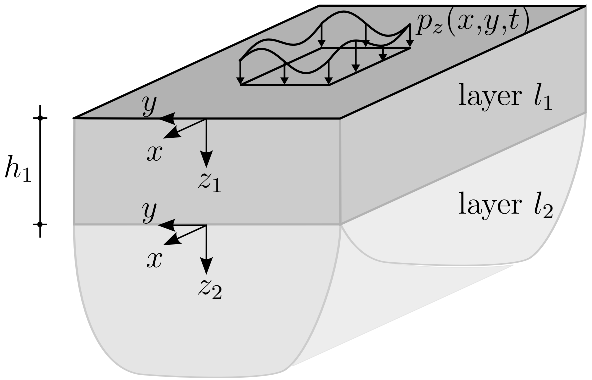

Figure 2.2: Schematic sketch of the layered halfspace model with an exemplary load

The equilibrium between the stresses in z-direction on the surface $z_1 = 0$ and the external loads is valid as presented in the equations (2.23). Additionally six transition conditions can be formulated concerning the equality of the displacements and stresses on the transition between $z_1 = h_1$ and $z_2 = 0$.

$$\hat{u}_x\left(k_x, k_y, z_2 = 0, \omega\right) = \hat{u}_x\left(k_x, k_y, z_1 = h_1, \omega\right) \tag{2.38a}$$

$$\hat{u}_y\left(k_x, k_y, z_2 = 0, \omega\right) = \hat{u}_y\left(k_x, k_y, z_1 = h_1, \omega\right) \tag{2.38b}$$

$$\hat{u}_z\left(k_x, k_y, z_2 = 0, \omega\right) = \hat{u}_z\left(k_x, k_y, z_1 = h_1, \omega\right) \tag{2.38c}$$

$$\hat{\sigma}_{zz}\left(k_x, k_y, z_2 = 0, \omega\right) = \hat{\sigma}_{zz}\left(k_x, k_y, z_1 = h_1, \omega\right) \tag{2.38d}$$

$$\hat{\sigma}_{yz}\left(k_x, k_y, z_2 = 0, \omega\right) = \hat{\sigma}_{yz}\left(k_x, k_y, z_1 = h_1, \omega\right) \tag{2.38e}$$

$$\hat{\sigma}_{xz}\left(k_x, k_y, z_2 = 0, \omega\right) = \hat{\sigma}_{xz}\left(k_x, k_y, z_1 = h_1, \omega\right) \tag{2.38f}$$

The equations (2.38) hold for a situation where there is no additional external load applied at the layer boundary. If there is an external load, it has to be taken into account in the equilibrium. Thus, in order to determine the unknowns of a layered halfspace system in general, three stress boundary conditions on the surface at $z_1 = 0$ and six transition conditions at each transition relating the displacements and stresses can be used.

However, to avoid numerical artifacts occurring for exponential functions with great arguments, [Grundmann and Müller 1988] replaced the unknowns $A_{1,l_1}, B_{x1,l_1}, B_{y1,l_1}$ which represent the surface waves in the spatially limited, upper layer whose amplitudes are exponentially increasing with increasing z-coordinate respectively the spatially propagating waves which are moving in negative z-direction by

$$A_{1,l_1} e^{\lambda_1 z} = \underline{A}_{1,l_1} e^{\lambda_1 (z - h_1)} \tag{2.39a}$$

$$B_{i1,l_1} e^{\lambda_2 z} = \underline{B}_{i1,l_1} e^{\lambda_2 (z - h_1)} \tag{2.39b}$$

The relationship between the modified unknowns and the stresses $\hat{\sigma}_{zz}$, $\hat{\sigma}_{yz}$ and $\hat{\sigma}_{xz}$ can be stated analogously to equation (2.33) as

$$\begin{pmatrix} \hat{\sigma}_{zz} \\ \hat{\sigma}_{yz} \\ \hat{\sigma}_{xz} \end{pmatrix} = \mu \begin{bmatrix} 2{\lambda_1}^2-\frac{\lambda}{\mu}{k_p}^2 & 2{\lambda_1}^2-\frac{\lambda}{\mu}{k_p}^2 & -2ik_y\lambda_2 & 2ik_y\lambda_2 & 2ik_x\lambda_2 & -2ik_x\lambda_2 \\ 2ik_y\lambda_1 & -2ik_y\lambda_1 & {\lambda_2}^2+{k_y}^2 & {\lambda_2}^2+{k_y}^2 & -k_xk_y & -k_xk_y \\ 2ik_x\lambda_1 & -2ik_x\lambda_1 & k_xk_y & k_xk_y & -{\lambda_2}^2-{k_x}^2 & -{\lambda_2}^2-{k_x}^2 \end{bmatrix} \begin{pmatrix} \underline{A}_{1,l_1} e^{\lambda_1(z-h_1)} \\ A_2 e^{-\lambda_1 z} \\ \underline{B}_{x1,l_1} e^{\lambda_2(z-h_1)} \\ B_{x2} e^{-\lambda_2 z} \\ \underline{B}_{y1,l_1} e^{\lambda_2(z-h_1)} \\ B_{y2} e^{-\lambda_2 z} \end{pmatrix} \tag{2.40}$$

and evaluated at the surface for $z_1 = 0$ and at the layer boundary for $z_1 = h_1$. For the displacement transition conditions (2.38a), (2.38b) and (2.38c) the relationship between the modified unknowns and the displacements can be formulated analogously to equation (2.37) as

$$\begin{pmatrix} \hat{u}_x \\ \hat{u}_y \\ \hat{u}_z \end{pmatrix} = \begin{bmatrix} ik_x & ik_x & 0 & 0 & -\lambda_2 & \lambda_2 \\ ik_y & ik_y & \lambda_2 & -\lambda_2 & 0 & 0 \\ \lambda_1 & -\lambda_1 & -ik_y & -ik_y & ik_x & ik_x \end{bmatrix} \begin{pmatrix} \underline{A}_{1,l_1} e^{\lambda_1(z-h_1)} \\ A_2 e^{-\lambda_1 z} \\ \underline{B}_{x1,l_1} e^{\lambda_2(z-h_1)} \\ B_{x2} e^{-\lambda_2 z} \\ \underline{B}_{y1,l_1} e^{\lambda_2(z-h_1)} \\ B_{y2} e^{-\lambda_2 z} \end{pmatrix} \tag{2.41}$$

for the spatially limited layer. Equation (2.41) is evaluated for $z_1 = h_1$ and introduced into the transition conditions (2.38a), (2.38b) and (2.38c).

Thus, using the non-local and local boundary and transition conditions, the unknowns can be determined. The solution for layered halfspace systems with more horizontal layers can be derived analogously by adding six transition conditions at each additional layer boundary and six unknowns for each additional spatially limited layer.

2.3.5 Static load on the halfspace

For a static load on the system ($\omega = 0 \Rightarrow k_p = 0$ and $k_s = 0$) the approaches in equation (2.19) are not complete as then $\lambda_1 = \lambda_2 = \sqrt{k_x^2 + k_y^2}$. Consequently, the determinant of matrix $\left[\hat{K}_{hs}\right]$ in equation (2.35) becomes zero and a solution for the unknowns is not possible. Therefore, extended approaches are necessary.

[Konrad 1985] presented a solution using the displacement approach of Papkovitch-Neuber. He introduced the Helmholtz decomposition of equation (2.9) in the Navier equation

$$\mu u^i|^j_j + (\lambda + \mu)\, u^j|^i_j = 0 \tag{2.42}$$

and determined a solution for the Papkovitch-Neuber potentials χ_0 and χ_α. The relationship between the Helmholtz potentials Φ and Ψ_i and the Papkovitch-Neuber potentials is derived in [Konrad 1985].

[Lenz 2003] used a different approach. He applied the threefold Fourier transformation $x \circ\!\!-\!\!\bullet\, k_x$, $y \circ\!\!-\!\!\bullet\, k_y$ and $t \circ\!\!-\!\!\bullet\, \omega$ on the Lamé differential equation (2.8) and solved the resulting system of coupled ordinary differential equations with an exponential approach. In order to compare the results to those obtained using the Helmholtz potentials, he expressed the solution also in dependency on the six unknown coefficients A_{01}, A_{02}, B_{0x1}, B_{0x2}, B_{0y1} and B_{0y2} of the Helmholtz potentials. The index 0 denotes the static case. The relationship between the stresses and the vector of the unknowns for the static case is formulated in equation (2.43)

$$\begin{pmatrix} \hat\sigma_{xx} \\ \hat\sigma_{yy} \\ \hat\sigma_{zz} \\ \hat\sigma_{xy} \\ \hat\sigma_{yz} \\ \hat\sigma_{xz} \end{pmatrix} = \mu \begin{bmatrix} -2k_x^2 z - 2\frac{\lambda k_r}{\lambda+\mu} & -2k_x^2 z + 2\frac{\lambda k_r}{\lambda+\mu} & 0 & 0 & -2ik_x k_r & 2ik_x k_r \\ -2k_y^2 - 2\frac{\lambda k_r}{\lambda+\mu} & -2k_y^2 + 2\frac{\lambda k_r}{\lambda+\mu} & 2ik_y k_r & -2ik_y k_r & 0 & 0 \\ 2k_r^2 z - 2\frac{(\lambda+2\mu)k_r}{\lambda+\mu} & 2k_r^2 z + 2\frac{(\lambda+2\mu)k_r}{\lambda+\mu} & -2ik_y k_r & 2ik_y k_r & 2ik_x k_r & -2ik_x k_r \\ -2k_x k_y z & -2k_x k_y z & ik_x k_r & -ik_x k_r & -ik_y k_r & ik_y k_r \\ 2ik_y\left(k_r z - \frac{\mu}{\lambda+\mu}\right) & -2ik_y\left(k_r z + \frac{\mu}{\lambda+\mu}\right) & k_r^2 + k_y^2 & k_r^2 + k_y^2 & -k_x k_y & -k_x k_y \\ 2ik_x\left(k_r z - \frac{\mu}{\lambda+\mu}\right) & -2ik_x\left(k_r z + \frac{\mu}{\lambda+\mu}\right) & k_x k_y & k_x k_y & -k_r^2 - k_x^2 & -k_r^2 - k_x^2 \end{bmatrix} \begin{pmatrix} A_{01} e^{\lambda_1 z} \\ A_{02} e^{-\lambda_1 z} \\ B_{0x1} e^{\lambda_2 z} \\ B_{0x2} e^{-\lambda_2 z} \\ B_{0y1} e^{\lambda_2 z} \\ B_{0y2} e^{-\lambda_2 z} \end{pmatrix} \tag{2.43}$$

with

$$k_r = |\sqrt{{k_x}^2 + {k_y}^2}| \tag{2.44}$$

A more detailed derivation of the matrix in equation (2.43) is also contained in [Ullmann 2013].

2.4 Fundamental solution for a fullspace with cylindrical cavity

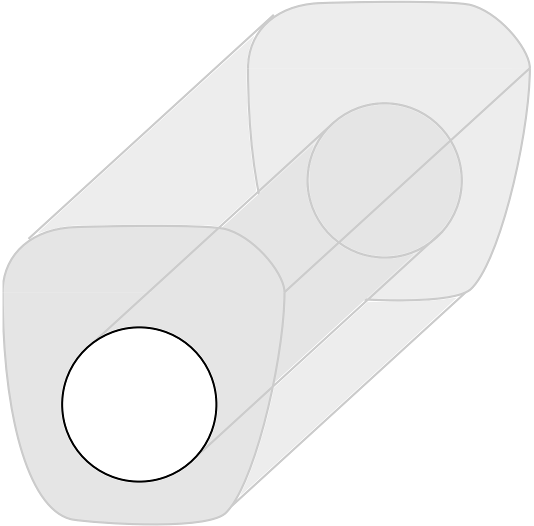

Figure 2.3: Schematic sketch of the fullspace with cylindrical cavity

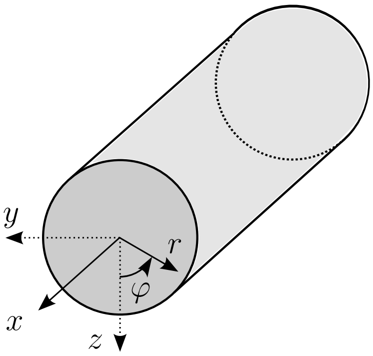

Figure 2.4: Cartesian and cylindrical coordinates

In order to determine the solution for the system of a fullspace with cylindrical cavity that is exemplarily depicted in figure 2.3 analogously to the system of a halfspace, the partial differential equations (2.11) are formulated for a cylindrical coordinate system. The coordinates (x, r, φ) are used according to the definition in figure 2.4. Introducing the Helmholtz approach (2.9) in the Lamé differential equation (2.8) does not directly yield in a decoupled system of equations as the components of the vector potential Ψ_i are not decoupled in the non-stationary cylindrical coordinate system. Therefore, an additional transformation is necessary. According to [Frühe 2010], the vector potential $\boldsymbol{\Psi}$ is replaced by two scalar functions ψ and χ so that condition (2.14) is fulfilled. As presented in [Eringen and Suhubi 1975] $\boldsymbol{\Psi}$ is expressed by

$$\boldsymbol{\Psi} = \psi \mathbf{g}^1 + \chi|^j \in_{ij1} \mathbf{g}^i \tag{2.45}$$

with $\in_{ijk}$ as the permutation symbol of the cylindrical coordinate system.

Thus, the system of decoupled partial differential equations is formulated in cylindrical coordinates as

$$\left[\frac{\partial^2}{\partial x^2}+\frac{\partial^2}{\partial r^2}+\frac{1}{r}\frac{\partial}{\partial r}+\frac{1}{r^2}\frac{\partial^2}{\partial \varphi^2}-\frac{1}{{c_p}^2}\frac{\partial^2}{\partial t^2}\right]\Phi\left(x,r,\varphi,t\right)=0 \tag{2.46a}$$

$$\left[\frac{\partial^2}{\partial x^2}+\frac{\partial^2}{\partial r^2}+\frac{1}{r}\frac{\partial}{\partial r}+\frac{1}{r^2}\frac{\partial^2}{\partial \varphi^2}-\frac{1}{{c_s}^2}\frac{\partial^2}{\partial t^2}\right]\psi\left(x,r,\varphi,t\right)=0 \tag{2.46b}$$

$$\left[\frac{\partial^2}{\partial x^2}+\frac{\partial^2}{\partial r^2}+\frac{1}{r}\frac{\partial}{\partial r}+\frac{1}{r^2}\frac{\partial^2}{\partial \varphi^2}-\frac{1}{{c_s}^2}\frac{\partial^2}{\partial t^2}\right]\chi\left(x,r,\varphi,t\right)=0 \tag{2.46c}$$

2.4.1 Solution of the system of partial differential equations

To transform the partial differential equations (2.46) into ordinary differential equations, a Fourier transformation is again applied. A twofold Fourier transformation from space into wavenumber domain $x \circ\!\!-\!\!\!-\!\!\bullet\, k_x$ and from time into frequency domain $t \circ\!\!-\!\!\!-\!\!\bullet\, \omega$ is carried out. Additionally a Fourier series expansion regarding the circumference of the cylindrical cavity is performed.

$$\tilde{\Phi}\left(k_x,r,\varphi,\omega\right)=\sum_{n=-\infty}^{\infty}\hat{\Phi}\left(k_x,r,n,\omega\right)e^{in\varphi} \tag{2.47a}$$

$$\tilde{\psi}\left(k_x,r,\varphi,\omega\right)=\sum_{n=-\infty}^{\infty}\hat{\psi}\left(k_x,r,n,\omega\right)e^{in\varphi} \tag{2.47b}$$

$$\tilde{\chi}\left(k_x,r,\varphi,\omega\right)=\sum_{n=-\infty}^{\infty}\hat{\chi}\left(k_x,r,n,\omega\right)e^{in\varphi} \tag{2.47c}$$

The ˜ symbol denotes parameters in the twofold Fourier transformed domain that are dependent on k_x and ω. After the Fourier series expansion, the parameters are again signified with the ˆ symbol to indicate the three transformations respectively the series expansion.

In the cylindrical coordinate system the coordinate r is not transformed, analogously to the z-coordinate in the Cartesian coordinate system. Different layers parallel to the respective surfaces can thus be implemented. After the transformation from the original into the transformed domain, the equations (2.46) form the following ordinary differential equations

$$\left[-{k_x}^2 + \frac{\partial^2}{\partial r^2} + \frac{1}{r}\frac{\partial}{\partial r} - \frac{n^2}{r^2} + {k_p}^2\right]\hat{\Phi}\left(k_x, r, n, \omega\right) = 0 \tag{2.48a}$$

$$\left[-{k_x}^2 + \frac{\partial^2}{\partial r^2} + \frac{1}{r}\frac{\partial}{\partial r} - \frac{n^2}{r^2} + {k_s}^2\right]\hat{\psi}\left(k_x, r, n, \omega\right) = 0 \tag{2.48b}$$

$$\left[-{k_x}^2 + \frac{\partial^2}{\partial r^2} + \frac{1}{r}\frac{\partial}{\partial r} - \frac{n^2}{r^2} + {k_s}^2\right]\hat{\chi}\left(k_x, r, n, \omega\right) = 0 \tag{2.48c}$$

These differential equations are Bessel's differential equations of the type

$$\left[\frac{\partial^2}{\partial r^2} + \frac{1}{r}\frac{\partial}{\partial r} + {k_i}^2 - \frac{n^2}{r^2}\right]\hat{\mathrm{f}}\left(r\right) = 0 \tag{2.49}$$

This type of differential equations can be solved for the unknown function $\hat{\mathrm{f}}$ using Hankel functions of the first kind $H_n^{(1)}\left(k_i r\right)$ and of the second kind $H_n^{(2)}\left(k_i r\right)$. Definitions regarding Bessel's differential equation and Hankel functions are summarized in appendix A.2. Thus, the solution for the unknown function $\hat{\mathrm{f}}$ can be expressed by

$$\hat{\mathrm{f}}\left(k_i r\right) = C_1 H_n^{(1)}\left(k_i r\right) + C_2 H_n^{(2)}\left(k_i r\right) \tag{2.50}$$

Using this information, the solution of the system of ordinary differential equations (2.48) can be expressed by Hankel functions in dependency on the coordinate r and the definition of ${k_1}^2 = {k_p}^2 - {k_x}^2$ respectively ${k_2}^2 = {k_s}^2 - {k_x}^2$.

$$\hat{\Phi}\left(k_x, r, n, \omega\right) = C_{1n}\, H_n^{(1)}\left(k_1 r\right) + C_{4n}\, H_n^{(2)}\left(k_1 r\right) \tag{2.51a}$$

$$\hat{\psi}\left(k_x, r, n, \omega\right) = C_{2n}\, H_n^{(1)}\left(k_2 r\right) + C_{5n}\, H_n^{(2)}\left(k_2 r\right) \tag{2.51b}$$

$$\hat{\chi}\left(k_x, r, n, \omega\right) = C_{3n}\, H_n^{(1)}\left(k_2 r\right) + C_{6n}\, H_n^{(2)}\left(k_2 r\right) \tag{2.51c}$$

In case k_1 respectively k_2 are equal to zero, the differential equations (2.48) are solved with a different approach as mentioned in [Frühe 2010]. As this case is only possible in an undamped material, it will not be further treated here.

2.4.2 Local and non-local boundary conditions

Analogously to the system of a halfspace, the different solution contributions correspond to different wave types. Using the information about physical limitations, coefficients can be excluded. [Müller 2007] showed that performing the calculations for negative frequencies, the coefficients C_{4n}, C_{5n} and C_{6n} can be set to zero if infinite extension of the medium without radial boundaries is assumed. The remaining unknowns C_{1n}, C_{2n} and C_{3n} are calculated for negative frequencies using the boundary conditions on the cylindrical boundary of the system with a radius $r = R$.

$$\hat{\sigma}_{rr}\left(k_x, r = R, n, \omega\right) = -\hat{p}_r\left(k_x, n, \omega\right) \tag{2.52a}$$

$$\hat{\sigma}_{xr}\left(k_x, r = R, n, \omega\right) = -\hat{p}_x\left(k_x, n, \omega\right) \tag{2.52b}$$

$$\hat{\sigma}_{\varphi r}\left(k_x, r = R, n, \omega\right) = -\hat{p}_\varphi\left(k_x, n, \omega\right) \tag{2.52c}$$

The results for positive frequencies are supplemented as the conjugate complex values of the results for negative frequencies comparably to the equations (2.22). If, analogously to the derivations for the layered halfspace in section 2.3.4, layers in the medium exist in dependency on the spatially untransformed coordinate r, no unknowns can be set to zero inside the limited layer and the unknowns are determined using the stress boundary conditions on the cylindrical surface, the transition conditions at the radial boundaries and the Sommerfeld condition of radiation.

2.4.3 Stresses in the cylindrical coordinate system

In order to apply the boundary conditions, the relationship between the stresses $\hat{\sigma}_{rr}$, $\hat{\sigma}_{xr}$ and $\hat{\sigma}_{\varphi r}$ and the unknowns $C_{1n}, C_{2n}, ..., C_{6n}$ is derived. The relationship between the displacements $\hat{u}_x$, $\hat{u}_r$ and $\hat{u}_\varphi$ and the scalar functions $\hat{\Phi}$, $\hat{\psi}$ and $\hat{\chi}$ can be formulated in matrix notation based on the equations (2.9) and (2.45) in the threefold transformed cylindrical coordinate system (k_x, r, n, ω) as

$$\begin{pmatrix} \hat{u}_x \\ \hat{u}_r \\ \hat{u}_\varphi \end{pmatrix} = \begin{bmatrix} ik_x & 0 & {k_2}^2 \\ \frac{\partial}{\partial r} & i\frac{n}{r} & ik_x\frac{\partial}{\partial r} \\ i\frac{n}{r} & -\frac{\partial}{\partial r} & -\frac{n}{r}k_x \end{bmatrix} \begin{pmatrix} \hat{\Phi} \\ \hat{\psi} \\ \hat{\chi} \end{pmatrix} \tag{2.53}$$

Substituting the scalar functions by the unknowns C_{1n}, C_{2n} and C_{3n} of an unlayered infinite medium leads to

$$\begin{pmatrix} \hat{u}_x \\ \hat{u}_r \\ \hat{u}_\varphi \end{pmatrix} = \begin{bmatrix} ik_x H_n^{(1)}\left(k_1 r\right) & 0 & {k_2}^2 H_n^{(1)}\left(k_2 r\right) \\ \frac{\partial}{\partial r} H_n^{(1)}\left(k_1 r\right) & i\frac{n}{r} H_n^{(1)}\left(k_2 r\right) & ik_x\frac{\partial}{\partial r} H_n^{(1)}\left(k_2 r\right) \\ i\frac{n}{r} H_n^{(1)}\left(k_1 r\right) & -\frac{\partial}{\partial r} H_n^{(1)}\left(k_2 r\right) & -\frac{n}{r}k_x H_n^{(1)}\left(k_2 r\right) \end{bmatrix} \begin{pmatrix} C_{1n} \\ C_{2n} \\ C_{3n} \end{pmatrix} \tag{2.54}$$

The relationship between the stresses and the unknowns can be derived in a general form analogously to the derivations in section 2.3.3. The result can be abbreviated in matrix notation as

$$\begin{aligned}
\begin{pmatrix} \hat{\sigma}_{xx} \\ \hat{\sigma}_{rr} \\ \hat{\sigma}_{\varphi\varphi} \\ \hat{\sigma}_{xr} \\ \hat{\sigma}_{\varphi r} \\ \hat{\sigma}_{x\varphi} \end{pmatrix} &= \begin{bmatrix} \hat{K}_{c,11} & \hat{K}_{c,12} & \hat{K}_{c,13} & \hat{K}_{c,14} & \hat{K}_{c,15} & \hat{K}_{c,16} \\ \hat{K}_{c,21} & \hat{K}_{c,22} & \hat{K}_{c,23} & \hat{K}_{c,24} & \hat{K}_{c,25} & \hat{K}_{c,26} \\ \hat{K}_{c,31} & \hat{K}_{c,32} & \hat{K}_{c,33} & \hat{K}_{c,34} & \hat{K}_{c,35} & \hat{K}_{c,36} \\ \hat{K}_{c,41} & \hat{K}_{c,42} & \hat{K}_{c,43} & \hat{K}_{c,44} & \hat{K}_{c,45} & \hat{K}_{c,46} \\ \hat{K}_{c,51} & \hat{K}_{c,52} & \hat{K}_{c,53} & \hat{K}_{c,54} & \hat{K}_{c,55} & \hat{K}_{c,56} \\ \hat{K}_{c,61} & \hat{K}_{c,62} & \hat{K}_{c,63} & \hat{K}_{c,64} & \hat{K}_{c,65} & \hat{K}_{c,66} \end{bmatrix} \begin{pmatrix} C_{1n} \\ C_{2n} \\ C_{3n} \\ C_{4n} \\ C_{5n} \\ C_{6n} \end{pmatrix} \\
\boldsymbol{\hat{\sigma}_c} &= \left[\hat{K}_c\right] \mathbf{C_c}
\end{aligned} \tag{2.55}$$

The elements of matrix $\left[\hat{K}_c\right]$ are contained in appendix A.3. A complete derivation is presented in [Frühe 2010].

If the unknowns C_{1n}, C_{2n} and C_{3n} of an unlayered, infinite medium shall be determined based on the stress boundary conditions (2.52) on the cylindrical surface, the following set of equations is obtained.

$$\begin{aligned}
-\hat{p}_r\left(k_x, n, \omega\right) = & \left[\left(\frac{n^2-n}{R^2} + {k_x}^2 - \frac{1}{2}{k_s}^2\right) 2\mu\, H_n^{(1)}(k_1 R) + \frac{1}{R} k_1\, 2\mu\, H_{n+1}^{(1)}(k_1 R)\right] C_{1n} \\
& + \left[i\, \frac{n^2-n}{R^2}\, 2\mu\, H_n^{(1)}(k_2 R) - i\, \frac{n}{R} k_2\, 2\mu\, H_{n+1}^{(1)}(k_2 R)\right] C_{2n} \\
& + \left[i \left(\frac{n^2-n}{R^2} - {k_2}^2\right) k_x\, 2\mu\, H_n^{(1)}(k_2 R) + i\, \frac{1}{R} k_x\, k_2\, 2\mu\, H_{n+1}^{(1)}(k_2 R)\right] C_{3n}
\end{aligned} \tag{2.56a}$$

$$\begin{aligned}
-\hat{p}_x\left(k_x, n, \omega\right) = & \left[i\, \frac{n}{R} k_x\, 2\mu\, H_n^{(1)}(k_1 R) - i\, k_x\, k_1\, 2\mu\, H_{n+1}^{(1)}(k_1 R)\right] C_{1n} \\
& + \left[-\frac{n}{2R} k_x\, 2\mu\, H_n^{(1)}(k_2 R)\right] C_{2n} \\
& + \left[\frac{n}{2R}\left({k_2}^2 - {k_x}^2\right) 2\mu\, H_n^{(1)}(k_2 R) + \frac{1}{2}\left({k_x}^2 k_2 - {k_2}^3\right) 2\mu\, H_{n+1}^{(1)}(k_2 R)\right] C_{3n}
\end{aligned} \tag{2.56b}$$

$$
\begin{aligned}
-\,\hat{p}_{\varphi}\,(k_x,n,\omega) = {} & \left[i\,\frac{n^2-n}{R^2}\,2\mu\,H_n^{(1)}(k_1R) - i\,\frac{n}{R}k_1\,2\mu\,H_{n+1}^{(1)}(k_1R)\right] C_{1n} \\
& + \left[\left(-\frac{n^2-n}{R^2} + \frac{1}{2}{k_2}^2 \right) 2\mu\,H_n^{(1)}(k_2R) - \frac{1}{R}k_2\,2\mu\,H_{n+1}^{(1)}(k_2R)\right] C_{2n} \\
& + \left[-\frac{n^2-n}{R^2}\,k_x\,2\mu\,H_n^{(1)}(k_2R) + \frac{n}{R}k_x\,k_2\,2\mu\,H_{n+1}^{(1)}(k_2R)\right] C_{3n}
\end{aligned}
\tag{2.56c}
$$

2.5 Fundamental solution for a fullspace with spherical cavity

The solution of a fullspace with spherical cavity as exemplarily depicted in figure 2.5 is derived for a spherical coordinate system as defined in figure 2.6 with the radial coordinate r, the azimuth angle φ and the elevation angle ϑ.

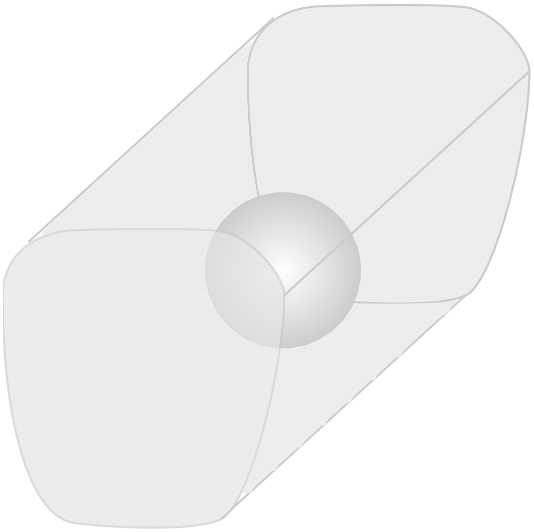

Figure 2.5: Schematic sketch of the fullspace with spherical cavity

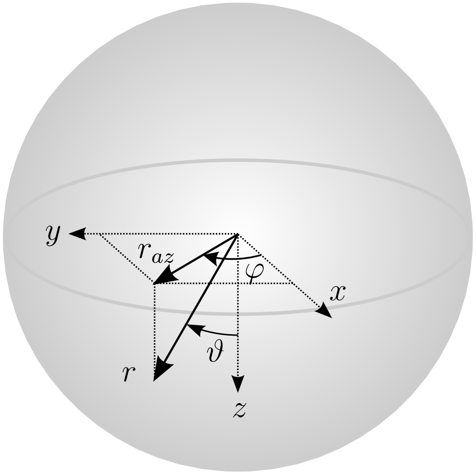

Figure 2.6: Cartesian and spherical coordinates

Using the spherical coordinate system, analogously to the derivations in section 2.4 the vector potential $\mathbf{\Psi}$ is replaced by two scalar functions ψ and χ by

$$
\mathbf{\Psi} = r\psi\mathbf{g}^1 + (r\chi)\,|^j \in_{ij1} \mathbf{g}^i \tag{2.57}
$$

with the permutation symbol of the spherical coordinate system $\in_{ijk}$.

With the definition (2.57), condition (2.14) $\Psi_i|^i = 0$ is fulfilled and the Helmholtz decomposition is applied. Following the derivations presented in [Eringen and Suhubi 1975] and [Frühe 2010] three decoupled partial differential equations for the scalar potentials Φ, ψ and χ are obtained.

$$\left[\frac{\partial^2}{\partial r^2} + \frac{2}{r}\frac{\partial}{\partial r} + \frac{1}{r^2}\left(\frac{\partial^2}{\partial \vartheta^2} + \frac{\cos(\vartheta)}{\sin(\vartheta)}\frac{\partial}{\partial \vartheta} + \frac{1}{\sin^2(\vartheta)}\frac{\partial^2}{\partial \varphi^2}\right) - \frac{1}{{c_p}^2}\frac{\partial^2}{\partial t^2}\right] \Phi\left(r, \vartheta, \varphi, t\right) = 0 \tag{2.58a}$$

$$\left[\frac{\partial^2}{\partial r^2} + \frac{2}{r}\frac{\partial}{\partial r} + \frac{1}{r^2}\left(\frac{\partial^2}{\partial \vartheta^2} + \frac{\cos(\vartheta)}{\sin(\vartheta)}\frac{\partial}{\partial \vartheta} + \frac{1}{\sin^2(\vartheta)}\frac{\partial^2}{\partial \varphi^2}\right) - \frac{1}{{c_s}^2}\frac{\partial^2}{\partial t^2}\right] \psi\left(r, \vartheta, \varphi, t\right) = 0 \tag{2.58b}$$

$$\left[\frac{\partial^2}{\partial r^2} + \frac{2}{r}\frac{\partial}{\partial r} + \frac{1}{r^2}\left(\frac{\partial^2}{\partial \vartheta^2} + \frac{\cos(\vartheta)}{\sin(\vartheta)}\frac{\partial}{\partial \vartheta} + \frac{1}{\sin^2(\vartheta)}\frac{\partial^2}{\partial \varphi^2}\right) - \frac{1}{{c_s}^2}\frac{\partial^2}{\partial t^2}\right] \chi\left(r, \vartheta, \varphi, t\right) = 0 \tag{2.58c}$$

2.5.1 Solution of the system of partial differential equations

As a first step to transform the partial differential equations (2.58) into ordinary differential equations again a Fourier transformation from time into frequency domain $t \circ\!\!-\!\!\!-\!\!\bullet\, \omega$ is applied leading to

$$\left[\frac{\partial^2}{\partial r^2} + \frac{2}{r}\frac{\partial}{\partial r} + \frac{1}{r^2}\left(\frac{\partial^2}{\partial \vartheta^2} + \frac{\cos(\vartheta)}{\sin(\vartheta)}\frac{\partial}{\partial \vartheta} + \frac{1}{\sin^2(\vartheta)}\frac{\partial^2}{\partial \varphi^2}\right) + {k_p}^2\right] \bar{\Phi}\left(r, \vartheta, \varphi, \omega\right) = 0 \tag{2.59a}$$

$$\left[\frac{\partial^2}{\partial r^2} + \frac{2}{r}\frac{\partial}{\partial r} + \frac{1}{r^2}\left(\frac{\partial^2}{\partial \vartheta^2} + \frac{\cos(\vartheta)}{\sin(\vartheta)}\frac{\partial}{\partial \vartheta} + \frac{1}{\sin^2(\vartheta)}\frac{\partial^2}{\partial \varphi^2}\right) + {k_s}^2\right] \bar{\psi}\left(r, \vartheta, \varphi, \omega\right) = 0 \tag{2.59b}$$

$$\left[\frac{\partial^2}{\partial r^2} + \frac{2}{r}\frac{\partial}{\partial r} + \frac{1}{r^2}\left(\frac{\partial^2}{\partial \vartheta^2} + \frac{\cos(\vartheta)}{\sin(\vartheta)}\frac{\partial}{\partial \vartheta} + \frac{1}{\sin^2(\vartheta)}\frac{\partial^2}{\partial \varphi^2}\right) + {k_s}^2\right] \bar{\chi}\left(r, \vartheta, \varphi, \omega\right) = 0 \tag{2.59c}$$

The $^-$ symbol denotes parameters in the singly Fourier transformed domain.

As clearly visible, the differential equations (2.59) consist of radius-dependent and angle-dependent terms. According to [Bronstein et al 2006] or [Arfken and Weber 1995], the angle-dependent part that is contained in the terms in parentheses can be solved with spherical harmonics $Y_m^l(\vartheta, \varphi)$ of degree m and order l. The spherical harmonics can be derived by further separating the angle-dependent term into its azimuthal-dependent parts containing the φ-dependency and into its polar angle-dependent contributions which are dependent only on ϑ.

$$Y_m^l(\vartheta,\varphi) = \Phi_l(\varphi)\;\Theta_m^l(\vartheta) \tag{2.60}$$

This separation is presented in appendix A.4. The solution of the azimuthal-dependent equation is described with an exponential function.

$$\Phi_l(\varphi) = e^{il\varphi} \tag{2.61}$$

The polar angle-dependent equation can be solved with normalized associated Legendre polynomials.

$$\Theta_m^l(\vartheta) = \sqrt{\frac{2m+1}{2}\frac{(m-l)!}{(m+l)!}}\;P_m^l\left(\cos\left(\vartheta\right)\right) = \check{P}_m^l\left(\cos\left(\vartheta\right)\right) \tag{2.62}$$

Further information concerning the Legendre polynomials is contained in appendix A.4. Thus, the spherical harmonics $Y_m^l(\vartheta,\varphi)$ can be formulated as

$$Y_m^l(\vartheta,\varphi) = \sqrt{\frac{2m+1}{2}\frac{(m-l)!}{(m+l)!}}\;P_m^l\left(\cos\left(\vartheta\right)\right)\;e^{il\varphi} = \check{P}_m^l\left(\cos\left(\vartheta\right)\right)\;e^{il\varphi} \tag{2.63}$$

and the angle-dependent derivatives of the equations (2.59) can be replaced by

$$\left(\frac{\partial^2}{\partial\vartheta^2} + \frac{\cos(\vartheta)}{\sin(\vartheta)}\frac{\partial}{\partial\vartheta} + \frac{1}{\sin^2(\vartheta)}\frac{\partial^2}{\partial\varphi^2}\right)Y_m^l(\vartheta,\varphi) = -m\left(m+1\right)Y_m^l(\vartheta,\varphi) \tag{2.64}$$

The first spherical harmonics are sketched in the following figure 2.7. They can be separated according to their behavior into zonal spherical harmonics ($m = 0$), which have constant values on each latitude independent of the longitude, sectoral spherical harmonics ($m = |l|$), which are independent of the latitude, and tesseral spherical harmonics, where the value changes in dependency on both angles ϑ and φ. As the spherical harmonics form an orthogonal system on the unit sphere, they generate a complete basis and each continuous function on the sphere can be developed into a series of spherical harmonics according to [Arens 2013].

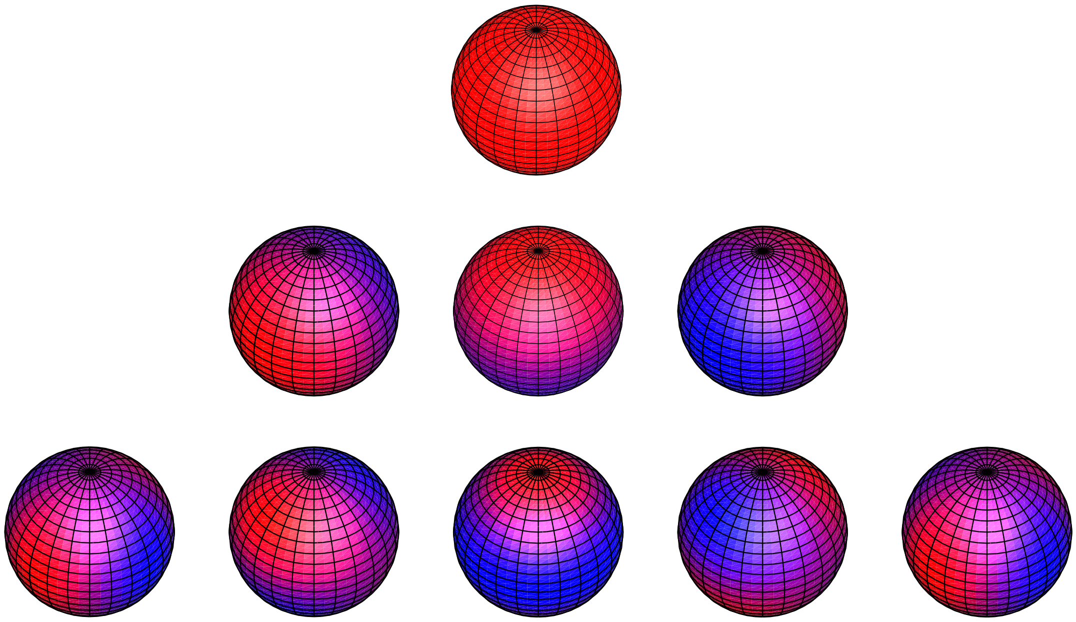

Figure 2.7: Spherical harmonics: First row: $Y_0^0(\vartheta,\varphi)$, Second row: $Y_1^{-1}(\vartheta,\varphi)$, $Y_1^0(\vartheta,\varphi)$ and $Y_1^1(\vartheta,\varphi)$, Third row: $Y_2^{-2}(\vartheta,\varphi)$, $Y_2^{-1}(\vartheta,\varphi)$, $Y_2^0(\vartheta,\varphi)$, $Y_2^1(\vartheta,\varphi)$ and $Y_2^2(\vartheta,\varphi)$

In order to apply relation (2.64) on the equations (2.59), the scalar potentials $\bar{\Phi}$, $\bar{\psi}$ and $\bar{\chi}$ are each developed into a series of spherical harmonics.

$$\bar{\Phi}\left(r,\vartheta,\varphi,\omega\right)=\sum_{m=0}^{\infty}\sum_{l=-m}^{m}\hat{\Phi}\left(r,m,l,\omega\right)Y_m^l(\vartheta,\varphi) \tag{2.65a}$$

$$\bar{\psi}\left(r,\vartheta,\varphi,\omega\right)=\sum_{m=0}^{\infty}\sum_{l=-m}^{m}\hat{\psi}\left(r,m,l,\omega\right)Y_m^l(\vartheta,\varphi) \tag{2.65b}$$

$$\bar{\chi}\left(r,\vartheta,\varphi,\omega\right)=\sum_{m=0}^{\infty}\sum_{l=-m}^{m}\hat{\chi}\left(r,m,l,\omega\right)Y_m^l(\vartheta,\varphi) \tag{2.65c}$$

It has to be stated that, in contrast to a Fourier transformation, where N parameters in the original domain are expressed by an identical number of parameters in the transformed domain, the number of parameters changes due to the development in spherical harmonics. As m and l are dependent from each other, with $l=-m,...,m$, each degree m can be combined with $(2m+1)$ different orders l. Thus, for $m=0,....,M$ the number of possible combinations can be calculated as $\sum\limits_{m=0}^{M}(2m+1)$. This is an arithmetic sequence of first order and is equal to $(M+1)^2$. Illustratively it could be explained that a sphere that is described by N_φ points on N_ϑ latitudes and thus $N_\vartheta N_\varphi$ points in the original domain, is modeled in the transformed domain by $(M+1)^2$ spherical harmonics with $(M+1)$ as the parameter that corresponds to the number of latitudes N_ϑ. Thus, the number of unknowns is different for the original and the transformed domain.

The equations (2.65) are introduced into the differential equations (2.59) and lead, in combination with the relationship (2.64), to ordinary differential equations for each series member.

$$\left[\frac{\partial^2}{\partial r^2}+\frac{2}{r}\frac{\partial}{\partial r}+\left({k_p}^2-\frac{m\,(m+1)}{r^2}\right)\right]\hat{\Phi}\,(r,m,l,\omega)=0 \tag{2.66a}$$

$$\left[\frac{\partial^2}{\partial r^2}+\frac{2}{r}\frac{\partial}{\partial r}+\left({k_s}^2-\frac{m\,(m+1)}{r^2}\right)\right]\hat{\psi}\,(r,m,l,\omega)=0 \tag{2.66b}$$

$$\left[\frac{\partial^2}{\partial r^2}+\frac{2}{r}\frac{\partial}{\partial r}+\left({k_s}^2-\frac{m\,(m+1)}{r^2}\right)\right]\hat{\chi}\,(r,m,l,\omega)=0 \tag{2.66c}$$

These differential equations can also be described as Bessel's differential equations after a substitution that is presented in appendix A.5 and can be solved using spherical Hankel functions of the first kind $h_m^{(1)}$ and of the second kind $h_m^{(2)}$.

$$\hat{\Phi}\,(r,m,l,\omega)=C_{1lm}\,h_m^{(1)}\,(|k_p|r)+C_{4lm}\,h_m^{(2)}\,(|k_p|r) \tag{2.67a}$$

$$\hat{\psi}\,(r,m,l,\omega)=C_{2lm}\,h_m^{(1)}\,(|k_s|r)+C_{5lm}\,h_m^{(2)}\,(|k_s|r) \tag{2.67b}$$

$$\hat{\chi}\,(r,m,l,\omega)=C_{3lm}\,h_m^{(1)}\,(|k_s|r)+C_{6lm}\,h_m^{(2)}\,(|k_s|r) \tag{2.67c}$$

2.5.2 Local and non-local boundary conditions

The unknowns C_{1lm} - C_{6lm} are calculated using the local and non-local boundary conditions. As non-local boundary conditions, analogously to the previously presented systems of half-space and fullspace with a cylindrical cavity, the Sommerfeld condition of radiation has to be fulfilled. Thus, surface waves on the spherical surface may not increase with increasing radius and spatially propagating waves can only radiate from the sphere towards infinity.

Analogously to the derivations for the fullspace with cylindrical cavity the solution contributions are analyzed concerning their physical meaning. According to [Frühe 2010] the spherical Hankel functions of the second kind describe for negative frequencies spatially propagating waves that are propagating against the radial coordinate respectively surface waves which are exponentially increasing with increasing distance to the sphere. These physically not existing waves can be excluded and C_{4lm} - C_{6lm} can be set to zero. The solution is described with the spherical Hankel functions of the first kind in dependency on C_{1lm} - C_{3lm}. They can be calculated using the local boundary conditions on the spherical surface. The stresses on the surface in radial direction have to be equal to the external loads.

$$\hat{\sigma}_{rr}\left(r=R,m,l,\omega\right)=-\hat{p}_{r}\left(m,l,\omega\right) \tag{2.68a}$$

$$\hat{\sigma}_{r\vartheta}\left(r=R,m,l,\omega\right)=-\hat{p}_{\vartheta}\left(m,l,\omega\right) \tag{2.68b}$$

$$\hat{\sigma}_{r\varphi}\left(r=R,m,l,\omega\right)=-\hat{p}_{\varphi}\left(m,l,\omega\right) \tag{2.68c}$$

2.5.3 Stresses in the spherical coordinate system

For the equations (2.68), the relationships between the stresses $\hat{\sigma}_{rr}$, $\hat{\sigma}_{r\vartheta}$ and $\hat{\sigma}_{r\varphi}$ and the unknowns C_{1lm} - C_{3lm} have to be derived. This is done analogously to the derivations in section 2.3.3 in [Frühe 2010] for the general case with all unknowns C_{1lm} - C_{6lm}. The result of his derivations is contained in appendix A.6 in a matrix $\left[\hat{K}_s\right]$ which relates the vector of the stress components $\hat{\boldsymbol{\sigma}}_{\mathbf{s}}$ to the vector of the unknowns $\mathbf{C_s}$.

$$\begin{array}{ccccc}
\begin{pmatrix}\hat{\sigma}_{rr}\\ \hat{\sigma}_{\vartheta\vartheta}\\ \hat{\sigma}_{\varphi\varphi}\\ \hat{\sigma}_{r\vartheta}\\ \hat{\sigma}_{r\varphi}\\ \hat{\sigma}_{\vartheta\varphi}\end{pmatrix} & = & \begin{bmatrix}\hat{K}_{s,11} & \hat{K}_{s,12} & \hat{K}_{s,13} & \hat{K}_{s,14} & \hat{K}_{s,15} & \hat{K}_{s,16}\\ \hat{K}_{s,21} & \hat{K}_{s,22} & \hat{K}_{s,23} & \hat{K}_{s,24} & \hat{K}_{s,25} & \hat{K}_{s,26}\\ \hat{K}_{s,31} & \hat{K}_{s,32} & \hat{K}_{s,33} & \hat{K}_{s,34} & \hat{K}_{s,35} & \hat{K}_{s,36}\\ \hat{K}_{s,41} & \hat{K}_{s,42} & \hat{K}_{s,43} & \hat{K}_{s,44} & \hat{K}_{s,45} & \hat{K}_{s,46}\\ \hat{K}_{s,51} & \hat{K}_{s,52} & \hat{K}_{s,53} & \hat{K}_{s,54} & \hat{K}_{s,55} & \hat{K}_{s,56}\\ \hat{K}_{s,61} & \hat{K}_{s,62} & \hat{K}_{s,63} & \hat{K}_{s,64} & \hat{K}_{s,65} & \hat{K}_{s,66}\end{bmatrix} & \begin{pmatrix}C_{1lm}\\ C_{2lm}\\ C_{3lm}\\ C_{4lm}\\ C_{5lm}\\ C_{6lm}\end{pmatrix} \\
\hat{\boldsymbol{\sigma}}_{\mathbf{s}} & = & \left[\hat{K}_s\right] & \mathbf{C_s}
\end{array} \tag{2.69}$$

With the elements of matrix $\left[\hat{K}_s\right]$, the equations (2.68) can be used to determine the unknowns C_{1lm} - C_{3lm} of the solutions of the scalar potentials (2.67). The relationships between the stresses $\hat{\sigma}_{rr}$, $\hat{\sigma}_{r\vartheta}$ and $\hat{\sigma}_{r\varphi}$ and the unknowns C_{1lm} -C_{3lm} are according to appendix A.6

$$\hat{\sigma}_{rr}\left(r=R,m,l,\omega\right)\,=A_1\check{P}_m^l \tag{2.70a}$$

$$\hat{\sigma}_{r\vartheta}\left(r=R,m,l,\omega\right)=m\cot\left(\vartheta\right)A_2\check{P}_m^l-\frac{m+l}{\sin\left(\vartheta\right)}A_2\check{P}_{m-1}^l+i\frac{l}{\sin\left(\vartheta\right)}A_3P_m^l \tag{2.70b}$$

$$\hat{\sigma}_{r\varphi}\left(r=R,m,l,\omega\right)=i\,\frac{l}{\sin\left(\vartheta\right)}A_2\check{P}_m^l-m\cot\left(\vartheta\right)A_3\check{P}_m^l+\frac{m+l}{\sin\left(\vartheta\right)}A_3\check{P}_{m-1}^l \tag{2.70c}$$

where $\check{P}_m^l$ serves as abbreviation for the normalized associated Legendre polynomial depending on $(\cos(\vartheta))$ and A_1, A_2 and A_3 are chosen as

$$\begin{aligned}A_1=&C_{1lm}\left(\left(\frac{m^2-m}{R^2}-\frac{1}{2}|k_s|^{\,2}\right)\,2\mu\;h_m^{(1)}(|k_p|R)+\frac{2}{R}\;|k_p|\;2\mu\;h_{m+1}^{(1)}(|k_p|R)\right)e^{il\varphi}\\&C_{3lm}\left(\frac{m^3-m}{R^2}\;2\mu\;h_m^{(1)}(|k_s|R)-\frac{m^2+m}{R}\;|k_s|\;2\mu\;h_{m+1}^{(1)}(|k_s|R)\right)e^{il\varphi}\end{aligned} \tag{2.71a}$$

$$\begin{aligned}A_2=&C_{1lm}\left(\frac{m-1}{R^2}\;2\mu\;h_m^{(1)}(|k_p|R)-\frac{1}{R}\;|k_p|\;2\mu\;h_{m+1}^{(1)}(|k_p|R)\right)e^{il\varphi}\;+\\&C_{3lm}\left(\left(\frac{m^2-1}{R^2}-\frac{1}{2}|k_s|^{\,2}\right)\,2\mu\;h_m^{(1)}(|k_s|R)+\frac{1}{R}\;|k_s|\;2\mu\;h_{m+1}^{(1)}(|k_s|R)\right)e^{il\varphi}\end{aligned} \tag{2.71b}$$

$$A_3=C_{2lm}\left(\frac{m-1}{2R}\;2\mu\;h_m^{(1)}(|k_s|R)-\frac{1}{2}\;|k_s|\;2\mu\;h_{m+1}^{(1)}(|k_s|R)\right)e^{il\varphi} \tag{2.71c}$$

Interpreting the equations (2.70), it is visible that the shear stress components $\hat{\sigma}_{r\vartheta}$ and $\hat{\sigma}_{r\varphi}$ contain for one combination of m and l, normalized associated Legendre polynomials with different degrees m or $(m-1)$. To generate parameters that are only dependent on a Legendre polynomial with one degree, [Frühe 2010] introduced in accordance with [Eringen and Suhubi 1975] two auxiliary quantities $\hat{F}$ and $\hat{G}$. They combine the stress contributions $\hat{\sigma}_{r\vartheta}$ and $\hat{\sigma}_{r\varphi}$ with

$$\hat{F}\left(r=R,m,l,\omega\right)=-\left(\frac{\partial\left(\hat{\sigma}_{r\vartheta}\sin\left(\vartheta\right)\right)}{\partial\vartheta}+\frac{\partial\hat{\sigma}_{r\varphi}}{\partial\varphi}\right)\frac{1}{\sin\left(\varphi\right)} \tag{2.72a}$$

$$\hat{G}\left(r=R,m,l,\omega\right)=-\left(\frac{\partial\hat{\sigma}_{r\vartheta}}{\partial\varphi}-\frac{\partial\left(\hat{\sigma}_{r\varphi}\sin\left(\vartheta\right)\right)}{\partial\vartheta}\right)\frac{1}{\sin\left(\vartheta\right)} \tag{2.72b}$$

Thus, if $\hat{\sigma}_{r\vartheta}$ and $\hat{\sigma}_{r\varphi}$ are introduced into the equations (2.72), the auxiliary quantities $\hat{F}$ and $\hat{G}$ depend for one combination of m and l only on Legendre polynomials with degree m and order l.

$$\hat{F}\,(r = R, m, l, \omega) = A_2\; m\,(m+1)\,\check{P}_m^l \tag{2.73a}$$

$$\hat{G}\,(r = R, m, l, \omega) = A_3\; m\,(m+1)\,\check{P}_m^l \tag{2.73b}$$

Using the substitution of $\hat{\sigma}_{r\vartheta}$ and $\hat{\sigma}_{r\varphi}$ by $\hat{F}$ and $\hat{G}$, the boundary conditions (2.68) can be used for the calculation of the unknowns C_{1lm} - C_{3lm} for each combination of m and l. For this, the shear loads $\hat{p}_{r\vartheta}$ and $\hat{p}_{r\varphi}$ also have to be expressed by analogous auxiliary components $\hat{F}_p$ and $\hat{G}_p$ according to the equations (2.72). This substitution leads to a system of equations

$$\begin{bmatrix} \hat{K}'_{s,11} & 0 & \hat{K}'_{s,11} \\ \hat{F}_1 & 0 & \hat{F}_3 \\ 0 & \hat{G}_2 & 0 \end{bmatrix} \begin{pmatrix} C_{1lm} \\ C_{2lm} \\ C_{3lm} \end{pmatrix} = \begin{pmatrix} -\hat{p}_{rr} \\ -\hat{F}_p \\ -\hat{G}_p \end{pmatrix} \tag{2.74}$$

with

$$\hat{K}'_{s,11} = \left(\frac{m^2 - m}{R^2} - \frac{1}{2} |k_s|^{\;2} \right) 2\mu h_m^{(1)}(|k_p|R) + \frac{2}{R} |k_p| 2\mu h_{m+1}^{(1)}(|k_p|R) \tag{2.75a}$$

$$\hat{K}'_{s,33} = \frac{m^3 - m}{R^2} 2\mu h_m^{(1)}(|k_s|R) - \frac{m^2 + m}{R} |k_s| 2\mu h_{m+1}^{(1)}(|k_s|R) \tag{2.75b}$$

$$\hat{F}_1 \quad = m(m+1) \left(\frac{m-1}{R^2} 2\mu h_m^{(1)}(|k_p|R) - \frac{1}{R} |k_p| 2\mu h_{m+1}^{(1)}(|k_p|R) \right) \tag{2.75c}$$

$$\hat{F}_3 \quad = m(m+1) \left(\left(\frac{m^2 - 1}{R^2} - \frac{1}{2} |k_s|^{\;2} \right) 2\mu h_m^{(1)}(|k_s|R) + \frac{1}{R} |k_s| 2\mu h_{m+1}^{(1)}(|k_s|R) \right) \tag{2.75d}$$

$$\hat{G}_2 \quad = m(m+1) \left(\frac{m-1}{2R} 2\mu h_m^{(1)}(|k_s|R) - \frac{1}{2} |k_s| 2\mu h_{m+1}^{(1)}(|k_s|R) \right) \tag{2.75e}$$

With this system of equations (2.74) the unknowns can be determined and thus the displacements and the stresses can be calculated at an arbitrary position due to given loads on the spherical surface.

3 Superposition of the Fundamental Solutions

3.1 Preliminary remark

In this chapter, the solutions of the two systems halfspace with a cylindrical cavity and halfspace with a spherical cavity are presented. The solution for the first substructure of a halfspace with a cylindrical cavity is derived in the section 3.2. The solution of the halfspace with a spherical cavity is presented in section 3.3. The derivation of the stiffness matrices for both systems is contained in section 3.4.

3.2 Halfspace with cylindrical cavity - General derivations

In this section, the solution for the substructure of a halfspace with cylindrical cavity shall be derived. This system contains two boundaries as depicted in figure 3.1. The first boundary is the halfspace surface Λ which is described in the Cartesian coordinate system. The second boundary of the cylindrical surface Γ inside the halfspace is described in cylindrical coordinates.

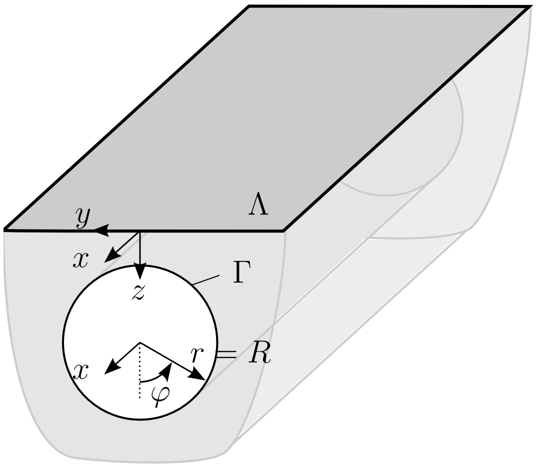

Figure 3.1: Schematic sketch of the halfspace with cylindrical cavity

The solution of the coupled system is determined superposing the two fundamental systems presented in the sections 2.3 and 2.4. The stresses and displacements on the boundaries Λ and Γ of the system have to fulfill the real boundary conditions.

$$\hat{\sigma}_{zz,\Lambda}\left(k_x, k_y, z=0, \omega\right) = -\hat{p}_{z,\Lambda}\left(k_x, k_y, \omega\right) \tag{3.1a}$$

$$\hat{\sigma}_{yz,\Lambda}\left(k_x, k_y, z=0, \omega\right) = -\hat{p}_{y,\Lambda}\left(k_x, k_y, \omega\right) \tag{3.1b}$$

$$\hat{\sigma}_{xz,\Lambda}\left(k_x, k_y, z=0, \omega\right) = -\hat{p}_{x,\Lambda}\left(k_x, k_y, \omega\right) \tag{3.1c}$$

$$\hat{\sigma}_{rr,\Gamma}\left(k_x, r=R, n, \omega\right) = -\hat{p}_{r,\Gamma}\left(k_x, n, \omega\right) \tag{3.1d}$$

$$\hat{\sigma}_{xr,\Gamma}\left(k_x, r=R, n, \omega\right) = -\hat{p}_{x,\Gamma}\left(k_x, n, \omega\right) \tag{3.1e}$$

$$\hat{\sigma}_{\varphi r,\Gamma}\left(k_x, r=R, n, \omega\right) = -\hat{p}_{\varphi,\Gamma}\left(k_x, n, \omega\right) \tag{3.1f}$$

Therefore, the superposition of the stresses and displacements of the two fundamental systems on the positions of the boundaries Λ and Γ also has to fulfill the given boundary conditions. As the calculations for both subsystems are carried out in the transformed domain in dependency on k_x and ω, the superposition can be performed in the respective domain. Thus, a two-dimensional, quasi-static computation is carried out for each combination of k_x and ω and the results in the original domain are obtained after an inverse Fourier transformation.

For each calculation for a given combination of k_x and ω, the results on the halfspace surface Λ are specified in dependency on the wavenumber k_y. As the calculations are carried out numerically, the continuous wavenumber k_y is expressed at discrete values $k_y = s\ \Delta k_y$ with $s = -\frac{N_y}{2}, ..., \left(\frac{N_y}{2} - 1\right)$. The parameters on the cylindrical boundary Γ are indicated in dependency on the Fourier series development regarding the circumferential angle $\varphi = n\ \Delta\varphi$ with $n = 1, 2, ..., N_\varphi$. As mentioned in A.1.2 the numbers of samples N_y and N_φ have to be chosen such that the computation time is acceptable but numerical artifacts are avoided. As the calculations are performed using a Fast Fourier transformation algorithm, the number of samples are powers of two. While the Fourier series members n range from 1 to N_φ, the wavenumber k_y is arranged with $k_y = 0$ in the middle of the vector. The discretization of a function in one domain leads to a repetition of the transformed signal as mentioned in A.1.2 so k_y could also be defined as $k_y = s\ \Delta k_y$ with $s = 0, ..., (N_y - 1)$.The first definition is chosen for convenience when interpreting the results in the transformed domain as they are symmetric with respect to $k_y = 0$.

Summarizing, the boundary conditions of equation (3.1) have to be fulfilled for each combination of k_x and ω. Moreover, the boundary conditions on the halfspace surface Λ in the equations (3.1a), (3.1b) and (3.1c) have to be fulfilled for each discrete wavenumber contribution s.

$$\hat{\sigma}_{zz,\Lambda}\left(s, z = 0\right) = -\hat{p}_{z,\Lambda}\left(s\right) \tag{3.2a}$$

$$\hat{\sigma}_{yz,\Lambda}\left(s, z = 0\right) = -\hat{p}_{y,\Lambda}\left(s\right) \tag{3.2b}$$

$$\hat{\sigma}_{xz,\Lambda}\left(s, z = 0\right) = -\hat{p}_{x,\Lambda}\left(s\right) \tag{3.2c}$$

For each discrete wavenumber s, three boundary conditions exist. Thus, in total $3N_y$ boundary conditions on the halfspace surface are given.

The boundary conditions on the cylindrical surface Γ in the equations (3.1d), (3.1e) and (3.1f) have to be fulfilled for each discrete Fourier series member n.

$$\hat{\sigma}_{rr,\Gamma}\left(r = R, n\right) = -\hat{p}_{r,\Gamma}\left(n\right) \tag{3.3a}$$

$$\hat{\sigma}_{xr,\Gamma}\left(r = R, n\right) = -\hat{p}_{x,\Gamma}\left(n\right) \tag{3.3b}$$

$$\hat{\sigma}_{\varphi r,\Gamma}\left(r = R, n\right) = -\hat{p}_{\varphi,\Gamma}\left(n\right) \tag{3.3c}$$

Thus, on the cylindrical surface $3N_\varphi$ boundary conditions are given.

In order to fulfill these $(3N_y + 3N_\varphi)$ boundary conditions, the fundamental systems have to be evaluated at the respective positions. Therefore, virtual surfaces are introduced as depicted in figure 3.2 and figure 3.3.

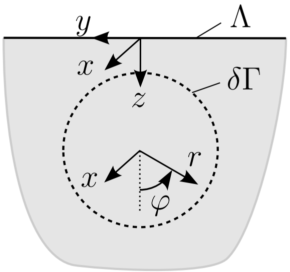

Figure 3.2: Halfspace with real surface Λ and virtual surface $\delta\Gamma$

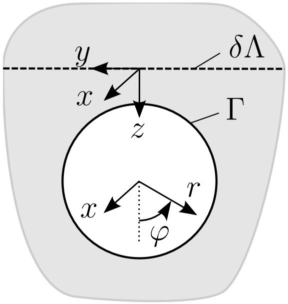

Figure 3.3: Fullspace with real surface Γ and virtual surface $\delta\Lambda$

In a first step, unit loads $\hat{\sigma}_{iz}\left(s\right)$ with $i = z, y, x$ are applied on the halfspace surface Λ where s denotes the wavenumber $k_y = s\ \Delta k_y$ for which the calculations are carried out. The resulting stresses on the virtual cylindrical surface $\delta\Gamma$ are calculated according to section 2.3.3 as illustrated in figure 3.4. The computations according to section 2.3.3 lead to a Cartesian description of the stresses in dependency on the wavenumber k_y. As the boundary conditions (3.3) on the cylindrical surface are given in dependency on the Fourier series member n along the circumference of the cylinder, a coordinate transformation is necessary. The calculated stresses have to be transformed to a cylindrical coordinate system and developed into a Fourier series regarding the circumference. After this coordinate transformation, the stresses on the virtual cylindrical surface $\hat{\sigma}_{jr}^{(iz,s)}\left(n\right)$ are obtained with $j = r, x, \varphi$. Thus, each unit load $\hat{\sigma}_{iz}$ with a defined wavenumber s leads to N_φ resulting stresses $\hat{\sigma}_{jr}^{(iz,s)}\left(n\right)$ for each $j = r, x, \varphi$ on the virtual surface $\delta\Gamma$.

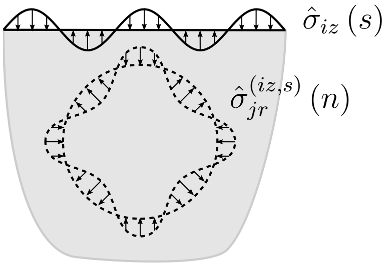

Figure 3.4: Unit load $\hat{\sigma}_{iz}\left(s\right)$ on the surface Λ and resulting stresses $\hat{\sigma}_{jr}^{(iz,s)}\left(n\right)$ on the virtual surface $\delta\Gamma$

Analogously, unit loads $\hat{\sigma}_{jr}\left(n\right)$, each with a defined Fourier series member n, are applied on the cylindrical surface Γ in the system of a fullspace with cylindrical cavity as depicted in figure 3.5. The resulting stresses are computed on the virtual halfspace surface $\delta\Lambda$ according to section 2.4.3. As they are calculated in dependency on the Fourier series member n, a coordinate transformation is required, analogously to the stresses in the halfspace system.

The calculated stresses on the halfspace surface $\delta\Lambda$ are transformed from a cylindrical coordinate system into the Cartesian coordinate system and Fourier transformed with respect to the y-coordinate. Thus, they can be expressed in dependency on the number of the discrete wavenumber s and each load $\hat{\sigma}_{jr}$ with a fixed Fourier series member n leads to N_y stresses $\hat{\sigma}_{iz}^{(jr,n)}(s)$ for each $i = z, y, x$ on the virtual surface $\delta\Lambda$.

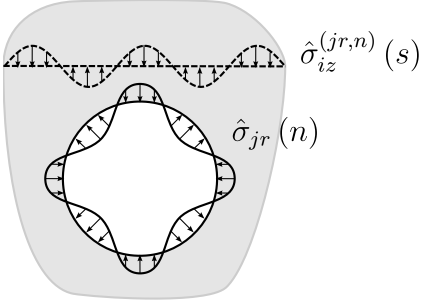

Figure 3.5: Unit load $\hat{\sigma}_{jr}(n)$ on the surface Γ and resulting stresses $\hat{\sigma}_{iz}^{(jr,n)}(s)$ on the virtual surface $\delta\Lambda$

Superposing the two fundamental systems, the superposition of the stresses has to fulfill all boundary conditions (3.1). Thus, the unknown amplitudes of the stresses $C_{iz}(s)$ on the halfspace surface Λ respectively $C_{jr}(n)$ on the cylindrical surface Γ can be determined.

$$\hat{\sigma}_{zz,\Lambda}(s) = C_{zz}(s)\,\hat{\sigma}_{zz}(s) + \sum_{n=1}^{N_\varphi} \sum_{j=r,x,\varphi} C_{jr}(n)\,\hat{\sigma}_{zz}^{(jr,n)}(s) = -\hat{p}_{z,\Lambda}(s) \tag{3.4a}$$

$$\hat{\sigma}_{yz,\Lambda}(s) = C_{yz}(s)\,\hat{\sigma}_{yz}(s) + \sum_{n=1}^{N_\varphi} \sum_{j=r,x,\varphi} C_{jr}(n)\,\hat{\sigma}_{yz}^{(jr,n)}(s) = -\hat{p}_{y,\Lambda}(s) \tag{3.4b}$$

$$\hat{\sigma}_{xz,\Lambda}(s) = C_{xz}(s)\,\hat{\sigma}_{xz}(s) + \sum_{n=1}^{N_\varphi} \sum_{j=r,x,\varphi} C_{jr}(n)\,\hat{\sigma}_{xz}^{(jr,n)}(s) = -\hat{p}_{x,\Lambda}(s) \tag{3.4c}$$

$$\hat{\sigma}_{rr,\Gamma}(n) = \sum_{s=-N_y/2}^{N_y/2-1} \sum_{i=z,y,x} C_{iz}(s)\,\hat{\sigma}_{rr}^{(iz,s)}(n) + C_{rr}(n)\,\hat{\sigma}_{rr}(n) = -\hat{p}_{r,\Gamma}(n) \tag{3.4d}$$

$$\hat{\sigma}_{xr,\Gamma}(n) = \sum_{s=-N_y/2}^{N_y/2-1} \sum_{i=z,y,x} C_{iz}(s)\,\hat{\sigma}_{xr}^{(iz,s)}(n) + C_{xr}(n)\,\hat{\sigma}_{xr}(n) = -\hat{p}_{x,\Gamma}(n) \tag{3.4e}$$

$$\hat{\sigma}_{\varphi r,\Gamma}(n) = \sum_{s=-N_y/2}^{N_y/2-1} \sum_{i=z,y,x} C_{iz}(s)\,\hat{\sigma}_{\varphi r}^{(iz,s)}(n) + C_{\varphi r}(n)\,\hat{\sigma}_{\varphi r}(n) = -\hat{p}_{\varphi,\Gamma}(n) \tag{3.4f}$$

The constants $C_{iz}(s)$ and $C_{jr}(n)$ contained in the vector of the unknowns $\mathbf{C}$ mark the unknown amplitudes of the associated unit loads. The $(3N_y + 3N_\varphi)$ unknowns are calculated using the given $(3N_y + 3N_\varphi)$ boundary conditions. The boundary conditions (3.4) can also be formulated in matrix notation as

$$\underbrace{\begin{bmatrix} \left[\hat{S}_{\Lambda\Lambda_{ITM}}\right] & \left[\hat{S}_{\Lambda\Gamma_{ITM}}\right] \\ \left[\hat{S}_{\Gamma\Lambda_{ITM}}\right] & \left[\hat{S}_{\Gamma\Gamma_{ITM}}\right] \end{bmatrix}}_{\left[\hat{S}_{ITM}\right]} \underbrace{\begin{pmatrix} \mathbf{C}_{\boldsymbol{\Lambda}} \\ \mathbf{C}_{\boldsymbol{\Gamma}} \end{pmatrix}}_{\mathbf{C}} = \underbrace{\begin{pmatrix} \hat{\mathbf{P}}_{\boldsymbol{\Lambda}\mathbf{ITM}} \\ \hat{\mathbf{P}}_{\boldsymbol{\Gamma}\mathbf{ITM}} \end{pmatrix}}_{\hat{\mathbf{P}}_{\mathbf{ITM}}} \tag{3.5}$$

The matrices $\left[\hat{S}_{\alpha\beta_{ITM}}\right]$ with $\alpha = \Lambda, \Gamma$ and $\beta = \Lambda, \Gamma$ contain the results for the stresses on the surface α for a unit load $\hat{\mathbf{P}}_{\boldsymbol{\beta}\mathbf{ITM}}$ on surface β in dependency on the unknown amplitudes $\mathbf{C}_{\boldsymbol{\alpha}}$ on surface α. The elements of the matrix $\left[\hat{S}_{ITM}\right]$ and the vectors $\mathbf{C}$ and $\hat{\mathbf{P}}_{\mathbf{ITM}}$ are repeated in detail in appendix A.7. Thus, the vector of the unknowns can be determined as

$$\mathbf{C} = \left[\hat{S}_{ITM}\right]^{-1} \hat{\mathbf{P}}_{\mathbf{ITM}} \tag{3.6}$$

3.3 Halfspace with spherical cavity - General derivations

The system halfspace with spherical cavity as exemplarily depicted in figure 3.6 is derived by a superposition of the two fundamental systems halfspace and fullspace with spherical cavity as presented in the sections 2.3 and 2.5. The superposition itself can be performed analogously to the one that was used to determine the solution of a halfspace with cylindrical cavity in section 3.2.

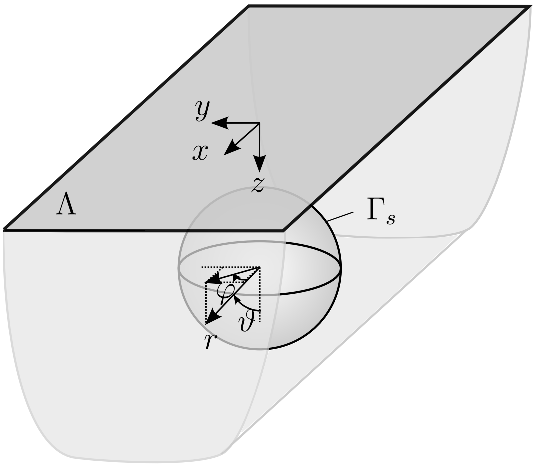

Figure 3.6: Schematic sketch of the halfspace with spherical cavity

The superposition of the two systems halfspace and fullspace with spherical cavity has to fulfill the given boundary conditions. Again, both fundamental systems are solved in different coordinate systems. While the solution of the halfspace is derived in $(k_x,\ k_y,\ z,\ \omega)$, the fullspace with spherical cavity is described in dependency on $(r,\ m,\ l,\ \omega)$. In contrast to section 3.2 the three-dimensional system cannot be reduced to a 2.5-dimensional one as there is no common spatial wavenumber coordinate. This leads to an increased computational effort but as the system is spatially finite, the effort is reasonably small. The reduction to quasi-static calculations by solving the system for each frequency ω can persist.

Summarizing, the parameters on the halfspace surface Λ with $z = 0$ are described in dependency on $k_x = o\ \Delta k_x$ with $o = -\frac{N_x}{2}, ..., \left(\frac{N_x}{2} - 1\right)$ and $k_y = s\ \Delta k_y$ with $s = -\frac{N_y}{2}, ..., \left(\frac{N_y}{2} - 1\right)$. The parameters Δk_x and Δk_y determine the resolution of the discrete Fourier transformation in the wavenumber domain and N_x and N_y are the number of samples with respect to the x- and y-coordinates. They are chosen according to the characteristics of the discrete Fourier transformation as they are presented shortly in appendix A.1.2. As the calculations are carried out using a Fast Fourier transformation algorithm, the number of samples are powers of two. For convenience the wavenumbers k_x and k_y are arranged with $k_x = 0$ respectively $k_y = 0$ in the middle of the vector. Analogously they could also be arranged with N_x or N_y values starting from zero with $k_x = 0, ..., (N_x - 1)\ \Delta k_x$ respectively $k_y = 0, ..., (N_y - 1)\ \Delta k_y$. As the discretization of the signals in one domain leads to a repetition in the transformed domain, both arrangements lead to identical results. The parameters on the spherical coupling surface Γ_s with $r = R$ depend on order and degree of the Legendre polynomials m and l $(m = 0, ..., M$ and $l = -m, ..., m)$. The maximum numbers of the samples of the discrete

Fourier transformation N_x and N_y as well as the maximum degree M have to be chosen such that the computational effort is acceptable but the results are sufficiently exact.

The procedure of the superposition itself is analogous to the one described in section 3.2:

- Unit loads $\hat{\sigma}_{iz}\left(o,s\right)$ with $i = z, y, x$ are applied on the halfspace surface Λ for each combination of k_x and k_y.

- The resulting stresses due to these loads are calculated on a virtual surface $\delta\Gamma_s$ which is equivalent to the position of the intended real spherical surface. They are originally described in the threefold Fourier transformed coordinate system (k_x, k_y, z, ω). To enable the superposition with the fullspace with spherical cavity, they are transformed into the coordinate system of the fullspace with spherical cavity (r, m, l, ω). Each unit load with a defined combination of k_x and k_y thus leads to stresses $\hat{\sigma}_{rj}^{(iz,os)}\left(m,l\right)$ with $j = r, \vartheta, \varphi$.

- In a second step, unit loads $\hat{\sigma}_{rj}\left(m,l\right)$ with $j = r, \vartheta, \varphi$ are applied on the spherical surface Γ_s for the different spherical harmonics with degree m and order l.

- The resulting stresses on the virtual halfspace surface $\delta\Lambda$ that is equivalent to the position of the intended real halfspace surface are calculated and transformed into the coordinate system of the halfspace (k_x, k_y, z, ω). Thus, for each spherical harmonic unit load $\hat{\sigma}_{rj}\left(m,l\right)$, stresses $\hat{\sigma}_{iz}^{(rj,ml)}\left(o,s\right)$ with $i = z, y, x$ are obtained.

- The superposition of all the stresses on both surfaces has to fulfill the given boundary conditions.

$$\hat{\sigma}_{zz,\Lambda}(o,s) = C_{zz}(o,s)\,\hat{\sigma}_{zz}(o,s) + \sum_{m=0}^{M}\sum_{l=-m}^{m}\sum_{j=r,\vartheta,\varphi} C_{rj}(m,l)\;\hat{\sigma}_{zz}^{(rj,ml)}(o,s) = -\hat{p}_{z,\Lambda}(o,s) \tag{3.7a}$$

$$\hat{\sigma}_{yz,\Lambda}(o,s) = C_{yz}(o,s)\,\hat{\sigma}_{yz}(o,s) + \sum_{m=0}^{M}\sum_{l=-m}^{m}\sum_{j=r,\vartheta,\varphi} C_{rj}(m,l)\;\hat{\sigma}_{yz}^{(rj,ml)}(o,s) = -\hat{p}_{y,\Lambda}(o,s) \tag{3.7b}$$

$$\hat{\sigma}_{xz,\Lambda}(o,s) = C_{xz}(o,s)\,\hat{\sigma}_{xz}(o,s) + \sum_{m=0}^{M}\sum_{l=-m}^{m}\sum_{j=r,\vartheta,\varphi} C_{rj}(m,l)\;\hat{\sigma}_{xz}^{(rj,ml)}(o,s) = -\hat{p}_{x,\Lambda}(o,s) \tag{3.7c}$$

$$\hat{\sigma}_{rr,\Gamma_s}(m,l) = \sum_{o=-N_x/2}^{N_x/2-1}\sum_{s=-N_y/2}^{N_y/2-1}\sum_{i=z,y,x} C_{iz}(o,s)\,\hat{\sigma}_{rr}^{(iz,os)}(m,l) + C_{rr}(m,l)\,\hat{\sigma}_{rr}(m,l) = -\hat{p}_{r,\Gamma_s}(m,l) \tag{3.7d}$$

$$\hat{\sigma}_{r\vartheta,\Gamma_s}(m,l) = \sum_{o=-N_x/2}^{N_x/2-1}\sum_{s=-N_y/2}^{N_y/2-1}\sum_{i=z,y,x} C_{iz}(o,s)\,\hat{\sigma}_{r\vartheta}^{(iz,os)}(m,l) + C_{r\vartheta}(m,l)\,\hat{\sigma}_{r\vartheta}(m,l) = -\hat{p}_{\vartheta,\Gamma_s}(m,l) \tag{3.7e}$$

$$\hat{\sigma}_{r\varphi,\Gamma_s}(m,l) = \sum_{o=-N_x/2}^{N_x/2-1}\sum_{s=-N_y/2}^{N_y/2-1}\sum_{i=z,y,x} C_{iz}(o,s)\,\hat{\sigma}_{r\varphi}^{(iz,os)}(m,l) + C_{r\varphi}(m,l)\,\hat{\sigma}_{r\varphi}(m,l) = -\hat{p}_{\varphi,\Gamma_s}(m,l) \tag{3.7f}$$

The system of equations (3.7) can be written in matrix notation as

$$\underbrace{\begin{bmatrix} \left[\hat{S}_{\Lambda\Lambda_{ITM}}\right] & \left[\hat{S}_{\Lambda\Gamma_s\,ITM}\right] \\ \left[\hat{S}_{\Gamma_s\Lambda_{ITM}}\right] & \left[\hat{S}_{\Gamma_s\Gamma_s\,ITM}\right] \end{bmatrix}}_{\left[\hat{S}_{s\,ITM}\right]} \underbrace{\begin{pmatrix} \mathbf{C}_{\boldsymbol{\Lambda}} \\ \mathbf{C}_{\boldsymbol{\Gamma}_\mathbf{s}} \end{pmatrix}}_{\mathbf{C}_\mathbf{s}} = \underbrace{\begin{pmatrix} \hat{\mathbf{P}}_{\boldsymbol{\Lambda}\mathbf{ITM}} \\ \hat{\mathbf{P}}_{\boldsymbol{\Gamma}_\mathbf{s}\,\mathbf{ITM}} \end{pmatrix}}_{\hat{\mathbf{P}}_{\mathbf{s}\,\mathbf{ITM}}} \tag{3.8}$$

Using equation (3.8), the unknowns can be determined and the solution of the superposed system is obtained.

3.4 Halfspace with cylindrical or spherical cavity - Stiffness matrix

The superposed systems of a halfspace with a cylindrical or a spherical cavity shall be coupled with the substructure technique to a cylindrical or spherical structure that is modeled with the Finite Element Method. As will be presented in chapter 5, the stiffness matrices of the two substructures are necessary to perform the coupling. Hence, the stiffness matrices of the two systems have to be derived in a post-processing step. This is done exemplarily for the first system halfspace with cylindrical cavity in this section. The stiffness matrix of the halfspace with spherical cavity can be determined analogously.

For any general system, the stiffness matrix $\left[\hat{K}_{ITM}\right]$ characterizes the relationship between the vector of the loads and the displacement vector by

$$\left[\hat{K}_{ITM}\right] \hat{\mathbf{u}}_{\mathbf{ITM}} = \hat{\mathbf{P}}_{\mathbf{ITM}} \tag{3.9}$$

The displacement field $\hat{\mathbf{u}}_{\mathbf{ITM}}$ of the system halfspace with cylindrical cavity is calculated superposing the displacements of the fundamental systems halfspace and fullspace with cylindrical cavity for given loads on the system.

Due to the unit stresses $\hat{\sigma}_{iz}\left(s\right)$ on the halfspace surface Λ with $i = z, y, x$ multiplied with the amplitudes $C_{iz}\left(s\right)$ that have been calculated out of the stress boundary conditions as described in section 3.2, the resulting displacements $\hat{u}_k^{(iz,s)}\left(s\right)$ on the halfspace surface Λ with $k = z, y, x$ and the displacements $\hat{u}_l^{(iz,s)}\left(n\right)$ with $l = r, x, \varphi$ on the virtual cylindrical surface $\delta\Gamma$ can be calculated. Analogously the unit stresses $\hat{\sigma}_{jr}\left(n\right)$ with $j = r, x, \varphi$ multiplied with the amplitudes $C_{jr}\left(n\right)$ lead to the displacements $\hat{u}_k^{(jr,n)}\left(s\right)$ on $\delta\Lambda$ and the displacements $\hat{u}_l^{(jr,n)}\left(n\right)$ on Γ. The displacements of the superposed system halfspace with cylindrical cavity at the halfspace surface $\hat{u}_{k,\Lambda}\left(s\right)$ and at the cylindrical coupling surface $\hat{u}_{l,\Gamma}\left(n\right)$ are obtained by superposing the respective displacement components of the fundamental systems.

$$\hat{u}_{z,\Lambda}(s) = \sum_{i=z,y,x} C_{iz}(s)\, \hat{u}_z^{(iz,s)}(s) + \sum_{n=1}^{N_\varphi} \sum_{j=r,x,\varphi} C_{jr}(n)\ \hat{u}_z^{(jr,n)}(s) \tag{3.10a}$$

$$\hat{u}_{y,\Lambda}(s) = \sum_{i=z,y,x} C_{iz}(s)\, \hat{u}_y^{(iz,s)}(s) + \sum_{n=1}^{N_\varphi} \sum_{j=r,x,\varphi} C_{jr}(n)\ \hat{u}_y^{(jr,n)}(s) \tag{3.10b}$$

$$\hat{u}_{x,\Lambda}(s) = \sum_{i=z,y,x} C_{iz}(s)\, \hat{u}_x^{(iz,s)}(s) + \sum_{n=1}^{N_\varphi} \sum_{j=r,x,\varphi} C_{jr}(n)\ \hat{u}_x^{(jr,n)}(s) \tag{3.10c}$$

$$\hat{u}_{r,\Gamma}(n) = \sum_{s=-N_y/2}^{N_y/2-1} \sum_{i=z,y,x} C_{iz}(s)\, u_r^{(iz,s)}(n) + \sum_{j=r,x,\varphi} C_{jr}(n)\, u_r^{(jr,n)}(n) \tag{3.10d}$$

$$\hat{u}_{x,\Gamma}(n) = \sum_{s=-N_y/2}^{N_y/2-1} \sum_{i=z,y,x} C_{iz}(s)\, u_x^{(iz,s)}(n) + \sum_{j=r,x,\varphi} C_{jr}(n)\, u_x^{(jr,n)}(n) \tag{3.10e}$$

$$\hat{u}_{\varphi,\Gamma}(n) = \sum_{s=-N_y/2}^{N_y/2-1} \sum_{i=z,y,x} C_{iz}(s)\, u_\varphi^{(iz,s)}(n) + \sum_{j=r,x,\varphi} C_{jr}(n)\, u_\varphi^{(jr,n)}(n) \tag{3.10f}$$

In matrix notation, the equations (3.10) can be written as

$$\underbrace{\begin{pmatrix} \hat{\mathbf{u}}_{\mathbf{\Lambda_{ITM}}} \\ \hat{\mathbf{u}}_{\mathbf{\Gamma_{ITM}}} \end{pmatrix}}_{\hat{\mathbf{u}}_{ITM}} = \underbrace{\begin{bmatrix} \left[\hat{U}_{\Lambda\Lambda_{ITM}}\right] & \left[\hat{U}_{\Lambda\Gamma_{ITM}}\right] \\ \left[\hat{U}_{\Gamma\Lambda_{ITM}}\right] & \left[\hat{U}_{\Gamma\Gamma_{ITM}}\right] \end{bmatrix}}_{\left[\hat{U}_{ITM}\right]} \underbrace{\begin{pmatrix} \mathbf{C_\Lambda} \\ \mathbf{C_\Gamma} \end{pmatrix}}_{\mathbf{C}} \tag{3.11}$$

with the elements of the matrix $\left[\hat{U}_{ITM}\right]$ also repeated in detail in appendix A.7.

Introducing the equations (3.5) and (3.11) into equation (3.9) leads to

$$\left[\hat{K}_{ITM}\right]\left[\hat{U}_{ITM}\right]\mathbf{C} = \left[\hat{S}_{ITM}\right]\mathbf{C} \tag{3.12}$$

and the stiffness matrix of the superposed system halfspace with cylindrical cavity is

$$\left[\hat{K}_{ITM}\right] = \left[\hat{S}_{ITM}\right]\left[\hat{U}_{ITM}\right]^{-1} \tag{3.13}$$

or with a differentiation for the two surfaces

$$\left[\hat{K}_{ITM}\right] = \begin{bmatrix} \left[\hat{K}_{\Lambda\Lambda_{ITM}}\right] & \left[\hat{K}_{\Lambda\Gamma_{ITM}}\right] \\ \left[\hat{K}_{\Gamma\Lambda_{ITM}}\right] & \left[\hat{K}_{\Gamma\Gamma_{ITM}}\right] \end{bmatrix} = \begin{bmatrix} \left[\hat{S}_{\Lambda\Lambda_{ITM}}\right] & \left[\hat{S}_{\Lambda\Gamma_{ITM}}\right] \\ \left[\hat{S}_{\Gamma\Lambda_{ITM}}\right] & \left[\hat{S}_{\Gamma\Gamma_{ITM}}\right] \end{bmatrix} \begin{bmatrix} \left[\hat{U}_{\Lambda\Lambda_{ITM}}\right] & \left[\hat{U}_{\Lambda\Gamma_{ITM}}\right] \\ \left[\hat{U}_{\Gamma\Lambda_{ITM}}\right] & \left[\hat{U}_{\Gamma\Gamma_{ITM}}\right] \end{bmatrix}^{-1} \tag{3.14}$$

and equation (3.9) can be formulated as

$$\begin{bmatrix} \left[\hat{K}_{\Lambda\Lambda_{ITM}}\right] & \left[\hat{K}_{\Lambda\Gamma_{ITM}}\right] \\ \left[\hat{K}_{\Gamma\Lambda_{ITM}}\right] & \left[\hat{K}_{\Gamma\Gamma_{ITM}}\right] \end{bmatrix} \begin{pmatrix} \hat{\mathbf{u}}_{\mathbf{\Lambda_{ITM}}} \\ \hat{\mathbf{u}}_{\mathbf{\Gamma_{ITM}}} \end{pmatrix} = \begin{pmatrix} \hat{\mathbf{P}}_{\mathbf{\Lambda_{ITM}}} \\ \hat{\mathbf{P}}_{\mathbf{\Gamma_{ITM}}} \end{pmatrix} \tag{3.15}$$

Thus, the stiffness matrix of the halfspace with cylindrical cavity is determined.

The stiffness matrix of the halfspace with spherical cavity $\left[\hat{K}_{s\,ITM}\right]$ can be analogously determined for the degrees of freedom on the halfspace surface $\hat{\mathbf{u}}_{\mathbf{\Lambda_{ITM}}}$ and the degrees of freedom on the spherical surface $\hat{\mathbf{u}}_{\mathbf{\Gamma_{s\,ITM}}}$.

$$\begin{bmatrix} \left[\hat{K}_{\Lambda\Lambda_{ITM}}\right] & \left[\hat{K}_{\Lambda\Gamma_{s ITM}}\right] \\ \left[\hat{K}_{\Gamma_s\Lambda_{ITM}}\right] & \left[\hat{K}_{\Gamma_s\Gamma_{s ITM}}\right] \end{bmatrix} \begin{pmatrix} \hat{\mathbf{u}}_{\mathbf{\Lambda_{ITM}}} \\ \hat{\mathbf{u}}_{\mathbf{\Gamma_{s\,ITM}}} \end{pmatrix} = \begin{pmatrix} \hat{\mathbf{P}}_{\mathbf{\Lambda_{ITM}}} \\ \hat{\mathbf{P}}_{\mathbf{\Gamma_{s\,ITM}}} \end{pmatrix} \tag{3.16}$$

4 Finite Element Substructure

4.1 Preliminary remark

As second substructure, the solution for the structure inside the cylindrical or spherical cavity shall be derived. This second substructure is modeled with the Finite Element Method. The stiffness matrix of the system will be determined and can be used in order to couple it to the stiffness matrix of the substructure of an halfspace with cylindrical or spherical cavity derived in section 3.4.

If the halfspace with cylindrical cavity shall be covered, for this system the derivations of the previous chapter 3 are carried out in the transformed domain for each combination of k_x and ω. Thus, also the Finite Element calculation can be performed as a quasi-static, two-dimensional calculation in the transformed domain in dependency on the combinations of k_x and ω. Therefore, a two-dimensional Finite Element mesh is defined in the transformed domain. After solving the two-dimensional system for each combination of k_x and ω, information about the behavior with respect to the third dimension x and the time dependency is contained in the solution. It is made visible by the inverse transformations $k_x \;\bullet\!\!-\!\!\!-\!\!\!-\!\!\circ\; x$ and $\omega \;\bullet\!\!-\!\!\!-\!\!\!-\!\!\circ\; t$. This approach is often called 2.5-dimensional as the calculations in the transformed domain are carried out for a two-dimensional system but contain information about the third dimension as for example in [Tadeu and Kausel 2000] or [Sheng et al 2006]. The derivation of the 2.5-dimensional elements is contained in the following sections 4.2, 4.3 and 4.4.

If the halfspace with spherical cavity is to be coupled to a Finite Element substructure, the computations are carried out in the frequency domain for each frequency ω. Regarding the spatial distribution, there is no Fourier transformation performed as the system is not invariant in any direction in contrast to the cylindrical Finite Element mesh. Therefore, the stiffness matrix of the spherical Finite Element substructure is derived with three-dimensional elements in Cartesian coordinates in section 4.5.

4.2 2.5-dimensional finite elements

The Finite Element Method (FEM) is based on the principle of virtual work. A variety of textbooks contains information regarding the FEM, e. g. [Schwarz 1991], [Bathe and Zimmermann 2002] or [Hughes 2000]. The principle of virtual work is based on the application of a virtual displacement field $\delta\mathbf{u}$ on a three-dimensional, isoparametric volume element with the natural, local coordinates (x, η, ζ) as depicted in figure 4.1.

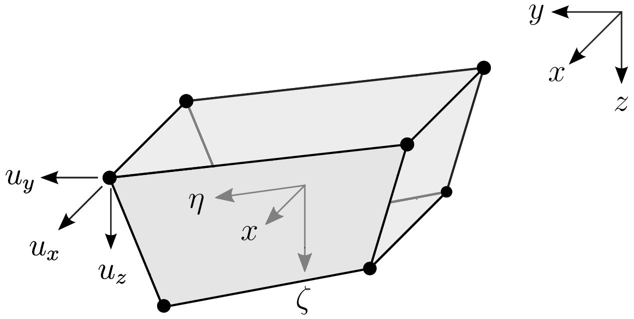

Figure 4.1: Three-dimensional finite element

It states that the sum of the resulting virtual work of the internal forces δW_i, of the external forces δW_e and of the inertia forces δW_I has to be equal to zero.

$$\delta W = \delta W_i + \delta W_e + \delta W_I = 0 \tag{4.1}$$

The weak formulation of the virtual work of the internal forces can be computed as the product of the virtual strains $\delta\boldsymbol{\varepsilon}$ due to the virtual displacements and the real stresses $\boldsymbol{\sigma}$ due to a given load on the system.

$$\delta W_i = -\int\limits_{(V)} \delta\boldsymbol{\varepsilon}(x,\eta,\zeta)\ \boldsymbol{\sigma}(x,\eta,\zeta)\ dV \tag{4.2}$$

As the cylindrical structure is infinite in x-direction, δW_i can be calculated as

$$\delta W_i = -\int\limits_{-\infty}^{\infty} \int\limits_{(A)} \delta\boldsymbol{\varepsilon}(x,\eta,\zeta)\ \boldsymbol{\sigma}(x,\eta,\zeta)\ dA\ dx \tag{4.3}$$

The derivations of chapter 3 are carried out in the transformed domain for each combination of k_x and ω. In order to allow a coupling of the two substructures, the Finite Element formulation has to refer to the same basis. Therefore, the virtual work of the finite elements is transformed to the wavenumber-frequency domain. The dependency on the frequency is implemented as the computation of the Finite Element substructure is performed for each frequency ω. The dependency of the virtual work on the wavenumber k_x is derived from equation (4.3) where the x-coordinate is replaced by a relationship regarding the wavenumber k_x. According to Parseval's identity, as presented e. g. in [Priestley 1981] or [Kammler 2008], the virtual work can also be formulated in the transformed domain using the relations of section A.1 as

$$\begin{aligned}
\delta W_i &= -\int\limits_{-\infty}^{\infty}\int\limits_{(A)} \delta\bar{\boldsymbol{\varepsilon}}(x,\eta,\zeta)\;\bar{\boldsymbol{\sigma}}(x,\eta,\zeta)\;dA\;dx \\
&= -\int\limits_{-\infty}^{\infty}\int\limits_{(A)} \delta\bar{\boldsymbol{\varepsilon}}(x,\eta,\zeta)\;\frac{1}{2\pi}\int\limits_{-\infty}^{\infty} \tilde{\boldsymbol{\sigma}}(k_x,\eta,\zeta)\;e^{ik_x x}dk_x\;\;dA\;dx \\
&= -\frac{1}{2\pi}\int\limits_{-\infty}^{\infty}\int\limits_{(A)}\int\limits_{-\infty}^{\infty} \delta\bar{\boldsymbol{\varepsilon}}(x,\eta,\zeta)\;e^{ik_x x}\;\tilde{\boldsymbol{\sigma}}(k_x,\eta,\zeta)\;dk_x\;dA\;dx \\
&= -\frac{1}{2\pi}\int\limits_{-\infty}^{\infty}\int\limits_{(A)}\int\limits_{-\infty}^{\infty} \delta\bar{\boldsymbol{\varepsilon}}(x,\eta,\zeta)\;e^{ik_x x}\;dx\;\tilde{\boldsymbol{\sigma}}(k_x,\eta,\zeta)\;dA\;dk_x \\
&= -\frac{1}{2\pi}\int\limits_{-\infty}^{\infty}\int\limits_{(A)} \delta\tilde{\boldsymbol{\varepsilon}}^{*}(k_x,\eta,\zeta)\;\tilde{\boldsymbol{\sigma}}(k_x,\eta,\zeta)\;dA\;dk_x
\end{aligned} \tag{4.4}$$

The ¯ symbol denotes again parameters in the frequency domain, while the ˜ symbol signifies again parameters in the twofold Fourier transformed domain depending on the wavenumber k_x and the frequency ω.

For numerical implementation, the integration over x respectively k_x from $-\infty$ to $+\infty$ is replaced by a sum each ranging over the number of samples N_x. For this purpose, Parseval's identity has to be adopted and is formulated using the equations (A.7) and (A.8) of appendix A.1 as

$$\delta W_i = -\int\limits_{(A)} \sum_{n=1}^{N_x} \delta\bar{\boldsymbol{\varepsilon}}^{T}(x_n,\eta,\zeta)\;\bar{\boldsymbol{\sigma}}(x_n,\eta,\zeta)\;dA = -\int\limits_{(A)} \frac{1}{N_x}\sum_{n=1}^{N_x} \delta\tilde{\boldsymbol{\varepsilon}}^{T*}(k_{x_n},\eta,\zeta)\;\tilde{\boldsymbol{\sigma}}(k_{x_n},\eta,\zeta)\;dA \tag{4.5}$$

In general, the conjugate complex transpose of a matrix $[A]$ can also be written as the adjugate matrix $[A]^H$ as stated for example in [Bronstein et al 2006]. Therefore, $\delta\tilde{\boldsymbol{\varepsilon}}^{T*}$ will be abbreviated by $\delta\tilde{\boldsymbol{\varepsilon}}^{H}$. With equation (4.5) the volume integral of equation (4.3) is replaced by an integral over the cross sectional area A and a summation over the wavenumbers k_{x_n}

with $n = 1, 2, ..., N_x$. Analogous derivations are possible for the virtual work of the external forces and for the virtual work of the inertia forces. Consequently, equation (4.1) can be written as

$$\begin{aligned} \delta W = \frac{1}{N_x} \int_{(A)} \sum_{n=1}^{N_x} \Big[& -\delta \tilde{\boldsymbol{\varepsilon}}^H(k_{x_n},\eta,\zeta)\ \tilde{\boldsymbol{\sigma}}(k_{x_n},\eta,\zeta) \\ & + \delta \tilde{\mathbf{u}}^H(k_{x_n},\eta,\zeta)\ \tilde{\mathbf{p}}(k_{x_n},\eta,\zeta) \\ & - \delta \tilde{\mathbf{u}}^H(k_{x_n},\eta,\zeta)\ \rho\ \ddot{\tilde{\mathbf{u}}}(k_{x_n},\eta,\zeta) \Big]\ dA = 0 \end{aligned} \tag{4.6}$$

Equation (4.6) is especially fulfilled if

$$\begin{aligned} \int_{(A)} & - \delta \tilde{\boldsymbol{\varepsilon}}^H(k_x,\eta,\zeta)\ \tilde{\boldsymbol{\sigma}}(k_x,\eta,\zeta) \\ & + \delta \tilde{\mathbf{u}}^H(k_x,\eta,\zeta)\ \tilde{\mathbf{p}}(k_x,\eta,\zeta) \\ & + \delta \tilde{\mathbf{u}}^H(k_x,\eta,\zeta)\ \rho\ \omega^2\ \tilde{\mathbf{u}}(k_x,\eta,\zeta)\ dA = 0 \end{aligned} \tag{4.7}$$

is fulfilled for each wavenumber k_x and for each frequency ω.

Thus, the integration over the three-dimensional volume in the original domain can be replaced by an integration over the cross section of the element for each combination of wavenumber k_x and frequency ω in the transformed domain. Therefore, the three-dimensional element of figure 4.1 is replaced by a two-dimensional element which also contains information about the third dimension in the form of the wavenumber k_x. Due to this reason, the element can also be named a 2.5-dimensional finite element. As two-dimensional geometry, a four-node element with the natural coordinates η and ζ and the global coordinates x, y, and z is chosen as depicted in figure 4.2.

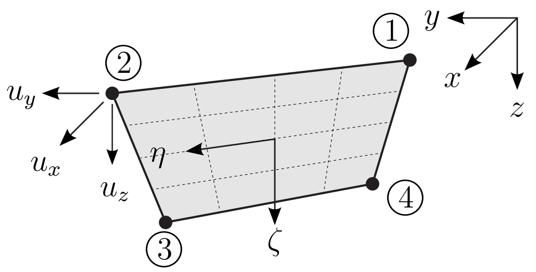

Figure 4.2: 2.5-dimensional finite element

Three degrees of freedom u_x, u_y and u_z are defined at each node and lead to the vector of the nodal displacements $\tilde{\mathbf{u}}_{\mathbf{n}}$ with

$$\tilde{\mathbf{u}}_{\mathbf{n}}{}^{T} = \begin{pmatrix} \tilde{u}_{x_1} & \tilde{u}_{y_1} & \tilde{u}_{z_1} & \tilde{u}_{x_2} & \tilde{u}_{y_2} & \tilde{u}_{z_2} & \tilde{u}_{x_3} & \tilde{u}_{y_3} & \tilde{u}_{z_3} & \tilde{u}_{x_4} & \tilde{u}_{y_4} & \tilde{u}_{z_4} \end{pmatrix} \tag{4.8}$$

The chosen elements are isoparametric where both geometry and displacements are represented by bilinear form functions.

$$N_1(\eta,\zeta) = \frac{1}{4}(1-\eta)(1-\zeta) \tag{4.9a}$$

$$N_2(\eta,\zeta) = \frac{1}{4}(1-\eta)(1+\zeta) \tag{4.9b}$$

$$N_3(\eta,\zeta) = \frac{1}{4}(1+\eta)(1+\zeta) \tag{4.9c}$$

$$N_4(\eta,\zeta) = \frac{1}{4}(1+\eta)(1-\zeta) \tag{4.9d}$$

Therefore, the relationship between the displacement field $\tilde{\mathbf{u}}$ and the vector of the nodal displacements $\tilde{\mathbf{u}}_{\mathbf{n}}$ is defined as

$$\tilde{\mathbf{u}} = [N]\,\tilde{\mathbf{u}}_{\mathbf{n}} \tag{4.10}$$

with the matrix of the form functions $[N]$

$$[N] = \begin{bmatrix} N_1(\eta,\zeta) & 0 & 0 & N_2(\eta,\zeta) & 0 & 0 & \cdots \\ 0 & N_1(\eta,\zeta) & 0 & 0 & N_2(\eta,\zeta) & 0 & \cdots \\ 0 & 0 & N_1(\eta,\zeta) & 0 & 0 & N_2(\eta,\zeta) & \cdots \end{bmatrix} \tag{4.11}$$

4.3 Derivation of the element stiffness matrix

The relationship between the stress vector $\tilde{\boldsymbol{\sigma}}$ and the strain vector $\tilde{\boldsymbol{\varepsilon}}$ in equation (4.7) is formulated analogously to equation (2.25) as

$$\begin{pmatrix} \tilde{\sigma}_{xx} \\ \tilde{\sigma}_{yy} \\ \tilde{\sigma}_{zz} \\ \tilde{\sigma}_{xy} \\ \tilde{\sigma}_{yz} \\ \tilde{\sigma}_{xz} \end{pmatrix} = \begin{bmatrix} \lambda+2\mu & \lambda & \lambda & 0 & 0 & 0 \\ \lambda & \lambda+2\mu & \lambda & 0 & 0 & 0 \\ \lambda & \lambda & \lambda+2\mu & 0 & 0 & 0 \\ 0 & 0 & 0 & \mu & 0 & 0 \\ 0 & 0 & 0 & 0 & \mu & 0 \\ 0 & 0 & 0 & 0 & 0 & \mu \end{bmatrix} \begin{pmatrix} \tilde{\varepsilon}_{xx} \\ \tilde{\varepsilon}_{yy} \\ \tilde{\varepsilon}_{zz} \\ \tilde{\gamma}_{xy} \\ \tilde{\gamma}_{yz} \\ \tilde{\gamma}_{xz} \end{pmatrix} \tag{4.12}$$

$$\tilde{\boldsymbol{\sigma}} = [D'] \quad \tilde{\boldsymbol{\varepsilon}}$$

where the strain vector $\tilde{\boldsymbol{\varepsilon}}$ contains the shear distortions $\tilde{\gamma}_{ij}$ with $i,j = x, y, z$ instead of the shear strains $\hat{\varepsilon}_{ij}$ compared to equation (2.25). This difference between section 2.3 and chapter 4 is chosen to provide a stringent sequence of derivations.

The strain vector $\tilde{\boldsymbol{\varepsilon}}$ is dependent on the displacements $\tilde{\mathbf{u}}^T = \begin{pmatrix} \tilde{u}_x(\eta,\zeta) & \tilde{u}_y(\eta,\zeta) & \tilde{u}_z(\eta,\zeta) \end{pmatrix}$ by

$$\tilde{\boldsymbol{\varepsilon}} = \left[\tilde{G}\right] \tilde{\mathbf{u}} \tag{4.13}$$

with the matrix $\left[\tilde{G}\right]$ in the Fourier transformed domain (k_x, y, z, ω).

$$\left[\tilde{G}\right] = \begin{bmatrix} ik_x & 0 & 0 \\ 0 & \frac{\partial}{\partial y} & 0 \\ 0 & 0 & \frac{\partial}{\partial z} \\ \frac{\partial}{\partial y} & ik_x & 0 \\ 0 & \frac{\partial}{\partial z} & \frac{\partial}{\partial y} \\ \frac{\partial}{\partial z} & 0 & ik_x \end{bmatrix} \tag{4.14}$$

The displacement field $\tilde{\mathbf{u}}$ is modeled in dependency on the nodal displacement vector $\tilde{\mathbf{u}}_{\mathbf{n}}$ with the chosen form functions of the equations (4.9). Thus, the relationship between the strain vector $\tilde{\boldsymbol{\varepsilon}}$ and the vector of the nodal displacements $\tilde{\mathbf{u}}_{\mathbf{n}}$ can be stated as

$$\tilde{\boldsymbol{\varepsilon}} = \left[\tilde{G}\right] [N] \, \tilde{\mathbf{u}}_{\mathbf{n}} = \left[\tilde{B}\right] \tilde{\mathbf{u}}_{\mathbf{n}} \tag{4.15}$$

where matrix $\left[\tilde{B}\right]$ contains the derivatives of the form functions.

$$\left[\tilde{B}\right] = \begin{bmatrix} ik_x N_1(\eta,\zeta) & 0 & 0 & ik_x N_2(\eta,\zeta) & 0 & \cdots \\ 0 & \frac{\partial N_1(\eta,\zeta)}{\partial y} & 0 & 0 & \frac{\partial N_2(\eta,\zeta)}{\partial y} & \cdots \\ 0 & 0 & \frac{\partial N_1(\eta,\zeta)}{\partial z} & 0 & 0 & \cdots \\ \frac{\partial N_1(\eta,\zeta)}{\partial y} & ik_x N_1(\eta,\zeta) & 0 & \frac{\partial N_2(\eta,\zeta)}{\partial y} & ik_x N_2(\eta,\zeta) & \cdots \\ 0 & \frac{\partial N_1(\eta,\zeta)}{\partial z} & \frac{\partial N_1(\eta,\zeta)}{\partial y} & 0 & \frac{\partial N_2(\eta,\zeta)}{\partial z} & \cdots \\ \frac{\partial N_1(\eta,\zeta)}{\partial z} & 0 & ik_x N_1(\eta,\zeta) & \frac{\partial N_2(\eta,\zeta)}{\partial z} & 0 & \cdots \end{bmatrix} \tag{4.16}$$

For the virtual displacement field $\delta\tilde{\mathbf{u}}$ the same behavior is assumed. Introducing the equations (4.10), (4.12) and (4.15) into the formulation of the virtual work, equation (4.7) is

$$\begin{aligned} \int\limits_{(A)} & -\delta\tilde{\mathbf{u}}_{\mathbf{n}}{}^{H}\left[\tilde{B}\right]^{H}\left[D'\right]\left[\tilde{B}\right]\tilde{\mathbf{u}}_{\mathbf{n}} \\ & +\delta\tilde{\mathbf{u}}_{\mathbf{n}}{}^{H}\left[N\right]^{H}\tilde{\mathbf{p}} \\ & +\delta\tilde{\mathbf{u}}_{\mathbf{n}}{}^{H}\left[N\right]^{H}\rho\,\omega^{2}\left[N\right]\tilde{\mathbf{u}}_{\mathbf{n}}\,dA = 0 \end{aligned} \tag{4.17}$$

and has to be fulfilled for each wavenumber k_x and each frequency ω. The virtual displacement field $\delta\tilde{\mathbf{u}}_{\mathbf{n}}$ is chosen arbitrarily. Therefore, equation (4.17) can be formulated as

$$\left[\tilde{K}\right]\ \tilde{\mathbf{u}}_{\mathbf{n}} - \omega^2\left[M\right]\ \tilde{\mathbf{u}}_{\mathbf{n}} = \tilde{\mathbf{p}}_{\mathbf{n}} \tag{4.18}$$

with the stiffness matrix $\left[\tilde{K}\right]$,

$$\left[\tilde{K}\right] = \int\limits_{(A)}\left[\tilde{B}\right]^{H}\left[D'\right]\left[\tilde{B}\right]\ dA \tag{4.19}$$

the mass matrix $[M]$

$$\left[M\right] = \int\limits_{(A)}\rho\left[N\right]^{H}\left[N\right]\ dA \tag{4.20}$$

and the nodal load vector $\tilde{\mathbf{p}}_{\mathbf{n}}$.

$$\tilde{\mathbf{p}}_{\mathbf{n}} = \int\limits_{(A)}\left[N\right]^{H}\tilde{\mathbf{p}}\,dA \tag{4.21}$$

4.4 Numerical implementation

The integrations to obtain stiffness and mass matrices in the equations (4.19) and (4.20) are carried out numerically with $n_{GP} = 4$ Gauß points (GP) as defined in figure 4.3.

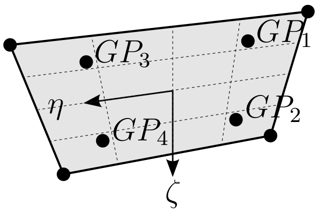

Figure 4.3: Gauß points

According to [Bronstein et al 2006] for example, the coordinates of the Gauß points are the zeros of the Legendre polynomials already presented in appendix A.4. The locations and weighting parameters for two Gauß points in each coordinate direction are given in the following table 4.1.

	η_k	ζ_k	w_k
GP_1	$-\frac{1}{\sqrt{3}}$	$-\frac{1}{\sqrt{3}}$	1
GP_2	$-\frac{1}{\sqrt{3}}$	$\frac{1}{\sqrt{3}}$	1
GP_3	$\frac{1}{\sqrt{3}}$	$-\frac{1}{\sqrt{3}}$	1
GP_4	$\frac{1}{\sqrt{3}}$	$\frac{1}{\sqrt{3}}$	1

Table 4.1: Coordinates and values of the associated weights of the Gauß points

Thus, the stiffness matrix $\left[\tilde{K}\right]$ and the mass matrix $[M]$ can be calculated as

$$\left[\tilde{K}\right] = \sum_{k=1}^{n_{GP}} \left[\tilde{B}(k_x, \eta_k, \zeta_k)\right]^H \; [D'] \; \left[\tilde{B}(k_x, \eta_k, \zeta_k)\right] \det(J) \; w_k \tag{4.22}$$

$$[M] = \sum_{k=1}^{n_{GP}} \rho \left[N(\eta_k, \zeta_k)\right]^H \; \left[N(\eta_k, \zeta_k)\right] \; \det(J) \; w_k \tag{4.23}$$

After determining the dynamic stiffness matrix $\left[\tilde{K}_{dyn}\right] = \left[\tilde{K}\right] - \omega^2 \left[M\right]$ of each element, the global stiffness matrix of the Finite Element mesh $\left[\tilde{K}_{FE}\right]$ as exemplarily depicted in figure 4.4 is assembled.

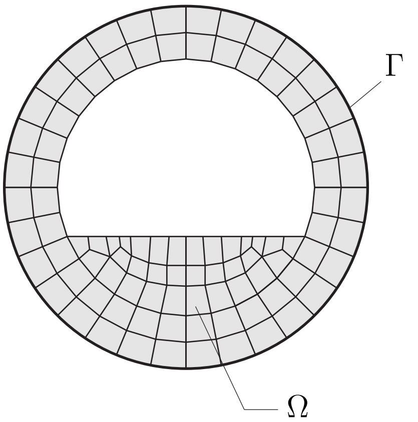

Figure 4.4: Schematic sketch of a global Finite Element mesh using the presented elements

With the global stiffness matrix, a relationship between the nodal load vector and the degrees of freedom is obtained. The system of equations is arranged such that the degrees of freedom on the coupling surface Γ are positioned in the upper part of the matrix and the degrees of freedom inside the Finite Element domain Ω in the lower part of the matrix. This is done to easily identify the coupling parameters.

$$\begin{bmatrix} \left[\tilde{K}_{\Gamma\Gamma_{FE}}\right] & \left[\tilde{K}_{\Gamma\Omega_{FE}}\right] \\ \left[\tilde{K}_{\Omega\Gamma_{FE}}\right] & \left[\tilde{K}_{\Omega\Omega_{FE}}\right] \end{bmatrix} \begin{pmatrix} \tilde{\mathbf{u}}_{\mathbf{\Gamma_{FE}}} \\ \tilde{\mathbf{u}}_{\mathbf{\Omega_{FE}}} \end{pmatrix} = \begin{pmatrix} \tilde{\mathbf{P}}_{\mathbf{\Gamma_{FE}}} \\ \tilde{\mathbf{P}}_{\mathbf{\Omega_{FE}}} \end{pmatrix} \tag{4.24}$$

4.5 Three-dimensional finite elements

In contrast to the cylindrical Finite Element substructure, the stiffness matrix of the spherical substructure is described in the frequency domain in Cartesian coordinates without spatial transformations and the degrees of freedom depend on $(x,\ y,\ z,\ \omega)$. Parameters in the frequency domain are labeled with the $^-$ symbol to signify the single transformation.

For the modeling of the Finite Element mesh that shall be coupled to the halfspace with spherical cavity, a three-dimensional eight-node element with three translational degrees of freedom at each node is used like the one sketched in figure 4.1. Linear form functions are chosen. The numerical calculation is performed with two Gauß points in each coordinate direction with the locations and weighting parameters presented analogously to the ones presented table 4.1.

The elements are arranged with $N_\vartheta N_\varphi$ nodes on a spherical surface determined by the N_ϑ latitudes and N_φ longitudes as depicted in figure 4.5. For the longitudes the azimuthal angle is divided equally into N_φ elements from $\varphi = 0, \frac{2\pi}{N_\varphi}, ..., \left(2\pi - \frac{2\pi}{N_\varphi}\right)$. Concerning the latitudes, the elevation angle ϑ is discretized with N_ϑ values between $\vartheta = 0$ and $\vartheta = \pi$. The z-coordinates of the latitudes are chosen on N_ϑ Gauß points that are distributed along the z-axis between $r = -R$ and $r = R$.

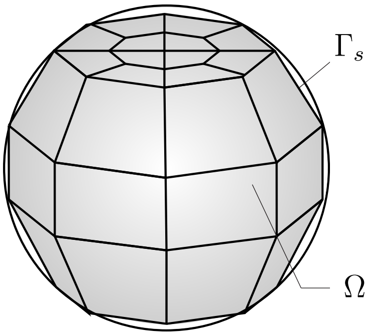

Figure 4.5: Schematic sketch of the three-dimensional Finite Element mesh

For a small number of latitudes, the modeling of the polar regions of the sphere is rather imprecise if the first Gauß points are positioned too far away from the poles. For example, for four Gauß points on the z-axis, the first Gauß point lies at $z = 0.8611R$. This would lead to an error in the discretization at the poles of the sphere and, thus, exactly at the point which is closest to the surface of the halfspace. To reduce this error, it is possible to introduce an additional latitude close to each pole and calculate the stiffness, mass and damping matrices taking into account these additional elements. To enable the coupling of the complex, dynamic stiffness matrix to the Integral Transform Method, the number of parameters on the surface has to be identical. Therefore, the additional degrees of freedom on the two additional latitudes are defined as slave degrees of freedom and after a condensation step, only the contributions of the master degrees of freedom remain in the system of equations.

As the elements do not require specific modifications before calculating the stiffness matrix, commercial elements are used with the Finite Element software ANSYS® using eight-node solid185 elements with an enhanced strain formulation (see [ANSYS 2012]). The stiffness, mass and damping matrices of the sphere are calculated with ANSYS® and imported into the MATLAB® program that contains the modeling of the soil as well as the coupling of the substructures. The degrees of freedom on the spherical surface $\bar{\mathbf{u}}_{\mathbf{\Gamma_s\ FE}}$ are again positioned in the upper part of the displacement vector and the parameters inside the domain in the lower part.

$$\begin{bmatrix} \left[\bar{K}_{\Gamma_s \Gamma_{sFE}}\right] & \left[\bar{K}_{\Gamma_s \Omega_{FE}}\right] \\ \left[\bar{K}_{\Omega \Gamma_{sFE}}\right] & \left[\bar{K}_{\Omega \Omega_{FE}}\right] \end{bmatrix} \begin{pmatrix} \bar{\mathbf{u}}_{\mathbf{\Gamma_s\ FE}} \\ \bar{\mathbf{u}}_{\mathbf{\Omega_{FE}}} \end{pmatrix} = \begin{pmatrix} \bar{\mathbf{P}}_{\mathbf{\Gamma_s\ FE}} \\ \bar{\mathbf{P}}_{\mathbf{\Omega_{FE}}} \end{pmatrix} \tag{4.25}$$

5 Coupling of the Substructures

5.1 Preliminary remark

After the stiffness matrices of the ITM substructure and the FEM substructure have been derived, the coupling of the substructures is performed in this chapter. In section 5.2 the halfspace with cylindrical cavity is coupled to a Finite Element structure with cylindrical coupling surface. Analogously the halfspace with spherical cavity and a spherical Finite Element structure are coupled in section 5.3. The same procedure of the coupling is also shown to be applicable to derive the solution of a layered halfspace with cylindrical or spherical cavity in section 5.4. The final section 5.5 of this chapter shows how parameters at an arbitrary point inside the soil can be evaluated in a post-processing procedure.

5.2 Coupling of the halfspace with cylindrical cavity with a Finite Element mesh with cylindrical surface

In the equations (3.15) and (4.24) the substructures “halfspace with cylindrical cavity” and “cylindrical Finite Element mesh” are solved separately. In both equations, the degrees of freedom on the cylindrical surface Γ are distinguished from the degrees of freedom on the halfspace surface Λ respectively inside the Finite Element domain Ω. The two substructures are coupled using the transition conditions on the interaction surface Γ.

The first transition condition states that the displacements on the coupling surface have to be the same for both substructures.

$$\mathbf{u}_{\boldsymbol{\Gamma}_{\mathbf{ITM}}} = \mathbf{u}_{\boldsymbol{\Gamma}_{\mathbf{FE}}} \tag{5.1}$$

As the equations (3.15) and (4.24) are formulated in different bases, a coordinate transformation is necessary before applying equation (5.1). During the derivations in chapter 3 the displacements $\hat{\mathbf{u}}_{\mathbf{\Gamma_{ITM}}}$ are calculated in the threefold Fourier transformed domain in dependency on (k_x, r, n, ω). The derivations of chapter 4 are based on a twofold Fourier transformed global coordinate system (k_x, y, z, ω) to obtain $\tilde{\mathbf{u}}_{\mathbf{\Gamma_{FE}}}$. The threefold Fourier transformed basis (k_x, r, n, ω) is chosen as coordinate system for the coupling and the degrees of freedom as well as the load vector in equation (4.24) are transformed into the new coordinate system. In the following, a transformation matrix $[T]$ is derived that contains the necessary conversions.

In a first step, the displacements on the coupling surface Γ are transformed from the Cartesian coordinate system (y, z) to a polar coordinate system (r, φ) as defined in figure 5.1.

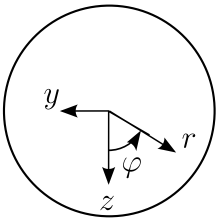

Figure 5.1: Definitions of the Cartesian (y, z) and polar (r, φ) coordinate systems

Thus, the displacements $\tilde{\mathbf{u}}_{\mathbf{\Gamma_{FE}}}$ can be replaced by the displacements $\tilde{\mathbf{u}}_{\mathbf{\Gamma_{FE,polar}}}$ of the polar coordinate system using the transformation matrix $[T_1]$ according to

$$
\begin{array}{ccc}
\begin{pmatrix} u_x(y_1,z_1) \\ u_y(y_1,z_1) \\ u_z(y_1,z_1) \\ u_x(y_2,z_2) \\ u_y(y_2,z_2) \\ u_z(y_2,z_2) \\ \vdots \end{pmatrix}
& = &
\begin{bmatrix}
1 & 0 & 0 & 0 & 0 & 0 & \cdots \\
0 & -\sin(\varphi_1) & -\cos(\varphi_1) & 0 & 0 & 0 & \cdots \\
0 & \cos(\varphi_1) & -\sin(\varphi_1) & 0 & 0 & 0 & \cdots \\
0 & 0 & 0 & 1 & 0 & 0 & \cdots \\
0 & 0 & 0 & 0 & -\sin(\varphi_2) & -\cos(\varphi_2) & \cdots \\
0 & 0 & 0 & 0 & \cos(\varphi_2) & -\sin(\varphi_2) & \cdots \\
\vdots & \vdots & \vdots & \vdots & \vdots & \vdots &
\end{bmatrix}
\begin{pmatrix} u_x(r_1,\varphi_1) \\ u_r(r_1,\varphi_1) \\ u_\varphi(r_1,\varphi_1) \\ u_x(r_2,\varphi_2) \\ u_r(r_2,\varphi_2) \\ u_\varphi(r_2,\varphi_2) \\ \vdots \end{pmatrix} \\
\tilde{\mathbf{u}}_{\mathbf{\Gamma_{FE}}} & = & [T_1] \qquad \tilde{\mathbf{u}}_{\mathbf{\Gamma_{FE,polar}}}
\end{array}
\tag{5.2}
$$

It shall be enhanced that only the parameters on the coupling surface are transformed. The parameters inside the Finite Element domain Ω are described in Cartesian coordinates through all the further derivations. Therefore, in the polar basis, the elements of $\tilde{\mathbf{u}}_{\mathbf{\Gamma_{FE,polar}}}$ depend on the constant radius of the cylinder $r_1 = r_2 = \ldots = R$.

In a second step, a Fourier series expansion of the displacements $\tilde{\mathbf{u}}_{\boldsymbol{\Gamma}_{\mathbf{FE,polar}}}$ is carried out regarding the circumference of the cylindrical coupling surface Γ. The Fourier series expansion can be noted in matrix notation by

$$\begin{array}{cccc}
\begin{pmatrix} u_x(R,\varphi_1) \\ u_r(R,\varphi_1) \\ u_\varphi(R,\varphi_1) \\ u_x(R,\varphi_2) \\ u_r(R,\varphi_2) \\ u_\varphi(R,\varphi_2) \\ \vdots \end{pmatrix} & = &
\begin{bmatrix}
e^{in_1\varphi_1} & 0 & 0 & e^{in_2\varphi_1} & 0 & 0 & e^{in_3\varphi_1} & \cdots \\
0 & e^{in_1\varphi_1} & 0 & 0 & e^{in_2\varphi_1} & 0 & 0 & \cdots \\
0 & 0 & e^{in_1\varphi_1} & 0 & 0 & e^{in_2\varphi_1} & 0 & \cdots \\
e^{in_1\varphi_2} & 0 & 0 & e^{in_2\varphi_2} & 0 & 0 & e^{in_3\varphi_2} & \cdots \\
0 & e^{in_1\varphi_2} & 0 & 0 & e^{in_2\varphi_2} & 0 & 0 & \cdots \\
\vdots & \vdots & \vdots & \vdots & \vdots & \vdots & \vdots &
\end{bmatrix} &
\begin{pmatrix} u_x(R,n_1) \\ u_r(R,n_1) \\ u_\varphi(R,n_1) \\ u_x(R,n_2) \\ u_r(R,n_2) \\ u_\varphi(R,n_2) \\ \vdots \end{pmatrix} \\
\tilde{\mathbf{u}}_{\boldsymbol{\Gamma}_{\mathbf{FE,polar}}} & = & [T_2] & \hat{\mathbf{u}}_{\boldsymbol{\Gamma}_{\mathbf{FE}}}
\end{array} \tag{5.3}$$

Combining the equations (5.2) and (5.3), the displacements on the cylindrical coupling surface are transformed from the twofold Fourier transformed global coordinate system (k_x, y, z, ω) denoted with the $\tilde{}$ symbol into the threefold transformed domain in dependency on (k_x, r, n, ω) that is signified by the $\hat{}$ symbol.

$$\tilde{\mathbf{u}}_{\boldsymbol{\Gamma}_{\mathbf{FE}}} = [T_1]\,[T_2]\,\hat{\mathbf{u}}_{\boldsymbol{\Gamma}_{\mathbf{FE}}} = [T]\,\hat{\mathbf{u}}_{\boldsymbol{\Gamma}_{\mathbf{FE}}} \tag{5.4}$$

The transition condition (5.1) is formulated as

$$\hat{\mathbf{u}}_{\boldsymbol{\Gamma}_{\mathbf{ITM}}} = \hat{\mathbf{u}}_{\boldsymbol{\Gamma}_{\mathbf{FE}}} = \hat{\mathbf{u}}_{\boldsymbol{\Gamma}} \tag{5.5}$$

Analogously to the displacements, the load vector is also transformed into the coordinate system (k_x, r, n, ω).

$$\tilde{\mathbf{P}}_{\boldsymbol{\Gamma}_{\mathbf{FE}}} = [T]\,\hat{\mathbf{P}}_{\boldsymbol{\Gamma}_{\mathbf{FE}}} \tag{5.6}$$

The system of equations (4.24) is transformed on the cylindrical coupling surface Γ into the new basis by

$$
\begin{aligned}
\begin{bmatrix} \left[\tilde{K}_{\Gamma\Gamma_{FE}}\right] & \left[\tilde{K}_{\Gamma\Omega_{FE}}\right] \\ \left[\tilde{K}_{\Omega\Gamma_{FE}}\right] & \left[\tilde{K}_{\Omega\Omega_{FE}}\right] \end{bmatrix}
\begin{pmatrix} \tilde{\mathbf{u}}_{\boldsymbol{\Gamma}_{\mathbf{FE}}} \\ \tilde{\mathbf{u}}_{\boldsymbol{\Omega}_{\mathbf{FE}}} \end{pmatrix}
&=
\begin{pmatrix} \tilde{\mathbf{P}}_{\boldsymbol{\Gamma}_{\mathbf{FE}}} \\ \tilde{\mathbf{P}}_{\boldsymbol{\Omega}_{\mathbf{FE}}} \end{pmatrix} \\
\begin{bmatrix} \left[\tilde{K}_{\Gamma\Gamma_{FE}}\right] & \left[\tilde{K}_{\Gamma\Omega_{FE}}\right] \\ \left[\tilde{K}_{\Omega\Gamma_{FE}}\right] & \left[\tilde{K}_{\Omega\Omega_{FE}}\right] \end{bmatrix}
\begin{pmatrix} [T]\,\hat{\mathbf{u}}_{\boldsymbol{\Gamma}_{\mathbf{FE}}} \\ \tilde{\mathbf{u}}_{\boldsymbol{\Omega}_{\mathbf{FE}}} \end{pmatrix}
&=
\begin{pmatrix} [T]\,\hat{\mathbf{P}}_{\boldsymbol{\Gamma}_{\mathbf{FE}}} \\ \tilde{\mathbf{P}}_{\boldsymbol{\Omega}_{\mathbf{FE}}} \end{pmatrix} \\
\begin{bmatrix} \left[\tilde{K}_{\Gamma\Gamma_{FE}}\right] & \left[\tilde{K}_{\Gamma\Omega_{FE}}\right] \\ \left[\tilde{K}_{\Omega\Gamma_{FE}}\right] & \left[\tilde{K}_{\Omega\Omega_{FE}}\right] \end{bmatrix}
\begin{bmatrix} [T] & 0 \\ 0 & [I] \end{bmatrix}
\begin{pmatrix} \hat{\mathbf{u}}_{\boldsymbol{\Gamma}_{\mathbf{FE}}} \\ \tilde{\mathbf{u}}_{\boldsymbol{\Omega}_{\mathbf{FE}}} \end{pmatrix}
&=
\begin{bmatrix} [T] & 0 \\ 0 & [I] \end{bmatrix}
\begin{pmatrix} \hat{\mathbf{P}}_{\boldsymbol{\Gamma}_{\mathbf{FE}}} \\ \tilde{\mathbf{P}}_{\boldsymbol{\Omega}_{\mathbf{FE}}} \end{pmatrix} \\
\begin{bmatrix} [T] & 0 \\ 0 & [I] \end{bmatrix}^{-1}
\begin{bmatrix} \left[\tilde{K}_{\Gamma\Gamma_{FE}}\right] & \left[\tilde{K}_{\Gamma\Omega_{FE}}\right] \\ \left[\tilde{K}_{\Omega\Gamma_{FE}}\right] & \left[\tilde{K}_{\Omega\Omega_{FE}}\right] \end{bmatrix}
\begin{bmatrix} [T] & 0 \\ 0 & [I] \end{bmatrix}
\begin{pmatrix} \hat{\mathbf{u}}_{\boldsymbol{\Gamma}_{\mathbf{FE}}} \\ \tilde{\mathbf{u}}_{\boldsymbol{\Omega}_{\mathbf{FE}}} \end{pmatrix}
&=
\begin{pmatrix} \hat{\mathbf{P}}_{\boldsymbol{\Gamma}_{\mathbf{FE}}} \\ \tilde{\mathbf{P}}_{\boldsymbol{\Omega}_{\mathbf{FE}}} \end{pmatrix} \\
\begin{bmatrix} [T]^{-1}\left[\tilde{K}_{\Gamma\Gamma_{FE}}\right][T] & [T]^{-1}\left[\tilde{K}_{\Gamma\Omega_{FE}}\right] \\ \left[\tilde{K}_{\Omega\Gamma_{FE}}\right][T] & \left[\tilde{K}_{\Omega\Omega_{FE}}\right] \end{bmatrix}
\begin{pmatrix} \hat{\mathbf{u}}_{\boldsymbol{\Gamma}_{\mathbf{FE}}} \\ \tilde{\mathbf{u}}_{\boldsymbol{\Omega}_{\mathbf{FE}}} \end{pmatrix}
&=
\begin{pmatrix} \hat{\mathbf{P}}_{\boldsymbol{\Gamma}_{\mathbf{FE}}} \\ \tilde{\mathbf{P}}_{\boldsymbol{\Omega}_{\mathbf{FE}}} \end{pmatrix}
\end{aligned}
\tag{5.7}
$$

With equation (5.7) the equilibrium of the Finite Element system is formulated on the coupling surface Γ with respect to a threefold transformed coordinate system (k_x, r, n, ω) and inside the domain Ω with respect to a twofold Fourier transformed Cartesian coordinate system (k_x, y, z, ω). Thus, a coupling to the ITM solution is possible. However, due to the multiplication of the stiffness matrix with the transformation matrix, the characteristics of the stiffness matrix are changed. Whereas the matrix $\left[\tilde{K}_{\Gamma\Gamma_{FE}}\right]$ is a sparse diagonal block matrix, because usually two neighboring nodes on the coupling surface are connected via one 2.5-dimensional element, the matrix product $[T]^{-1}\left[\tilde{K}_{\Gamma\Gamma_{FE}}\right][T]$ is denser. Concerning the Fourier series members along the circumference, there are more than two members coupled which leads to a matrix that is still sparse but denser than the original matrix $\left[\tilde{K}_{\Gamma\Gamma_{FE}}\right]$. Also, $[T]^{-1}\left[\tilde{K}_{\Gamma\Omega_{FE}}\right]$ and $\left[\tilde{K}_{\Omega\Gamma_{FE}}\right][T]$ have more entries than the original $\left[\tilde{K}_{\Gamma\Omega_{FE}}\right]$ and $\left[\tilde{K}_{\Omega\Gamma_{FE}}\right]$. Thus, the computational effort of the calculations increases, but still, without the transformation a coupling would not be possible.

For the coupling, a second transition condition is necessary. It relates the external loads of the two substructures on the coupling surface $\mathbf{P}_{\boldsymbol{\Gamma}_{\mathbf{ITM}}}$ and $\mathbf{P}_{\boldsymbol{\Gamma}_{\mathbf{FE}}}$. Their sum has to be equal to a given external load $\mathbf{P}_{\boldsymbol{\Gamma}}$ which can be applied at the coupling surface. For practical applications, $\mathbf{P_\Gamma}$ is usually set to zero. Generally, the equilibrium states, that

$$\mathbf{P_{\Gamma_{ITM}}} + \mathbf{P_{\Gamma_{FE}}} = \mathbf{P_\Gamma} \tag{5.8}$$

Again, the different bases have to be taken into account. Using equation (5.6), the loads on the coupling surface of the Finite Element mesh are transformed into the new coordinate system. Additionally, the nodal loads of the Finite Element computation have to be transformed into the continuous loads of the ITM calculations. Thus, for an element with the element dimension ds, the nodal load $\mathbf{\hat{P}_{\Gamma_{FE}}}$ is divided by the element length ds.

$$\mathbf{\hat{P}_{\Gamma_{ITM}}} + \frac{1}{ds}\mathbf{\hat{P}_{\Gamma_{FE}}} = \mathbf{\hat{P}_\Gamma} \tag{5.9}$$

Due to the discretization, of course, an error is introduced into the calculations. As the circular cross section is discretized by elements with bilinear form functions, an exact modeling of the structure is not possible and an error is unavoidable. However, as will be shown in section 6.2, this error is acceptable even for a comparably small number of nodes on the coupling surface. H- or p-refinements could be applied in order to further increase the accuracy of the method.

Combining the two transition conditions (5.5) and (5.9), the substructures that are described with the equations (3.15) and (5.7) are coupled and the system of equations can be derived to model the complete system.

$$\begin{bmatrix} \left[\hat{K}_{\Lambda\Lambda_{ITM}}\right] & \left[\hat{K}_{\Lambda\Gamma_{ITM}}\right] & 0 \\ \left[\hat{K}_{\Gamma\Lambda_{ITM}}\right] & \left[\hat{K}_{\Gamma\Gamma_{ITM}}\right] + \frac{1}{ds}\left[T\right]^{-1}\left[\tilde{K}_{\Gamma\Gamma_{FE}}\right]\left[T\right] & \frac{1}{ds}\left[T\right]^{-1}\left[\tilde{K}_{\Gamma\Omega_{FE}}\right] \\ 0 & \left[\tilde{K}_{\Omega\Gamma_{FE}}\right]\left[T\right] & \left[\tilde{K}_{\Omega\Omega_{FE}}\right] \end{bmatrix} \begin{pmatrix} \mathbf{\hat{u}_{\Lambda_{ITM}}} \\ \mathbf{\hat{u}_\Gamma} \\ \mathbf{\tilde{u}_{\Omega_{FE}}} \end{pmatrix} = \begin{pmatrix} \mathbf{\hat{P}_{\Lambda_{ITM}}} \\ \mathbf{\hat{P}_\Gamma} \\ \mathbf{\tilde{P}_{\Omega_{FE}}} \end{pmatrix} \tag{5.10}$$

With this complete system of equations (5.10) the displacements on the halfspace surface Λ, the cylindrical coupling surface Γ and at the nodes inside the Finite Element domain Ω due to loads on the respective locations can be calculated. They are obtained with respect to their respective basis $\mathbf{\hat{u}_{\Lambda_{ITM}}}(k_x, s\ \Delta k_y, z = 0, \omega)$, $\mathbf{\hat{u}_\Gamma}(k_x, r = R, n, \omega)$ and $\mathbf{\tilde{u}_{\Omega_{FE}}}(k_x, y, z, \omega)$. The values of the displacements in the original domain can be calculated with inverse Fourier transformations as shortly presented in appendix A.1.

5.3 Coupling of the halfspace with spherical cavity with a Finite Element mesh with spherical surface

In general, the procedure for the coupling of the ITM substructure and the FEM substructure on a spherical coupling surface is identical to the one described in section 5.2 for the cylindrical coupling surface. The two coupling conditions of the compatibility of the displacements and the equilibrium of forces on the coupling surface have to be fulfilled. The difference lies in the different coordinate systems. Again, the ITM and FEM substructures are described by the respective systems of equations with the degrees of freedom on the halfspace surface Λ, on the spherical coupling surface Γ_s and inside the Finite Element domain Ω.

$$\begin{bmatrix} \left[\hat{K}_{\Lambda\Lambda_{ITM}}\right] & \left[\hat{K}_{\Lambda\Gamma_{s\,ITM}}\right] \\ \left[\hat{K}_{\Gamma_s\Lambda_{ITM}}\right] & \left[\hat{K}_{\Gamma_s\Gamma_{s\,ITM}}\right] \end{bmatrix} \begin{pmatrix} \hat{\mathbf{u}}_{\mathbf{\Lambda_{ITM}}} \\ \hat{\mathbf{u}}_{\mathbf{\Gamma_{s\,ITM}}} \end{pmatrix} = \begin{pmatrix} \hat{\mathbf{P}}_{\mathbf{\Lambda_{ITM}}} \\ \hat{\mathbf{P}}_{\mathbf{\Gamma_{s\,ITM}}} \end{pmatrix} \tag{5.11}$$

$$\begin{bmatrix} \left[\bar{K}_{\Gamma_s\Gamma_{s\,FE}}\right] & \left[\bar{K}_{\Gamma_s\Omega_{FE}}\right] \\ \left[\bar{K}_{\Omega\Gamma_{s\,FE}}\right] & \left[\bar{K}_{\Omega\Omega_{FE}}\right] \end{bmatrix} \begin{pmatrix} \bar{\mathbf{u}}_{\mathbf{\Gamma_{s\,FE}}} \\ \bar{\mathbf{u}}_{\mathbf{\Omega_{FE}}} \end{pmatrix} = \begin{pmatrix} \bar{\mathbf{P}}_{\mathbf{\Gamma_{s\,FE}}} \\ \bar{\mathbf{P}}_{\mathbf{\Omega_{FE}}} \end{pmatrix} \tag{5.12}$$

In the system of equations (5.11), the parameters on the halfspace surface Λ are described with respect to the threefold Fourier transformed Cartesian coordinate system (k_x, k_y, z, ω), while the parameters on the spherical coupling surface Γ_s are determined in the threefold transformed spherical coordinate system (r, m, l, ω).

In the second system of equations (5.12), all the degrees of freedom are described in Cartesian coordinates in the frequency domain (x, y, z, ω).

To enable the coupling, again the basis of the ITM solution is chosen as common coordinate system and the parameters of the FEM calculation on the interaction surface Γ_s are transformed into this coordinate system. This is again performed in two steps: At first, the degrees of freedom are transformed from the Cartesian into a spherical coordinate system as it is defined in figure 2.6.

$$\begin{array}{ccccc}
\begin{pmatrix} u_x(x_1,y_1,z_1) \\ u_y(x_1,y_1,z_1) \\ u_z(x_1,y_1,z_1) \\ u_x(x_2,y_2,z_2) \\ u_y(x_2,y_2,z_2) \\ u_z(x_2,y_2,z_2) \\ \vdots \end{pmatrix} & = & \begin{bmatrix} \sin(\vartheta_1)\cos(\varphi_1) & \cos(\vartheta_1)\cos(\varphi_1) & -\sin(\varphi_1) & 0 & \cdots \\ \sin(\vartheta_1)\sin(\varphi_1) & \cos(\vartheta_1)\sin(\varphi_1) & \cos(\varphi_1) & 0 & \cdots \\ \cos(\vartheta_1) & -\sin(\vartheta_1) & 0 & 0 & \cdots \\ 0 & 0 & 0 & \sin(\vartheta_2)\cos(\varphi_2) & \cdots \\ 0 & 0 & 0 & \sin(\vartheta_2)\sin(\varphi_2) & \cdots \\ 0 & 0 & 0 & \cos(\vartheta_2) & \cdots \\ \vdots & \vdots & \vdots & \vdots & \end{bmatrix} & \begin{pmatrix} u_r(r_1,\vartheta_1,\varphi_1) \\ u_\vartheta(r_1,\vartheta_1,\varphi_1) \\ u_\varphi(r_1,\vartheta_1,\varphi_1) \\ u_r(r_2,\vartheta_2,\varphi_2) \\ u_\vartheta(r_2,\vartheta_2,\varphi_2) \\ u_\varphi(r_2,\vartheta_2,\varphi_2) \\ \vdots \end{pmatrix} \\
\bar{\mathbf{u}}_{\mathbf{\Gamma_s\,FE}} & = & [T_{s\,1}] & \bar{\mathbf{u}}_{\mathbf{\Gamma_s\,FE,sph}}
\end{array} \tag{5.13}$$

The points on the surface of the sphere are arranged such that each latitude, starting from the lowest one, is labeled from $\varphi = 0, \frac{2\pi}{N_\varphi}, ..., \left(2\pi - \frac{2\pi}{N_\varphi}\right)$ and then the next latitude is appointed. Thus, the first N_φ points lie on the same latitude and thus possess the same angle $\vartheta = \vartheta_1 = \vartheta_2 = ... = \vartheta_{N_\varphi}$.

The second transformation matrix $[T_{s\,2}]$ contains the development of the degrees of freedom on Γ_s which possess the same radial coordinate $r_1 = r_2 = ... = R$ into spherical harmonics

$$[T_{s\,2}] = \begin{bmatrix} Y_{m_1}^{l_1}(\vartheta_1,\varphi_1) & 0 & 0 & Y_{m_2}^{l_2}(\vartheta_1,\varphi_1) & \cdots \\ 0 & Y_{m_1}^{l_1}(\vartheta_1,\varphi_1) & 0 & 0 & \cdots \\ 0 & 0 & Y_{m_1}^{l_1}(\vartheta_1,\varphi_1) & 0 & \cdots \\ Y_{m_1}^{l_1}(\vartheta_2,\varphi_2) & 0 & 0 & Y_{m_2}^{l_2}(\vartheta_2,\varphi_2) & \cdots \\ 0 & Y_{m_1}^{l_1}(\vartheta_2,\varphi_2) & 0 & 0 & \cdots \\ \vdots & \vdots & \vdots & \vdots & \vdots \end{bmatrix} \tag{5.14}$$

and leads to the following transformation equation

$$\begin{array}{cccc}
\begin{pmatrix} u_r(R,\vartheta_1,\varphi_1) \\ u_\vartheta(R,\vartheta_1,\varphi_1) \\ u_\varphi(R,\vartheta_1,\varphi_1) \\ u_r(R,\vartheta_2,\varphi_2) \\ u_\vartheta(R,\vartheta_2,\varphi_2) \\ u_\varphi(R,\vartheta_2,\varphi_2) \\ \vdots \end{pmatrix} & = & [T_{s\,2}] & \begin{pmatrix} u_r(R,m_1,l_1) \\ u_\vartheta(R,m_1,l_1) \\ u_\varphi(R,m_1,l_1) \\ u_r(R,m_2,l_2) \\ u_\vartheta(R,m_2,l_2) \\ u_\varphi(R,m_2,l_2) \\ \vdots \end{pmatrix} \\
\bar{\mathbf{u}}_{\mathbf{\Gamma_s\,FE,sph}} & = & [T_{s\,2}] & \hat{\mathbf{u}}_{\mathbf{\Gamma_s\,FE}}
\end{array} \tag{5.15}$$

with the degrees m_i and orders l_i arranged as summarized in table 5.1.

	$i=1$	$i=2$	$i=3$	$i=4$	$i=5$	$i=6$	$i=7$	$i=8$	$i=9$	$\dots$
m_i	0	1	1	1	2	2	2	2	2	$\dots$
l_i	0	-1	0	1	-2	-1	0	1	2	$\dots$

Table 5.1: Degree and order of the spherical polynomials

After the transformations $\bar{\mathbf{u}}_{\mathbf{\Gamma_s\,FE}} = [T_{s\,1}]\,[T_{s\,2}]\,\hat{\mathbf{u}}_{\mathbf{\Gamma_s\,FE}} = [T_s]\,\hat{\mathbf{u}}_{\mathbf{\Gamma_s\,FE}}$ and $\bar{\mathbf{p}}_{\mathbf{\Gamma_s\,FE}} = [T_s]\,\hat{\mathbf{p}}_{\mathbf{\Gamma_s\,FE}}$, the coupling conditions can be applied. Again, the displacements on the coupling surface have to be equal

$$\hat{\mathbf{u}}_{\mathbf{\Gamma_s\,ITM}} = \hat{\mathbf{u}}_{\mathbf{\Gamma_s\,FE}} = \hat{\mathbf{u}}_{\mathbf{\Gamma_s}} \tag{5.16}$$

and the load that is acting on the coupling surface is equally distributed onto the two substructures.

$$\hat{\mathbf{P}}_{\mathbf{\Gamma_s\,ITM}} + \frac{1}{ds_\vartheta ds_\varphi}\hat{\mathbf{P}}_{\mathbf{\Gamma_s\,FE}} = \hat{\mathbf{P}}_{\mathbf{\Gamma_s}} \tag{5.17}$$

The nodal loads of the Finite Element system of equations have to be replaced by distributed loads on the surface of the sphere. This is done by dividing them by the element lengths in the two directions ds_ϑ and ds_φ.

Using the two coupling conditions (5.16) and (5.17), the system of equations can be transformed to the new coordinates analogously to the derivation (5.7). Still, it has to be regarded that the second transformation matrix $[T_{s\,2}]$ is not quadratic. As already mentioned in section 2.5.1, the development into spherical harmonics changes the number of parameters, so $[T_{s\,2}]$ has $3N_\vartheta N_\varphi$ rows but $3(M+1)^2$ columns. Therefore, an inversion of the transformation matrix as necessary in (5.7) is not possible. Still, the solution can be performed using the Moore-Penrose-pseudoinverse. The Moore-Penrose-pseudoinverse of a matrix $[A]$ which is often denoted by $[A]^+$ satisfies the following equations which are called Penrose equations by [Ben-Israel and Greville 2003]

$$[A]\,[A]^+\,[A] = [A] \tag{5.18a}$$

$$[A]^+\,[A]\,[A]^+ = [A]^+ \tag{5.18b}$$

$$\left([A]\,[A]^+\right)^H = [A]\,[A]^+ \tag{5.18c}$$

$$\left([A]^+\,[A]\right)^H = [A]^+\,[A] \tag{5.18d}$$

An additional proposition holds for $m \times n$ matrices with $n \leq m$ and $\operatorname{rank}[A] = n$ that $[A]^+\,[A] = [I]$ according to [Koecher 1997]. The transformation matrix $[T_{s\,2}]$ consists of a different number of rows and columns with more rows than columns and linearly independent columns, so a left multiplication of $[T_{s\,2}]$ with the Moore-Penrose-pseudoinverse $[T_{s\,2}]^+$ leads to the identity matrix $[I]$.

$$[T_{s\,2}]^+\,[T_{s\,2}] = [I] \tag{5.19}$$

With the above equation (5.19), equation (5.12) can be written in the transformed domain.

$$\begin{bmatrix} [T_{s\,2}]^+\,[T_{s\,1}]^{-1}\left[\bar{K}_{\Gamma_s\Gamma_{sFE}}\right][T_{s\,1}]\,[T_{s\,2}] & [T_{s\,2}]^+\,[T_{s\,1}]^{-1}\left[\bar{K}_{\Gamma_s\Omega_{FE}}\right] \\ \left[\bar{K}_{\Omega\Gamma_{sFE}}\right][T_{s\,1}]\,[T_{s\,2}] & \left[\bar{K}_{\Omega\Omega_{FE}}\right] \end{bmatrix} \begin{pmatrix} \hat{\mathbf{u}}_{\boldsymbol{\Gamma}_{\mathbf{s\,FE}}} \\ \bar{\mathbf{u}}_{\boldsymbol{\Omega}_{\mathbf{FE}}} \end{pmatrix} = \begin{pmatrix} \hat{\mathbf{P}}_{\boldsymbol{\Gamma}_{\mathbf{s\,FE}}} \\ \bar{\mathbf{P}}_{\boldsymbol{\Omega}_{\mathbf{FE}}} \end{pmatrix} \tag{5.20}$$

As the Moore-Penrose-pseudoinverse of a quadratic, invertible matrix is identical to the inverse of the matrix, $[T_{s\,2}]^+\,[T_{s\,1}]^{-1}$ is abbreviated by $[T_s]^+$. This leads to the complete coupled system of equations with

$$\begin{bmatrix} \left[\hat{K}_{\Lambda\Lambda_{ITM}}\right] & \left[\hat{K}_{\Lambda\Gamma_{sITM}}\right] & 0 \\ \left[\hat{K}_{\Gamma_s\Lambda_{ITM}}\right] & \left[\hat{K}_{\Gamma_s\Gamma_{sITM}}\right] + \frac{1}{ds_\vartheta ds_\varphi}\,[T_s]^+\left[\bar{K}_{\Gamma_s\Gamma_{sFE}}\right][T_s] & \frac{1}{ds_\vartheta ds_\varphi}\,[T_s]^+\left[\bar{K}_{\Gamma_s\Omega_{FE}}\right] \\ 0 & \left[\bar{K}_{\Omega\Gamma_{sFE}}\right][T_s] & \left[\bar{K}_{\Omega\Omega_{FE}}\right] \end{bmatrix} \begin{pmatrix} \hat{\mathbf{u}}_{\boldsymbol{\Lambda}_{\mathbf{ITM}}} \\ \hat{\mathbf{u}}_{\boldsymbol{\Gamma}_{\mathbf{s}}} \\ \bar{\mathbf{u}}_{\boldsymbol{\Omega}_{\mathbf{FE}}} \end{pmatrix} = \begin{pmatrix} \hat{\mathbf{P}}_{\boldsymbol{\Lambda}_{\mathbf{ITM}}} \\ \hat{\mathbf{P}}_{\boldsymbol{\Gamma}_{\mathbf{s}}} \\ \bar{\mathbf{P}}_{\boldsymbol{\Omega}_{\mathbf{FE}}} \end{pmatrix} \tag{5.21}$$

5.4 Layered halfspace with cylindrical or spherical cavity

The substructure technique described in the previous sections can also be applied to derive the solution for a layered halfspace with cylindrical or spherical cavity as presented in [Rathjens 2016] and [Freisinger 2016].

In a first step, two layered halfspaces as presented in section 2.3.4 are superposed. They are, as sketched in the figures 5.2 and 5.3 rotated against each other by an angle of 180° with respect to the x-axes.

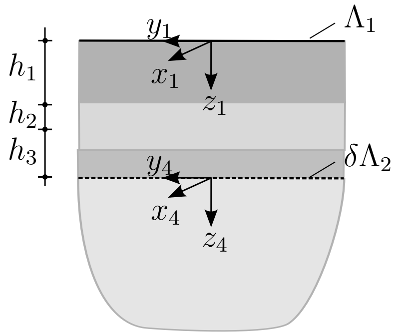

Figure 5.2: Halfspace with real surface Λ_1, virtual surface $\delta\Lambda_2$ and the local coordinate systems (x_i, y_i, z_i)

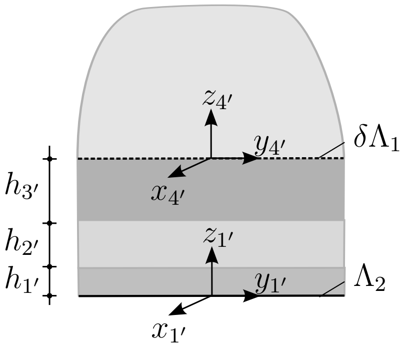

Figure 5.3: Rotated halfspace with real surface Λ_2, virtual surface $\delta\Lambda_1$ and the local coordinate systems ($x_{i'}$, $y_{i'}$, $z_{i'}$)

As boundary conditions the stress states at the two surfaces Λ_1 and Λ_2 are given. Thus, as result of the superposition an artificial system is obtained that consists of the spatially limited layers of the layered halfspace as illustrated in figure 5.4. Alternatively, the solution of this system of layers can also be deduced by solving the layered halfspace of figure 5.2 with stress boundary conditions on the free surfaces Λ_1 and Λ_2.

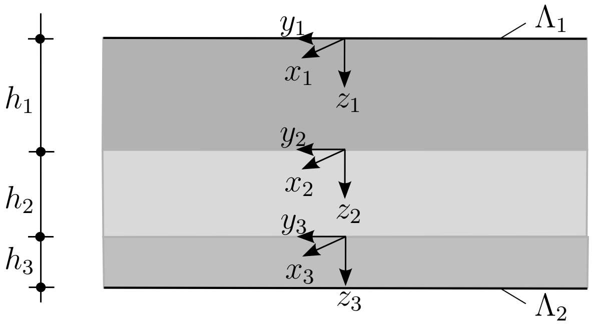

Figure 5.4: Result of the superposition of the two halfspaces

The relationship between the external loads on the surfaces Λ_1 and Λ_2 and the displacements on these surfaces can be written in matrix notation.

$$\begin{bmatrix} \left[\hat{K}_{\Lambda_1\Lambda_{1L}}\right] & \left[\hat{K}_{\Lambda_1\Lambda_{2L}}\right] \\ \left[\hat{K}_{\Lambda_2\Lambda_{1L}}\right] & \left[\hat{K}_{\Lambda_2\Lambda_{2L}}\right] \end{bmatrix} \begin{pmatrix} \hat{\mathbf{u}}_{\mathbf{\Lambda_{1L}}} \\ \hat{\mathbf{u}}_{\mathbf{\Lambda_{2L}}} \end{pmatrix} = \begin{pmatrix} \hat{\mathbf{P}}_{\mathbf{\Lambda_{1L}}} \\ \hat{\mathbf{P}}_{\mathbf{\Lambda_{2L}}} \end{pmatrix} \tag{5.22}$$

The index L in equation (5.22) signifies that the parameters refer to the system of layers.

In a second step the system of layers is coupled to a halfspace with cylindrical or spherical cavity as depicted in the figures 5.5 and 5.6 exemplarily for a cylindrical cavity.

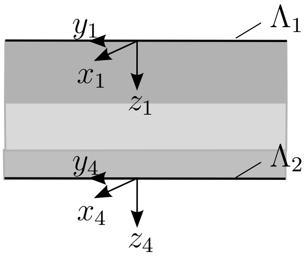

Figure 5.5: System of layers with the surfaces Λ_1 and Λ_2

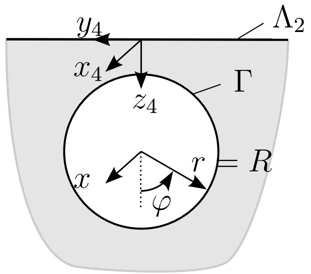

Figure 5.6: Halfspace with cylindrical cavity

The halfspace with cylindrical cavity is described by the system of equations derived in section 3.4.

$$\begin{bmatrix} \left[\hat{K}_{\Lambda_2\Lambda_{2HC}}\right] & \left[\hat{K}_{\Lambda_2\Gamma_{HC}}\right] \\ \left[\hat{K}_{\Gamma\Lambda_{2HC}}\right] & \left[\hat{K}_{\Gamma\Gamma_{HC}}\right] \end{bmatrix} \begin{pmatrix} \hat{\mathbf{u}}_{\mathbf{\Lambda_{2HC}}} \\ \hat{\mathbf{u}}_{\mathbf{\Gamma_{HC}}} \end{pmatrix} = \begin{pmatrix} \hat{\mathbf{P}}_{\mathbf{\Lambda_{2HC}}} \\ \hat{\mathbf{P}}_{\mathbf{\Gamma_{HC}}} \end{pmatrix} \tag{5.23}$$

The index HC denotes that the parameters are derived for the system of a halfspace with cylindrical cavity. As the parameters on the coupling surface Λ_2 are described in both systems in the threefold Fourier transformed coordinate system (k_x, k_y, z, ω), no further transformations are necessary and the systems can be coupled directly.

The equality of the displacements of the two systems on the coupling surface

$$\hat{\mathbf{u}}_{\mathbf{\Lambda_{2L}}} = \hat{\mathbf{u}}_{\mathbf{\Lambda_{2HC}}} = \hat{\mathbf{u}}_{\mathbf{\Lambda_2}} \tag{5.24}$$

and the equilibrium of forces on the coupling surface

$$\mathbf{\hat{P}}_{\mathbf{\Lambda_{2L}}} + \mathbf{\hat{P}}_{\mathbf{\Lambda_{2HC}}} = \mathbf{\hat{P}}_{\mathbf{\Lambda_2}} \tag{5.25}$$

lead to the system of equations that describes the layered halfspace with cylindrical cavity as depicted in figure 5.7.

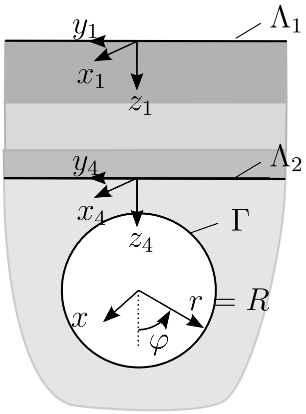

Figure 5.7: Layered halfspace with cylindrical cavity

$$\begin{bmatrix} \left[\hat{K}_{\Lambda_1\Lambda_{1L}}\right] & \left[\hat{K}_{\Lambda_1\Lambda_{2L}}\right] & 0 \\ \left[\hat{K}_{\Lambda_2\Lambda_{1L}}\right] & \left[\hat{K}_{\Lambda_2\Lambda_{2L}}\right] + \left[K_{\Lambda_2\Lambda_{2HC}}\right] & \left[K_{\Lambda_2\Gamma_{HC}}\right] \\ 0 & \left[K_{\Gamma\Lambda_{2HC}}\right] & \left[K_{\Gamma\Gamma_{HC}}\right] \end{bmatrix} \begin{pmatrix} \mathbf{\hat{u}}_{\mathbf{\Lambda_{1L}}} \\ \mathbf{\hat{u}}_{\mathbf{\Lambda_2}} \\ \mathbf{\hat{u}}_{\mathbf{\Gamma_{HC}}} \end{pmatrix} = \begin{pmatrix} \mathbf{\hat{P}}_{\mathbf{\Lambda_{1L}}} \\ \mathbf{\hat{P}}_{\mathbf{\Lambda_2}} \\ \mathbf{\hat{P}}_{\mathbf{\Gamma_{HC}}} \end{pmatrix} \tag{5.26}$$

The derivations can be analogously applied to model a halfspace with spherical cavity.

5.5 Halfspace with cylindrical or spherical cavity - Post-processing

If stresses or displacements at an arbitrary point P inside the soil shall be determined which is not already modeled as part of the Finite Element domain as exemplarily depicted in figure 5.8, they can be computed in a post-processing step based on the displacements $\mathbf{\hat{u}}_{\mathbf{\Lambda_{ITM}}}(k_x, s\ \Delta k_y, z = 0, \omega)$, $\mathbf{\hat{u}}_{\mathbf{\Gamma}}(k_x, r = R, n, \omega)$ and $\mathbf{\tilde{u}}_{\mathbf{\Omega_{FE}}}(k_x, y, z, \omega)$. These are derived using equation (5.10), in which loads can be applied at the surfaces Λ or Γ or inside the Finite Element domain Ω.

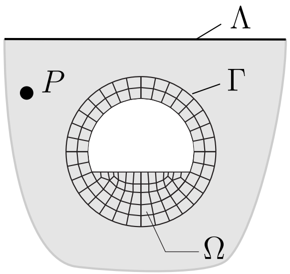

Figure 5.8: Sketch of a coupled ITM-FEM system with an arbitrary point of evaluation P

As the point on which the stresses or displacements are to be calculated lies not within the Finite Element domain Ω, the stresses or displacements at P can be derived using the solution of the system halfspace with cylindrical cavity, which was presented in chapter 3. The displacements $\hat{\mathbf{u}}_{\mathbf{\Lambda_{ITM}}}(k_x, s\ \Delta k_y, z = 0, \omega)$ and $\hat{\mathbf{u}}_{\mathbf{\Gamma}}(k_x, r = R, n, \omega)$ are applied as boundary conditions on the superposed system.

According to equation (3.11), the displacements of the superposed system halfspace with cylindrical cavity are obtained superposing the displacements of the fundamental systems halfspace and fullspace with cylindrical cavity. If the displacements of the superposed system are given, the vector $\hat{\mathbf{u}}_{ITM}$ of equation (3.11) is known

$$\hat{\mathbf{u}}_{ITM} = \begin{pmatrix} \hat{\mathbf{u}}_{\mathbf{\Lambda_{ITM}}}(k_x, s\ \Delta k_y, z = 0, \omega) \\ \hat{\mathbf{u}}_{\mathbf{\Gamma}}(k_x, r = R, n, \omega) \end{pmatrix} \tag{5.27}$$

with $s = -\frac{N_y}{2}, ..., \left(\frac{N_y}{2} - 1\right)$ and $n\ \Delta\varphi$ with $n = 1, 2, ..., N_\varphi$. The unknown amplitudes $\mathbf{C_\Lambda}$ and $\mathbf{C_\Gamma}$ can be calculated for each combination of the discrete values of the wavenumber k_x and the frequency ω with

$$\begin{pmatrix} \mathbf{C_\Lambda} \\ \mathbf{C_\Gamma} \end{pmatrix} = \begin{bmatrix} \left[\hat{U}_{\Lambda\Lambda_{ITM}}\right] & \left[\hat{U}_{\Lambda\Gamma_{ITM}}\right] \\ \left[\hat{U}_{\Gamma\Lambda_{ITM}}\right] & \left[\hat{U}_{\Gamma\Gamma_{ITM}}\right] \end{bmatrix}^{-1} \begin{pmatrix} \hat{\mathbf{u}}_{\mathbf{\Lambda_{ITM}}}(s\ \Delta k_y, z = 0) \\ \hat{\mathbf{u}}_{\mathbf{\Gamma}}(r = R, n) \end{pmatrix} \tag{5.28}$$

The elements $\left[\hat{U}_{\alpha\beta_{ITM}}\right]$ with $\alpha = \Lambda, \Gamma$ and $\beta = \Lambda, \Gamma$ contain the displacements on the surface α due to an applied unit stress on surface β as described in detail in section 3.4.

The vector of the amplitudes of the applied stresses on the surfaces $\mathbf{C}$ contains in its upper part $\mathbf{C_\Lambda}$ the amplitudes of the stresses on the halfspace surface $C_{iz}(s)$ with $i = z, y, x$ for each discrete wavenumber $k_y = s\ \Delta k_y$. In $\mathbf{C_\Gamma}$, the lower part of vector $\mathbf{C}$, the amplitudes of the stresses on the cylindrical coupling surface $C_{jr}\,(n)$ with $j = r, x, \varphi$ are organized for each Fourier series member n.

After solving equation (5.28), it is possible to specify for each discrete combination of wavenumber k_x and frequency ω the stresses on the surface Λ of the fundamental system of a halfspace as $C_{iz}\,(s)\,\hat{\sigma}_{iz}\,(s)$ and the stresses on the surface Γ of the fundamental system fullspace with cylindrical cavity $C_{jr}\,(n)\,\hat{\sigma}_{jr}\,(n)$ that lead to the displacement state of the superposed system halfspace with cylindrical cavity described by $\hat{\mathbf{u}}_{\mathbf{\Lambda_{ITM}}}(k_x, s\,\Delta k_y, z = 0, \omega)$ and $\hat{\mathbf{u}}_{\mathbf{\Gamma}}(k_x, r = R, n, \omega)$. In figure 5.9 the superposition is graphically displayed in a simplified manner.

The stresses $C_{iz}\,(s)\,\hat{\sigma}_{iz}\,(s)$ are applied at the halfspace surface (figure 5.9 (a)) and for each discrete wavenumber $k_y = s\,\Delta k_y$ they lead to displacement components $C_{iz}\,(s)\,\hat{u}_k^{(iz,s)}\,(s)$ with $k = z, y, x$ on Λ (figure 5.9 (b)). Additionally on the virtual cylindrical coupling surface displacement components are generated. Each stress component on the surface leads to N_φ displacement components in each coordinate direction $C_{iz}\,(s)\,\hat{u}_l^{(iz,s)}\,(n)$ with $l = x, r, \varphi$ on Γ (figure 5.9 (b) - 5.9 (c)). Analogously the stresses $C_{jr}\,(n)\,\hat{\sigma}_{jr}\,(n)$ on the cylindrical surface Γ (figure 5.9 (d)) generate for each Fourier series member n displacement components $C_{jr}\,(n)\,\hat{u}_l^{(jr,n)}\,(n)$ in the three cylindrical coordinate directions on Γ (figure 5.9 (e)). Regarding the virtual halfspace surface each series member leads to N_y displacement components in each Cartesian coordinate direction $C_{jr}\,(n)\,\hat{u}_k^{(jr,n)}\,(s)$ (figure 5.9 (e) - 5.9 (f)). The superposition of all displacement components on the two surfaces has to be equal to the given boundary conditions $\hat{\mathbf{u}}_{\mathbf{\Lambda_{ITM}}}(k_x, s\,\Delta k_y, z = 0, \omega)$ and $\hat{\mathbf{u}}_{\mathbf{\Gamma}}(k_x, r = R, n, \omega)$ that are depicted in figure 5.9 (g).

If the calculated stresses on the surfaces Λ and Γ are regarded as external loads

$$\hat{p}_i\,(k_x, s, \omega) \;= -C_{iz}\,(k_x, s, \omega)\,\hat{\sigma}_{iz}\,(k_x, s, \omega) \tag{5.29a}$$

$$\hat{p}_j\,(k_x, n, \omega) = -C_{jr}\,(k_x, n, \omega)\,\hat{\sigma}_{jr}\,(k_x, n, \omega) \tag{5.29b}$$

the displacements and stresses at point $P\,(x_P, y_P, z_P)$ can be calculated separately for the two fundamental systems.

At the halfspace system the loads $\hat{p}_i\,(k_x, s, \omega)$ are applied as illustrated in figure 5.10 and the displacements $\hat{u}_i\,(k_x, s, z = z_P, \omega)$ can be calculated in the threefold Fourier transformed domain in dependency on z_P as the z-coordinate of point P with $i = z, y, x$.

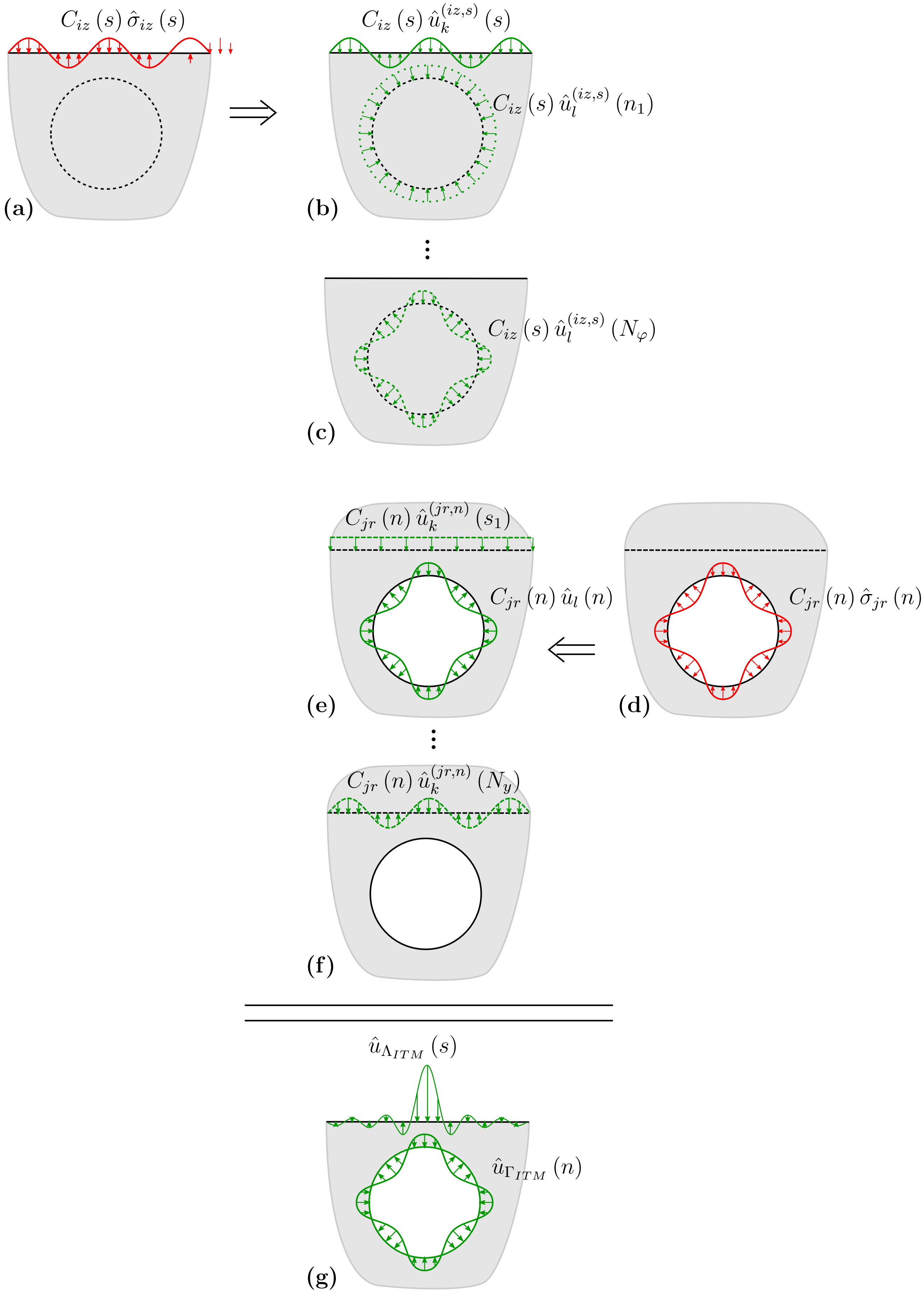

Figure 5.9: Graphical representation of the superposition of displacements

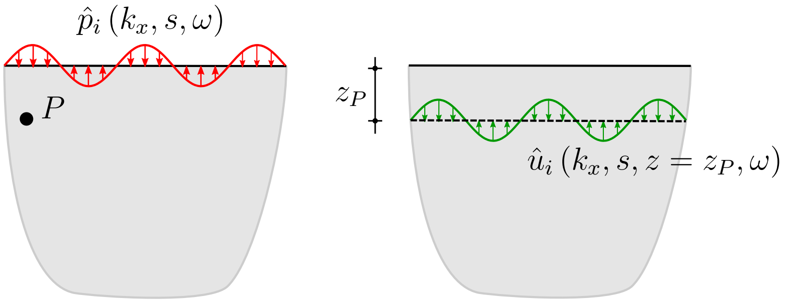

Figure 5.10: Displacements $\hat{u}_i\left(k_x, s, z = z_P, \omega\right)$ at point P in the halfspace due to $\hat{p}_i\left(k_x, s, \omega\right)$

With equation (2.36) the unknowns of the exponential approach of the halfspace A_2, B_{x2} and B_{y2} are calculated in dependency on $\hat{p}_i\left(k_x, s, \omega\right)$. Evaluating equation (2.37) for $z = z_P$, the displacements are obtained.

$$\begin{pmatrix} \hat{u}_x\left(k_x, s, z_P, \omega\right) \\ \hat{u}_y\left(k_x, s, z_P, \omega\right) \\ \hat{u}_z\left(k_x, s, z_P, \omega\right) \end{pmatrix} = \begin{bmatrix} ik_x e^{-\lambda_1 z_P} & 0 & \lambda_2 e^{-\lambda_2 z_P} \\ ik_y e^{-\lambda_1 z_P} & -\lambda_2 e^{-\lambda_2 z_P} & 0 \\ -\lambda_1 e^{-\lambda_1 z_P} & -ik_y e^{-\lambda_2 z_P} & ik_x e^{-\lambda_2 z_P} \end{bmatrix} \begin{pmatrix} A_2 \\ B_{x2} \\ B_{y2} \end{pmatrix} \tag{5.30}$$

The stresses at point P can be calculated using equation (2.33) also based on the unknowns A_2, B_{x2} and B_{y2}.

$$\begin{pmatrix} \hat{\sigma}_{xx}\left(k_x, s, z_P, \omega\right) \\ \hat{\sigma}_{yy}\left(k_x, s, z_P, \omega\right) \\ \hat{\sigma}_{zz}\left(k_x, s, z_P, \omega\right) \\ \hat{\sigma}_{xy}\left(k_x, s, z_P, \omega\right) \\ \hat{\sigma}_{yz}\left(k_x, s, z_P, \omega\right) \\ \hat{\sigma}_{xz}\left(k_x, s, z_P, \omega\right) \end{pmatrix} = \mu \begin{bmatrix} -2{k_x}^2 - \frac{\lambda}{\mu}{k_p}^2 & 0 & ik_x\lambda_2 \\ -2{k_y}^2 - \frac{\lambda}{\mu}{k_p}^2 & -2ik_y\lambda_2 & 0 \\ 2{\lambda_1}^2 - \frac{\lambda}{\mu}{k_p}^2 & 2ik_y\lambda_2 & -2ik_x\lambda_2 \\ -2k_x k_y & -ik_x\lambda_2 & ik_y\lambda_2 \\ -2ik_y\lambda_1 & {\lambda_2}^2 + {k_y}^2 & -k_x k_y \\ -2ik_x\lambda_1 & k_x k_y & -{\lambda_2}^2 - {k_x}^2 \end{bmatrix} \begin{pmatrix} A_2 e^{-\lambda_1 z_P} \\ B_{x2} e^{-\lambda_2 z_P} \\ B_{y2} e^{-\lambda_2 z_P} \end{pmatrix} \tag{5.31}$$

Analogously, the fullspace with cylindrical cavity is loaded at Γ with $\hat{p}_j\left(k_x, n, \omega\right)$ and the displacements $\hat{u}_j\left(k_x, r = R_P, n, \omega\right)$ are calculated on a circle with the radius R_P of point P as depicted in figure 5.11 with $j = r, x, \varphi$.

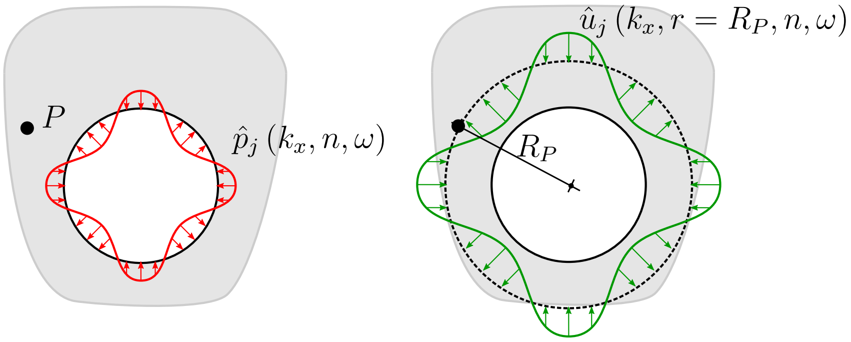

Figure 5.11: Displacements $\hat{u}_j(k_x,r=R_P,n,\omega)$ at point P in the halfspace due to $\hat{p}_j(k_x,n,\omega)$

With the equations (2.56) the unknown amplitudes of the Hankel functions C_{1n}, C_{2n} and C_{3n} can be calculated for the solution of the fullspace with cylindrical cavity. These values can be introduced into equation (2.54) and the displacements can be calculated at each point of the fullspace with cylindrical cavity. Thus, the displacements $\hat{u}_j(k_x,R_P,n,\omega)$ at point P are obtained in the threefold transformed cylindrical coordinate system $(k_x,\ n,\ \omega)$. The computation of the stresses at point P in the fullspace with cylindrical cavity can be done with equation (2.55) with $r=R_P$.

The displacements and stresses of the superposed system are obtained by superposing the values of the fundamental systems. As they are described with respect to different coordinate systems, a transformation is necessary. Hence, the displacements $\hat{u}_j(k_x,R_P,n,\omega)$ and stresses $\hat{\sigma}_{jk}(k_x,R_P,n,\omega)$ with $j,k=r,x,\varphi$ at point P of the system fullspace with cylindrical cavity can be transformed into the threefold Fourier transformed Cartesian basis of the halfspace. In order to distinguish the arising displacements and stresses that are depending on (k_x,s,ω) formally from the displacements and stresses that are calculated in the system halfspace, the fundamental systems are abbreviated by HS for the halfspace and FC for the fullspace with cylindrical cavity. Thus, the superposition of the fundamental systems can be formulated for the displacements and stresses as

$$\hat{u}_i(k_x,s,z_P,\omega)=\hat{u}_{i,HS}(k_x,s,z_P,\omega)+\hat{u}_{i,FC}(k_x,s,z_P,\omega) \tag{5.32a}$$

$$\hat{\sigma}_{ij}(k_x,s,z_P,\omega)=\hat{\sigma}_{ij,HS}(k_x,s,z_P,\omega)+\hat{\sigma}_{ij,FC}(k_x,s,z_P,\omega) \tag{5.32b}$$

with $i,j=z,y,x$. With this post-processing step, the displacements or stresses at an arbitrary point inside the halfspace with cylindrical Finite Element structure can be determined.

6 Verification

6.1 Preliminary remark

The method presented in the previous chapters shall be verified. In section 6.2 this is done for a halfspace with cylindrical Finite Element structure. The system and general parameters of the verification example are presented in section 6.2.1 for one specific parameter combination. By a quantitative similarity assessment, the accordance of the coupled approach and the analytical solution is evaluated in section 6.2.2. For a more general estimation of the accordance independent of certain chosen parameters and also for a reduction of the number of influence quantities, a dimensionless representation of the results is contained in section 6.2.3. Finally, after verifying the program for an excitation with a vertical load and evaluating it for a vertical displacement, different load-displacement combinations are checked in section 6.3. The coupling of ITM and FEM on a spherical coupling surface is presented in section 6.4.

6.2 Verification example for the system halfspace with cylindrical Finite Element structure

In this section the results of a coupled ITM-FEM approach are compared to an analytical solution. The verification is performed for a halfspace with cylindrical cavity that is coupled to a Finite Element mesh with cylindrical surface. The finite elements have the same material parameters as the surrounding soil so the solution can be compared to the analytical solution of a layered halfspace consisting of two layers with identical material.

6.2.1 Overview

A sketch of the verification system is depicted in figure 6.1a. As benchmark the analytical solution for a layered halfspace is used as shown in figure 6.1b. The layer boundary inside the halfspace is introduced in order to be able to apply loads inside the halfspace and also to directly evaluate the displacements at a certain depth.

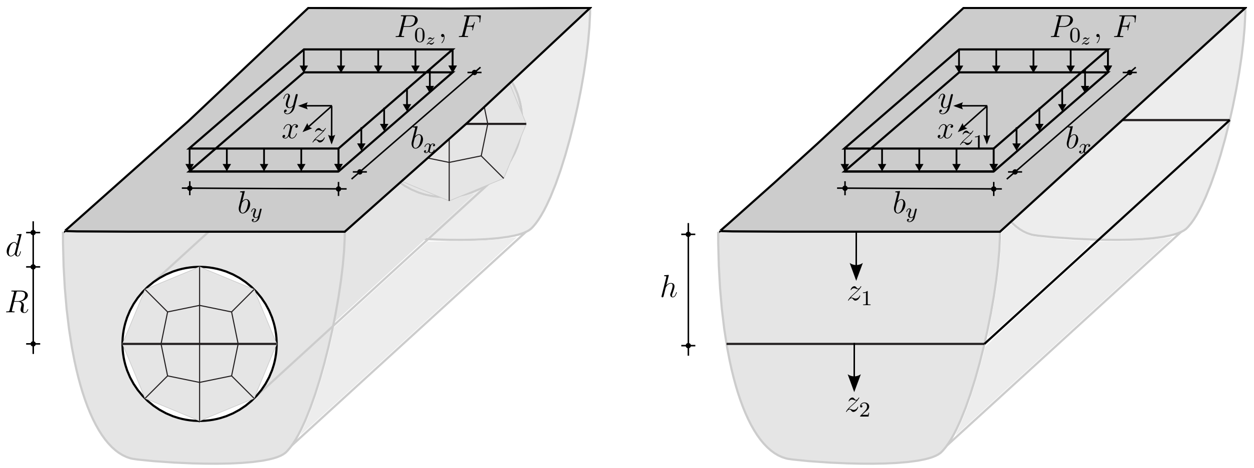

(a) **(b)**

Figure 6.1: Schematic sketch of the coupled ITM-FEM system (6.1a) and the layered halfspace (6.1b)

The following material parameters of table 6.1 are used for the calculations of the displacements.

Young's modulus E $\left[\frac{\mathrm{N}}{\mathrm{m}^2}\right]$	Poisson ratio ν $[-]$	Density ρ $\left[\frac{\mathrm{kg}}{\mathrm{m}^3}\right]$	Damping ratio ζ $[-]$
$260 \cdot 10^6 (1 + i \,\mathrm{sign}\,(\omega)\ \zeta)$	0.3	2000	0.1

Table 6.1: Material parameters of the verification of the halfspace with cylindrical Finite Element structure

With the given material parameters, the velocities of the compressional, shear and Rayleigh waves can be calculated as rounded $c_p = 419\ \frac{\mathrm{m}}{\mathrm{s}}$, $c_s = 224\ \frac{\mathrm{m}}{\mathrm{s}}$ and $c_r = 208\ \frac{\mathrm{m}}{\mathrm{s}}$.

The chosen geometry of the verification example consists of a tunnel with a radius R of 2 m and a depth of the covering d of 0.1 m. This corresponds to a depth of the top layer of the reference system h of 2.1 m. For the verification of the coupled ITM-FEM approach, the vertical displacements $u_{z_{hs}}$ on the surface of the halfspace due to a centric, vertical, harmonic block load P_z on the halfspace with the parameters given in table 6.2 are calculated.

Amplitude P_{0z} $\left[\frac{\mathrm{N}}{\mathrm{m}^2}\right]$	Width in x-direction b_x [m]	Width in y-direction b_y [m]	Frequency of excitation f [Hz]
1	8	8	20

Table 6.2: Load parameters of the verification example

The three-dimensional displacement on the surface of the halfspace of the coupled approach is exemplarily depicted in figure 6.2a in dependency on the x- and y-coordinate. The result of the analytical calculation is analogously presented in figure 6.2b. Both figures are presented in the time domain for the moment of the maximum displacement $t = t_{max}$.

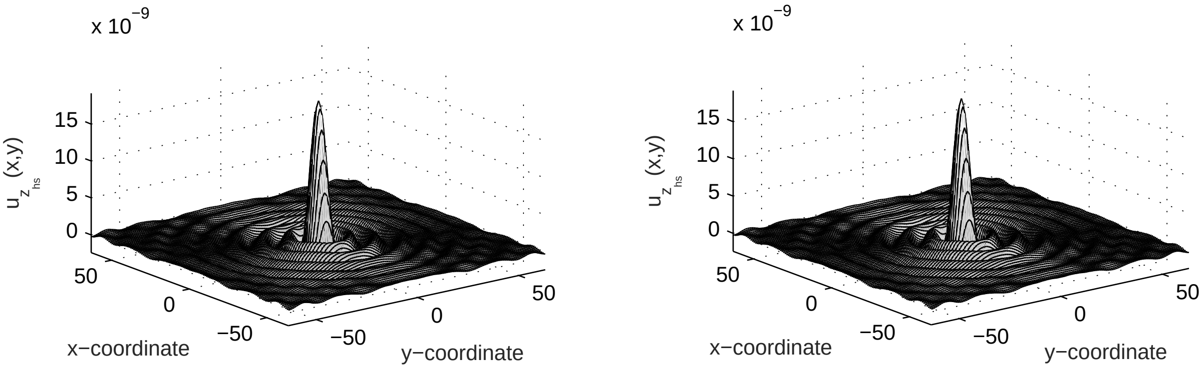

(a) **(b)**

Figure 6.2: Vertical displacement on the surface of the halfspace calculated with the coupled approach (6.2a) and the analytical solution of a layered halfspace (6.2b)

For a quantitative estimation of the error between analytical solution and the coupled approach, a two-dimensional profile is depicted in the following figure 6.3 with respect to the y-coordinate at the position $x = 0$. The accordance between the analytical solution and the result of the coupled ITM-FEM approach is clearly visible. Both methods obtain nearly identical vertical displacements on the surface of the halfspace. A quantitative assessment of the similarity of the results is presented in the following section 6.2.2.

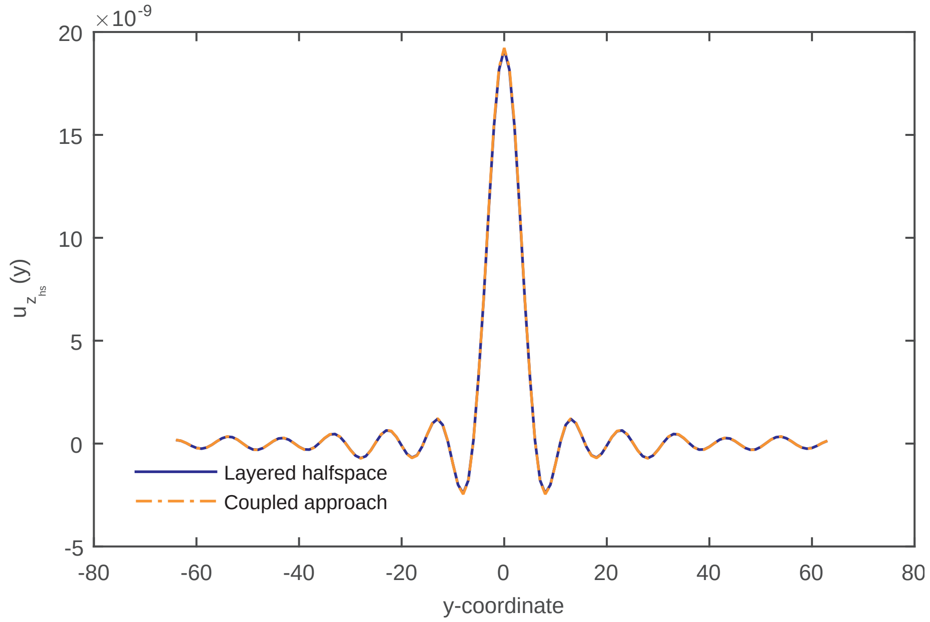

Figure 6.3: Vertical displacement on the surface of the halfspace in dependency on the y-coordinate $u_{z_{hs}}(y)$

6.2.2 Quantitative similarity assessment

The maximum error between the analytical solution of the halfspace and the solution of the coupled ITM-FEM approach is identified at $x = 0$, $y = 2$ m for $t = t_{max}$ as $\Delta u_z = 1.11 \cdot 10^{-10}$ m which is 0.7 % of the analytical value at the respective position.

In order to assess the quality of the calculated result with respect to the total domain quantitatively, there are several proximity measures available that enable quantitative comparisons of vectors. Their definitions and possible applications are summarized in a variety of textbooks, for example in [Backhaus et al 2011], [Bortz and Schuster 2010], [Fahrmeir et al 1996] or [Bock 1974]. The City-Block metric (also named Manhattan metric) can be calculated comparing the vectors that are depicted in figure 6.3 by adding the absolute values of their differences. In general, the City-Block metric d_1 is defined for the comparison of two vectors $\mathbf{a}$ and $\mathbf{b}$ with n elements as

$$d_1 = \sum_{i=1}^{n} |a_i - b_i| \tag{6.1}$$

It is a specification of the Minkowski-metrics that are defined as

$$d_r = \sqrt[r]{\sum_{i=1}^{n} |a_i - b_i|^r} \tag{6.2}$$

The City-Block metric is chosen because all the differences are weighted equally during the calculation. For Minkowski-metrics with $r > 1$, bigger differences are contributing more to the result of the calculated distance than smaller differences due to calculating the power of the differences.

Applying equation (6.1) on the vectors that are depicted in figure 6.3 leads to a distance of $d_1 = 1.82 \cdot 10^{-9}$ m. Distributed over the measurement points, an average error of $d_{1,av} = 1.42 \cdot 10^{-11}$ m is calculated.

For an assessment of the similarity of vectors instead of their differences there are several coefficients existing. In appendix A.8 information about the Pearson correlation coefficient, the cosine coefficient and the modal assurance criterion are summarized. They possess values in a defined range and can be used to quantify the similarity of vectors. But all three coefficients are not able to mirror the difference of two vectors with identical phase information but different amplitudes ($\mathbf{b} = \lambda\mathbf{a}$). Thus, they are not used in the scope of the verification example.

Another similarity measure is the Tanimoto coefficient. Published by [Jaccard 1901] and [Rogers and Tanimoto 1960] for a quantification of the similarity of different classes of plants, it is a measure often used to classify the similarity of dichotomous variables. A possible extension on the use for continuous variables is published for example in [Willet 1998]. Here the Tanimoto coefficient for the comparison of two vectors $\mathbf{a}$ and $\mathbf{b}$ with n elements ranging on an interval scale is defined as

$$T = \frac{\sum\limits_{i=1}^{n} a_i b_i}{\sum\limits_{i=1}^{n} {a_i}^2 + \sum\limits_{i=1}^{n} {b_i}^2 - \sum\limits_{i=1}^{n} a_i b_i} \tag{6.3}$$

and ranges between 1 for identical vectors and $-\frac{1}{3}$ for vectors pointing in opposite direction. In [Kreutz 2013] the Tanimoto coefficient is used to compare the stress states of a Finite Element approach with augmented elements to the stress state of a reference solution. Its applicability for the verification example is checked in [Schneider 2014]. In his thesis, [Schneider 2014] compares two exponentially decaying cosine functions that show similar characteristics as the result of the verification example. Starting from two identical functions, three different modifications are applied on one of the cosine functions one by one. A change of the phase shift is applied as well as a change of the amplitude of the function. In a third step, individual values of the function are modified. For each combination, different similarity measures are evaluated. The Tanimoto coefficient is shown to be sensitive to each of the applied changes and is, thus, chosen as the measure for comparing the results of the analytical solution and of the solution of the coupled ITM-FEM approach. Moreover, [Schneider 2014] shows that the Tanimoto coefficient does not react on the absolute value of the difference between two functions but on the relative difference.

Monotonous with the Tanimoto coefficient, the Dice coefficient is also a possible similarity measure which ranges between 1 in case of comparing identical measures and -1 for vectors pointing in opposite direction as presented for example in [Willet 1998] or [Holliday et al 1995]. In appendix A.8, the Dice coefficient is defined and it is shown that it reacts less sensitively than the Tanimoto coefficient to the different changes described above.

Thus, the Tanimoto coefficient is used for a quantitative assessment of the similarity between the analytical solution and the coupled ITM-FEM approach. Calculating the Tanimoto coefficient for the two functions depicted in figure 6.3, a result of 0.99996 is obtained thus also confirming a good accordance of the coupled ITM-FEM result with the analytical solution. If the two-dimensional profile is not only analyzed at $x = 0$ and $t = t_{max}$ but in dependency on the x- and t-coordinate, a minimum Tanimoto coefficient is obtained of 0.9992.

Of course, as the calculations are performed numerically, the results depend on the accuracy of the numerical computation. The results presented so far have been achieved for a repetition length of the spatial domain of $B_x = B_y = 128$ m and a period of the calculated time of exactly one period of the excitation frequency according to table 6.2. In the following table 6.3, the results are presented for different discretizations where the first line contains the results presented so far. In the first four columns the number of the samples on the halfspace surface in x- and y-direction (N_x and N_y), the number of samples with respect to time (N_t) and the number of Fourier series members on the cylindrical coupling surface (N_φ) are listed. The parameters that are modified compared to the standard parameters of the first line are marked in bold numbers. The error measures as well as the computation time are listed in table 6.3. The computation time was determined in calculations performed with a computer with 16 GB RAM and a 3.40 GHz quad core processor.

N_x	N_y	N_t	N_φ	Maximum value u_z [m]	Maximum error [m]	City-Block average [m] [m]	Minimum Tanimoto [−]	Comp. time [s]
2^7	2^7	2^5	2^5	$1.92 \cdot 10^{-8}$	$1.11 \cdot 10^{-10}$	$1.42 \cdot 10^{-11}$	0.9992	97
$\mathbf{2^6}$	$\mathbf{2^6}$	2^5	2^5	$1.88 \cdot 10^{-8}$	$1.15 \cdot 10^{-10}$	$1.63 \cdot 10^{-11}$	0.9981	30
2^7	2^7	$\mathbf{2^4}$	2^5	$1.90 \cdot 10^{-8}$	$1.02 \cdot 10^{-10}$	$1.35 \cdot 10^{-11}$	0.9993	78
2^7	2^7	2^5	$\mathbf{2^4}$	$1.92 \cdot 10^{-8}$	$4.33 \cdot 10^{-10}$	$5.55 \cdot 10^{-11}$	0.9890	69
$\mathbf{2^6}$	2^7	2^5	2^5	$1.90 \cdot 10^{-8}$	$1.06 \cdot 10^{-10}$	$1.47 \cdot 10^{-11}$	0.9993	54
2^7	$\mathbf{2^6}$	2^5	2^5	$1.90 \cdot 10^{-8}$	$1.09 \cdot 10^{-10}$	$1.49 \cdot 10^{-11}$	0.9977	66

Table 6.3: Comparison of the quality of the results in dependency on the numerical accuracy

Interpreting table 6.3 it can be stated that even with less samples the error between analytical solution and coupled ITM-FEM approach is acceptably small. Considering the computational costs, a calculation with $N_x = N_y = 2^6$, $N_t = 2^5$ and $N_\varphi = 2^5$ is advantageous. As presented in row 2 of table 6.3, the error rates are small and the computation time is acceptable.

The displacements are also calculated inside the soil. The result u_{z_s} is displayed for $x = 0$ and at the moment of the maximum displacement $t = t_{max}$ in figure 6.4.

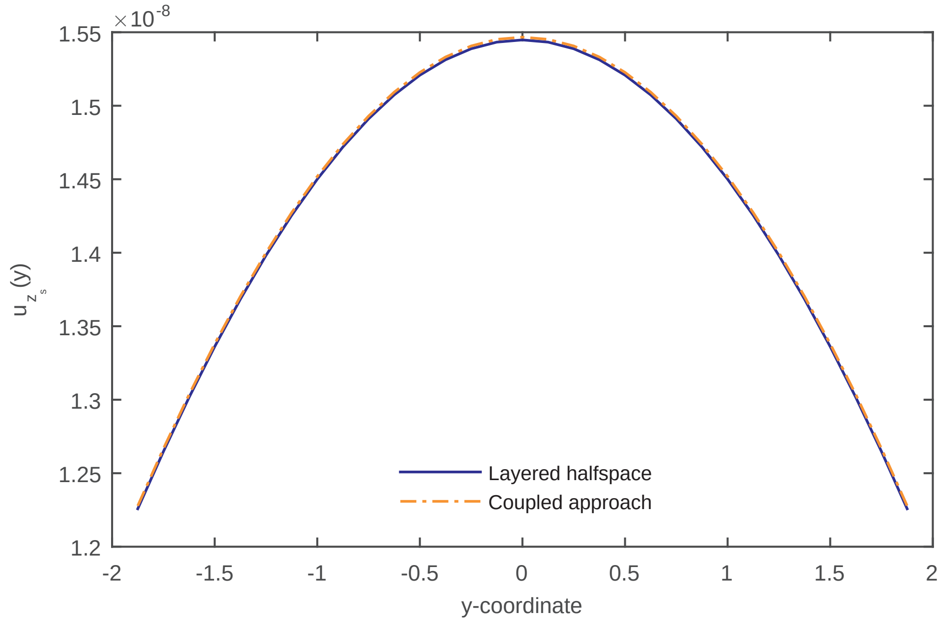

Figure 6.4: Vertical displacement inside the halfspace in dependency on the y-coordinate $u_{z_s}(y)$

For the computation of the coupled ITM-FEM system, the displacements on the horizontal middle line of the Finite Element mesh are calculated. They are compared to the displacements of the analytical solution in the layer boundary.

The maximum error between the depicted graphs is $1.84 \cdot 10^{-11}$ m and the average City-Block metric is $5.75 \cdot 10^{-13}$ m. The similarity in total is described by the minimum Tanimoto coefficient if the analytical and the coupled ITM-FEM solution are compared with respect to the y-axis for each possible combination of x-coordinate. It takes a value of 0.9604. Though the accordance between analytical solution and coupled ITM-FEM solution is still high, the evaluation inside the soil is worse than the one on the surface of the halfspace. This can be explained with the discretization error of the Finite Element mesh which is more significant inside the mesh as the circular circumference of the Finite Element mesh can only be approximated by a linear polygon. But, as the result of figure 6.4 shows, a good approximation can be achieved.

6.2.3 Dimensionless representation of the results

The presentation of the results in section 6.2.1 and 6.2.2 was carried out for the material defined in table 6.1 and the load parameters specified in table 6.2. A description of the results that is more independent of the chosen material can be achieved using dimensionless parameters. By presenting the results in a dimensionless form, the number of variables can be reduced and the results can be compared independent of some of the parameters.

6.2.4 Derivation of the dimensionless parameters

The description and calculations presented so far, have been based on dimensional or concrete quantities. These are quantities who have values depending on the chosen system of units [Sedov 1993]. They show the characteristics that the value $\overline{Q}$ of a quantity Q depends on the scale on which it is described i. e. on the unit of the quantity [Q].

$$Q = \overline{Q}\ [\mathrm{Q}] \tag{6.4}$$

In mechanical systems, a variety of different scales exists, all belonging to the three basic quantities of length, mass and time. There are different basic quantities possible, but generally these three quantities are used for the description of physical and mechanical relations as also stated for example in [Sedov 1993]. The basic unit system of engineering systems is usually described by the units meter [m], kilogram [kg] and second [s] also named as MKS unit system. If the representation of physical or mechanical relations shall be independent of a chosen unit system, dimensionless or abstract quantities can be used. Some quantities are by default dimensionless as for example the Poisson ratio or the damping ratio because they are calculated as the ratio of dimensional quantities with the same dimensions. This example shows that calculating ratios changes the dimension of a quantity and can thus be used to transform dimensional into dimensionless quantities. This transformation is possible because each derived quantity Q can be shown to be describable as a constant C multiplied with the power product of the basic quantities length L, mass M and time T.

$$Q = C\ L^{\alpha} M^{\beta} T^{\gamma} \tag{6.5}$$

A proof of equation (6.5) is presented for example in [Bridgman and Holl 1932] and is also summarized in appendix A.9. If the quantity Q can be expressed as power product of the basic quantities length, mass and time, also the unit of Q depends on the power product of the basic units meter [m], kilogram [kg] and second [s].

$$[Q] = [L]^{\alpha}\,[M]^{\beta}\,[T]^{\gamma} = \mathrm{m}^{\alpha}\mathrm{kg}^{\beta}\mathrm{s}^{\gamma} \tag{6.6}$$

To obtain dimensionless parameters, the dimensions of all quantities that influence the system under consideration have to be analyzed. According to [Stichlmair 1990], dimensionless parameters can be derived if the relationship between quantities is known, even if it is not possible to specify an analytical description of the relationships. In a list of relevance, all n quantities which are relevant for a given system are listed.

$$\mathrm{f}\left(Q_1, Q_2, \ldots, Q_n\right) = 0 \tag{6.7}$$

All relevant parameters Q_n have to be listed according to [Stichlmair 1990], only those that are dimensionless by default, as the Poisson ratio for example, can be neglected. According to equation (6.6) the units of each quantity Q_i in equation (6.7) are power products of the basic units [m], kilogram [kg] and second [s] with powers α_i, β_i and γ_i.

$$[Q_1] = \mathrm{m}^{\alpha_1}\mathrm{kg}^{\beta_1}\mathrm{s}^{\gamma_1} \tag{6.8a}$$

$$[Q_2] = \mathrm{m}^{\alpha_2}\mathrm{kg}^{\beta_2}\mathrm{s}^{\gamma_2} \tag{6.8b}$$

$$\vdots$$

$$[Q_n] = \mathrm{m}^{\alpha_n}\mathrm{kg}^{\beta_n}\mathrm{s}^{\gamma_n} \tag{6.8c}$$

According to [Zierep 1982], the task consists in finding dimensionless representations of the system with

$$\pi = {Q_1}^{k_1} {Q_2}^{k_2} \ldots {Q_n}^{k_n} \tag{6.9}$$

Considering the units of equation (6.9) the statement can be formulated that

$$\begin{aligned}[\pi] &= [Q_1]^{k_1} [Q_2]^{k_2} \ldots [Q_n]^{k_n} \\ &= \left(\mathrm{m}^{\alpha_1}\mathrm{kg}^{\beta_1}\mathrm{s}^{\gamma_1}\right)^{k_1} \left(\mathrm{m}^{\alpha_2}\mathrm{kg}^{\beta_2}\mathrm{s}^{\gamma_2}\right)^{k_2} \ldots \left(\mathrm{m}^{\alpha_n}\mathrm{kg}^{\beta_n}\mathrm{s}^{\gamma_n}\right)^{k_n} \overset{!}{=} \mathrm{m}^0\mathrm{kg}^0\mathrm{s}^0 \end{aligned} \tag{6.10}$$

Comparing the exponents of the units in equation (6.10) leads to a system of equations for the determination of the unknown coefficients k_1, k_2, …, k_n. As there are three basic units [m], kilogram [kg] and second [s], the system of equations consists of three equations and n unknowns

$$\alpha_1 k_1 + \alpha_2 k_2 + \ldots + \alpha_n k_n \overset{!}{=} 0 \tag{6.11a}$$

$$\beta_1 k_1 + \beta_2 k_2 + \ldots + \beta_n k_n \overset{!}{=} 0 \tag{6.11b}$$

$$\gamma_1 k_1 + \gamma_2 k_2 + \ldots + \gamma_n k_n \overset{!}{=} 0 \tag{6.11c}$$

or formulated in matrix notation

$$\begin{bmatrix} \alpha_1 & \alpha_2 & \ldots & \alpha_n \\ \beta_1 & \beta_2 & \ldots & \beta_n \\ \gamma_1 & \gamma_2 & \ldots & \gamma_n \end{bmatrix} \begin{pmatrix} k_1 \\ k_2 \\ \vdots \\ k_n \end{pmatrix} = \begin{pmatrix} 0 \\ 0 \\ \vdots \\ 0 \end{pmatrix} \tag{6.12}$$

The matrix containing the exponents α_i, β_i and γ_i of the power products of the quantities Q_i is also labeled as dimension matrix according to [Zierep 1982].

$$\begin{array}{r c} & \begin{matrix} Q_1 & Q_2 & \ldots & Q_n \end{matrix} \\ \begin{matrix} [\mathrm{m}] \\ [\mathrm{kg}] \\ [\mathrm{s}] \end{matrix} & \begin{bmatrix} \alpha_1 & \alpha_2 & \ldots & \alpha_n \\ \beta_1 & \beta_2 & \ldots & \beta_n \\ \gamma_1 & \gamma_2 & \ldots & \gamma_n \end{bmatrix} \end{array} \tag{6.13}$$

The solvability of the system of equations (6.12) depends on the rank of the dimension matrix (6.13). If the rank r of the dimension matrix, which is in mechanical systems maximal three, is smaller than the number of quantities n, then $(n - r)$ linearly independent solutions exist. This means that r values of k_i can be chosen arbitrarily and the corresponding $(n-r)$ values of k_i can only be determined in dependency on the free values. Thus, $(n-r)$ different dimensionless quantities π can be determined and the general description (6.7) can be formulated as

$$\mathrm{f}\left(\pi_1, \pi_2, \ldots, \pi_{n-r}\right) = 0 \tag{6.14}$$

Summarizing, it can be stated that, if n quantities $Q_1, Q_2, \ldots Q_n$ are given which are related to each other, there are exact $(n-r)$ dimensionless quantities $\pi_1, \pi_2, \ldots, \pi_{n-r}$ with $\mathrm{f}\left(\pi_1, \pi_2, \ldots, \pi_{n-r}\right) = 0$ describing the complete system where $r \leq n$ is the rank of the dimension matrix. This theorem is often also named the Buckingham-π-theorem after the publication of [Buckingham 1914] even if, as [Görtler 1975] points out, [Buckingham 1914] was not the first author that published this theorem and also did not formally correct refer the solvability to the rank of the dimension matrix but to the number of basic units.

6.2.5 Dimensionless representation of the verification example

In order to describe the results of the verification example using dimensionless parameters, a list of relevance has to be formulated. Therefore, the quantities that are determining the system have to be identified.

The first quantity is the one to be assessed. For the systems depicted in figure 6.5 that are loaded with a vertical load on the surface of the halfspace, the vertical displacement $u_{z_{hs}}$ at the halfspace surface is evaluated at a point in the middle of the block load ($x = 0$, $y = 0$).

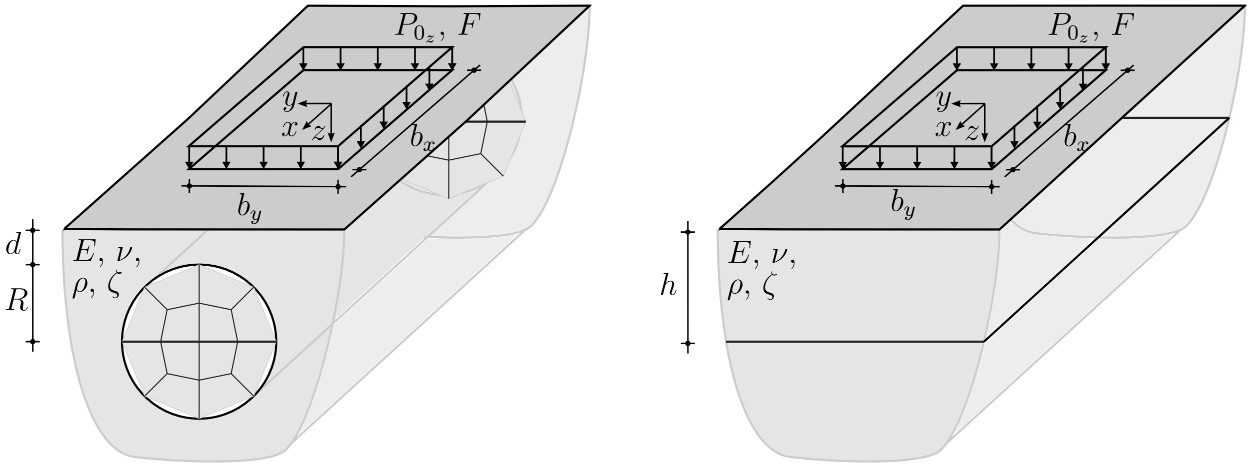

(a) **(b)**

Figure 6.5: Relevant parameters of the coupled ITM-FEM system (6.5a) and the layered halfspace (6.5b)

The value of the evaluation quantity depends first on the material of the soil which is the only material that is used for the verification example. This is modeled by the parameters of Young's modulus E, Poisson ratio ν, damping ratio ζ and density ρ. As mentioned in section 6.2.4, quantities that are dimensionless by default, can be neglected. Therefore, the Poisson ratio ν and the damping ratio ζ will not be taken into account in the list of relevance and are chosen as the constant values presented in table 6.1.

Furthermore, the evaluation quantity is influenced by the load parameters. The load is modeled with the quantities of the amplitude of the load P_{0_z}, the frequency of excitation f and the width of the block load in x- and y-direction b_x and b_y.

The response of the coupled ITM-FEM approach is also dependent on the geometry of the system, represented by the radius R of the tunnel and the depth of the covering above the tunnel d. The geometry of the reference system of the layered halfspace is determined by the depth of the layer boundary h.

Thus, the lists of relevance can be formulated for the depicted systems as

$$\mathrm{f}\left(u_{z_{hs}}, E, \rho, P_{0_z}, f, b_x, b_y, R, d\right) = 0 \tag{6.15a}$$

$$\mathrm{f}\left(u_{z_{hs}}, E, \rho, P_{0_z}, f, b_x, b_y, h\right) = 0 \tag{6.15b}$$

For the coupled ITM-FEM approach $n = 9$ quantities are identified that are necessary to model the system, for the layered halfspace $n = 8$ quantities. In the following table 6.4 the quantities of the verification example are summarized and described by the powers α, β and γ of the respective basic units meter [m], kilogram [kg] and second [s] as defined in equation (6.6).

Quantity	Abbreviation	Unit	α	β	γ
Maximum vertical displacement at $x = 0$, $y = 0$, $z = 0$	$u_{z_{hs}}$	m	1	0	0
Young's modulus	E	$\frac{\mathrm{N}}{\mathrm{m}^2}$	-1	1	-2
Density	ρ	$\frac{\mathrm{kg}}{\mathrm{m}^3}$	-3	1	0
Amplitude of the load	P_{0_z}	$\frac{\mathrm{N}}{\mathrm{m}^2}$	-1	1	-2
Frequency of the load	f	$\frac{1}{\mathrm{s}}$	0	0	-1
Width of the load in x-direction	b_x	m	1	0	0
Width of the load in y-direction	b_y	m	1	0	0
Radius of the cylindrical coupling surface	R	m	1	0	0
Depth of the covering	d	m	1	0	0
Depth of the top layer	h	m	1	0	0

Table 6.4: List of relevance of the quantities of the verification example

In a next step, the dimension matrix has to be defined. As derived in section 6.2.4, $(n - r)$ dimensionless parameters can be derived out of a dimension matrix with the rank r.

These dimensionless quantities will be defined in dependency on the r quantities that are chosen as independent quantities. Before formulating the dimension matrix, the independent quantities have to be determined. These are the parameters which are used for the calculation of the $(n - r)$ dimensionless parameters and may appear in one or more of the π-quantities (in contrast to the dependent quantities which only appear in one of the dimensionless π-quantities as mentioned for example in [Stichlmair 1990]). Thus, a functional relationship between the independent quantities and the evaluation quantity will not be visible in the dimensionless description of the system. This has to be taken into account as the independent quantities are chosen. Moreover, as the goal of a dimensional analysis is also to reduce the number of quantities from n to $(n - r)$, it is advantageous if r takes the maximum value which is, for mechanical systems, three. Therefore, it has to be considered that the chosen independent variables are able to represent the basic unit system.

For the verification example the Young's modulus E, the density ρ and the width of the load in x-direction b_x as geometrical quantity are chosen as independent variables and written in the first three columns of the dimension matrix. Thus, the dimension matrix can be formulated for the coupled ITM-FEM system (matrix on the left) and for the layered halfspace (matrix on the right) as

$$\begin{array}{c} \\ [\mathrm{m}] \\ [\mathrm{kg}] \\ [\mathrm{s}] \end{array} \begin{array}{ccccccccc} E & \rho & b_x & P_{0_z} & f & b_y & R & d & u_{z_{hs}} \\ \hline -1 & -3 & 1 & -1 & 0 & 1 & 1 & 1 & 1 \\ 1 & 1 & 0 & 1 & 0 & 0 & 0 & 0 & 0 \\ -2 & 0 & 0 & -2 & -1 & 0 & 0 & 0 & 0 \end{array} \quad \begin{array}{cccccccc} E & \rho & b_x & P_{0_z} & f & b_y & h & u_{z_{hs}} \\ \hline -1 & -3 & 1 & -1 & 0 & 1 & 1 & 1 \\ 1 & 1 & 0 & 1 & 0 & 0 & 0 & 0 \\ -2 & 0 & 0 & -2 & -1 & 0 & 0 & 0 \end{array} \tag{6.16}$$

The rank of both matrices in (6.16) is the maximum possible value of $r = 3$. To determine the relationships between the independent and dependent variables, the dimension matrices (6.16) have to be transformed such that a 3×3 identity matrix is obtained in the columns that are representing the independent quantities. For this equivalent transformations can be applied. As a result the following matrices are obtained.

$$\begin{array}{c} \\ [\mathrm{m}] \\ [\mathrm{kg}] \\ [\mathrm{s}] \end{array} \begin{array}{ccccccccc} E & \rho & b_x & P_{0_z} & f & b_y & R & d & u_{z_{hs}} \\ \hline 1 & 0 & 0 & 1 & \frac{1}{2} & 0 & 0 & 0 & 0 \\ 0 & 1 & 0 & 0 & -\frac{1}{2} & 0 & 0 & 0 & 0 \\ 0 & 0 & 1 & 0 & -1 & 1 & 1 & 1 & 1 \end{array} \quad \begin{array}{cccccccc} E & \rho & b_x & P_{0_z} & f & b_y & h & u_{z_{hs}} \\ \hline 1 & 0 & 0 & 1 & \frac{1}{2} & 0 & 0 & 0 \\ 0 & 1 & 0 & 0 & -\frac{1}{2} & 0 & 0 & 0 \\ 0 & 0 & 1 & 0 & -1 & 1 & 1 & 1 \end{array} \tag{6.17}$$

After this transformation, the exponents k_i of equation (6.9) can be determined, for example for the coupled ITM-FEM system, by

$$k_1 = -k_4 - \frac{1}{2} k_5 \tag{6.18a}$$

$$k_2 = \frac{1}{2} k_5 \tag{6.18b}$$

$$k_3 = k_5 - k_6 - k_7 - k_8 - k_9 \tag{6.18c}$$

The dimensionless representation of the system can be formulated as

$$\pi = E^{-k_4 - \frac{1}{2} k_5} \, \rho^{\frac{1}{2} k_5} \, {b_x}^{k_5 - k_6 - k_7 - k_8 - k_9} \, P_{0_z}^{k_4} \, f^{k_5} \, {b_y}^{k_6} \, R^{k_7} \, d^{k_8} \, u_{z_{hs}}^{k_9} \tag{6.19}$$

Now each one of the exponents k_i can be set to be equal to 1 consecutively and the others respectively chosen to be 0. Hence, the six dimensionless quantities of the coupled ITM-FEM system are the dimensionless amplitude of the load π_P, the dimensionless frequency π_f, the dimensionless width of the load in y-direction π_y, the dimensionless radius π_R, the dimensionless depth of the covering π_d and as evaluation quantity the dimensionless vertical displacement π_u.

$$\pi_P = \frac{P_{0_z}}{E} \qquad \pi_f = \frac{f b_x}{\sqrt{\frac{E}{\rho}}} \qquad \pi_y = \frac{b_y}{b_x} \qquad \pi_R = \frac{R}{b_x} \qquad \pi_d = \frac{d}{b_x} \qquad \pi_u = \frac{u_{z_{hs}}}{b_x} \tag{6.20}$$

The dimensionless displacement π_u can be specified as a function of the five dimensionless parameters in a general form as

$$\pi_u = \mathrm{f}\left(\pi_P, \pi_f, \pi_y, \pi_R, \pi_d\right) \tag{6.21}$$

For linear material behavior the relationship between the amplitude of the load and the displacement are known as the displacement $u_{z_{hs}}$ is directly proportional to the amplitude of the load P_{0_z}. Thus, the number of influencing parameters of the unknown function f can be reduced to four.

$$\pi_u = \pi_P \, \mathrm{f}\left(\pi_f, \pi_y, \pi_R, \pi_d\right) \tag{6.22}$$

If the widths of the load in the x- and y-directions are additionally limited to an excitation with a square geometry $b_x = b_y$, one more dimensionless parameter can be reduced.

$$\pi_u = \pi_P \, \mathrm{f}\left(\pi_f, \pi_R, \pi_d\right) \qquad \text{with } \pi_y = \frac{b_y}{b_x} = 1 \tag{6.23}$$

If the same procedure is repeated analogously for the system of a layered halfspace, the dimensionless displacement π_u is defined in dependency on the dimensionless frequency π_f and the dimensionless depth of the top layer π_h.

$$\pi_u = \pi_P \, \mathrm{f}\left(\pi_f, \pi_h\right) \qquad \text{with } \pi_y = \frac{b_y}{b_x} = 1 \tag{6.24}$$

To compare the results of both systems, a three-dimensional plot is possible, depicting the dimensionless displacement π_u in dependency on the dimensionless frequency π_f and the dimensionless radius π_R respectively the dimensionless depth of the top layer π_h. This is performed for the system of the coupled ITM-FEM approach for a fixed value of the dimensionless depth of the covering π_d. In doing so, it has to be ensured that the chosen radius R plus the depth of the covering d are equal to the depth of the top layer of the reference system h.

6.2.6 Dimensionless results of the verification example

As mentioned in section 6.2.5, the Young's modulus E, the density ρ and the width of the load in x-direction are chosen as independent variables. Their values are, as introduced in the tables 6.1 and 6.2, $E = 260 \cdot 10^6 \, (1 - 0.1i) \, \frac{\mathrm{N}}{\mathrm{m}^2}$, $\rho = 2000 \, \frac{\mathrm{kg}}{\mathrm{m}^3}$, $b_x = 8$ m. To ensure that $\pi_y = 1$, b_y is chosen to be 8 m. The dimensionless flexibility $\frac{\pi_u}{\pi_P}$ is presented in the following figures 6.6 in dependency on the dimensionless frequency π_f and the dimensionless geometrical quantity π_R respectively π_h. In the dimensionless frequency π_f, the frequency f is varied in the range $[-1 \text{ Hz}, -100 \text{ Hz}]$ in steps of 1 Hz, the radius R is varied between $[1 \text{ m}, 5.9 \text{ m}]$ in steps of 0.1 m, the height of the second layer h equivalently from 1.1 m to 6.0 m.

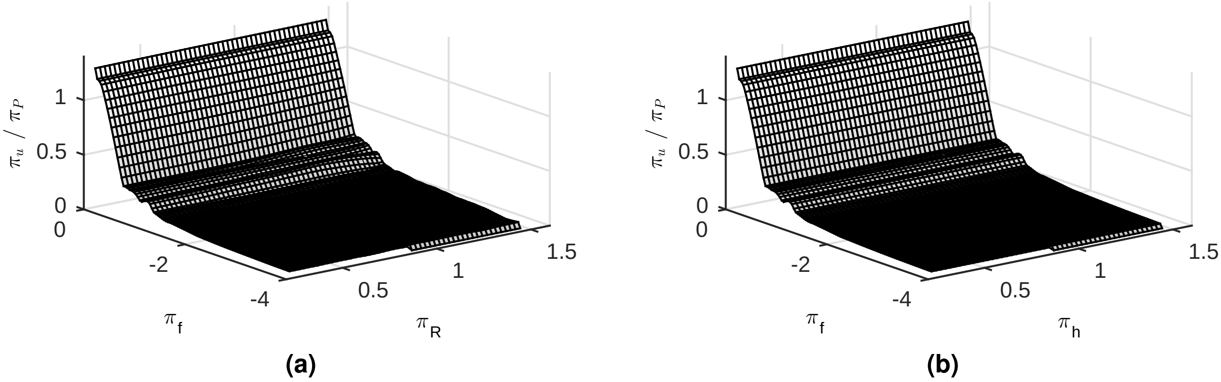

(a) **(b)**

Figure 6.6: Dimensionless flexibility $\frac{\pi_u}{\pi_P}$ of the coupled ITM-FEM system (6.6a) and the layered half-space (6.6b) in dependency on the dimensionless frequency π_f and the dimensionless radius π_R respectively the dimensionless depth of the top layer π_h

A good accordance of the coupled ITM-FEM solutions with the analytical calculations can be stated. In both figures, the dependency of the displacement on the geometrical quantity R respectively h is rather unincisive. While the displacement calculated with the analytical solution is independent of the quantity h, the displacement calculated with the coupled ITM-FEM approach is slightly changing in dependency on the radius R. If the Tanimoto coefficient is calculated comparing the vectors $\pi_u(\pi_f)$ for different values of π_R respectively π_{h-d} as presented in figure 6.7, it can be stated that the quality of the accordance decreases with increasing dimensionless radius π_R.

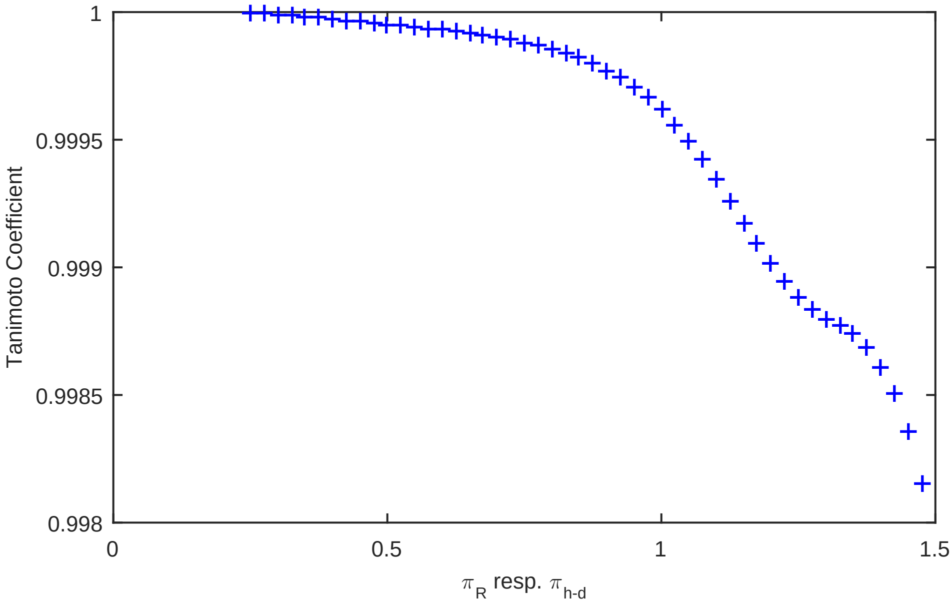

Figure 6.7: Tanimoto coefficient comparing the vector of the dimensionless displacement $\pi_u(\pi_f)$ for different values of π_R respectively π_{h-d}

This decrease of the accordance with increasing radius of the tunnel can be explained as the number of discrete elements along the circumference of the cylindrical coupling surface N_φ is constant for all calculations. Therefore, for increasing values of the radius, the element size is increasing and the error that occurs when discretizing a circular geometry with linear elements increases. In figure 6.8 the calculation is repeated for different discretizations. The results are presented for $N_\varphi = 16$, $N_\varphi = 32$ and $N_\varphi = 64$ elements on the circumference on the cylindrical coupling surface. The sampling concerning the frequency resolution is decreased for this comparison. The frequency f is varied in steps of 2 Hz. Also the radius is varied with a coarser sampling in steps of 0.2 m.

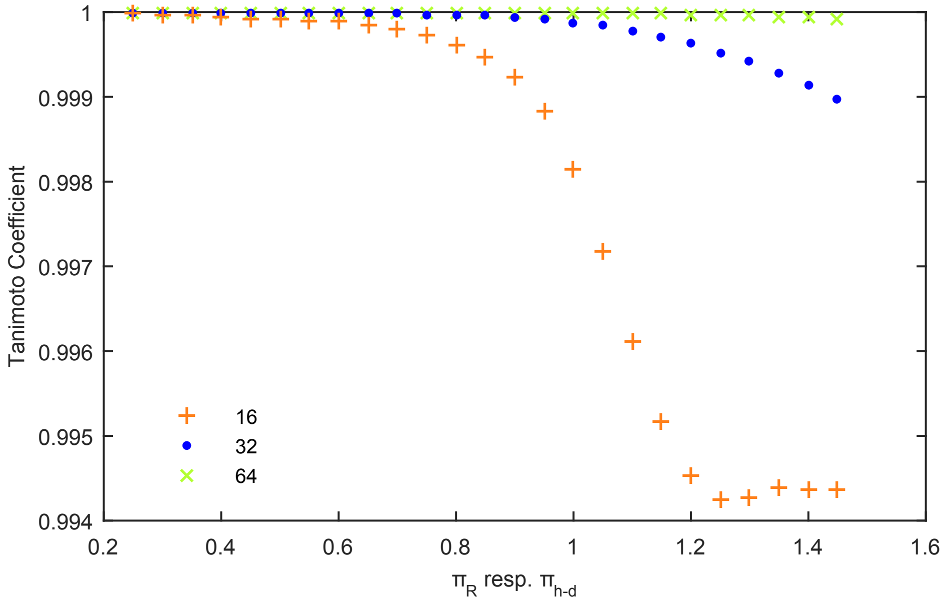

Figure 6.8: Tanimoto coefficient comparing the vector of the dimensionless displacement $\pi_u(\pi_f)$ in dependency on π_R respectively π_{h-d} for different discretizations $N_\varphi = 16$, $N_\varphi = 32$ and $N_\varphi = 64$

In figure 6.8 the influence of the discretization on the quality of the result is clearly visible. The higher the spatial resolution is chosen, the better is the accordance between analytical solution and coupled ITM-FEM approach.

6.3 Verification for different load-displacement combinations

Analogously to the procedure described in the previous sections, the accordance between analytical solution and coupled ITM-FEM solution is evaluated for different loads acting on the system. Additionally to the application of the block load on the surface of the halfspace, it is also applied inside the Finite Element mesh respectively at the layer boundary of the analytical solution. The displacements in x-, y- and z-direction on the surface of the halfspace as well as inside the soil are evaluated. The results of the computations show good accordance of the coupled ITM-FEM solution with the solution of the layered halfspace for all combinations of load and displacement.

6.4 Verification example for the system halfspace with spherical Finite Element structure

Analogously to the verification of the coupled approach for a halfspace with cylindrical Finite Element structure in section 6.2, also the halfspace with spherical inclusion is compared to the analytical solution of a layered halfspace. For this, the Finite Element domain is completely filled with elements possessing the same material parameters as the surrounding soil. An exemplary sketch of the system is shown in figure 6.9.

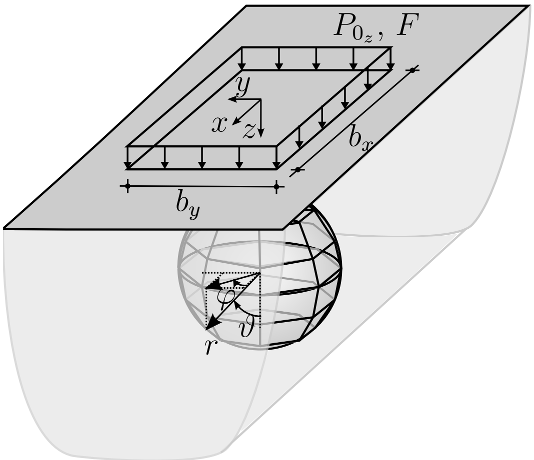

Figure 6.9: Schematic sketch of the coupled spherical ITM-FEM system

The Young's modulus of the material is changed in comparison to the verification example presented for the halfspace coupled to a cylindrical Finite Element mesh. This is done as the verification of the coupled approach shall not be presented again in a dimensionless, extensive form but only selected parameter combinations shall be presented in this section. Therefore, a material is modeled with wave velocities that generate in the frequency range between 1 Hz and 100 Hz wavelengths in the [m] dimension. The material parameters are given in the following table 6.5.

Young's modulus E $\left[\frac{\mathrm{N}}{\mathrm{m}^2}\right]$	Poisson ratio ν $[-]$	Density ρ $\left[\frac{\mathrm{kg}}{\mathrm{m}^3}\right]$	Damping ratio ζ $[-]$
$260 \cdot 10^5 (1 + i \,\mathrm{sign}\,(\omega)\ \zeta)$	0.3	2000	0.1

Table 6.5: Material parameters of the verification of the halfspace with spherical Finite Element structure

With the material defined in table 6.5 wave velocities $c_p = 132\ \frac{\mathrm{m}}{\mathrm{s}}$, $c_s = 71\ \frac{\mathrm{m}}{\mathrm{s}}$ and $c_r = 66\ \frac{\mathrm{m}}{\mathrm{s}}$ are obtained. Thus, with excitation frequencies of $f = 2$ Hz, $f = 20$ Hz and $f = 50$ Hz, wavelengths in the soil are modeled which are given in table 6.6.

	λ_p [m]	λ_s [m]	λ_r [m]
$f = 2$ Hz	66.31	35.44	32.88
$f = 20$ Hz	6.62	3.54	3.28
$f = 50$ Hz	2.65	1.42	1.32

Table 6.6: Wavelengths of the verification example for different frequencies

The radius of the sphere is chosen for the first two calculations with $f = 2$ Hz and $f = 20$ Hz as $R = 1$ m and it is positioned with a depth of the covering $d = 0.5$ m. In the scope of the calculation with $f = 50$ Hz, the radius is reduced to $R = 0.5$ m with $d = 0.25$ m. This is done to achieve a reduced computation time. As the wavelengths are comparably small for $f = 50$ Hz, a high sampling rate is necessary to model them appropriately. For the initial radius of $R = 1$ m this would lead to large computation times. Moreover, as the wavelengths are that small, even with a radius of $R = 0.5$ m it can be ensured that the waves are propagating through the spherical structure so the phenomena for the verification can be examined also with a reduced radius.

A vertical, harmonic block load is applied at the surface of the halfspace with dimensions in x- and y-direction of each $b_x = b_y = 2$ m and an amplitude of $P_{0,z} = 1\ \frac{\mathrm{N}}{\mathrm{m}^2}$. The center of the block load is located at the center of the halfspace surface $(x, y) = (0\ \mathrm{m}, 0\ \mathrm{m})$. The frequency of the load f is varied as mentioned above. Exemplary results are plotted in the figures 6.10. A layered halfspace consisting of two layers with identical material is again used as analytical reference solution analogously to the verification of the halfspace with cylindrical Finite Element structure as depicted in figure 6.1b. The layer boundary is introduced in order to easily evaluate the behavior of the soil in a certain depth. The absolute values and the phases of the vertical displacements are depicted in dependency on the y-coordinate for $x = 0$ each in the frequency domain for $\omega = -2\pi f$.

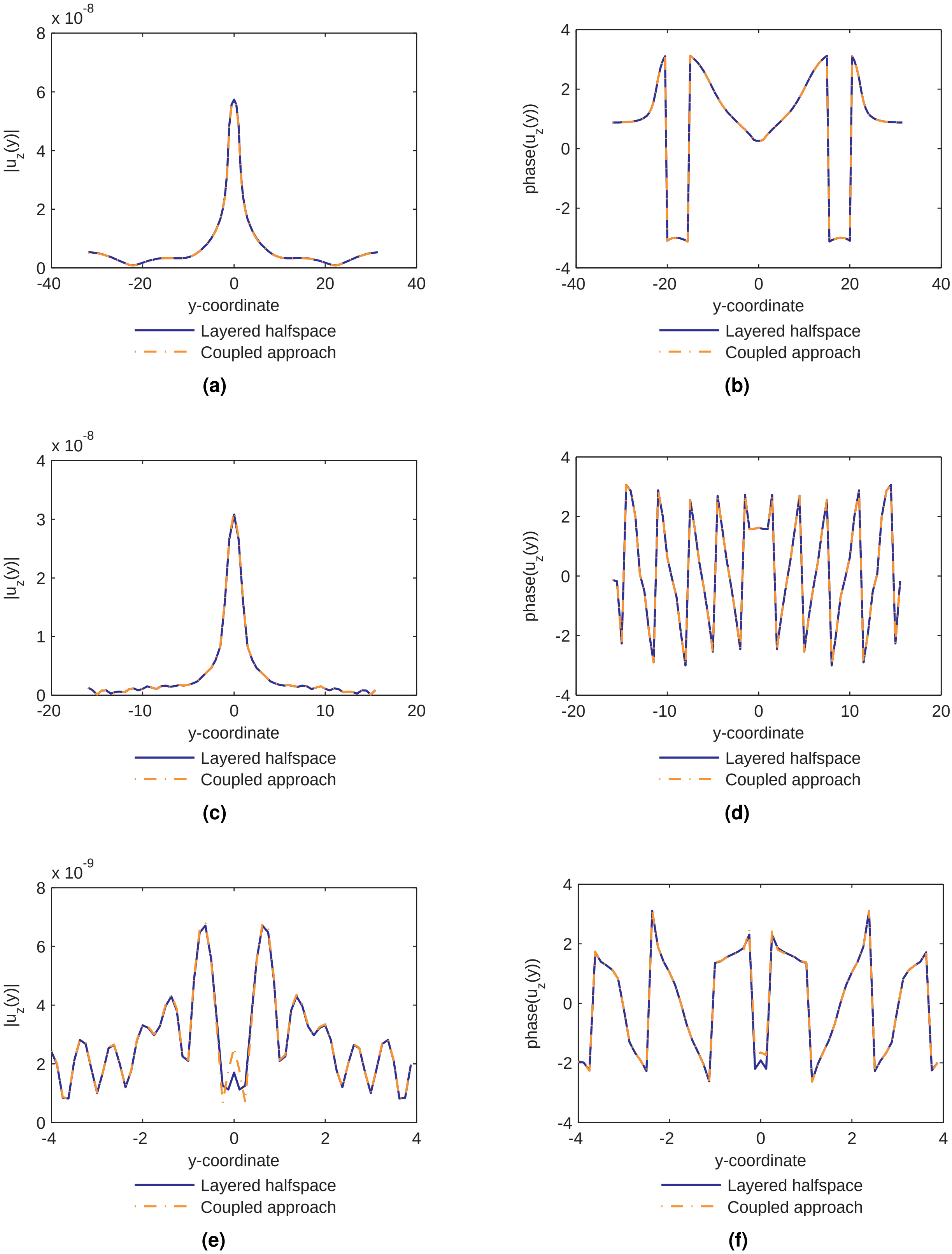

Figure 6.10: Absolute values (left column) and phases (right column) of the vertical displacement on the surface of a halfspace in dependency on the y-coordinate in the frequency domain for $f = 2\ \mathrm{Hz}$ (6.10a, 6.10b), $f = 20\ \mathrm{Hz}$ (6.10c, 6.10d) and $f = 50\ \mathrm{Hz}$ (6.10e, 6.10f)

Interpreting the graphs in figure 6.10 a good accordance between the coupled approach and the analytical solution can be stated. The result of the calculation for $f = 50$ Hz shows an error in the middle of the system around $y = 0$. This can be explained with the discretization error that happens when discretizing the spherical surface with linear polynomials. As the latitudes are not positioned at the poles of the sphere, a small gap is present at the poles. For lower frequencies this gap is too small compared to the wavelengths to influence the accuracy of the result, but for higher frequencies the influence is visible.

A quantitative comparison analogously to the one presented in section 6.2.2 is shown in the following table 6.7. There the maximum values of the vertical displacements on the surface as well as some error measures are given for the different excitation frequencies. All the parameters are obtained by comparing the absolute values of the displacements in the frequency domain for $\omega = -2\pi f$. The maximum error between the analytical solution and the result of the coupled approach as well as the average City-Block metric are calculated on the total surface of the halfspace for all x- and y-coordinates. The given Tanimoto coefficient determines the similarity of the vectors plotted in figure 6.10 for $x = 0$.

Frequency f [Hz]	Maximum value $\lvert u_{z,max}\rvert$ [m]	Maximum error [m]	City-Block average [m]	Tanimoto Coefficient [−]	Computation time [s]
2	$5.73 \cdot 10^{-8}$	$2.01 \cdot 10^{-9}$	$9.42 \cdot 10^{-11}$	0.9998	4880
20	$3.08 \cdot 10^{-8}$	$5.64 \cdot 10^{-11}$	$8.49 \cdot 10^{-12}$	0.9998	1976
50	$1.19 \cdot 10^{-8}$	$3.91 \cdot 10^{-10}$	$2.34 \cdot 10^{-11}$	0.9316	1618

Table 6.7: Comparison of the results for different excitation frequencies

Evaluating the quantitative results of the comparison of the coupled approach and the analytical solution, also a good accordance can be stated in general. The maximum error is small compared to the general level of the displacements and also the City-Block average and the Tanimoto coefficient are rather good.

As visible in table 6.7, the results for $f = 50$ Hz are worse than the results for the lower frequencies. This can be explained by the decrease in the wavelength and the higher discretization that would be necessary to achieve a better accordance. As summarized in table 6.6 the wavelength of the Rayleigh wave is $\lambda_r = 1.3$ m at 50 Hz compared to $\lambda_r = 32.9$ m at 2 Hz. The repetition lengths B_x and B_y of the system are adapted partly to the reduced dimension of the wavelength but still the sampling distance in the y-coordinate is 0.125 m at

50 Hz which means there are roughly 10 elements per wavelength while at 2 Hz with 0.5 m sampling distance in y-direction there are rounded 66 elements per wavelength.

If the modeling of the Finite Element structure is analyzed, the theoretical arc length of one element on the equator of the spherical coupling surface is taken as evaluation parameter for a comparison of the discretization. For both frequencies the sphere is discretized with N_φ elements on the circumference. As the radius of the sphere is 1.0 m at 2 Hz and 0.5 m at 50 Hz, the theoretical arc length of one element on the equator is 0.39 m respectively 0.20 m. Thus at 50 Hz the ratio between the wavelength λ_r and the arc length is 6.5 compared to 84 at $f = 2$ Hz. Thus, the worse accordance of the calculated results at 50 Hz can be explained with a coarser discretization on the halfspace surface as well as on the spherical coupling surface.

Analogously the results inside the soil are compared. The vertical displacements that are calculated with the coupled ITM-FEM approach are calculated at the nodes inside the Finite Element mesh that are positioned at the first latitude below the equator and thus at the widest extension of the sphere. The displacements of the nodes with $x = 0$ are depicted in the figures 6.11 and compared to the displacements of the corresponding points of the layered halfspace. Again the results are plotted as absolute values and phases of the displacements in the frequency domain for $\omega = -2\pi f$.

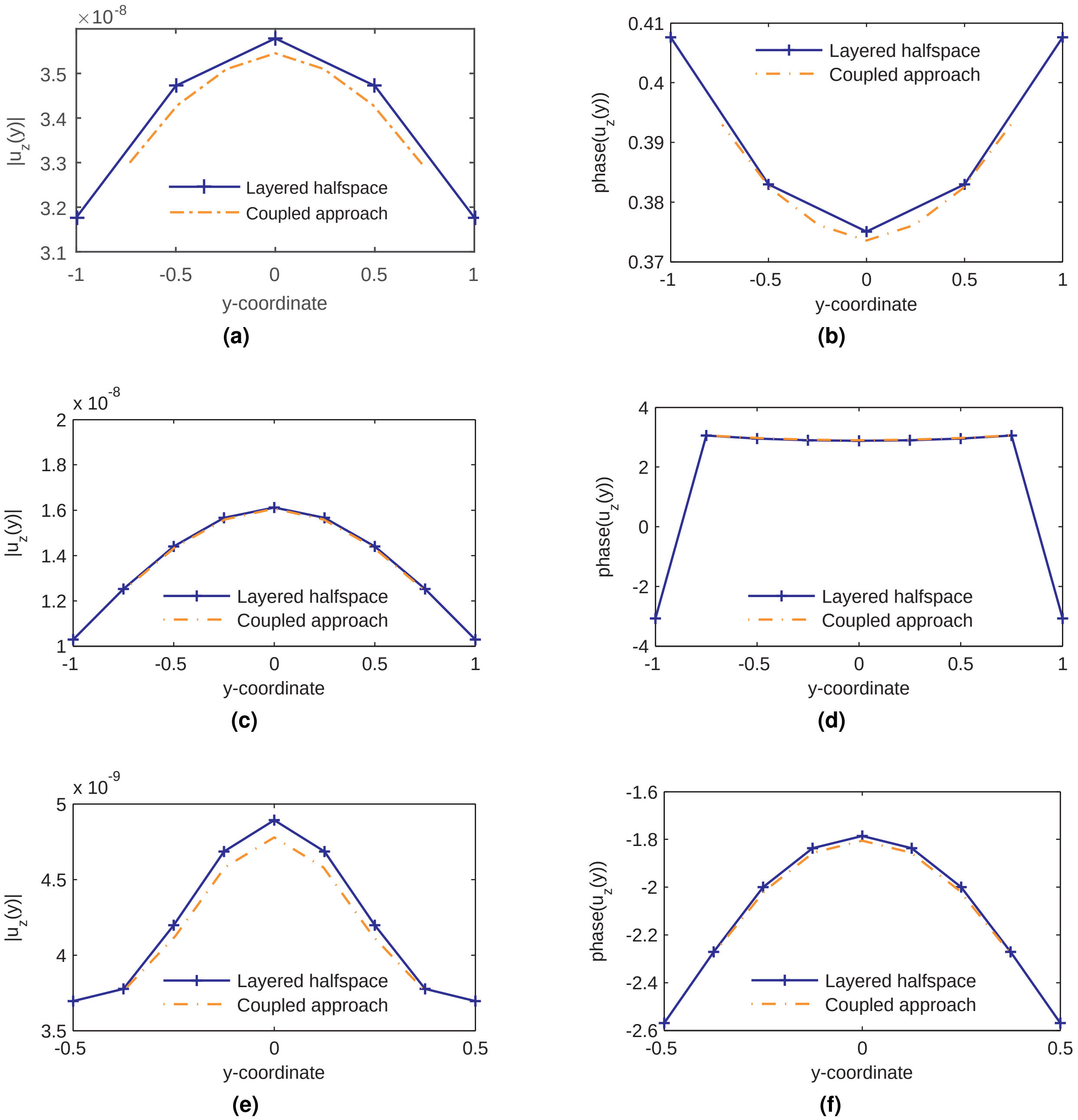

(a) (b) (c) (d) (e) (f)

Figure 6.11: Absolute values (left column) and phases (right column) of the vertical displacement inside the soil at a line at $x = 0$ in dependency on the y-coordinate for $|y| \leq R$ in the frequency domain for $f = 2\,\mathrm{Hz}$ (6.11a, 6.11b), $f = 20\,\mathrm{Hz}$ (6.11c, 6.11d) and $f = 50\,\mathrm{Hz}$ (6.11e, 6.11f)

In general it can be stated that for an excitation of the system on the surface of the halfspace the transmission between ITM substructure and FEM substructure can be modeled appropriately. The accordance between analytical solution and the result of the coupled approach is good, even if it is decreasing with increasing excitation frequency.

7 Numerical examples

7.1 Preliminary remark

In this chapter numerical examples are presented to illustrate the applicability of the method. So the possible implementation of moving loads is presented in section 7.2 and some of the effects that can occur due to moving loads are mentioned. Also the modeling of practically used mitigation measures is examined. The effect of a mass-spring system in a tunnel that is introduced to prevent the excitation of the tunnel and thus the soil itself is modeled in section 7.3. Moreover, the reduction of vibrations due to trenches on the surface to hinder the transmission of vibrations from the point of load application to the receiving structure can be predicted with a coupled ITM-FEM approach as presented in section 7.4.

7.2 Modeling of moving loads in a tunnel

In order to obtain a more realistic model of the load inserted by a train, the harmonic load can be defined as a harmonic block load moving in positive direction of the longitudinal coordinate x of the tunnel with the velocity v by

$$p_{mov}(x,y,t) = p_0(x - vt, y)\ \mathrm{f}(t) \tag{7.1}$$

As derived for example in [Müller 2007], the Fourier transformed of the given load function is

$$\hat{p}_{mov}(k_x,k_y,\omega) = \hat{p}_0(k_x,k_y)\ \hat{\mathrm{f}}(\omega + vk_x) \tag{7.2}$$

Thus, the movement of the load in the original domain leads to a frequency shift in the threefold Fourier transformed domain and the transformed function of the moving load is obtained by calculating the transformed function of the stationary load $\hat{p}_{sta}(k_x,k_y,\bar{\omega}) = \hat{p}_0(k_x,k_y)\ \hat{\mathrm{f}}(\bar{\omega})$

for a wavenumber-dependent shifted frequency $\bar{\omega} = \omega + vk_x$ as already mentioned in [Müller 1989].

$$\hat{p}_{mov}(k_x, k_y, \omega) = \hat{p}_{sta}(k_x, k_y, \omega + vk_x) \tag{7.3}$$

If the stiffness of the modeled system in the transformed domain is labeled as $\hat{K}(k_x, k_y, \omega)$, the displacement due to the moving load can be calculated in the transformed domain as

$$\hat{u}_{mov}(k_x, k_y, \omega) = \frac{\hat{p}_{mov}(k_x, k_y, \omega)}{\hat{K}(k_x, k_y, \omega)} = \frac{\hat{p}_{sta}(k_x, k_y, \omega + vk_x)}{\hat{K}(k_x, k_y, \omega)} \tag{7.4}$$

The displacement in the original domain is obtained after the threefold inverse Fourier transformation.

Equation (7.4) is applied in order to calculate the dynamic response of the system depicted in figure 7.1 to a harmonic block load on the track that oscillates harmonically with an excitation frequency f and is moving along the longitudinal coordinate x of the tunnel with a constant velocity v.

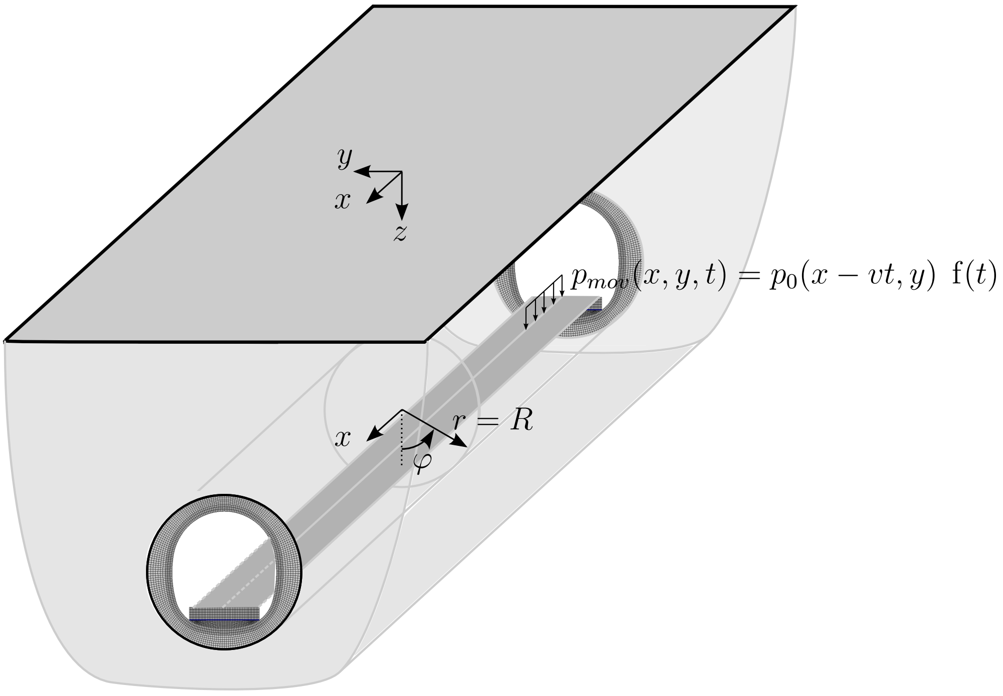

Figure 7.1: Tunnel cross section for the calculation of the displacements on the halfspace surface due to a moving load in the tunnel

The Fourier transformed load $\hat{p}_{mov}(k_x, \omega)$ at the point of the load application is depicted for a stationary load ($v = 0$) and a load moving with a given velocity ($v = V_L$) in the figures 7.2a and 7.2b. As in this specific case the load is applied on a point inside the Finite Element domain, there is no transformation regarding the y-coordinate necessary because the parameters inside the Finite element domain are described in Cartesian coordinates. The wavenumber dependent shift of the frequency is clearly visible in the figures 7.2.

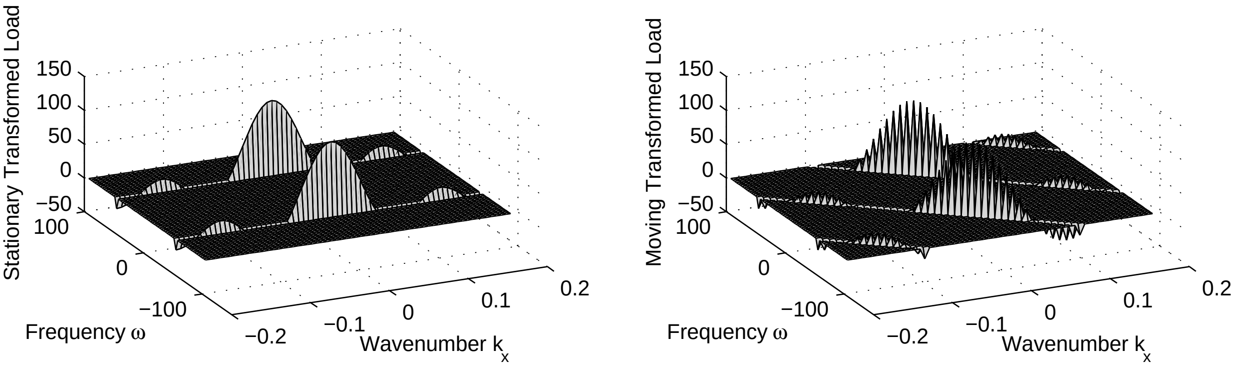

(a) **(b)**

Figure 7.2: Fourier transformed load $\hat{p}_{mov}(k_x, \omega)$ at the middle of the track for $v = 0$ (7.2a) and $v = V_L$ (7.2b)

The vertical displacement $u(x, y, t)$ on the surface of the halfspace due to the harmonic, moving load on the track is calculated in the original domain for different velocities of the load. As expected, the response of the system changes in dependency on the velocity of the load v. [Krylov 1995] and [Sheng et al 1999] for example examined a change in the dynamic behavior of the response if the velocity of the load reaches the propagation velocities of the Rayleigh wave inside the soil which can be approximated as

$$c_r = \frac{0.87 + 1.12\ \nu}{1 + \nu} c_s \tag{7.5}$$

according to [Viktorov 1967] for example. [Dieterman and Metrikine 1996] analyzed the analytical solution for a beam on a halfspace and identified two critical velocities if a uniformly moving load is applied on the beam. The first critical velocity is equal to the Rayleigh wave velocity c_r. The second critical velocity lies below this value, but for realistic parameters of the material and geometry of the system, is rather close to c_r, so for practical applications the assumption of one critical velocity at the Rayleigh wave velocity can be used. One year later, [Dieterman and Metrikine 1997] also examined the critical velocities of an elastic layer that is loaded with a harmonic, moving load. For this system, they identified the group velocity of the waves that arise due to the load, as the critical velocity. In dependency on the system-dependent critical velocity, the characteristics of the solution changes.

Therefore, the system depicted in figure 7.1 is solved with the coupled ITM-FEM approach for a harmonic block load with the length $b_x = 12.5$ m applied in the middle of the track. The radius of the circular coupling surface is chosen as $r = 4.5$ m and the tunnel is positioned with a covering of $d = 4.5$ m as well. The load is harmonically oscillating with a frequency $f = 10$ Hz and moves with different velocities along the longitudinal coordinate of the tunnel. The calculations are performed for two different kind of soils with different Rayleigh wave velocities to illustrate the behavior of the response. The material parameters as well as the respective Rayleigh wave velocities are presented in table 7.1. For both types of soil, the Young's modulus is chosen smaller than the value used in the verification examples. This is due to the fact that the Rayleigh wave velocity of the soil presented in table 7.2 is $c_r = 208\ \frac{\text{m}}{\text{s}}$. As the maximum train speed lies currently at $v_{max} = 575\ \frac{\text{km}}{\text{h}} = 160\ \frac{\text{m}}{\text{s}}$ for trains running on wheels according to [Werske 2013], only in softer soil with smaller Rayleigh wave velocities the train speed exceeds the Rayleigh wave velocity.

	Young's modulus $E\ \left[\frac{\text{N}}{\text{m}^2}\right]$	Poisson ratio $\nu\ [-]$	Density $\rho\ \left[\frac{\text{kg}}{\text{m}^3}\right]$	Damping ratio $\zeta\ [-]$	Rayleigh wave velocity $c_r\ \left[\frac{\text{m}}{\text{s}}\right]$
Soil 1	$60 \cdot 10^6(1 + i\,\text{sign}\,(\omega)\ \zeta)$	0.3	2000	0.10	99.8
Soil 2	$10 \cdot 10^6(1 + i\,\text{sign}\,(\omega)\ \zeta)$	0.3	2000	0.10	40.7
Concrete	$34 \cdot 10^9(1 + i\,\text{sign}\,(\omega)\ \zeta)$	0.2	2600	0.10	-
Elastic Layer	$0.9 \cdot 10^6(1 + i\,\text{sign}\,(\omega)\ \zeta)$	0.3	620	0.07	-

Table 7.1: Material parameters of the system depicted in figure 7.1

In figure 7.3, the vertical displacements on the halfspace surface due to a moving load in the tunnel are depicted for different velocities v of the load.

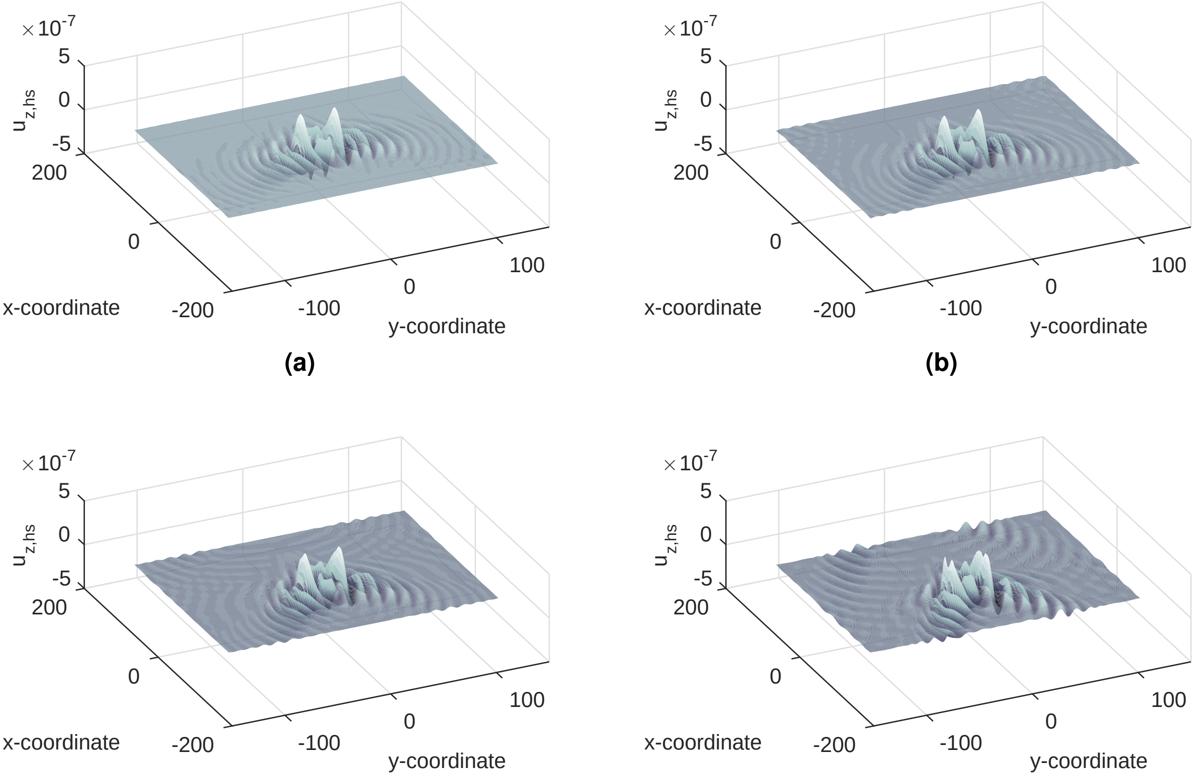

(a) (b) (c) (d)

Figure 7.3: Vertical displacement on the surface of a halfspace with soil material 1 due to a harmonic, moving load in the tunnel for $v = 32\ \frac{\mathrm{m}}{\mathrm{s}}$ (7.3a), $v = 64\ \frac{\mathrm{m}}{\mathrm{s}}$ (7.3b), $v = 96\ \frac{\mathrm{m}}{\mathrm{s}}$ (7.3c), and $v = 160\ \frac{\mathrm{m}}{\mathrm{s}}$ (7.3d)

As clearly visible, the characteristics of the response changes with increasing velocity of the load. While at low velocities the propagation of the waves on the surface is still roughly circular, a concentration of the displacements is visible for higher velocities. If the velocity of the load exceeds the critical velocity of the system, which, as mentioned, can be identified as the Rayleigh wave velocity, radiation effects can be observed. The load is moving faster than the waves can propagate in the medium, a similar effect as Mach radiation of shock waves generated by supersonic jets or the Cherenkov radiation of light induced by electrons that are moving with higher velocities than the speed of light as mentioned in [Krylov 1995]. The angle of this spatial cone that is developing is depending on the ratio of the velocities as

$$\theta = \arccos\left(\frac{c_r}{v}\right) \tag{7.6}$$

as derived in [Krylov 1995].

The spatial concentration of the displacements on the halfspace surface also leads to a numerical artifact that can be observed in the figures 7.3c and 7.3d. Due to the discrete Fourier transformation that is applied concerning the spatial and time coordinates $x \circ\!\!-\!\!\!-\!\!\bullet\ k_x$, $y \circ\!\!-\!\!\!-\!\!\bullet\ k_y$ and $t \circ\!\!-\!\!\!-\!\!\bullet\ \omega$, a repetition of the signals occurs as presented in appendix A.1.2. As the discretization is necessary in the original as well as in the transformed domain, also repetitions cannot be avoided in both domains. In case of the load that is moving with high velocity, the concentration of the displacements leads to the phenomenon that the oscillations do not decay completely between the point of load application and end of the sampled region with a repetition length of 256 m. Thus, displacements that are induced by a repeated load in the neighboring repetition are visible in the figures 7.3c and 7.3d for positive values of the x-coordinate. If these oscillations shall be avoided, a bigger repetition length can be chosen.

The figures 7.4 display the results of the second soil with a velocity of the Rayleigh wave $c_r = 40.7\ \frac{\mathrm{m}}{\mathrm{s}}$. Again the displacements on the halfspace surface are plotted for different velocities of the load. The cone that is formed for high velocities is also visible for soil 2.

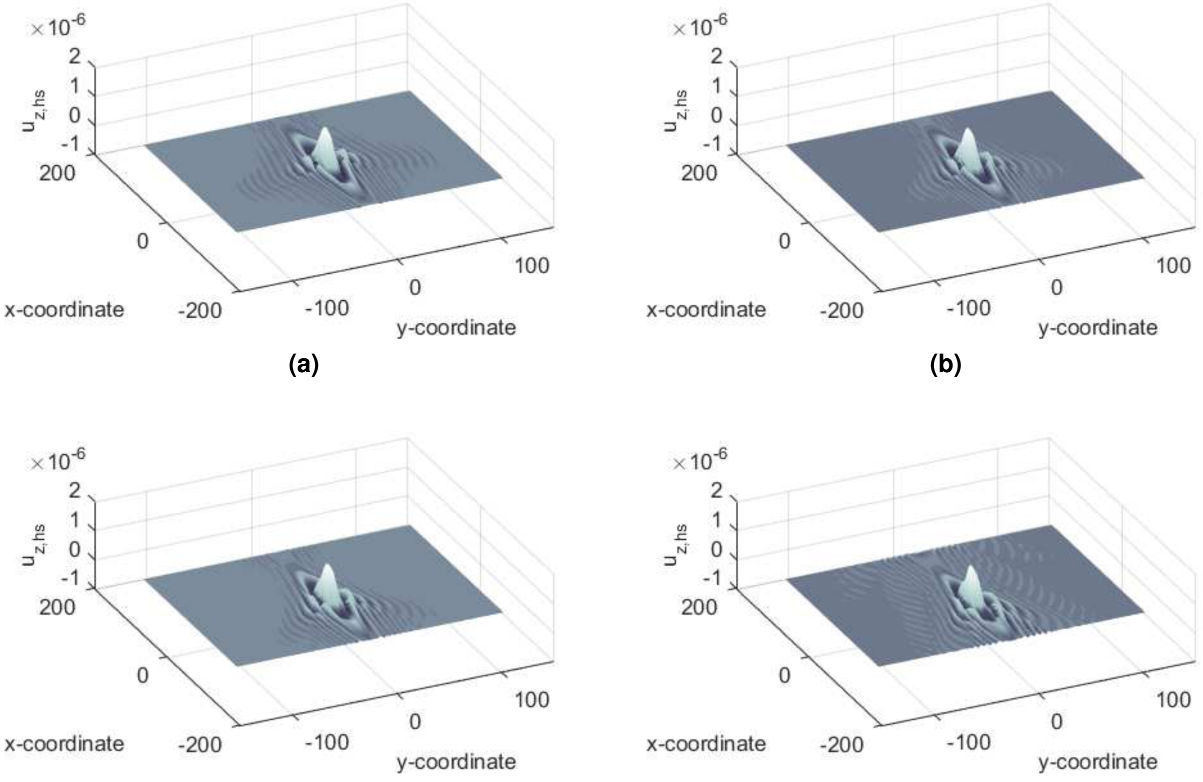

(a)

(b)

(c)

(d)

Figure 7.4: Vertical displacement on the surface of a halfspace with soil material 2 due to a harmonic, moving load in the tunnel for $v = 32\ \frac{\mathrm{m}}{\mathrm{s}}$ (7.4a), $v = 64\ \frac{\mathrm{m}}{\mathrm{s}}$ (7.4b), $v = 96\ \frac{\mathrm{m}}{\mathrm{s}}$ (7.4c), and $v = 160\ \frac{\mathrm{m}}{\mathrm{s}}$ (7.4d)

As the Rayleigh wave velocity of soil 2 is lower than the one of soil 1, the cone is formed at a lower velocity of the load. Thus, the phenomena due to moving loads on the surface of a halfspace can also be observed for a load that is applied in a tunnel. In further studies the effects of layers in the soil or the depth of the tunnel can be examined.

7.3 Insertion loss of a mass-spring system

A possible application of the coupled ITM-FEM approach to assess the effects of mitigation measures for vibrations is presented in this section. An exemplary tunnel cross section is modeled inside the Finite Element mesh analogously to [Müller 2015] as depicted in figure 7.5. As one possible measure to reduce the vibrations caused by trains in tunnels, elastic layers can be inserted between track and tunnel thus creating a mass-spring system in the tunnel where the load is applied. The effectiveness of such a mass-spring system can be predicted by a numerical model as presented in this section where the displacements on the surface of the halfspace are compared for the situation with and without elastic layer between track and tunnel.

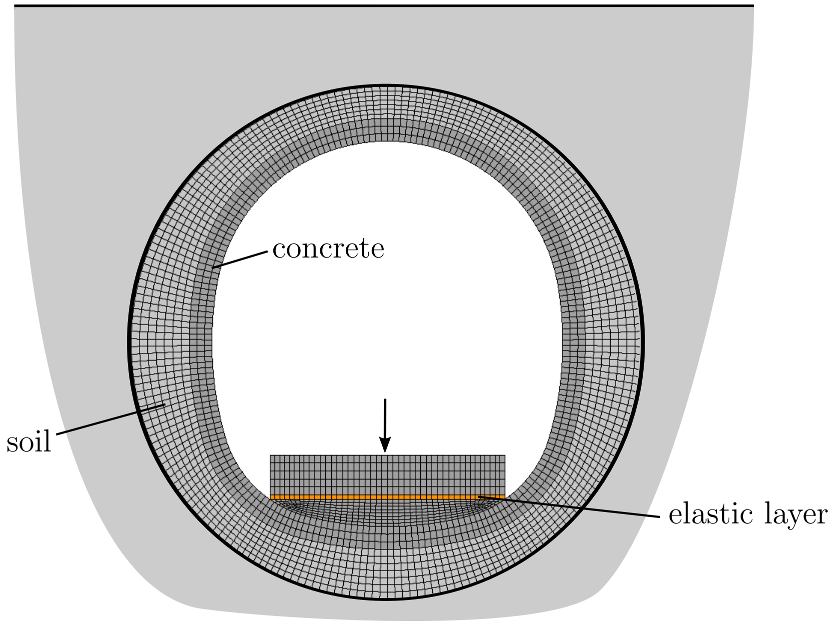

Figure 7.5: Tunnel cross section for the calculation of the insertion loss of a mass-spring system with complete bedding of the elastic layer

The elements displayed in dark gray are modeled with material parameters of concrete, whereas the material parameters of the soil are assigned to the elements illustrated in light gray. The orange colored elements are modeled in a reference configuration as concrete elements and in the model configuration as an elastic layer thus creating a mass-spring system with the elastic layer as spring and the concrete block above representing the mass. Using these two different constellations, the insertion loss of the mass-spring system is calculated. The material parameters are summarized in table 7.2.

	Young's modulus $E\ \left[\frac{\mathrm{N}}{\mathrm{m}^2}\right]$	Poisson ratio $\nu\ [-]$	Density $\rho\ \left[\frac{\mathrm{kg}}{\mathrm{m}^3}\right]$	Damping ratio $\zeta\ [-]$
Soil	$260 \cdot 10^6 (1 + i\,\mathrm{sign}\,(\omega)\ \zeta)$	0.3	2000	0.10
Concrete	$34 \cdot 10^9 (1 + i\,\mathrm{sign}\,(\omega)\ \zeta)$	0.2	2600	0.10
Elastic Layer	$0.9 \cdot 10^6 (1 + i\,\mathrm{sign}\,(\omega)\ \zeta)$	0.3	620	0.07

Table 7.2: Material parameters of the system depicted in figure 7.5

For the calculations, the radius of the circular coupling surface is chosen as $r = 4.5$ m and the tunnel is positioned with a covering of $d = 4.5$ m as well. A harmonically oscillating load is applied in the middle of the concrete block. The maximum vertical displacements are determined at the point of load application and in the central point on the surface of the halfspace. The frequency of the load is varied between 2 Hz and 100 Hz in steps of 2 Hz.

In figure 7.6 the maximum vertical displacements are depicted in dependency on the varied frequency for a configuration both with and without elastic layer. Figure 7.6a illustrates the maximum vertical displacements on the point of load application, figure 7.6b contains the results on the halfspace surface at the center point of the surface.

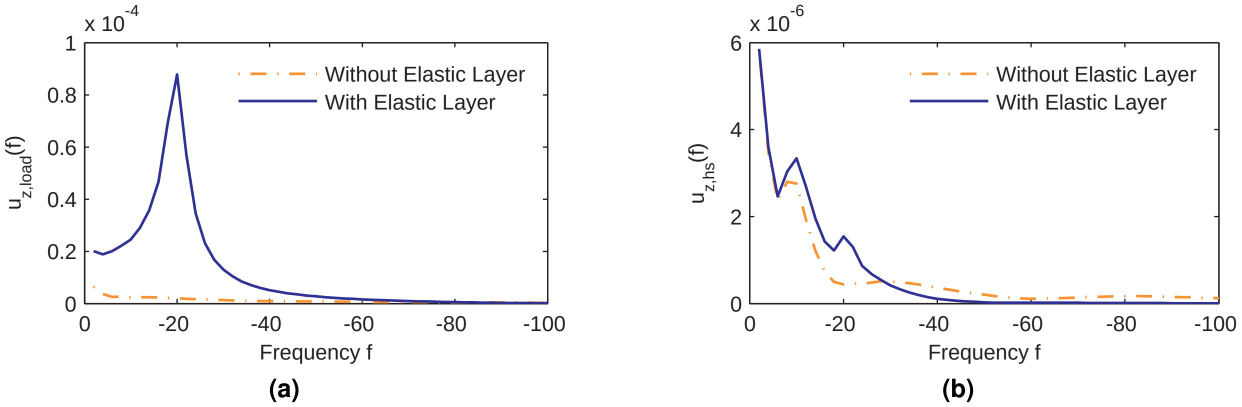

Figure 7.6: Maximum vertical displacement at the point of load application (7.6a) and at the center point of the halfspace surface (7.6b) in dependency on the frequency of the applied harmonic load

As depicted in figure 7.6a, the installation of the elastic layer leads to increased displacements at the point of load application. Here, the eigenfrequency of the established mass-spring system is clearly visible at a frequency of 20 Hz. This also corresponds to an estimation based on modeling the mass-spring system as Single-Degree-of-Freedom system. Interpreting the results on the halfspace surface in figure 7.6b, an increase of the displacements in the low-frequency range due to the insertion of the elastic layer has to be stated. The desired reduction of the displacements can be observed in the frequency range above a critical value of 28 Hz. This corresponds approximately to the $\sqrt{2}$-fold value of the eigenfrequency of the mass-spring system as it is also mentioned in a variety of textbooks, as [Zeller 2012] for example. For each frequency step the insertion loss R is calculated in [dB] comparing the vertical displacements directly above the point of load application on the surface of the halfspace $u_{z,hs}$ of the reference configuration and the model configuration according to

$$R = 20\lg\left(\frac{u_{z,hs,reference}}{u_{z,hs,model}}\right) \tag{7.7}$$

The insertion loss calculated according to equation (7.7) is presented in figure 7.7.

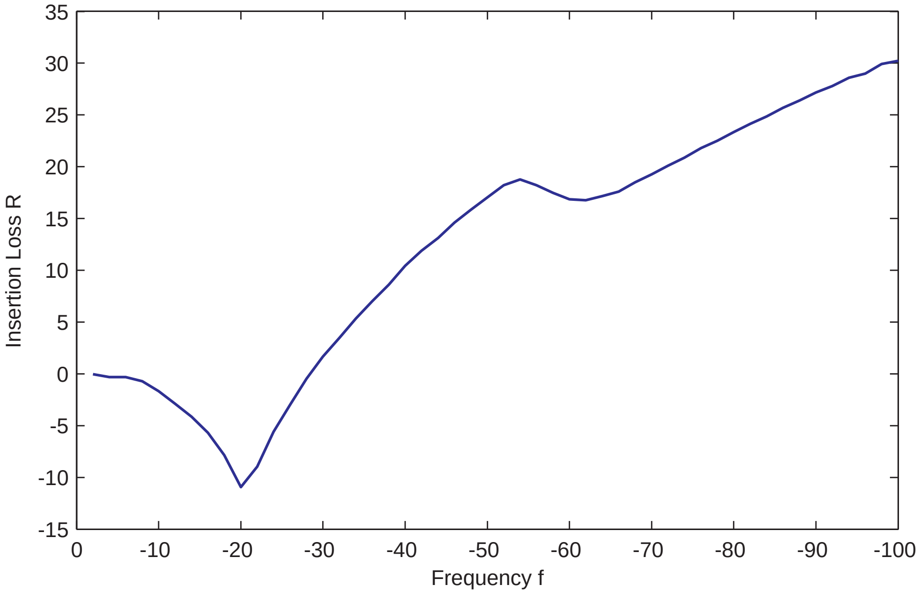

Figure 7.7: Insertion loss

The reduction of the vibrations on the surface of the halfspace above the mentioned critical value is also visible in this figure. A comparison of the general characteristics of the calculated insertion loss with measured graphs that are published in the literature yields similar behavior. In [Müller and Möser 2004] the insertion loss of an elastic mount of a train track is measured. Analogously to the result depicted in figure 7.7, the displacements are increased in the low-frequency range and the eigenfrequency of the mass-spring system is visible at the peak of the insertion loss with a negative value. Above the critical value, the insertion loss takes positive values. In [Müller and Möser 2004] a decline of the insertion loss is mentioned at the π-fold value of the eigenfrequency of the mass-spring system. This decline can also be seen in figure 7.7 where the π-fold value of the eigenfrequency can be calculated as 62.8 Hz.

As a second alternative the elastic layer can also be mounted in stripes instead of a complete bedding. According to manufacturer specifications, this will lead to a better reduction of the structure-borne sound (for example see [Getzner Werkstoffe GmbH 2015]). This effect can be explained as the installation of the elastic layer not on the complete area between track and tunnel leads to a reduced stiffness of the spring component due to the air that is enclosed between the stripes of elastic layers. Thus, a lower eigenfrequency of the mass-spring system is obtained and the elastic layer is efficient at lower frequencies. Therefore, as a second model the elastic layer will only be installed in two stripes under the concrete block as depicted in figure 7.8 and the displacements on the surface of the halfspace are calculated.

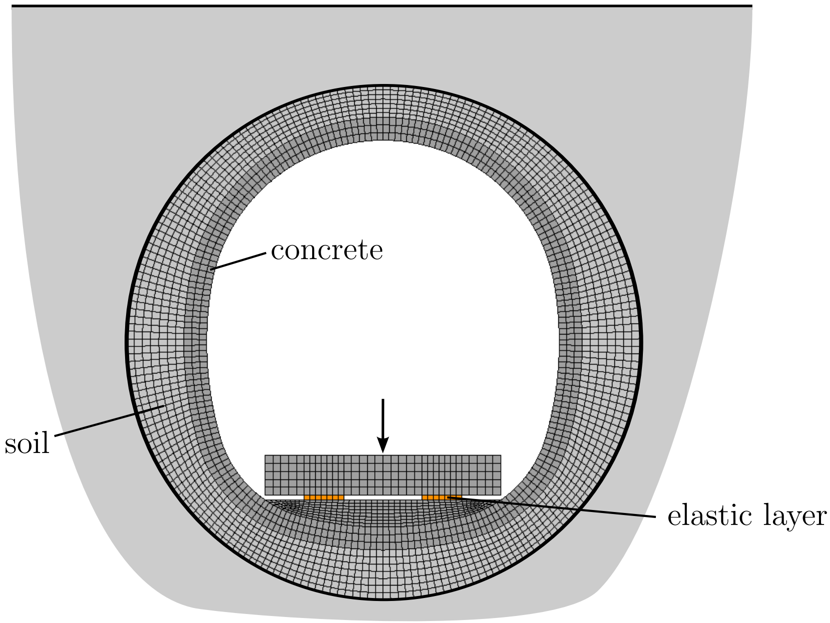

Figure 7.8: Tunnel cross section for the calculation of the insertion loss of a mass-spring system with striped mount of the elastic layer

The insertion loss of the striped elastic layer is depicted in figure 7.9 together with the result already presented in figure 7.7.

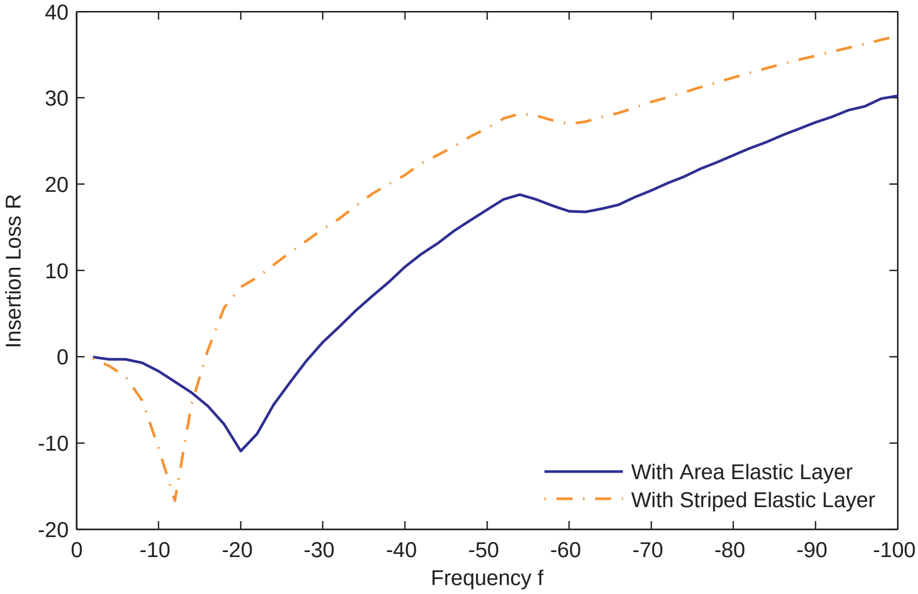

Figure 7.9: Insertion loss

As expected, a reduced eigenfrequency of the striped mass-spring system compared to the complete bedding can be stated as well as an efficiency of the elastic layer at lower frequencies. Thus, if identical materials are installed as complete bedding or as striped elastic layers, the second alternative leads to reduced vibration levels on the surface of the halfspace.

Concluding, it can be stated that the effects of installing a mass-spring system in an underground tunnel can also be modeled for different installation situations and material parameters using the coupled ITM-FEM approach. Thus, different alternatives can be analyzed and compared. The results can afterwards be evaluated as decision supports for the installation in a real structure.

7.4 Reduction of vibrations by trenches

Another possibility to reduce the vibrations on the halfspace surface besides measures directly at the source as presented in the preceding section 7.3 are mitigation measures regarding the transmission of vibrations between source and receiver. These can be inserted if it is necessary to improve existing railway lines where measures at the track or the receiving buildings are not feasible. According to VDI 2038-2 [VDI 2013], different measures in the transmission path like cutting, trenches or soil compaction for example are possible. In this section, the effect of a trench on the halfspace surface is regarded. As presented in figure 7.10, the trench is modeled as an infinite element which is positioned next to a vertical block load that is applied at the halfspace surface. The displacements on the surface of the halfspace are compared for a situation with and without trench.

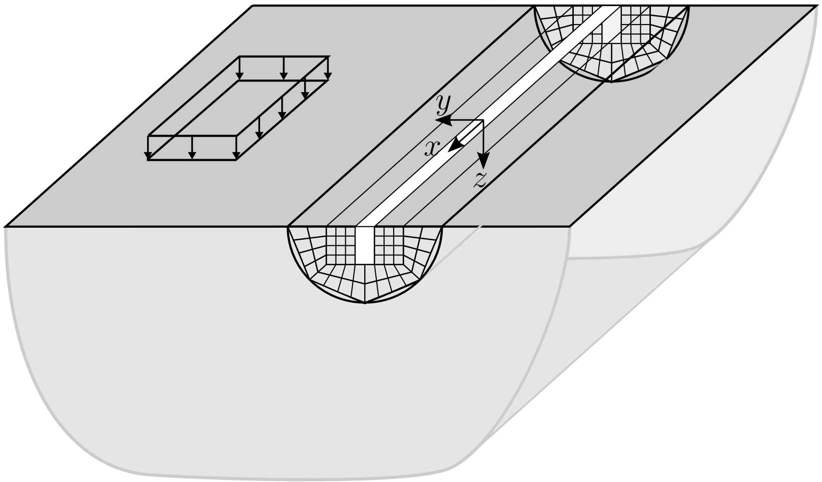

Figure 7.10: Sketch of a system for vibration reduction by a trench on the halfspace surface in the transmission path

To model the trench on the surface, the Finite Element mesh has to be positioned on the surface of the halfspace. Therefore, the ITM solution of the halfspace with cylindrical cavity requires the superposition of a halfspace and a fullspace with cylindrical cavity where the virtual surfaces intersect with the real surfaces. For example in the system of a halfspace the cylindrical virtual surface $\delta\Gamma$ is introduced as presented in section 3.2. In contrast to the system depicted in figure 3.2, now a part of the virtual surface $\delta\Gamma$ is located above the halfspace surface Λ as it is depicted in figure 7.11. Analogously also the surfaces in the system fullspace with cylindrical cavity are intersecting as can be seen in figure 7.12.

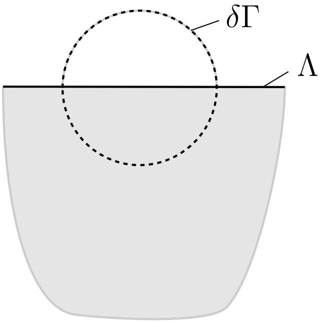

Figure 7.11: Halfspace with intersecting real surface Λ and virtual surface $\delta\Gamma$

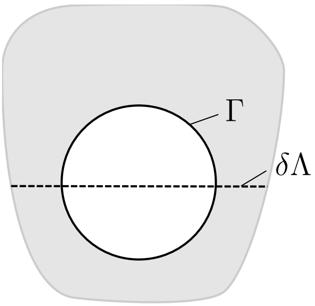

Figure 7.12: Fullspace with intersecting real surface Γ and virtual surface $\delta\Lambda$

The resulting stresses are calculated on the part of the virtual surfaces that are positioned inside the fundamental systems. At the positions where the virtual surface is not part of the fundamental system the vector of the stress components contains zero elements. The extension of a signal with zero elements is often called zero-padding. According to [Meyer 2009] for example it is used intentionally in order to increase the resolution in the transformed domain according to the rules of the discrete Fourier transformation as presented in section A.1.2. Still, a verification of the halfspace with half-cylindrical Finite Element mesh is recommended to check that there are no artifacts arising due to the changed system and also to check if the square cut of the cylinder directly in the middle leads to numerical problems. Thus the solution of the halfspace with half-cylindrical cavity at the surface of the halfspace is derived and coupled to the respective stiffness terms of a Finite Element system with the appropriate coupling surface as depicted in figure 7.13.

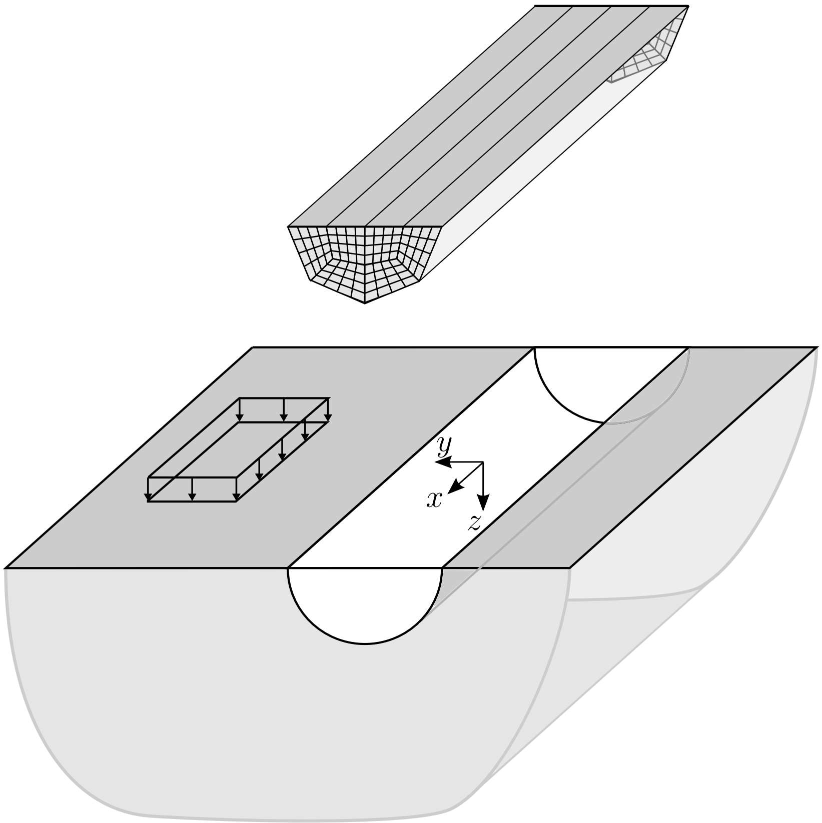

Figure 7.13: Coupling of a halfspace with half-cylindrical trench on the surface and a half-cylindrical Finite Element mesh

The coupling on the half-cylindrical coupling surface is verified for different load-material combinations analogously to the procedure described in section 6.2. Thus, the Finite Element domain is discretized by elements possessing the same material parameters as the surrounding soil and the result is compared to the analytical solution of the homogeneous halfspace. As the verification will be presented for one material that is excited with different frequencies, the Young's modulus of the material is changed compared to the one specified in table 6.1. The new material parameters are defined in table 7.3.

Young's modulus E $\left[\frac{\mathrm{N}}{\mathrm{m}^2}\right]$	Poisson ratio ν $[-]$	Density ρ $\left[\frac{\mathrm{kg}}{\mathrm{m}^3}\right]$	Damping ratio ζ $[-]$
$260 \cdot 10^5 (1 + i \operatorname{sign}(\omega)\ \zeta)$	0.3	2000	0.1

Table 7.3: Material parameters of the verification of the halfspace with half-cylindrical Finite Element structure on the surface of the halfspace

Due to the change of the Young's modulus, wave velocities $c_p = 132\ \frac{\mathrm{m}}{\mathrm{s}}$, $c_s = 71\ \frac{\mathrm{m}}{\mathrm{s}}$ and $c_r = 66\ \frac{\mathrm{m}}{\mathrm{s}}$ are obtained, which, in combination with excitation frequencies in the interesting frequency range, lead to waves with wavelengths that are significantly influenced by the half-cylinder. The radius of the half-cylinder is chosen as $R = 2$ m and it is positioned such that exactly half the cylinder lies inside the soil ($h = R + d = 0$ m). The amplitude of the vertical harmonic block load is $P_{0,z} = 1\ \frac{\mathrm{N}}{\mathrm{m}^2}$ and the widths of the block in x- and y-direction are $b_x = b_y = 2$ m, with the center of the block located at $(x, y) = (0\ \mathrm{m}, -4\ \mathrm{m})$. The frequency of the load f is varied between $f = 2$ Hz, $f = 20$ Hz and $f = 100$ Hz. Exemplary results are plotted in the figures 7.14 with the results of the homogeneous halfspace as analytical reference solution. The absolute values of the vertical displacements are depicted in dependency on the x-coordinate for $y = 0$ respectively in dependency on the y-coordinate for $x = 0$ each in the frequency domain for $\omega = -2\pi f$.

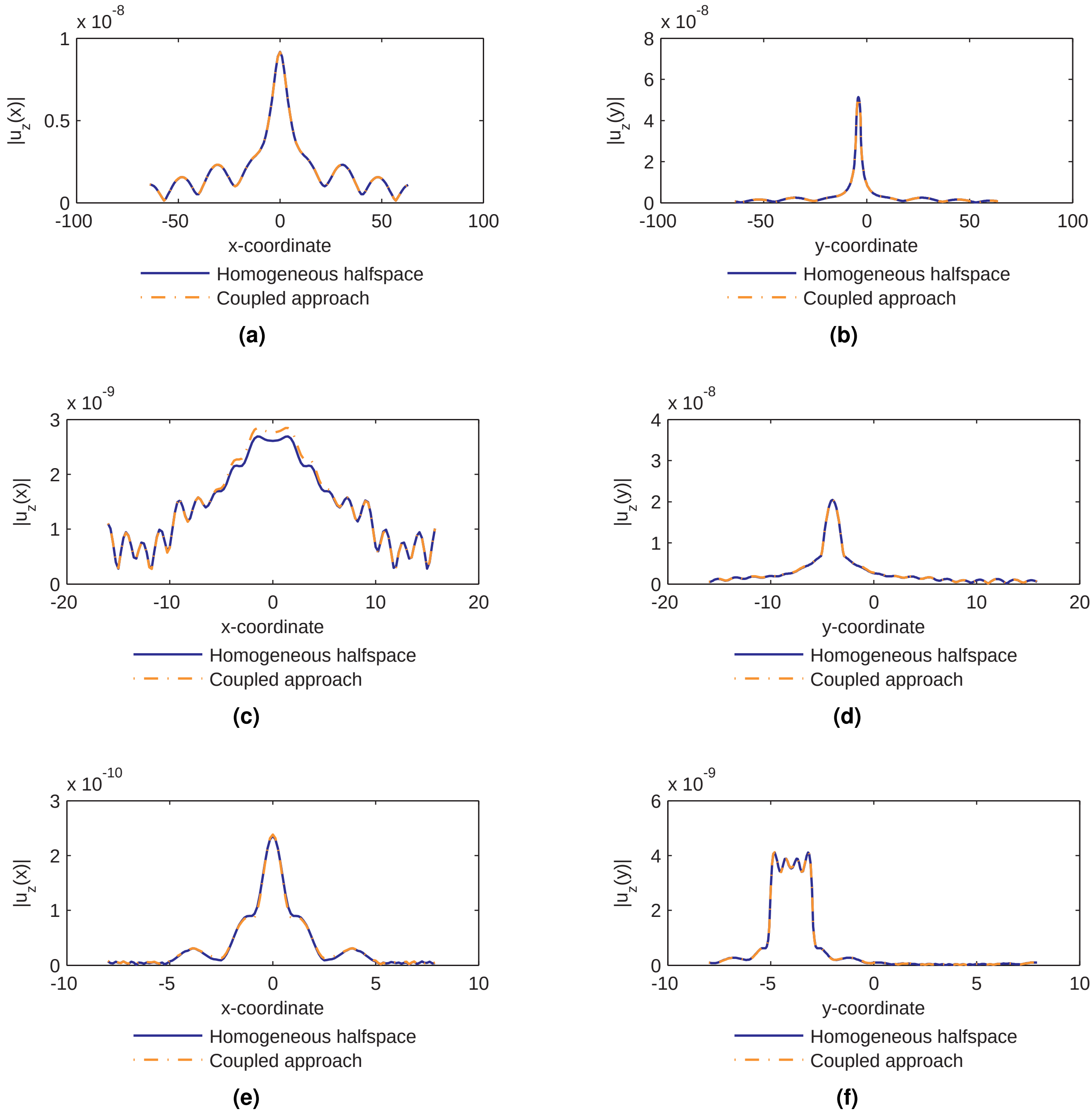

(a) (b) (c) (d) (e) (f)

Figure 7.14: Absolute values of the vertical displacement on the surface of the halfspace for the verification of the halfspace with half-cylindrical Finite Element structure in dependency on the x-coordinate $|u_z(x)|$ at $y = 0$ (left column) and on the y-coordinate $|u_z(y)|$ at $x = 0$ (right column) in the frequency domain for $f = 2\ \mathrm{Hz}$ (7.14a, 7.14b), $f = 20\ \mathrm{Hz}$ (7.14c, 7.14d) and $f = 100\ \mathrm{Hz}$ (7.14e, 7.14f)

For a quantitative comparison, several parameters are summarized in the following table 7.4. The maximum analytical value of the vertical displacement at $x = 0$ at the halfspace surface $u_{z,max}(x = 0, y, \omega = -2\pi f)$ is given as well as the maximum error that is stated at the halfspace surface for $\omega = -2\pi f$. The City-Block average contains the average difference between the analytical solution and the result of the coupled approach on all points of the halfspace surface for $\omega = -2\pi f$. As the minimum Tanimoto coefficient characterizes the similarity between two vectors and the repetition lengths in x- and y-direction B_x and B_y are changed in dependency on the frequency to adapt them to the corresponding wavelengths, the Tanimoto coefficient is calculated for this verification example for the points which are positioned at $|y| < R$. The Tanimoto coefficient is calculated for $\omega = -2\pi f$ and for all values of x and the minimum value is presented in table 7.4.

Frequency f [Hz]	Maximum value $u_{z,max}$ [m]	Maximum error [m]	City-Block average [m]	Minimum Tanimoto [$-$]	Computation time [s]
2	$4.98 \cdot 10^{-8} - 1.25 \cdot 10^{-8}\, i$	$2.21 \cdot 10^{-10} - 3.25 \cdot 10^{-11}\, i$	$2.42 \cdot 10^{-12}$	0.9999	421
20	$4.43 \cdot 10^{-9} + 2.91 \cdot 10^{-8}\, i$	$3.52 \cdot 10^{-10} - 3.88 \cdot 10^{-10}$	$2.17 \cdot 10^{-11}$	0.9977	2484
100	$1.40 \cdot 10^{-9} + 3.93 \cdot 10^{-9}\, i$	$1.27 \cdot 10^{-10} + 8.13 \cdot 10^{-12}\, i$	$1.93 \cdot 10^{-12}$	0.9838	132415

Table 7.4: Comparison of the quality of the results in dependency on the different excitation frequencies for the system depicted in figure 7.13

Interpreting the values of table 7.4, a good accordance of the coupled approach with the analytical solution can be stated. Clearly visible is the considerable increase in the computation time with the frequency. This is due to the fact, that the dimensions of the load block require a minimum repetition length even if the wavelengths are small ($\lambda_p = 1.32$ m, $\lambda_s = 0.71$ m and $\lambda_r = 0.66$ m for $f = 100$ Hz), but the discretization has to be fine enough to be able to model the wave propagation properly. For high frequencies this leads in this verification example to long computation times.

Additionally, the vertical harmonic load is applied inside the Finite Element domain and the vertical displacements on the surface of the halfspace are compared to the result of a homogeneous halfspace. The system is exemplarily sketched in figure 7.15.

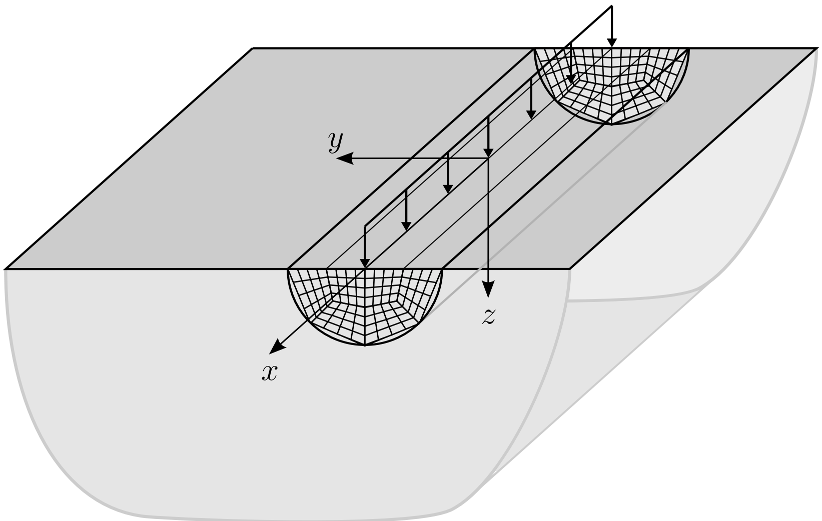

Figure 7.15: Coupling of a halfspace with half-cylindrical trench on the surface and a half-cylindrical Finite Element mesh with the load application inside the Finite Element mesh

The material is defined by the parameters mentioned in table 7.3 and also the radius of the cylinder and the position of the center of the cylinder are not changed ($R = 2$ m, $h = 0$ m). The excitation frequencies are varied again between $f = 2$ Hz, $f = 20$ Hz and $f = 100$ Hz, but the load is now applied on a line at $y = 0$ as depicted in figure 7.15 in order to check if the transmission of vibrations from the Finite Element domain into the Integral Transform domain is modeled properly.

Analogously to the previous explanations, the absolute values of the vertical displacements on the halfspace surface are plotted in dependency on the y-coordinate in the figures 7.16. The results of the analytical calculation and the coupled ITM-FEM approach show a good accordance for all the chosen excitation frequencies. The transmission of the arising vibrations due to the excitation within the Finite Element domain into the Integral Transform domain is visible in the results.

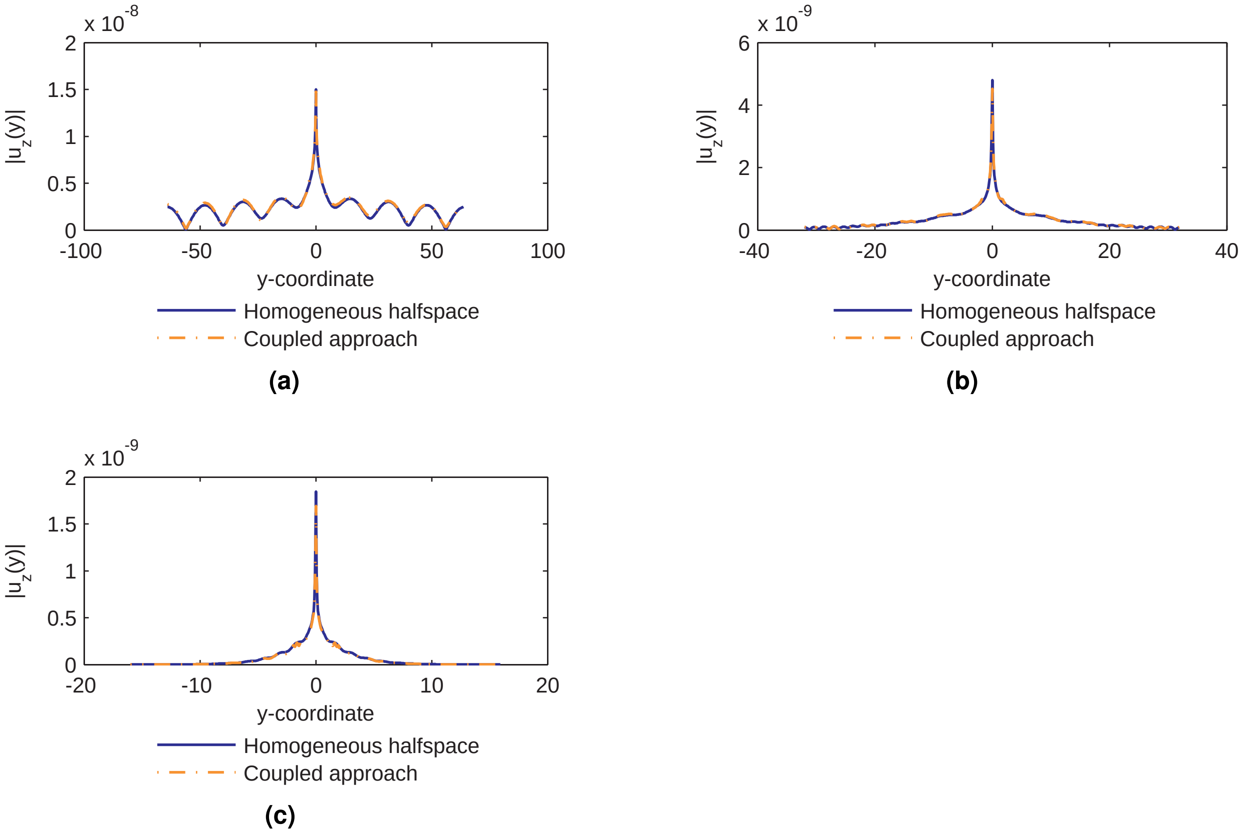

(a) **(b)** **(c)**

Figure 7.16: Absolute values of the vertical displacement on the surface of a halfspace in dependency on the y-coordinate $|u_z(y)|$ in the frequency domain for $f = 2$ Hz (7.16a), $f = 20$ Hz (7.16b) and $f = 100$ Hz (7.16c)

The results of the quantitative comparison are contained in table 7.5. Again a good accordance can be stated and the solution of a halfspace with half-cylindrical cavity coupled to a Finite Element structure is used to assess the effect of an open trench on the surface.

Frequency f [Hz]	Maximum value $u_{z,max}$ [m]	Maximum error d [m]	City-Block average [m]	Minimum Tanimoto [$-$]	Computation time [s]
2	$1.35 \cdot 10^{-8} + 6.43 \cdot 10^{-9}\ i$	$3.32 \cdot 10^{-10} + 3.73 \cdot 10^{-10}\ i$	$1.50 \cdot 10^{-10}$	0.9982	103
20	$4.08 \cdot 10^{-9} + 2.52 \cdot 10^{-9}\ i$	$3.71 \cdot 10^{-10} - 6.62 \cdot 10^{-10}\ i$	$1.44 \cdot 10^{-11}$	0.9979	126
100	$1.40 \cdot 10^{-9} + 1.20 \cdot 10^{-9}\ i$	$1.50 \cdot 10^{-10} + 5.96 \cdot 10^{-11}\ i$	$4.38 \cdot 10^{-12}$	0.9954	1154

Table 7.5: Comparison of the quality of the results in dependency on the different excitation frequencies for the system depicted in figure 7.15

After the verification, the effect of trenches as mitigation measures shall be exemplarily illustrated. As depicted in the introductory figure 7.10 a vertical, harmonic block load is applied on the halfspace surface. In the center of the Finite Element domain an open trench is modeled and the vibrations on the halfspace surface are compared to the situation without trench. The ratio of the amplitude of the displacement in the presence of an open trench A_t to the amplitude of the displacement without trench A_0 is called amplitude reduction factor (ARF) A_r according to [Dolling 1969]. While [Dolling 1969] calculated the amplitude reduction factor based on an energy balance on one point behind the trench which should lie far enough behind the trench, [Woods 1968] examined also the average amplitude reduction factor on lines perpendicular to the trench. [Haupt 1995] took into account for his analyses the displacement behind the trench up to a limit distance of approximately ten times the wavelength of the Rayleigh wave λ_r. Therefore, in this thesis an average amplitude reduction factor will be calculated on a line perpendicular to the trench in the area between the trench up to a limit value of approximately 10 λ_r. An additional average amplitude reduction factor describing the behavior on the surface behind the trench more general is calculated taking into account all values lying inside a half circle with a radius of 10 λ_r.

The trench is introduced into a model for which the material and load parameters are chosen equal to the verification system. As, according to [Woods 1968], the width of an open trench has little influence on its effectiveness, it is chosen as 0.5 m. The main parameter influencing the effectiveness of open trenches is the ratio between the depth of the trench and the wavelength of the Rayleigh wave $\frac{d_t}{\lambda_r}$ as already stated in [Woods 1968] and [Dolling 1969]. Therefore, in an example, the amplitude reduction factor is calculated for the soil material specified in table 7.3 and an excitation frequency is chosen of $f = 20$ Hz which results in a wavelength of the Rayleigh wave of $\lambda_r = 3.29$ m. Trenches with different depths d_t are inserted and a single load at $x = 0$, $y = -3$ m is applied. The amplitudes of the displacements on the surface are calculated for each coordinate x, y in the frequency domain for $\omega = -2\pi f$. Thus, for each trench, the amplitude reduction factor A_r can be calculated for each point x, y as depicted in figure 7.17 for a trench with depth $d_t = 4$ m.

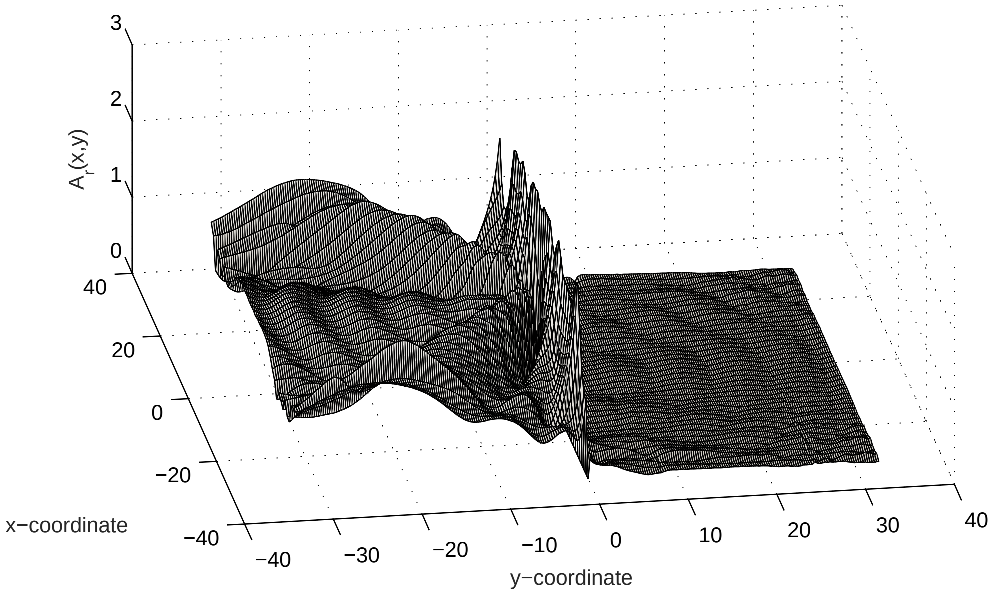

Figure 7.17: Amplitude reduction factor A_r for the vertical displacement on the halfspace surface for an infinite trench at $y = 0$ with a depth $d_t = 4\,\mathrm{m}$ and a single, harmonic load at $x = 0, y = -3\,\mathrm{m}$ with $f = 20\,\mathrm{Hz}$

The reduction of the vibrations in the area on the opposite side of the trench where no load is positioned is clearly visible. In the following figures 7.18, the amplitude reduction factor is plotted at a line perpendicular to the trench at $x = 0$ for different trench depths d_t. For all situations, an increase in the amplitudes is visible on the side of the trench where the load is positioned. This is due to the fact that part of the energy of the oscillations propagating from the point of excitation is reflected at the trench and leads to an increase of the vibrations on the side of the load. On the opposite site of the trench, a reduction of the amplitudes can be observed.

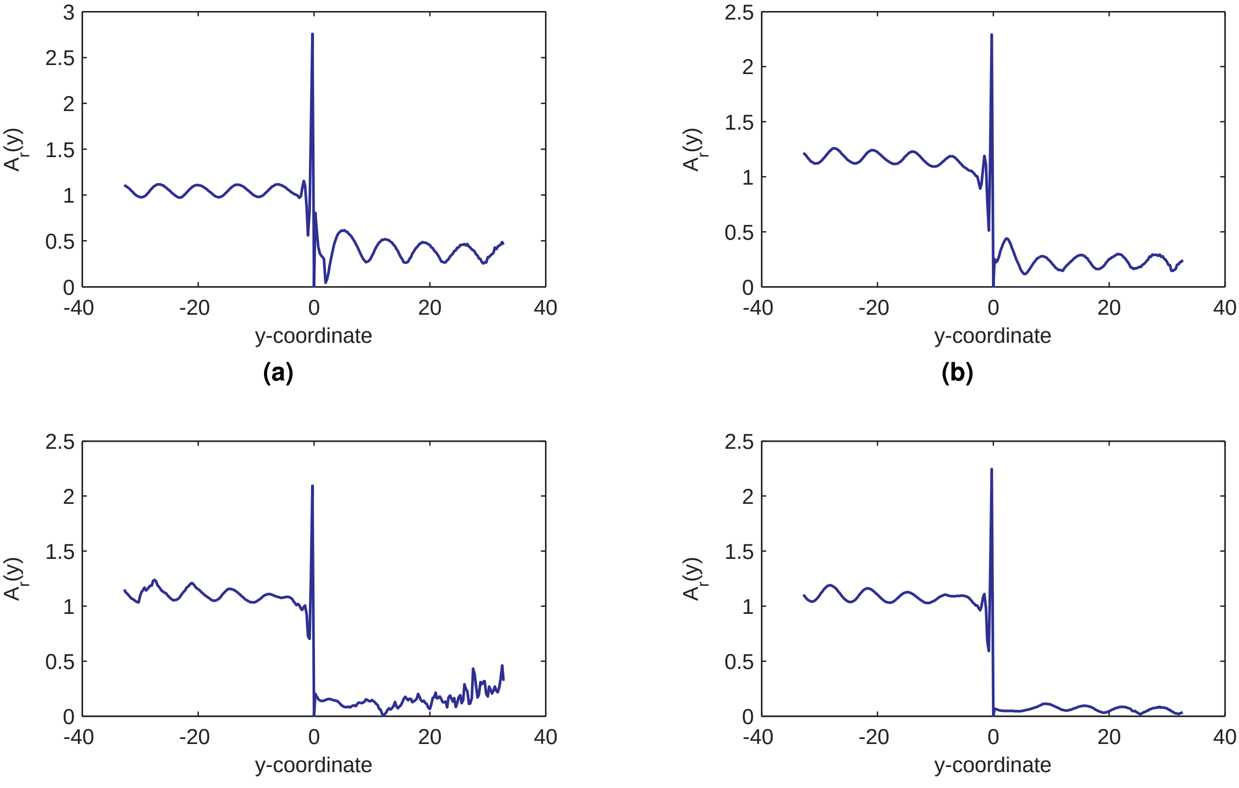

(a) (b) (c) (d)

Figure 7.18: Amplitude reduction factor A_r for the vertical displacement on a line at $x = 0$ due to an infinite trench at $y = 0$ and a single, harmonic load at $x = 0$, $y = -3$ m with $f = 20$ Hz. The trench depth is varied from $d_t = 1$ m (7.18a), $d_t = 2$ m (7.18b), $d_t = 3$ m (7.18c), and $d_t = 4$ m (7.18d)

The influence of the depth is clearly visible. The deeper the trench is built, the better is the mitigation effect concerning the displacements. In table 7.6 the corresponding average values of the amplitude reduction factors are calculated. In the second column the average amplitude reduction factor is calculated using the values A_r on the line at $x = 0$ in the range between $y = 0$ m and $y = 32.75$ m $\approx 10\ \lambda_r$. This range also corresponds roughly to [Lombaert et al 2013] where a soft trench was formulated to be effective until at least 32 m from the track, even if no further specifications of the material and load parameters were published. In the third column, the average amplitude reduction factor is calculated on the halfspace surface behind the trench within a half-circle with the radius 10 λ_r. Also analyzing these average values, the influence of the depth of the trench is dominant.

Trench depth d_t [m]	Average ARF at $x = 0$ $A_{r,av}$ $[-]$	Average ARF on surface $A_{r,av,surf}$ $[-]$	Computation time [s]
1	0.40	0.62	785
2	0.23	0.20	4504
3	0.15	0.14	30826
4	0.06	0.06	167461

Table 7.6: Average values of the amplitude reduction factor A_r for different trench depths

If the behavior of the ARF in dependency on the trench depth is plotted, the relationship is clearly visible. In figure 7.19 the amplitude reduction factors of table 7.6 supplemented by calculations for more different trench depths are depicted in relationship to the depth of the trench normalized with the wavelength of the Rayleigh wave.

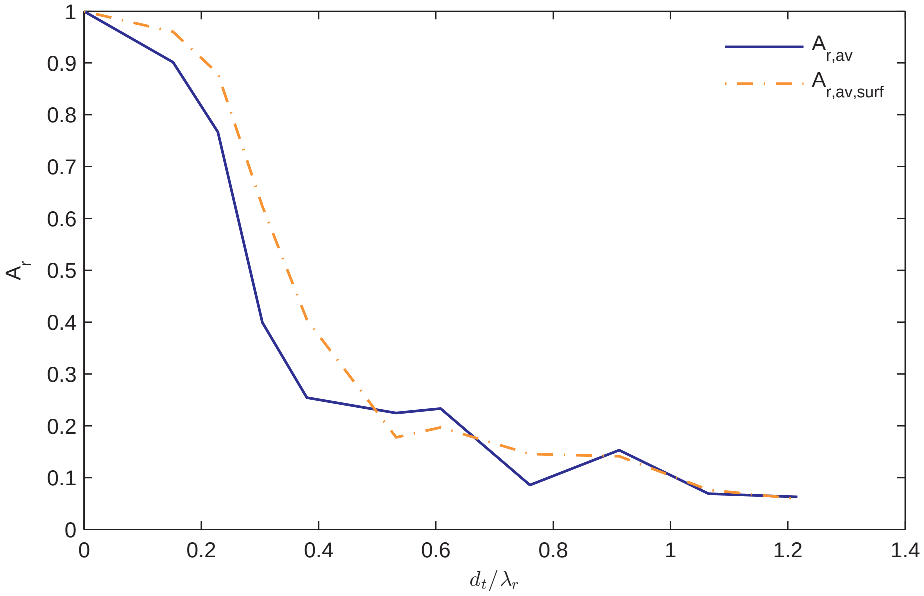

Figure 7.19: Amplitude reduction factor A_r for the vertical displacement on the halfspace surface for an infinite trench at $y = 0$ in dependency on the depth of the trench d_t normalized with the wavelength of the Rayleigh wave λ_r

The graph corresponds to the diagram by [Dolling 1969] who calculated the ARF for materials with different Poisson ratios in dependency on the dimensionless trench depth. In order to enable a more detailed comparison, the calculations are repeated for the material that was also modeled by [Dolling 1969]. The Young's modulus is chosen as $E = 163 \cdot 10^6\,(1 - 0.1i)\ \frac{\mathrm{N}}{\mathrm{m}^2}$

and the density is $\rho = 1830\ \frac{\mathrm{kg}}{\mathrm{m}^3}$. The Poisson ratio is $\nu = 0.33$ and the frequency is chosen as $f = 80$ Hz. The result is depicted in figure 7.20.

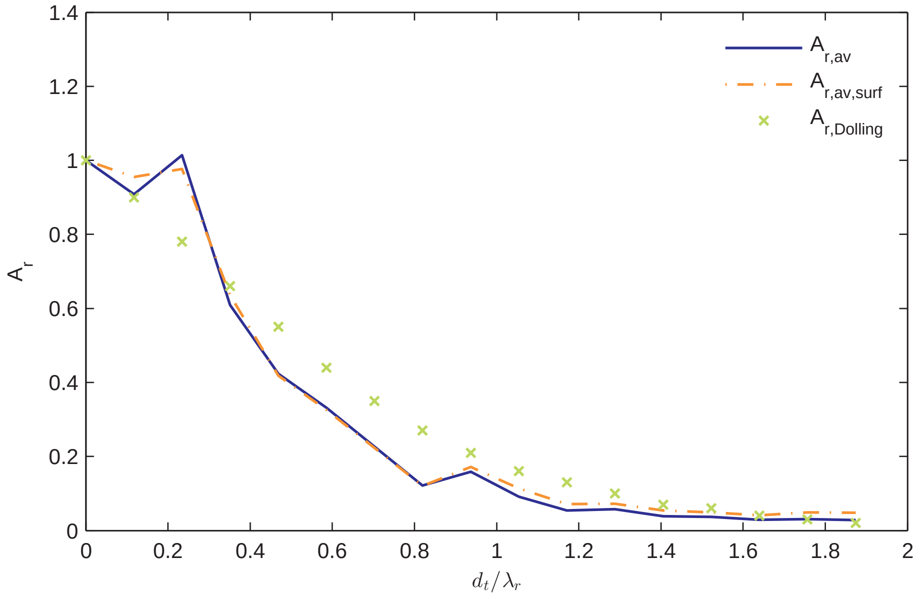

Figure 7.20: Amplitude reduction factor A_r for the vertical displacement on the halfspace surface for an infinite trench at $y = 0$ in dependency on the depth of the trench d_t normalized with the wavelength of the Rayleigh wave λ_r for the material defined in [Dolling 1969]

Again, the average ARF $A_{r,av}$ is calculated on a line perpendicular to the trench at $x = 0$ and $A_{r,av,surf}$ is the average value on the half-circle behind the trench with a radius of 10 λ_r. The results of the coupled ITM-FEM approach show a good accordance with those presented in [Dolling 1969], so the effect of an open trench can be modeled and mitigation measures in the transmission path between a point of load application and a receiving element can be assessed.

8 Summary and Outlook

The excitation of structures due to dynamic or moving loads causes vibrations that are transmitted through the soil. The realistic prediction of the resulting displacements is of increasing importance because on the one hand the excitation forces are increasing and on the other hand the sensitivity of machines or humans to vibrations is also raised. The difficulty of the modeling consists of the different subsystems that are affecting the response of the immission system.

The emission system where the loads are introduced into the total system as well as the immission system where the vibrations are perceived are usually complex structures consisting of different materials. They can be modeled properly by the Finite Element Method. The soil as the medium where the oscillations are transmitted from the emission to the immission system cannot be described by Finite Elements without further adaptations as the infinite extension cannot be taken into account with finite elements. The Integral Transform Method leading to analytical solutions of the Lamé differential equation is able to describe the behavior of the infinite medium completely but is derived under certain assumptions. The material of the soil has to be homogeneous with linear elastic material behavior, the introduction of surfaces is possible for simple geometries and layers in the material can only be taken into account if they are parallel to the respective surface. In this thesis the Integral Transform Method is used to model the transmission medium of the soil. At the surfaces of the soil, a coupling with the Finite Element Method is performed so the emission or immission system can be described with their geometry and material distribution numerically. Thus, both substructures are modeled with their best appropriate method and the total system can be described.

First, the stiffness matrix of the Integral Transform substructure is determined. In this thesis two different systems are presented to model the soil: a halfspace with a cylindrical cavity and a halfspace with a spherical cavity. Thus, different spatial behavior can be implemented. Both systems have a horizontal surface and a second, additional surface which is cylindrical or spherical. The fundamental systems for which analytical solutions exist possess one surface each. These are the fundamental systems: halfspace, which is a fullspace with a horizontal surface, fullspace with a cylindrical surface and fullspace with a spherical surface. To obtain systems with two surfaces as intended for the coupling, two of the fundamental systems are superposed. To determine the solution of a halfspace with cylindrical cavity for example, the halfspace and the fullspace with cylindrical surface are superposed. At each of the fundamental systems unit stresses are applied at its surface and the resulting stresses at this surface are calculated as well as the resulting stresses at the position where the second surface shall be introduced. For the superposed system the boundary conditions are known, thus, the unit loads can be multiplied with unknown amplitudes such that their superposition fulfills the given boundary conditions. After calculating the amplitudes of the unit stresses, the displacements of the fundamental systems can also be superposed in a post-processing step. Thus, the stiffness matrix of the superposed system halfspace with cylindrical cavity can be calculated. The procedure to obtain the solution of a halfspace with spherical cavity is analogous.

The calculation of the stiffness matrix of the Finite Element substructure is regularly performed in Finite Element derivations. The elements of the spherical structure are common three-dimensional eight-node elements with linear form functions. Concerning the elements of the cylindrical structure the information is used that the structure is infinite in longitudinal direction. The derivations of the Integral Transform Method for the halfspace with cylindrical cavity are carried out for a quasi-static, two-dimensional system. Fourier transformations from time into frequency domain $t \circ\!\!-\!\!\!-\!\!\bullet\ \omega$ and from the spatial coordinate in longitudinal direction into the respective wavenumber domain $x \circ\!\!-\!\!\!-\!\!\bullet\ k_x$ are carried out. Thus, the integration over the longitudinal coordinate x that is necessary in the Finite Element Method is replaced by a sum over the calculations carried out for each wavenumber k_x. This means that instead of three-dimensional elements the two-dimensional, circular cross section of the cylinder is discretized with three degrees of freedom at each node. Thus, the two-dimensional elements contain information about the behavior of the structure in the third dimension wherefore the elements are also called 2.5-dimensional elements.

After calculating the stiffness matrices of the two substructures separately they are coupled using the compatibility of the displacements as well as the equilibrium of forces on the coupling surface. In order to perform the coupling, the parameters of both substructures on the interaction surface must refer to the same basis. As the Finite Element calculations are carried out in a two-dimensional (for the cylindrical structure) respectively three-dimensional (for the spherical structure) Cartesian coordinate system they are transformed into the associated coordinate systems of the Integral Transform substructure. Then the coupling can be performed and the solutions of a halfspace with a cylindrical or a spherical Finite Element structure inside are derived.

To verify the presented approach the Finite Element structures are modeled with a completely filled Finite Element mesh that possesses the same material parameters as the surrounding soil. The result of these systems is compared to the analytical solution of an undisturbed soil. The results show a good accordance that depends strongly on the discretization of the Finite Element mesh as expected. The finer the discretization is chosen, the better is the accordance of the coupled approach and the analytical solution.

Concluding, numerical examples are presented to show the applicability of the method. The implementation of moving loads in the system is shown as well as the possibility to model the effects of mitigation measures that are used to reduce the vibrations of a system. Mass-spring systems that are often implemented in an underground tunnel to reduce the transmission of vibrations from the track into the tunnel can be assessed with the coupled Integral Transform Method - Finite Element Method approach. Also trenches on the surface of the halfspace that shall hinder the transmission of vibrations via the trench can be modeled with this approach by shifting the Finite Element structure to the surface of the soil.

Thus, the coupling of the Integral Transform Method and the Finite Element Method enables to describe construction situations by taking into account the behavior of the soil with analytical solutions.

Of course, further work can be done in this field. On the one hand side, a further comparison of the developed method with measurement results would be advantageous to assess the applicability for real situations. On the side of the Integral Transform substructure more substructures could be generated out of the fundamental systems. A solution of a layered halfspace where the layer boundary crosses a cylindrical or spherical cavity could be determined or layers could be implemented that are not horizontal but are inclined with respect to the halfspace surface. Moreover, improvements of the Finite Element substructure are possible. Instead of using linear form functions, it could be possible to improve the accuracy of the Finite Element substructure by describing the behavior between the nodes with higher or improved elements. As both the circular cross section of the cylinder as well as the surface of the sphere are strongly curved, the approximation with linear functions is rough. The use of higher order polynomials or splines instead of polynomials could lead to improved results.

A Appendix

A.1 Fundamentals of Fourier transformation

A.1.1 Continuous Fourier transformation

The Fourier transformed function $H(\omega)$ of a given function $h(t)$ is defined as

$$H(\omega) = \int\limits_{-\infty}^{\infty} h(t)\; e^{-i\omega t}\; dt \tag{A.1}$$

following the derivations of [Brigham 2010].

In section 2.3.1 a threefold Fourier transformation is carried out from spatial coordinates into the wavenumber domain $x \circ\!\!-\!\!\!-\!\!\bullet\; k_x$ and $y \circ\!\!-\!\!\!-\!\!\bullet\; k_y$ and from time into frequency domain $t \circ\!\!-\!\!\!-\!\!\bullet\; \omega$. This is done by applying equation (A.1) threefold on the scalar potential Φ (see equation (A.2)) and the components of the vector potential Ψ_i respectively.

$$\hat{\Phi}\left(k_x, k_y, z, \omega\right) = \int\limits_{-\infty}^{\infty} \int\limits_{-\infty}^{\infty} \int\limits_{-\infty}^{\infty} \Bigg(\bigg(\Big(\Phi\left(x, y, z, t\right)\; e^{-ik_x x}\; dx \Big)\; e^{-ik_y y}\; dy \bigg)\; e^{-i\omega t}\; dt \Bigg) \tag{A.2}$$

To obtain parameters in the original domain, an inverse Fourier transformation is carried out with

$$h(t) = \frac{1}{2\pi} \int\limits_{-\infty}^{\infty} H(\omega)\; e^{i\omega t}\; d\omega \tag{A.3}$$

Also the scalar potential Φ or the components of the vector potential Ψ_i can be computed in the original domain via a threefold inverse Fourier transformation.

$$\Phi\left(x,y,z,t\right)=\frac{1}{\left(2\pi\right)^3}\int\limits_{-\infty}^{\infty}\int\limits_{-\infty}^{\infty}\int\limits_{-\infty}^{\infty}\left(\left(\left(\hat{\Phi}\left(k_x,k_y,z,\omega\right)\ e^{ik_xx}\ dk_x\right)\ e^{ik_yy}\ dk_y\right)\ e^{i\omega t}\ d\omega\right) \tag{A.4}$$

Calculating the n^{th} derivative of a function $h(t)$ in the original domain corresponds to a multiplication of the transformed function $H(\omega)$ with $\left(i\omega\right)^n$ in the transformed domain.

$$\frac{\partial^n h(t)}{\partial t^n}\ \circ\!\!-\!\!\!-\!\!\bullet\ \left(i\omega\right)^n H(\omega) \tag{A.5}$$

Thus, the derivatives in equation (2.15) can be replaced by multiplications with the respective transformed coordinates, as stated in the equations (A.6).

$$\frac{\partial^2 h(x)}{\partial x^2}\ \circ\!\!-\!\!\!-\!\!\bullet\ \left(ik_x\right)^2 H(k_x)=-{k_x}^2 H(k_x) \tag{A.6a}$$

$$\frac{\partial^2 h(y)}{\partial y^2}\ \circ\!\!-\!\!\!-\!\!\bullet\ \left(ik_y\right)^2 H(k_y)=-{k_y}^2 H(k_y) \tag{A.6b}$$

$$\frac{\partial^2 h(t)}{\partial t^2}\ \circ\!\!-\!\!\!-\!\!\bullet\ \left(i\omega\right)^2 H(\omega)\ \ =-\omega^2 H(\omega) \tag{A.6c}$$

A.1.2 Discrete Fourier transformation

For numerical applications, the discrete Fourier transformation of a function $g(t)$ which is defined at N equally distributed positions at intervals of $t = T$ is defined according to [Brigham 2010] for example as

$$G\left(\frac{n}{NT}\right)=\sum_{k=0}^{N-1} g\left(kT\right)\ e^{-i\frac{2\pi nk}{N}} \tag{A.7}$$

The result of this discrete Fourier transformation is a function $G(\omega)$ that is defined at N equally distributed positions at intervals of $\omega = \frac{1}{NT}$.

The inverse discrete Fourier transformation is defined as

$$g\left(kT\right)=\frac{1}{N}\sum_{n=0}^{N-1} G\left(\frac{n}{NT}\right)\ e^{i\frac{2\pi nk}{N}} \tag{A.8}$$

As the discrete Fourier transformation is an approximation of the continuous transformation, the quality of the results is depending on the chosen numerical parameters. Information regarding the characteristics of a discrete Fourier transformation is contained in a variety of textbooks as [Brigham 2010] or [Kammler 2008]. The differences between a continuous transformation as presented in section A.1.1 and a discrete transformation are the necessary limitation of the signal in the original as well as in the transformed domain and the sampling of continuous functions at a limited number of sampling points.

In the original domain, the interval $T_W = NT$ as the length of the sampling window has to be chosen adequately as the integration of a function from $+\infty$ to ∞ as it is formulated in the continuous transformation in equation (A.1) is replaced by a sum over N samples equally spaced by T. If the signal is transient in the original domain and the window length is chosen bigger than the signal, the window has no effect on the transformed signal. Otherwise, if the signal is artificially limited by the applied window, numerical effects can be observed depending on the characteristics of the window function. The most simple window function is a multiplication of the continuous function with a rectangular window. This corresponds to a cut off of all values of the function that are smaller than the lower limit of the window T_{W1} or bigger than the upper limit of the window T_{W2}. The multiplication of the original function with the rectangular window corresponds to a convolution of the transformed signal in the transformed domain with a cardinal sine function. Thus, additional frequency components are obtained except for the special case that the window length T_W of a periodic function is chosen as exactly one period of the signal or a multiple of the period. But for all other cases, the windowing of a function leads to artificial frequency components in the transformed domain which is often called the leakage effect and to discontinuities in the original domain. Instead of rectangular windows more sophisticated window functions can be used as filters for the limitation of the signal in the original domain.

A second parameter that has to be chosen in the discrete Fourier transformation besides the window length is the number of samples N on which the function is evaluated. As a high sampling rate increases the computation time, on the one hand it is advantageous to use only as many samples as are necessary to model the function. On the other hand, the discretization of the function in one domain leads to a repetition of the signal in the transformed domain. Depending on the interval $T = \frac{T_W}{N}$ in the original domain, the signal is repeated in the transformed domain with a period of $F_R = \frac{1}{T}$. In order to avoid aliasing, which is the overlapping of the signals of the different repetitions, it is necessary that F_R is big enough. Thus, T shall be small which corresponds to a high sampling rate N. Therefore, a balance has to be found between the necessity to have enough samples to avoid aliasing on the one hand but only as much samples as are necessary to avoid large computation times. The Nyquist condition states that if F_{max} is the highest frequency component of a given function, the repetition frequency F_R should be chosen as

$$F_R \geq 2F_{max} \tag{A.9}$$

This corresponds to the condition for the sampling interval in the original domain $T \leq \frac{1}{2F_{max}}$. Thus, for a given window length T_W, the number of samples N should be chosen as

$$N \geq 2\, T_W\, F_{max} \tag{A.10}$$

Concerning the discrete Fourier transformations that are applied in this thesis regarding the spatial and time coordinates $x \circ\!\!-\!\!\!-\!\!\!-\!\!\bullet\; k_x$, $y \circ\!\!-\!\!\!-\!\!\!-\!\!\bullet\; k_y$ and $t \circ\!\!-\!\!\!-\!\!\!-\!\!\bullet\; \omega$ the parameters are chosen to avoid the numerical artifacts of leakage and aliasing as good as possible. The loads that are transformed into the wavenumber-frequency domain in the different presented examples are time-harmonic functions with a window length of one period of the function so leakage concerning the time component can be excluded. The spatial distribution of the loads are block loads or single loads which are both limited in their spatial extension. Thus, also spatial leakage effects can be excluded for the Fourier transformation of the load. Aliasing effects cannot be excluded completely. Concerning the repetition of the signals, it is examined that the repetition frequency and wavenumbers are big enough so that an overlapping of the signals of the different repetitions is reduced.

The algorithm that is used for the discrete Fourier transformation is a Fast Fourier transformation algorithm that is optimized concerning computation time. It can be applied if the number of samples is a power of two

$$N = 2^m \tag{A.11}$$

with m chosen big enough to avoid aliasing effects.

A.2 Bessel's differential equation and Bessel functions

The differential equations (2.48) in section 2.4.1 are Bessel's differential equations.

$$\left[\frac{\partial^2}{\partial r^2}+\frac{1}{r}\frac{\partial}{\partial r}+k^2-\frac{n^2}{r^2}\right]\hat{\mathrm{f}}\,(r)=0 \tag{A.12}$$

In general, Bessel's differential equations are of the type

$$x^2\,\mathrm{f}''+x\,\mathrm{f}'+\left(x^2-n^2\right)\mathrm{f}=0 \tag{A.13}$$

The differential equation (A.13) can be solved using Bessel functions of the first kind $J_\nu(x)$ with

$$J_\nu(x)=\sum_{k=0}^{\infty}\frac{(-1)^k\left(\frac{x}{2}\right)^{\nu+2k}}{k!\,\Gamma\left(\nu+k+1\right)} \tag{A.14}$$

For nonintegral ν the solution of Bessel's differential equation can be determined as

$$\mathrm{f}(x)=C_1J_\nu(x)+C_2J_{-\nu}(x) \tag{A.15}$$

When ν is an integral value n, the solutions $J_n(x)$ and $J_{-n}(x)$ are linearly dependent via

$$J_n(x)=(-1)^nJ_{-n}(x) \tag{A.16}$$

and exhibit but one independent solution. In this case, the solution for $J_{-n}(x)$ can be expressed by Bessel functions of the second kind, also called Neumann functions, $Y_n(x)$ as the limit

$$Y_n(x)=\lim_{\nu\to n}\frac{J_\nu(x)\cos\left(\nu\pi\right)-J_{-\nu}(x)}{\sin\left(\nu\pi\right)} \tag{A.17}$$

and the solution of Bessel's differential equation results in

$$\mathrm{f}(x)=C_1J_n(x)+C_2Y_n(x) \tag{A.18}$$

The Bessel and Neumann functions are exemplarily depicted in the figures A.1 in dependency on the x-coordinate and in dependency on ν.

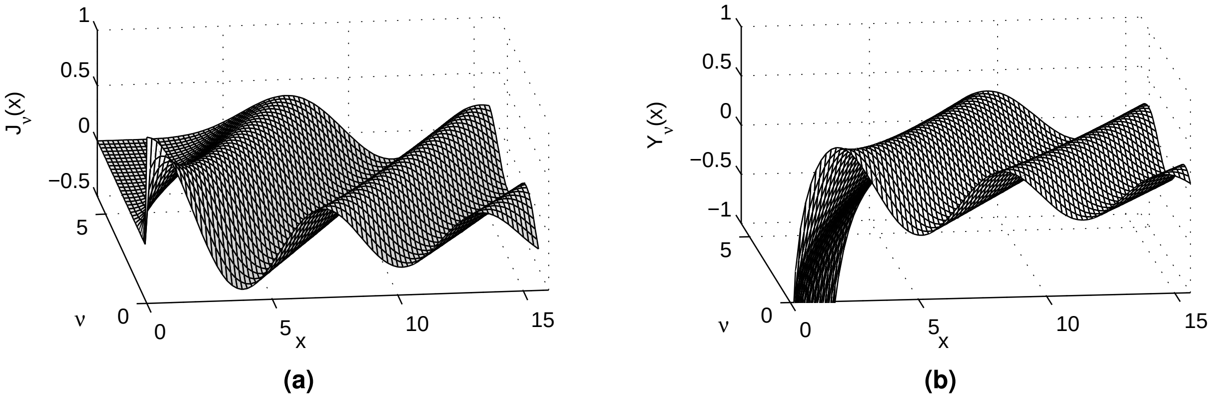

(a) (b)

Figure A.1: Bessel functions $J_\nu(x)$ (A.1a) and Neumann functions $Y_\nu(x)$ (A.1b) in dependency on the x-coordinate and ν

As an alternative, instead of using Bessel functions of the first and second kind, also Bessel functions of the third kind, Hankel functions, can be introduced. They can be derived from $J_n(x)$ and $Y_n(x)$ by

$$H_n^{(1)}(x) = J_n(x) + iY_n(x) \tag{A.19a}$$

$$H_n^{(2)}(x) = J_n(x) - iY_n(x) \tag{A.19b}$$

with $H_n^{(1)}$ as Hankel functions of the first kind and $H_n^{(2)}$ as Hankel functions of the second kind. Thus, the solution for Bessel's differential equation can be expressed by

$$\mathrm{f}(x) = C_1 H_n^{(1)}(x) + C_2 H_n^{(2)}(x) \tag{A.20}$$

A.3 Stresses in the cylindrical coordinate system

The relationship between the vector containing the components of the stress tensor $\hat{\boldsymbol{\sigma}}_{\mathbf{c}}$ and the vector of the unknowns $\mathbf{C_c}$ is derived for cylindrical coordinates analogously to the procedure for Cartesian coordinates. As a result a matrix $\left[\hat{K}_c\right]$ is obtained describing the relationship:

$$\hat{\boldsymbol{\sigma}}_{\mathbf{c}} = \left[\hat{K}_c\right] \mathbf{C_c} \tag{A.21}$$

with the vector of the stresses $\hat{\boldsymbol{\sigma}}_{\mathbf{c}}$

$$\hat{\boldsymbol{\sigma}}_{\mathbf{c}} = \begin{pmatrix} \hat{\sigma}_{xx} \\ \hat{\sigma}_{rr} \\ \hat{\sigma}_{\varphi\varphi} \\ \hat{\sigma}_{xr} \\ \hat{\sigma}_{\varphi r} \\ \hat{\sigma}_{x\varphi} \end{pmatrix} \tag{A.22}$$

and the vector of the unknowns

$$\mathbf{C_c} = \begin{pmatrix} C_{1n} \\ C_{2n} \\ C_{3n} \\ C_{4n} \\ C_{5n} \\ C_{6n} \end{pmatrix} \tag{A.23}$$

The elements of matrix $\left[\hat{K}_c\right]$ are derived using the material law and the kinematic relations for cylindrical coordinates in the (k_x, r, n, ω) domain.

Elements of the matrix $\left[\hat{K}_c\right]$ for the computation of the component $\hat{\sigma}_{xx}$ of the stress tensor:

$$\hat{K}_{c,11} = \left({k_1}^2 - \frac{1}{2}{k_s}^2\right) 2\mu \, H_n^{(1)}(k_1 r)$$

$$\hat{K}_{c,12} = 0$$

$$\hat{K}_{c,13} = i \; k_x \, {k_2}^2 \, 2\mu \, H_n^{(1)}(k_2 r)$$

$$\hat{K}_{c,14} = \left({k_1}^2 - \frac{1}{2}{k_s}^2\right) 2\mu \, H_n^{(2)}(k_1 r)$$

$$\hat{K}_{c,15} = 0$$

$$\hat{K}_{c,16} = i \; k_x \, {k_2}^2 \, 2\mu \, H_n^{(2)}(k_2 r)$$

Elements of the matrix $\left[\hat{K}_c\right]$ for the computation of the component $\hat{\sigma}_{rr}$ of the stress tensor:

$$\hat{K}_{c,21} = \left(\frac{n^2 - n}{r^2} + {k_x}^2 - \frac{1}{2}{k_s}^2\right) 2\mu \, H_n^{(1)}(k_1 r) + \frac{1}{r} k_1 \, 2\mu \, H_{n+1}^{(1)}(k_1 r)$$

$$\hat{K}_{c,22} = i \; \frac{n^2 - n}{r^2} \; 2\mu \, H_n^{(1)}(k_2 r) - i \; \frac{n}{r} k_2 \, 2\mu \, H_{n+1}^{(1)}(k_2 r)$$

$$\hat{K}_{c,23} = i \left(\frac{n^2 - n}{r^2} - {k_2}^2\right) k_x \, 2\mu \, H_n^{(1)}(k_2 r) + i \; \frac{1}{r} k_x \, k_2 \, 2\mu \, H_{n+1}^{(1)}(k_2 r)$$

$$\hat{K}_{c,24} = \left(\frac{n^2 - n}{r^2} + {k_x}^2 - \frac{1}{2}{k_s}^2\right) 2\mu \, H_n^{(2)}(k_1 r) + \frac{1}{r} k_1 \, 2\mu \, H_{n+1}^{(2)}(k_1 r)$$

$$\hat{K}_{c,25} = i \; \frac{n^2 - n}{r^2} \; 2\mu \, H_n^{(2)}(k_2 r) - i \; \frac{n}{r} k_2 \, 2\mu \, H_{n+1}^{(2)}(k_2 r)$$

$$\hat{K}_{c,26} = i \left(\frac{n^2 - n}{r^2} - {k_2}^2\right) k_x \, 2\mu \, H_n^{(2)}(k_2 r) + i \; \frac{1}{r} k_x \, k_2 \, 2\mu \, H_{n+1}^{(2)}(k_2 r)$$

Elements of the matrix $\left[\hat{K}_c\right]$ for the computation of the component $\hat{\sigma}_{\varphi\varphi}$ of the stress tensor:

$$\hat{K}_{c,31} = -\left(\frac{n^2-n}{r^2} + \frac{1}{2}{k_s}^2 - {k_1}^2 - k_x^2\right) 2\mu\, H_n^{(1)}(k_1 r) - \frac{1}{r} k_1\, 2\mu\, H_{n+1}^{(1)}(k_1 r)$$

$$\hat{K}_{c,32} = -i\ \frac{n^2-n}{r^2}\, 2\mu\, H_n^{(1)}(k_2 r) + i\ \frac{n}{r} k_2\, 2\mu\, H_{n+1}^{(1)}(k_2 r)$$

$$\hat{K}_{c,33} = -i\ \frac{n^2-n}{r^2}\, k_x\, 2\mu\, H_n^{(1)}(k_2 r) - i\ \frac{1}{r} k_x\, k_2\, 2\mu\, H_{n+1}^{(1)}(k_2 r)$$

$$\hat{K}_{c,34} = -\left(\frac{n^2-n}{r^2} + \frac{1}{2}{k_s}^2 - {k_1}^2 - k_x^2\right) 2\mu\, H_n^{(2)}(k_1 r) - \frac{1}{r} k_1\, 2\mu\, H_{n+1}^{(2)}(k_1 r)$$

$$\hat{K}_{c,35} = -i\ \frac{n^2-n}{r^2}\, 2\mu\, H_n^{(2)}(k_2 r) + i\ \frac{n}{r} k_2\, 2\mu\, H_{n+1}^{(2)}(k_2 r)$$

$$\hat{K}_{c,36} = -i\ \frac{n^2-n}{r^2}\, k_x\, 2\mu\, H_n^{(2)}(k_2 r) - i\ \frac{1}{r} k_x\, k_2\, 2\mu\, H_{n+1}^{(2)}(k_2 r)$$

Elements of the matrix $\left[\hat{K}_c\right]$ for the computation of the component $\hat{\sigma}_{xr}$ of the stress tensor:

$$\hat{K}_{c,41} = i\ \frac{n}{r} k_x\, 2\mu\, H_n^{(1)}(k_1 r) - i\ k_x\, k_1\, 2\mu\, H_{n+1}^{(1)}(k_1 r)$$

$$\hat{K}_{c,42} = -\frac{n}{2r} k_x\, 2\mu\, H_n^{(1)}(k_2 r)$$

$$\hat{K}_{c,43} = \frac{n}{2r}\left({k_2}^2 - {k_x}^2\right) 2\mu\, H_n^{(1)}(k_2 r) + \frac{1}{2}\left({k_x}^2 k_2 - {k_2}^3\right) 2\mu\, H_{n+1}^{(1)}(k_2 r)$$

$$\hat{K}_{c,44} = i\ \frac{n}{r} k_x\, 2\mu\, H_n^{(2)}(k_1 r) - i\ k_x\, k_1\, 2\mu\, H_{n+1}^{(2)}(k_1 r)$$

$$\hat{K}_{c,45} = -\frac{n}{2r} k_x\, 2\mu\, H_n^{(2)}(k_2 r)$$

$$\hat{K}_{c,46} = \frac{n}{2r}\left({k_2}^2 - {k_x}^2\right) 2\mu\, H_n^{(2)}(k_2 r) + \frac{1}{2}\left({k_x}^2 k_2 - {k_2}^3\right) 2\mu\, H_{n+1}^{(2)}(k_2 r)$$

Elements of the matrix $\left[\hat{K}_c\right]$ for the computation of the component $\hat{\sigma}_{\varphi r}$ of the stress tensor:

$$\hat{K}_{c,51} = i\;\frac{n^2-n}{r^2}\,2\mu\,H_n^{(1)}(k_1 r) - i\;\frac{n}{r}k_1\,2\mu\,H_{n+1}^{(1)}(k_1 r)$$

$$\hat{K}_{c,52} = \left(-\frac{n^2-n}{r^2}+\frac{1}{2}{k_2}^2\right)2\mu\,H_n^{(1)}(k_2 r) - \frac{1}{r}k_2\,2\mu\,H_{n+1}^{(1)}(k_2 r)$$

$$\hat{K}_{c,53} = -\frac{n^2-n}{r^2}\,k_x\,2\mu\,H_n^{(1)}(k_2 r) + \frac{n}{r}k_x\,k_2\,2\mu\,H_{n+1}^{(1)}(k_2 r)$$

$$\hat{K}_{c,54} = i\;\frac{n^2-n}{r^2}\,2\mu\,H_n^{(2)}(k_1 r) - i\;\frac{n}{r}k_1\,2\mu\,H_{n+1}^{(2)}(k_1 r)$$

$$\hat{K}_{c,55} = \left(-\frac{n^2-n}{r^2}+\frac{1}{2}{k_2}^2\right)2\mu\,H_n^{(2)}(k_2 r) - \frac{1}{r}k_2\,2\mu\,H_{n+1}^{(2)}(k_2 r)$$

$$\hat{K}_{c,56} = -\frac{n^2-n}{r^2}\,k_x\,2\mu\,H_n^{(2)}(k_2 r) + \frac{n}{r}k_x\,k_2\,2\mu\,H_{n+1}^{(2)}(k_2 r)$$

Elements of the matrix $\left[\hat{K}_c\right]$ for the computation of the component $\hat{\sigma}_{x\varphi}$ of the stress tensor:

$$\hat{K}_{c,61} = -\frac{n}{r}k_x\,2\mu\,H_n^{(1)}(k_1 r)$$

$$\hat{K}_{c,62} = -i\;\frac{n}{2r}k_x\,2\mu\,H_n^{(1)}(k_2 r) + i\;\frac{1}{2}k_x\,k_2\,2\mu\,H_{n+1}^{(1)}(k_2 r)$$

$$\hat{K}_{c,63} = i\;\frac{n}{2r}\left({k_2}^2-{k_x}^2\right)2\mu\,H_n^{(1)}(k_2 r))$$

$$\hat{K}_{c,64} = -\frac{n}{r}k_x\,2\mu\,H_n^{(2)}(k_1 r)$$

$$\hat{K}_{c,65} = -i\;\frac{n}{2r}k_x\,2\mu\,H_n^{(2)}(k_2 r) + i\;\frac{1}{2}k_x\,k_2\,2\mu\,H_{n+1}^{(2)}(k_2 r)$$

$$\hat{K}_{c,66} = i\;\frac{n}{2r}\left({k_2}^2-{k_x}^2\right)2\mu\,H_n^{(2)}(k_2 r))$$

A.4 Legendre polynomials and spherical harmonics

The differential equations (2.59) consist of radius-dependent terms and angle-dependent terms as repeated in the following equation (A.24) for a general function $\mathrm{f}\,(r, \vartheta, \varphi, t)$ as

$$\left[\frac{\partial^2}{\partial r^2} + \frac{2}{r}\frac{\partial}{\partial r} + \frac{1}{r^2}\left(\frac{\partial^2}{\partial \vartheta^2} + \frac{\cos(\vartheta)}{\sin(\vartheta)}\frac{\partial}{\partial \vartheta} + \frac{1}{\sin^2(\vartheta)}\frac{\partial^2}{\partial \varphi^2}\right) + {k_i}^2\right] \mathrm{f}\,(r, \vartheta, \varphi, \omega) = 0 \qquad \text{(A.24)}$$

Analogously to [Bronstein et al 2006] or [Arfken and Weber 1995], a solution for the function $\mathrm{f}\,(r, \vartheta, \varphi)$ can be derived for each frequency ω with a separation approach.

$$\mathrm{f}\,(r, \vartheta, \varphi) = \mathrm{R}(r)\; Y^l_m(\vartheta, \varphi) \qquad \text{(A.25)}$$

Introducing the separation approach (A.25) into equation (A.24) leads to

$$\begin{gathered} \frac{1}{\mathrm{R}(r)} r^2 \frac{d^2\,\mathrm{R}(r)}{dr^2} + \frac{1}{\mathrm{R}(r)} \frac{2}{r} \frac{d\,\mathrm{R}(r)}{dr} + r^2 {k_i}^2 = \\ - \frac{1}{Y^l_m(\vartheta, \varphi)} \frac{\partial^2 Y^l_m(\vartheta, \varphi)}{\partial \vartheta^2} - \frac{1}{Y^l_m(\vartheta, \varphi)} \frac{\cos(\vartheta)}{\sin(\vartheta)} \frac{\partial Y^l_m(\vartheta, \varphi)}{\partial \vartheta} - \frac{1}{Y^l_m(\vartheta, \varphi)} \frac{1}{\sin^2(\vartheta)} \frac{\partial^2 Y^l_m(\vartheta, \varphi)}{\partial \varphi^2} \end{gathered} \qquad \text{(A.26)}$$

Equation (A.26) is only fulfilled if both sides of the equation are independent of each other and equal to the same, constant separation value. This value is chosen to be $[m\,(m+1)]$. Thus, the partial differential equation of the right hand side can be written as

$$\frac{\partial^2 Y^l_m(\vartheta, \varphi)}{\partial \vartheta^2} + \frac{\cos(\vartheta)}{\sin(\vartheta)} \frac{\partial Y^l_m(\vartheta, \varphi)}{\partial \vartheta} + \frac{1}{\sin^2(\vartheta)} \frac{\partial^2 Y^l_m(\vartheta, \varphi)}{\partial \varphi^2} = -m\,(m+1)\, Y^l_m(\vartheta, \varphi) \qquad \text{(A.27)}$$

This relation (A.27) is also used in equation (2.64). A solution is possible with an additional separation approach. The function $Y^l_m(\vartheta, \varphi)$ is replaced by two functions $\Phi_l(\varphi)$ containing the azimuthal-dependency and $\Theta^l_m(\vartheta)$ with the polar angle-dependency.

$$Y^l_m(\vartheta, \varphi) = \Phi_l(\varphi)\; \Theta^l_m(\vartheta) \qquad \text{(A.28)}$$

Introducing equation (A.28) into equation (A.27) yields

$$\sin^2(\vartheta) \left[m\,(m+1) + \frac{1}{\Theta^l_m(\vartheta)} \frac{\partial^2 \Theta^l_m(\vartheta)}{\partial \vartheta^2} + \frac{1}{\Theta^l_m(\vartheta)} \frac{\cos(\vartheta)}{\sin(\vartheta)} \frac{\partial \Theta^l_m(\vartheta)}{\partial \vartheta}\right] = -\frac{1}{\Phi_l(\varphi)} \frac{\partial^2 \Phi_l(\varphi)}{\partial \varphi^2} \qquad \text{(A.29)}$$

Again, this equation is only fulfilled if both sides are equal to one constant value which is chosen to be l^2. Thus, the right hand side of equation (A.29) leads to the azimuthal equation

$$\frac{d^2\Phi_l(\varphi)}{d\varphi^2} + l^2\Phi_l(\varphi) = 0 \tag{A.30}$$

which can be solved with the exponential function

$$\Phi_l(\varphi) = e^{il\varphi} \tag{A.31}$$

If the orthogonal condition

$$\int\limits_0^{2\pi} \Phi_{l_1}(\varphi)\Phi_{l_2}(\varphi)\; d\varphi = \delta_{l_1 l_2} \tag{A.32}$$

is normalized to a value 1 for $l_1 = l_2$ then Φ_l can be formulated in a normalized form as

$$\check{\Phi}_l(\varphi) = \frac{1}{\sqrt{2\pi}}\; e^{il\varphi} \tag{A.33}$$

The left hand side of equation (A.29) leads to the polar angle equation.

$$\frac{d^2\Theta^l_m(\vartheta)}{d\vartheta^2} + \frac{\cos(\vartheta)}{\sin(\vartheta)}\frac{d\Theta^l_m(\vartheta)}{d\vartheta} + m\,(m+1)\,\Theta^l_m(\vartheta) - \frac{l^2}{\sin^2(\vartheta)}\Theta^l_m(\vartheta) = 0 \tag{A.34}$$

Using the substitution $\cos(\vartheta) = x$ as presented in [Arfken and Weber 1995], equation (A.34) can be formulated as

$$\left(1 - x^2\right)\; \frac{d^2\Theta^l_m(x)}{dx^2} - 2x\; \frac{d\Theta^l_m(x)}{dx} + \left[m\,(m+1) - \frac{l^2}{1-x^2}\right]\Theta^l_m(x) = 0 \tag{A.35}$$

Equation (A.35) can now be identified as associated Legendre differential equation and can be solved using associated Legendre polynomials. The associated Legendre polynomials $P^l_m\,(x)$ of degree m and order l are defined for $l \neq 0$ in dependency on the Legendre polynomials $P_m\,(x)$

$$P^l_m\,(x) = (-1)^l \left(1 - x^2\right)^{l/2} \frac{d^l}{dx^l} P_m\,(x) \tag{A.36}$$

with $x = \cos(\vartheta)$.

For $l = 0$, the associated Legendre differential equation is transformed into the Legendre differential equation and $P^0_m\,(x) = P_m\,(x)$. The Legendre polynomials $P_m\,(x)$ can be formulated in different ways. Using Rodrigues' formula, they are defined as

$$P_m\left(x\right)=\frac{1}{2^m m!}\frac{d^m\left(x^2-1\right)^m}{dx^m} \tag{A.37}$$

For a first impression, the analytical functions of the first Legendre polynomials $P_0\left(x\right)$–$P_5\left(x\right)$ are collected in the following table A.1 and are also displayed for $x=\cos(\vartheta)$ in figure A.2.

$$\begin{aligned}
P_0\left(x\right) &= 1\\
P_1\left(x\right) &= x\\
P_2\left(x\right) &= \tfrac{1}{2}\left(3x^2-1\right)\\
P_3\left(x\right) &= \tfrac{1}{2}\left(5x^3-3x\right)\\
P_4\left(x\right) &= \tfrac{1}{8}\left(35x^4-30x^2+3\right)\\
P_5\left(x\right) &= \tfrac{1}{8}\left(63x^5-70x^3+15x\right)
\end{aligned}$$

Table A.1: Analytical functions of the first six Legendre polynomials

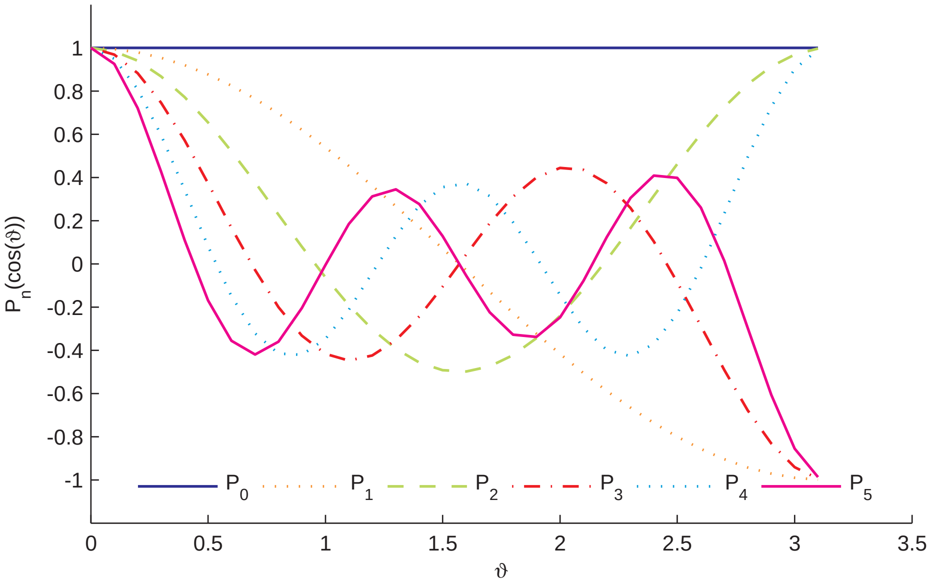

Figure A.2: Graphical representation of the first six Legendre polynomials

As the exponent of x in equation (A.37) is maximum $2m$ and equation (A.37) is introduced into equation (A.36), $l<m$ has to be valid. The associated Legendre polynomials for

negative l can be added with

$$P_m^{-l}(x) = (-1)^l \, \frac{(m-l)!}{(m+l)!} \, P_m^l(x) \tag{A.38}$$

Analogously to equation (A.32), the orthogonality integral is calculated.

$$\int_{-1}^{1} P_{m_1}^l(x) \, P_{m_2}^l(x) \; dx = \frac{2}{2m_1+1} \frac{(m_1+l)!}{(m_1-l)!} \, \delta_{m_1 m_2} \tag{A.39}$$

Thus, again applying a normalization such that the result of integration (A.39) is 1 for $m_1 = m_2$ the solution of the polar-angle dependent differential equation is

$$\Theta_m^l(\vartheta) = \sqrt{\frac{2m+1}{2} \frac{(m-l)!}{(m+l)!}} \, P_m^l(\cos(\vartheta)) \tag{A.40}$$

A.5 Bessel's differential equation and spherical Bessel functions

The equations (2.66) share the common structure

$$\left[\frac{\partial^2}{\partial r^2}+\frac{2}{r}\frac{\partial}{\partial r}+\left({k_i}^2-\frac{m\,(m+1)}{r^2}\right)\right]\mathrm{f}\,(r,m,l,\omega)=0 \tag{A.41}$$

After a substitution $\mathrm{z}=\sqrt{k_i r}\,\mathrm{f}(k_i r)$ according to [Arfken and Weber 1995] a differential equation for the new function z is obtained.

$$\left[r^2\frac{\partial^2}{\partial r^2}+r\frac{\partial}{\partial r}+{k_i}^2r^2-\left(m+\frac{1}{2}\right)^2\right]\mathrm{z}\,(k_i r,m,l)=0 \tag{A.42}$$

Clearly, equation (A.42) corresponds to the definition of Bessel's differential equation (A.12) and can be solved with Bessel functions of nonintegral order $m+\frac{1}{2}$. For convenience, the solution of this type of differential equation, spherical Bessel functions are defined. According to [Abramowitz and Stegun 1965] spherical Bessel functions of the first kind $j_m(x)$, of the second kind $y_m(x)$ (spherical Neumann functions) and of the third kind $h_m^{(1)}(x)$ and $h_m^{(2)}(x)$ (spherical Hankel functions) can be defined as

$$j_m(x)=\sqrt{\frac{\pi}{2x}}J_{m+\frac{1}{2}}(x) \tag{A.43a}$$

$$y_m(x)=\sqrt{\frac{\pi}{2x}}Y_{m+\frac{1}{2}}(x) \tag{A.43b}$$

$$h_m^{(1)}(x)=\sqrt{\frac{\pi}{2x}}H^{(1)}_{m+\frac{1}{2}}(x)=j_m(x)+i\;y_m(x) \tag{A.43c}$$

$$h_m^{(2)}(x)=\sqrt{\frac{\pi}{2x}}H^{(2)}_{m+\frac{1}{2}}(x)=j_m(x)-i\;y_m(x) \tag{A.43d}$$

Analogously to Bessel functions for integral values, the pairs $j_m(x)$ and $y_m(x)$ or $h_m^{(1)}(x)$ and $h_m^{(2)}(x)$ form linearly independent solutions of the differential equation for each variable m.

A.6 Stresses in the spherical coordinate system

The relationship between the vector containing the components of the stress tensor $\hat{\boldsymbol{\sigma}}_{\mathbf{s}}$ and the vector of the unknowns $\mathbf{C}_{\mathbf{s}}$ is derived for spherical coordinates analogously to the procedure for Cartesian or cylindrical coordinates. As a result a matrix $\left[\hat{K}_s\right]$ is obtained describing the relationship:

$$\hat{\boldsymbol{\sigma}}_{\mathbf{s}} = \left[\hat{K}_s\right] \mathbf{C}_{\mathbf{s}} \tag{A.44}$$

with the vector of the stresses $\hat{\boldsymbol{\sigma}}_{\mathbf{s}}$

$$\hat{\boldsymbol{\sigma}}_{\mathbf{s}} = \begin{pmatrix} \hat{\sigma}_{rr} \\ \hat{\sigma}_{\vartheta\vartheta} \\ \hat{\sigma}_{\varphi\varphi} \\ \hat{\sigma}_{r\vartheta} \\ \hat{\sigma}_{r\varphi} \\ \hat{\sigma}_{\vartheta\varphi} \end{pmatrix} \tag{A.45}$$

and the vector of the unknowns

$$\mathbf{C}_{\mathbf{s}} = \begin{pmatrix} C_{1lm} \\ C_{2lm} \\ C_{3lm} \\ C_{4lm} \\ C_{5lm} \\ C_{6lm} \end{pmatrix} \tag{A.46}$$

The elements of matrix $\left[\hat{K}_s\right]$ are derived using the material law and the kinematic relations for spherical coordinates in the (r, m, l,ω) domain.

Elements of the matrix $\left[\hat{K}_s\right]$ for the computation of the component $\hat{\sigma}_{rr}$ of the stress tensor:

$$\hat{K}_{s,11} = \left(\frac{m^2-m}{r^2} - \frac{1}{2}|k_s|^2\right) \check{P}^l_m(\cos\vartheta)\ e^{il\varphi}\ 2\mu\ h^{(1)}_m(|k_p|r) + \\ + \frac{2}{r}\ |k_p|\ \check{P}^l_m(\cos\vartheta)\ e^{il\varphi}\ 2\mu\ h^{(1)}_{m+1}(|k_p|r)$$

$$\hat{K}_{s,12} = 0$$

$$\hat{K}_{s,13} = \frac{m^3-m}{r^2}\ \check{P}^l_m(\cos\vartheta)\ e^{il\varphi}\ 2\mu\ h^{(1)}_m(|k_s|r) - \\ - \frac{m^2+m}{r}\ |k_s|\ \check{P}^l_m(\cos\vartheta)\ e^{il\varphi}\ 2\mu\ h^{(1)}_{m+1}(|k_s|r)$$

$$\hat{K}_{s,14} = \left(\frac{m^2-m}{r^2} - \frac{1}{2}|k_s|^2\right) \check{P}^l_m(\cos\vartheta)\ e^{il\varphi}\ 2\mu\ h^{(2)}_m(|k_p|r) + \\ + \frac{2}{r}\ |k_p|\ \check{P}^l_m(\cos\vartheta)\ e^{il\varphi}\ 2\mu\ h^{(2)}_{m+1}(|k_p|r)$$

$$\hat{K}_{s,15} = 0$$

$$\hat{K}_{s,16} = \frac{m^3-m}{r^2}\ \check{P}^l_m(\cos\vartheta)\ e^{il\varphi}\ 2\mu\ h^{(2)}_m(|k_s|r) - \\ - \frac{m^2+m}{r}\ |k_s|\ \check{P}^l_m(\cos\vartheta)\ e^{il\varphi}\ 2\mu\ h^{(2)}_{m+1}(|k_s|r)$$

Elements of the matrix $\left[\hat{K}_s\right]$ for the computation of the component $\hat{\sigma}_{\vartheta\vartheta}$ of the stress tensor:

$$\begin{aligned}\hat{K}_{s,21} = \Bigg[& \left(-\frac{m^2}{r^2} - \frac{1}{2}|k_s|^2 + |k_p|^2 + \frac{l^2 - m\cos^2\vartheta}{r^2\sin^2\vartheta}\right) \check{P}_m^l(\cos\vartheta)\ e^{il\varphi} + \\ & + \frac{(m+l)\cos\vartheta}{r^2\sin^2\vartheta}\ \check{P}_{m-1}^l(\cos\vartheta)\ e^{il\varphi}\Bigg] 2\mu\ h_m^{(1)}(|k_p|r) - \\ & - \frac{1}{r}\ |k_p|\ \check{P}_m^l(\cos\vartheta)\ e^{il\varphi}\ 2\mu\ h_{m+1}^{(1)}(|k_p|r)\end{aligned}$$

$$\hat{K}_{s,22} = \left(i\ \frac{l(m-1)\cos\vartheta}{r\sin^2\vartheta}\ \check{P}_m^l(\cos\vartheta)\ e^{il\varphi} - i\ \frac{l(l+m)}{r\sin^2\vartheta}\ \check{P}_{m-1}^l(\cos\vartheta)\ e^{il\varphi}\right) 2\mu\ h_m^{(1)}(|k_s|r)$$

$$\begin{aligned}\hat{K}_{s,23} = \Bigg[& \left(-\frac{m^3+m^2}{r^2} + \frac{l^2 - m\cos^2\vartheta}{r^2\sin^2\vartheta}(m+1)\right) \check{P}_m^l(\cos\vartheta)\ e^{il\varphi} + \\ & + \frac{(m+l)\cos\vartheta}{r^2\sin^2\vartheta}(m+1)\ \check{P}_{m-1}^l(\cos\vartheta)\ e^{il\varphi}\Bigg] 2\mu\ h_m^{(1)}(|k_s|r) + \\ & + \Bigg[\left(\frac{m^2+m}{r}\ |k_s| - \frac{l^2 - m\cos^2\vartheta}{r\sin^2\vartheta}\ |k_s|\right) \check{P}_m^l(\cos\vartheta)\ e^{il\varphi} - \\ & \quad - \frac{(m+l)\cos\vartheta}{r\sin^2\vartheta}\ |k_s|\ \check{P}_{m-1}^l(\cos\vartheta)\ e^{il\varphi}\Bigg] 2\mu\ h_{m+1}^{(1)}(|k_s|r)\end{aligned}$$

$$\begin{aligned}\hat{K}_{s,24} = \Bigg[& \left(-\frac{m^2}{r^2} - \frac{1}{2}|k_s|^2 + |k_p|^2 + \frac{l^2 - m\cos^2\vartheta}{r^2\sin^2\vartheta}\right) \check{P}_m^l(\cos\vartheta)\ e^{il\varphi} + \\ & + \frac{(m+l)\cos\vartheta}{r^2\sin^2\vartheta}\ \check{P}_{m-1}^l(\cos\vartheta)\ e^{il\varphi}\Bigg] 2\mu\ h_m^{(2)}(|k_p|r) - \\ & - \frac{1}{r}\ |k_p|\ \check{P}_m^l(\cos\vartheta)\ e^{il\varphi}\ 2\mu\ h_{m+1}^{(2)}(|k_p|r)\end{aligned}$$

$$\hat{K}_{s,25} = \left(i\ \frac{l(m-1)\cos\vartheta}{r\sin^2\vartheta}\ \check{P}_m^l(\cos\vartheta)\ e^{il\varphi} - i\ \frac{l(l+m)}{r\sin^2\vartheta}\ \check{P}_{m-1}^l(\cos\vartheta)\ e^{il\varphi}\right) 2\mu\ h_m^{(2)}(|k_s|r)$$

$$\begin{aligned}\hat{K}_{s,26} = \Bigg[& \left(-\frac{m^3+m^2}{r^2} + \frac{l^2 - m\cos^2\vartheta}{r^2\sin^2\vartheta}(m+1)\right) \check{P}_m^l(\cos\vartheta)\ e^{il\varphi} + \\ & + \frac{(m+l)\cos\vartheta}{r^2\sin^2\vartheta}(m+1)\ \check{P}_{m-1}^l(\cos\vartheta)\ e^{il\varphi}\Bigg] 2\mu\ h_m^{(2)}(|k_s|r) + \\ & + \Bigg[\left(\frac{m^2+m}{r}\ |k_s| - \frac{l^2 - m\cos^2\vartheta}{r\sin^2\vartheta}\ |k_s|\right) \check{P}_m^l(\cos\vartheta)\ e^{il\varphi} - \\ & \quad - \frac{(m+l)\cos\vartheta}{r\sin^2\vartheta}\ |k_s|\ \check{P}_{m-1}^l(\cos\vartheta)\ e^{il\varphi}\Bigg] 2\mu\ h_{m+1}^{(2)}(|k_s|r)\end{aligned}$$

Elements of the matrix $\left[\hat{K}_s\right]$ for the computation of the component $\hat{\sigma}_{\varphi\varphi}$ of the stress tensor:

$$\begin{aligned}
\hat{K}_{s,31} = & \Bigg[\left(\frac{m}{r^2} - \frac{1}{2}|k_s|^2 + |k_p|^2 - \frac{l^2 - m\cos^2\vartheta}{r^2\sin^2\vartheta} \right) \check{P}^l_m(\cos\vartheta)\ e^{il\varphi} - \\
& - \frac{(m+l)\cos\vartheta}{r^2\sin^2\vartheta}\ \check{P}^l_{m-1}(\cos\vartheta)\ e^{il\varphi} \Bigg]\ 2\mu\ h^{(1)}_m(|k_p|r) - \\
& - \frac{1}{r}\ |k_p|\ \check{P}^l_m(\cos\vartheta)\ e^{il\varphi}\ 2\mu\ h^{(1)}_{m+1}(|k_p|r)
\end{aligned}$$

$$\hat{K}_{s,32} = \left(-i\ \frac{l(m-1)\cos\vartheta}{r\sin^2\vartheta} \check{P}^l_m(\cos\vartheta)\ e^{il\varphi} + i\ \frac{l(l+m)}{r\sin^2\vartheta}\ \check{P}^l_{m-1}(\cos\vartheta)\ e^{il\varphi} \right) 2\mu\ h^{(1)}_m(|k_s|r)$$

$$\begin{aligned}
\hat{K}_{s,33} = & \Bigg[\left(\frac{m^2+m}{r^2} - \frac{l^2 - m\cos^2\vartheta}{r^2\sin^2\vartheta}(m+1) \right) \check{P}^l_m(\cos\vartheta)\ e^{il\varphi} - \\
& - \frac{(m+l)\cos\vartheta}{r^2\sin^2\vartheta}(m+1)\ \check{P}^l_{m-1}(\cos\vartheta)\ e^{il\varphi} \Bigg] 2\mu\ h^{(1)}_m(|k_s|r) + \\
& + \Bigg(\frac{l^2 - m\cos^2\vartheta}{r\sin^2\vartheta}\ |k_s|\ \check{P}^l_m(\cos\vartheta)\ e^{il\varphi} + \\
& \quad + \frac{(m+l)\cos\vartheta}{r\sin^2\vartheta}\ |k_s|\ \check{P}^l_{m-1}(\cos\vartheta)\ e^{il\varphi} \Bigg) 2\mu\ h^{(1)}_{m+1}(|k_s|r)
\end{aligned}$$

$$\begin{aligned}
\hat{K}_{s,34} = & \Bigg[\left(\frac{m}{r^2} - \frac{1}{2}|k_s|^2 + |k_p|^2 - \frac{l^2 - m\cos^2\vartheta}{r^2\sin^2\vartheta} \right) \check{P}^l_m(\cos\vartheta)\ e^{il\varphi} - \\
& - \frac{(m+l)\cos\vartheta}{r^2\sin^2\vartheta}\ \check{P}^l_{m-1}(\cos\vartheta)\ e^{il\varphi} \Bigg]\ 2\mu\ h^{(2)}_m(|k_p|r) - \\
& - \frac{1}{r}\ |k_p|\ \check{P}^l_m(\cos\vartheta)\ e^{il\varphi}\ 2\mu\ h^{(2)}_{m+1}(|k_p|r)
\end{aligned}$$

$$\hat{K}_{s,35} = \left(-i\ \frac{l(m-1)\cos\vartheta}{r\sin^2\vartheta} \check{P}^l_m(\cos\vartheta)\ e^{il\varphi} + i\ \frac{l(l+m)}{r\sin^2\vartheta}\ \check{P}^l_{m-1}(\cos\vartheta)\ e^{il\varphi} \right) 2\mu\ h^{(2)}_m(|k_s|r)$$

$$\begin{aligned}
\hat{K}_{s,36} = & \Bigg[\left(\frac{m^2+m}{r^2} - \frac{l^2 - m\cos^2\vartheta}{r^2\sin^2\vartheta}(m+1) \right) \check{P}^l_m(\cos\vartheta)\ e^{il\varphi} - \\
& - \frac{(m+l)\cos\vartheta}{r^2\sin^2\vartheta}(m+1)\ \check{P}^l_{m-1}(\cos\vartheta)\ e^{il\varphi} \Bigg] 2\mu\ h^{(2)}_m(|k_s|r) + \\
& + \Bigg(\frac{l^2 - m\cos^2\vartheta}{r\sin^2\vartheta}\ |k_s|\ \check{P}^l_m(\cos\vartheta)\ e^{il\varphi} + \\
& \quad + \frac{(m+l)\cos\vartheta}{r\sin^2\vartheta}\ |k_s|\ \check{P}^l_{m-1}(\cos\vartheta)\ e^{il\varphi} \Bigg) 2\mu\ h^{(2)}_{m+1}(|k_s|r)
\end{aligned}$$

Elements of the matrix $\left[\hat{K}_s\right]$ for the computation of the component $\hat{\sigma}_{r\vartheta}$ of the stress tensor:

$$\begin{aligned}
\hat{K}_{s,41} = &\left(\frac{m\cot\vartheta}{r^2}\ (m-1)\ \check{P}_m^l(\cos\vartheta)\ e^{il\varphi}\ - \right.\\
&\left. -\ \frac{m+l}{r^2\sin\vartheta}\ (m-1)\ \check{P}_{m-1}^l(\cos\vartheta)\ e^{il\varphi}\right) 2\mu\ h_m^{(1)}(|k_p|r)\ + \\
&+\left(-\frac{m\cot\vartheta}{r}\ |k_p|\ \check{P}_m^l(\cos\vartheta)\ e^{il\varphi} + \frac{m+l}{r\sin\vartheta}\ |k_p|\ \check{P}_{m-1}^l(\cos\vartheta)\ e^{il\varphi}\right) 2\mu\ h_{m+1}^{(1)}(|k_p|r)
\end{aligned}$$

$$\begin{aligned}
\hat{K}_{s,42} = &\ i\ \frac{l}{2r\sin\vartheta}\ (m-1)\ \check{P}_m^l(\cos\vartheta)\ e^{il\varphi}\ 2\mu\ h_m^{(1)}(|k_s|r)\ - \\
&-\ i\ \frac{l}{2\sin\vartheta}\ |k_s|\ \check{P}_m^l(\cos\vartheta)\ e^{il\varphi}\ 2\mu\ h_{m+1}^{(1)}(|k_s|r)
\end{aligned}$$

$$\begin{aligned}
\hat{K}_{s,43} = &\left[m\cot\vartheta\left(\frac{m^2-1}{r^2} - \frac{1}{2}\ |k_s|^2\right)\check{P}_m^l(\cos\vartheta)\ e^{il\varphi}\ - \right.\\
&\left. -\ \frac{m+l}{\sin\vartheta}\left(\frac{m^2-1}{r^2} - \frac{1}{2}\ |k_s|^2\right)\check{P}_{m-1}^l(\cos\vartheta)\ e^{il\varphi}\right] 2\mu\ h_m^{(1)}(|k_s|r)\ + \\
&+\left(\frac{m\cot\vartheta}{r}\ |k_s|\ \check{P}_m^l(\cos\vartheta)\ e^{il\varphi} - \frac{m+l}{r\sin\vartheta}\ |k_s|\ \check{P}_{m-1}^l(\cos\vartheta)\ e^{il\varphi}\right) 2\mu\ h_{m+1}^{(1)}(|k_s|r)
\end{aligned}$$

$$\begin{aligned}
\hat{K}_{s,44} = &\left(\frac{m\cot\vartheta}{r^2}\ (m-1)\ \check{P}_m^l(\cos\vartheta)\ e^{il\varphi}\ - \right.\\
&\left. -\ \frac{m+l}{r^2\sin\vartheta}\ (m-1)\ \check{P}_{m-1}^l(\cos\vartheta)\ e^{il\varphi}\right) 2\mu\ h_m^{(2)}(|k_p|r)\ + \\
&+\left(-\frac{m\cot\vartheta}{r}\ |k_p|\ \check{P}_m^l(\cos\vartheta)\ e^{il\varphi} + \frac{m+l}{r\sin\vartheta}\ |k_p|\ \check{P}_{m-1}^l(\cos\vartheta)\ e^{il\varphi}\right) 2\mu\ h_{m+1}^{(2)}(|k_p|r)
\end{aligned}$$

$$\begin{aligned}
\hat{K}_{s,45} = &\ i\ \frac{l}{2r\sin\vartheta}\ (m-1)\ \check{P}_m^l(\cos\vartheta)\ e^{il\varphi}\ 2\mu\ h_m^{(2)}(|k_s|r)\ - \\
&-\ i\ \frac{l}{2\sin\vartheta}\ |k_s|\ \check{P}_m^l(\cos\vartheta)\ e^{il\varphi}\ 2\mu\ h_{m+1}^{(2)}(|k_s|r)
\end{aligned}$$

$$\begin{aligned}
\hat{K}_{s,46} = &\left[m\cot\vartheta\left(\frac{m^2-1}{r^2} - \frac{1}{2}\ |k_s|^2\right)\check{P}_m^l(\cos\vartheta)\ e^{il\varphi}\ - \right.\\
&\left. -\ \frac{m+l}{\sin\vartheta}\left(\frac{m^2-1}{r^2} - \frac{1}{2}\ |k_s|^2\right)\check{P}_{m-1}^l(\cos\vartheta)\ e^{il\varphi}\right] 2\mu\ h_m^{(2)}(|k_s|r)\ + \\
&+\left(\frac{m\cot\vartheta}{r}\ |k_s|\ \check{P}_m^l(\cos\vartheta)\ e^{il\varphi} - \frac{m+l}{r\sin\vartheta}\ |k_s|\ \check{P}_{m-1}^l(\cos\vartheta)\ e^{il\varphi}\right) 2\mu\ h_{m+1}^{(2)}(|k_s|r)
\end{aligned}$$

Elements of the matrix $\left[\hat{K}_s\right]$ for the computation of the component $\hat{\sigma}_{r\varphi}$ of the stress tensor:

$$\begin{aligned}\hat{K}_{s,51} = {} & i\ \frac{l}{r^2 \sin\vartheta}\ (m-1)\ \check{P}_m^l(\cos\vartheta)\ e^{il\varphi}\ 2\mu\ h_m^{(1)}(|k_p|r) - \\ & - i\ \frac{l}{r\sin\vartheta}\ |k_p|\ \check{P}_m^l(\cos\vartheta)\ e^{il\varphi}\ 2\mu\ h_{m+1}^{(1)}(|k_p|r)\end{aligned}$$

$$\begin{aligned}\hat{K}_{s,52} = {} & \Bigg(- \frac{m\cos\vartheta}{2r\sin\vartheta}\ (m-1)\ \check{P}_m^l(\cos\vartheta)\ e^{il\varphi} + \\ & \quad + \frac{m+l}{2r\sin\vartheta}\ (m-1)\ \check{P}_{m-1}^l(\cos\vartheta)\ e^{il\varphi}\Bigg) 2\mu\ h_m^{(1)}(|k_s|r) + \\ & + \left(\frac{m\cos\vartheta}{2\sin\vartheta}\ |k_s|\ \check{P}_m^l(\cos\vartheta)\ e^{il\varphi} - \frac{m+l}{2\sin\vartheta}\ |k_s|\ \check{P}_{m-1}^l(\cos\vartheta)\ e^{il\varphi}\right) 2\mu\ h_{m+1}^{(1)}(|k_s|r)\end{aligned}$$

$$\begin{aligned}\hat{K}_{s,53} = {} & i\ \frac{l}{\sin\vartheta}\left(\frac{m^2-1}{r^2} - \frac{1}{2}|k_s|^2\right) \check{P}_m^l(\cos\vartheta)\ e^{il\varphi}\ 2\mu\ h_m^{(1)}(|k_s|r) + \\ & + i\ \frac{l}{r\sin\vartheta}\ |k_s|\ \check{P}_m^l(\cos\vartheta)\ e^{il\varphi}\ 2\mu\ h_{m+1}^{(1)}(|k_s|r)\end{aligned}$$

$$\begin{aligned}\hat{K}_{s,54} = {} & i\ \frac{l}{r^2 \sin\vartheta}\ (m-1)\ \check{P}_m^l(\cos\vartheta)\ e^{il\varphi}\ 2\mu\ h_m^{(2)}(|k_p|r) - \\ & - i\ \frac{l}{r\sin\vartheta}\ |k_p|\ \check{P}_m^l(\cos\vartheta)\ e^{il\varphi}\ 2\mu\ h_{m+1}^{(2)}(|k_p|r)\end{aligned}$$

$$\begin{aligned}\hat{K}_{s,55} = {} & \Bigg(- \frac{m\cos\vartheta}{2r\sin\vartheta}\ (m-1)\ \check{P}_m^l(\cos\vartheta)\ e^{il\varphi} + \\ & \quad + \frac{m+l}{2r\sin\vartheta}\ (m-1)\ \check{P}_{m-1}^l(\cos\vartheta)\ e^{il\varphi}\Bigg) 2\mu\ h_m^{(2)}(|k_s|r) + \\ & + \left(\frac{m\cos\vartheta}{2\sin\vartheta}\ |k_s|\ \check{P}_m^l(\cos\vartheta)\ e^{il\varphi} - \frac{m+l}{2\sin\vartheta}\ |k_s|\ \check{P}_{m-1}^l(\cos\vartheta)\ e^{il\varphi}\right) 2\mu\ h_{m+1}^{(2)}(|k_s|r)\end{aligned}$$

$$\begin{aligned}\hat{K}_{s,56} = {} & i\ \frac{l}{\sin\vartheta}\left(\frac{m^2-1}{r^2} - \frac{1}{2}|k_s|^2\right) \check{P}_m^l(\cos\vartheta)\ e^{il\varphi}\ 2\mu\ h_m^{(2)}(|k_s|r) + \\ & + i\ \frac{l}{r\sin\vartheta}\ |k_s|\ \check{P}_m^l(\cos\vartheta)\ e^{il\varphi}\ 2\mu\ h_{m+1}^{(2)}(|k_s|r)\end{aligned}$$

Elements of the matrix $\left[\hat{K}_s\right]$ for the computation of the component $\hat{\sigma}_{\vartheta\varphi}$ of the stress tensor:

$$\hat{K}_{s,61} = \left(i\ \frac{l(m-1)\cos\vartheta}{r^2\sin^2\vartheta}\ \check{P}^l_m(\cos\vartheta)\ e^{il\varphi} - i\ \frac{l(m+l)}{r^2\sin^2\vartheta}\ \check{P}^l_{m-1}(\cos\vartheta)\ e^{il\varphi} \right) 2\mu\ h^{(1)}_m(|k_p|r)$$

$$\begin{aligned} \hat{K}_{s,62} = \Bigg[& \left(\frac{m^2-m}{2r} + \frac{m-l^2}{r\sin^2\vartheta} \right) \check{P}^l_m(\cos\vartheta)\ e^{il\varphi} - \\ & - \frac{(m+l)\cos\vartheta}{r\sin^2\vartheta}\ \check{P}^l_{m-1}(\cos\vartheta)\ e^{il\varphi} \Bigg] 2\mu\ h^{(1)}_m(|k_s|r) \end{aligned}$$

$$\begin{aligned} \hat{K}_{s,63} = \Bigg(& i\ \frac{l(m-1)\cos\vartheta}{r^2\sin^2\vartheta}\ (m+1)\ \check{P}^l_m(\cos\vartheta)\ e^{il\varphi} - \\ & - i\ \frac{l(m+l)}{r^2\sin^2\vartheta}\ (m+1)\ \check{P}^l_{m-1}(\cos\vartheta)\ e^{il\varphi} \Bigg) 2\mu\ h^{(1)}_m(|k_s|r) + \\ & + \Bigg(- i\ \frac{l(m-1)\cos\vartheta}{r\sin^2\vartheta}\ |k_s|\ \check{P}^l_m(\cos\vartheta)\ e^{il\varphi} + \\ & + i\ \frac{l(m+l)}{r\sin^2\vartheta}\ |k_s|\ \check{P}^l_{m-1}(\cos\vartheta)\ e^{il\varphi} \Bigg) 2\mu\ h^{(1)}_{m+1}(|k_s|r) \end{aligned}$$

$$\hat{K}_{s,64} = \left(i\ \frac{l(m-1)\cos\vartheta}{r^2\sin^2\vartheta}\ \check{P}^l_m(\cos\vartheta)\ e^{il\varphi} - i\ \frac{l(m+l)}{r^2\sin^2\vartheta}\ \check{P}^l_{m-1}(\cos\vartheta)\ e^{il\varphi} \right) 2\mu\ h^{(2)}_m(|k_p|r)$$

$$\begin{aligned} \hat{K}_{s,65} = \Bigg[& \left(\frac{m^2-m}{2r} + \frac{m-l^2}{r\sin^2\vartheta} \right) \check{P}^l_m(\cos\vartheta)\ e^{il\varphi} - \\ & - \frac{(m+l)\cos\vartheta}{r\sin^2\vartheta}\ \check{P}^l_{m-1}(\cos\vartheta)\ e^{il\varphi} \Bigg] 2\mu\ h^{(2)}_m(|k_s|r) \end{aligned}$$

$$\begin{aligned} \hat{K}_{s,66} = \Bigg(& i\ \frac{l(m-1)\cos\vartheta}{r^2\sin^2\vartheta}\ (m+1)\ \check{P}^l_m(\cos\vartheta)\ e^{il\varphi} - \\ & - i\ \frac{l(m+l)}{r^2\sin^2\vartheta}\ (m+1)\ \check{P}^l_{m-1}(\cos\vartheta)\ e^{il\varphi} \Bigg) 2\mu\ h^{(2)}_m(|k_s|r) + \\ & + \Bigg(- i\ \frac{l(m-1)\cos\vartheta}{r\sin^2\vartheta}\ |k_s|\ \check{P}^l_m(\cos\vartheta)\ e^{il\varphi} + \\ & + i\ \frac{l(m+l)}{r\sin^2\vartheta}\ |k_s|\ \check{P}^l_{m-1}(\cos\vartheta)\ e^{il\varphi} \Bigg) 2\mu\ h^{(2)}_{m+1}(|k_s|r) \end{aligned}$$

A.7 Coefficients of the superposition matrices

Equation (3.5) describes the equilibrium on the halfspace surface Λ and the cylindrical coupling surface Γ. Matrix $\left[\hat{S}_{ITM}\right]$ contains the stresses on the two surfaces Λ and Γ that arise if unit loads are applied. The matrices $\left[\hat{S}_{\alpha\beta_{ITM}}\right]$ have the form

$$\left[\hat{S}_{\Lambda\Lambda_{ITM}}\right] = \begin{bmatrix} \hat{\sigma}_{zz}(s_1) & 0 & 0 & 0 & 0 & 0 & \cdots \\ 0 & \hat{\sigma}_{yz}(s_1) & 0 & 0 & 0 & 0 & \cdots \\ 0 & 0 & \hat{\sigma}_{xz}(s_1) & 0 & 0 & 0 & \cdots \\ 0 & 0 & 0 & \hat{\sigma}_{zz}(s_2) & 0 & 0 & \cdots \\ 0 & 0 & 0 & 0 & \hat{\sigma}_{yz}(s_2) & 0 & \cdots \\ 0 & 0 & 0 & 0 & 0 & \hat{\sigma}_{xz}(s_2) & \cdots \\ \vdots & \vdots & \vdots & \vdots & \vdots & \vdots & \end{bmatrix} \tag{A.47}$$

$$\left[\hat{S}_{\Lambda\Gamma_{ITM}}\right] = \begin{bmatrix} \hat{\sigma}_{zz}^{(rr,n_1)}(s_1) & \hat{\sigma}_{zz}^{(xr,n_1)}(s_1) & \hat{\sigma}_{zz}^{(\varphi r,n_1)}(s_1) & \hat{\sigma}_{zz}^{(rr,n_2)}(s_1) & \hat{\sigma}_{zz}^{(xr,n_2)}(s_1) & \hat{\sigma}_{zz}^{(\varphi r,n_2)}(s_1) & \cdots \\ \hat{\sigma}_{yz}^{(rr,n_1)}(s_1) & \hat{\sigma}_{yz}^{(xr,n_1)}(s_1) & \hat{\sigma}_{yz}^{(\varphi r,n_1)}(s_1) & \hat{\sigma}_{yz}^{(rr,n_2)}(s_1) & \hat{\sigma}_{yz}^{(xr,n_2)}(s_1) & \hat{\sigma}_{yz}^{(\varphi r,n_2)}(s_1) & \cdots \\ \hat{\sigma}_{xz}^{(rr,n_1)}(s_1) & \hat{\sigma}_{xz}^{(xr,n_1)}(s_1) & \hat{\sigma}_{xz}^{(\varphi r,n_1)}(s_1) & \hat{\sigma}_{xz}^{(rr,n_2)}(s_1) & \hat{\sigma}_{xz}^{(xr,n_2)}(s_1) & \hat{\sigma}_{xz}^{(\varphi r,n_2)}(s_1) & \cdots \\ \hat{\sigma}_{zz}^{(rr,n_1)}(s_2) & \hat{\sigma}_{zz}^{(xr,n_1)}(s_2) & \hat{\sigma}_{zz}^{(\varphi r,n_1)}(s_2) & \hat{\sigma}_{zz}^{(rr,n_2)}(s_2) & \hat{\sigma}_{zz}^{(xr,n_2)}(s_2) & \hat{\sigma}_{zz}^{(\varphi r,n_2)}(s_2) & \cdots \\ \hat{\sigma}_{yz}^{(rr,n_1)}(s_2) & \hat{\sigma}_{yz}^{(xr,n_1)}(s_2) & \hat{\sigma}_{yz}^{(\varphi r,n_1)}(s_2) & \hat{\sigma}_{yz}^{(rr,n_2)}(s_2) & \hat{\sigma}_{yz}^{(xr,n_2)}(s_2) & \hat{\sigma}_{yz}^{(\varphi r,n_2)}(s_2) & \cdots \\ \hat{\sigma}_{xz}^{(rr,n_1)}(s_2) & \hat{\sigma}_{xz}^{(xr,n_1)}(s_2) & \hat{\sigma}_{xz}^{(\varphi r,n_1)}(s_2) & \hat{\sigma}_{xz}^{(rr,n_2)}(s_2) & \hat{\sigma}_{xz}^{(xr,n_2)}(s_2) & \hat{\sigma}_{xz}^{(\varphi r,n_2)}(s_2) & \cdots \\ \vdots & \vdots & \vdots & \vdots & \vdots & \vdots & \end{bmatrix} \tag{A.48}$$

$$\left[\hat{S}_{\Gamma\Lambda_{ITM}}\right] = \begin{bmatrix} \hat{\sigma}_{rr}^{(zz,s_1)}(n_1) & \hat{\sigma}_{rr}^{(yz,s_1)}(n_1) & \hat{\sigma}_{rr}^{(xz,s_1)}(n_1) & \hat{\sigma}_{rr}^{(zz,s_2)}(n_1) & \hat{\sigma}_{rr}^{(yz,s_2)}(n_1) & \hat{\sigma}_{rr}^{(xz,s_2)}(n_1) & \cdots \\ \hat{\sigma}_{xr}^{(zz,s_1)}(n_1) & \hat{\sigma}_{xr}^{(yz,s_1)}(n_1) & \hat{\sigma}_{xr}^{(xz,s_1)}(n_1) & \hat{\sigma}_{xr}^{(zz,s_2)}(n_1) & \hat{\sigma}_{xr}^{(yz,s_2)}(n_1) & \hat{\sigma}_{xr}^{(xz,s_2)}(n_1) & \cdots \\ \hat{\sigma}_{\varphi r}^{(zz,s_1)}(n_1) & \hat{\sigma}_{\varphi r}^{(yz,s_1)}(n_1) & \hat{\sigma}_{\varphi r}^{(xz,s_1)}(n_1) & \hat{\sigma}_{\varphi r}^{(zz,s_2)}(n_1) & \hat{\sigma}_{\varphi r}^{(yz,s_2)}(n_1) & \hat{\sigma}_{\varphi r}^{(xz,s_2)}(n_1) & \cdots \\ \hat{\sigma}_{rr}^{(zz,s_1)}(n_2) & \hat{\sigma}_{rr}^{(yz,s_1)}(n_2) & \hat{\sigma}_{rr}^{(xz,s_1)}(n_2) & \hat{\sigma}_{rr}^{(zz,s_2)}(n_2) & \hat{\sigma}_{rr}^{(yz,s_2)}(n_2) & \hat{\sigma}_{rr}^{(xz,s_2)}(n_2) & \cdots \\ \hat{\sigma}_{xr}^{(zz,s_1)}(n_2) & \hat{\sigma}_{xr}^{(yz,s_1)}(n_2) & \hat{\sigma}_{xr}^{(xz,s_1)}(n_2) & \hat{\sigma}_{xr}^{(zz,s_2)}(n_2) & \hat{\sigma}_{xr}^{(yz,s_2)}(n_2) & \hat{\sigma}_{xr}^{(xz,s_2)}(n_2) & \cdots \\ \hat{\sigma}_{\varphi r}^{(zz,s_1)}(n_2) & \hat{\sigma}_{\varphi r}^{(yz,s_1)}(n_2) & \hat{\sigma}_{\varphi r}^{(xz,s_1)}(n_2) & \hat{\sigma}_{\varphi r}^{(zz,s_2)}(n_2) & \hat{\sigma}_{\varphi r}^{(yz,s_2)}(n_2) & \hat{\sigma}_{\varphi r}^{(xz,s_2)}(n_2) & \cdots \\ \vdots & \vdots & \vdots & \vdots & \vdots & \vdots & \end{bmatrix} \tag{A.49}$$

$$\left[\hat{S}_{\Gamma\Gamma_{ITM}}\right] = \begin{bmatrix} \hat{\sigma}_{rr}(n_1) & 0 & 0 & 0 & 0 & 0 & \cdots \\ 0 & \hat{\sigma}_{xr}(n_1) & 0 & 0 & 0 & 0 & \cdots \\ 0 & 0 & \hat{\sigma}_{\varphi r}(n_1) & 0 & 0 & 0 & \cdots \\ 0 & 0 & 0 & \hat{\sigma}_{rr}(n_2) & 0 & 0 & \cdots \\ 0 & 0 & 0 & 0 & \hat{\sigma}_{xr}(n_2) & 0 & \cdots \\ 0 & 0 & 0 & 0 & 0 & \hat{\sigma}_{\varphi r}(n_2) & \cdots \\ \vdots & \vdots & \vdots & \vdots & \vdots & \vdots & \end{bmatrix} \tag{A.50}$$

The vector of the unknown amplitudes of the loads on the surfaces Λ and Γ is

$$\mathbf{C}^T = \begin{pmatrix} C_{zz}(s_1) & C_{yz}(s_1) & C_{xz}(s_1) & C_{zz}(s_2) & \cdots & C_{rr}(n_1) & C_{xr}(n_1) & C_{\varphi r}(n_1) & C_{rr}(n_2) & \cdots \end{pmatrix} \tag{A.51}$$

The vector of the external loads on the surfaces Λ and Γ is

$$\begin{aligned} \hat{\mathbf{P}}_{\mathbf{ITM}}{}^T = -\Big(& \hat{p}_{z,\Lambda}(s_1) \quad \hat{p}_{y,\Lambda}(s_1) \quad \hat{p}_{x,\Lambda}(s_1) \quad \hat{p}_{z,\Lambda}(s_2) \quad \cdots \\ & \hat{p}_{r,\Gamma}(n_1) \quad \hat{p}_{x,\Gamma}(n_1) \quad \hat{p}_{\varphi,\Gamma}(n_1) \quad \hat{p}_{r,\Gamma}(n_2) \quad \cdots \Big) \end{aligned} \tag{A.52}$$

Equation (3.11) describes the dependency of the displacements on the halfspace surface Λ and the cylindrical coupling surface Γ on the vector of the unknowns $\mathbf{C}$. Matrix $\left[\hat{U}_{ITM}\right]$ contains the respective relationships. The matrices $\left[\hat{U}_{\alpha\beta_{ITM}}\right]$ have the form

$$\left[\hat{U}_{\Lambda\Lambda_{ITM}}\right] = \begin{bmatrix} \hat{u}_z^{(zz,s_1)}(s_1) & \hat{u}_z^{(yz,s_1)}(s_1) & \hat{u}_z^{(xz,s_1)}(s_1) & 0 & 0 & 0 & \cdots \\ \hat{u}_y^{(zz,s_1)}(s_1) & \hat{u}_y^{(yz,s_1)}(s_1) & \hat{u}_y^{(xz,s_1)}(s_1) & 0 & 0 & 0 & \cdots \\ \hat{u}_x^{(zz,s_1)}(s_1) & \hat{u}_x^{(yz,s_1)}(s_1) & \hat{u}_x^{(xz,s_1)}(s_1) & 0 & 0 & 0 & \cdots \\ 0 & 0 & 0 & \hat{u}_z^{(zz,s_2)}(s_2) & \hat{u}_z^{(yz,s_2)}(s_2) & \hat{u}_z^{(xz,s_2)}(s_2) & \cdots \\ 0 & 0 & 0 & \hat{u}_y^{(zz,s_2)}(s_2) & \hat{u}_y^{(yz,s_2)}(s_2) & \hat{u}_y^{(xz,s_2)}(s_2) & \cdots \\ 0 & 0 & 0 & \hat{u}_x^{(zz,s_2)}(s_2) & \hat{u}_x^{(yz,s_2)}(s_2) & \hat{u}_x^{(xz,s_2)}(s_2) & \cdots \\ \vdots & \vdots & \vdots & \vdots & \vdots & \vdots & \end{bmatrix} \tag{A.53}$$

$$\left[\hat{U}_{\Lambda\Gamma_{ITM}}\right] = \begin{bmatrix} \hat{u}_z^{(rr,n_1)}(s_1) & \hat{u}_z^{(xr,n_1)}(s_1) & \hat{u}_z^{(\varphi r,n_1)}(s_1) & \hat{u}_z^{(rr,n_2)}(s_1) & \hat{u}_z^{(xr,n_2)}(s_1) & \hat{u}_z^{(\varphi r,n_2)}(s_1) & \cdots \\ \hat{u}_y^{(rr,n_1)}(s_1) & \hat{u}_y^{(xr,n_1)}(s_1) & \hat{u}_y^{(\varphi r,n_1)}(s_1) & \hat{u}_y^{(rr,n_2)}(s_1) & \hat{u}_y^{(xr,n_2)}(s_1) & \hat{u}_y^{(\varphi r,n_2)}(s_1) & \cdots \\ \hat{u}_x^{(rr,n_1)}(s_1) & \hat{u}_x^{(xr,n_1)}(s_1) & \hat{u}_x^{(\varphi r,n_1)}(s_1) & \hat{u}_x^{(rr,n_2)}(s_1) & \hat{u}_x^{(xr,n_2)}(s_1) & \hat{u}_x^{(\varphi r,n_2)}(s_1) & \cdots \\ \hat{u}_z^{(rr,n_1)}(s_2) & \hat{u}_z^{(xr,n_1)}(s_2) & \hat{u}_z^{(\varphi r,n_1)}(s_2) & \hat{u}_z^{(rr,n_2)}(s_2) & \hat{u}_z^{(xr,n_2)}(s_2) & \hat{u}_z^{(\varphi r,n_2)}(s_2) & \cdots \\ \hat{u}_y^{(rr,n_1)}(s_2) & \hat{u}_y^{(xr,n_1)}(s_2) & \hat{u}_y^{(\varphi r,n_1)}(s_2) & \hat{u}_y^{(rr,n_2)}(s_2) & \hat{u}_y^{(xr,n_2)}(s_2) & \hat{u}_y^{(\varphi r,n_2)}(s_2) & \cdots \\ \hat{u}_x^{(rr,n_1)}(s_2) & \hat{u}_x^{(xr,n_1)}(s_2) & \hat{u}_x^{(\varphi r,n_1)}(s_2) & \hat{u}_x^{(rr,n_2)}(s_2) & \hat{u}_x^{(xr,n_2)}(s_2) & \hat{u}_x^{(\varphi r,n_2)}(s_2) & \cdots \\ \vdots & \vdots & \vdots & \vdots & \vdots & \vdots & \end{bmatrix} \tag{A.54}$$

$$\left[\hat{U}_{\Gamma\Lambda_{ITM}}\right] = \begin{bmatrix} \hat{u}_r^{(zz,s_1)}(n_1) & \hat{u}_r^{(yz,s_1)}(n_1) & \hat{u}_r^{(xz,s_1)}(n_1) & \hat{u}_r^{(zz,s_2)}(n_1) & \hat{u}_r^{(yz,s_2)}(n_1) & \hat{u}_r^{(xz,s_2)}(n_1) & \cdots \\ \hat{u}_x^{(zz,s_1)}(n_1) & \hat{u}_x^{(yz,s_1)}(n_1) & \hat{u}_x^{(xz,s_1)}(n_1) & \hat{u}_x^{(zz,s_2)}(n_1) & \hat{u}_x^{(yz,s_2)}(n_1) & \hat{u}_x^{(xz,s_2)}(n_1) & \cdots \\ \hat{u}_\varphi^{(zz,s_1)}(n_1) & \hat{u}_\varphi^{(yz,s_1)}(n_1) & \hat{u}_\varphi^{(xz,s_1)}(n_1) & \hat{u}_\varphi^{(zz,s_2)}(n_1) & \hat{u}_\varphi^{(yz,s_2)}(n_1) & \hat{u}_\varphi^{(xz,s_2)}(n_1) & \cdots \\ \hat{u}_r^{(zz,s_1)}(n_2) & \hat{u}_r^{(yz,s_1)}(n_2) & \hat{u}_r^{(xz,s_1)}(n_2) & \hat{u}_r^{(zz,s_2)}(n_2) & \hat{u}_r^{(yz,s_2)}(n_2) & \hat{u}_r^{(xz,s_2)}(n_2) & \cdots \\ \hat{u}_x^{(zz,s_1)}(n_2) & \hat{u}_x^{(yz,s_1)}(n_2) & \hat{u}_x^{(xz,s_1)}(n_2) & \hat{u}_x^{(zz,s_2)}(n_2) & \hat{u}_x^{(yz,s_2)}(n_2) & \hat{u}_x^{(xz,s_2)}(n_2) & \cdots \\ \hat{u}_\varphi^{(zz,s_1)}(n_2) & \hat{u}_\varphi^{(yz,s_1)}(n_2) & \hat{u}_\varphi^{(xz,s_1)}(n_2) & \hat{u}_\varphi^{(zz,s_2)}(n_2) & \hat{u}_\varphi^{(yz,s_2)}(n_2) & \hat{u}_\varphi^{(xz,s_2)}(n_2) & \cdots \\ \vdots & \vdots & \vdots & \vdots & \vdots & \vdots & \end{bmatrix} \tag{A.55}$$

$$\left[\hat{U}_{\Gamma\Gamma_{ITM}}\right] = \begin{bmatrix} \hat{u}_r^{(rr,n_1)}(n_1) & \hat{u}_r^{(xr,n_1)}(n_1) & \hat{u}_r^{(\varphi r,n_1)}(n_1) & 0 & 0 & 0 & \cdots \\ \hat{u}_x^{(rr,n_1)}(n_1) & \hat{u}_x^{(xr,n_1)}(n_1) & \hat{u}_x^{(\varphi r,n_1)}(n_1) & 0 & 0 & 0 & \cdots \\ \hat{u}_\varphi^{(rr,n_1)}(n_1) & \hat{u}_\varphi^{(xr,n_1)}(n_1) & \hat{u}_\varphi^{(\varphi r,n_1)}(n_1) & 0 & 0 & 0 & \cdots \\ 0 & 0 & 0 & \hat{u}_r^{(rr,n_2)}(n_2) & \hat{u}_r^{(xr,n_2)}(n_2) & \hat{u}_r^{(\varphi r,n_2)}(n_2) & \cdots \\ 0 & 0 & 0 & \hat{u}_x^{(rr,n_2)}(n_2) & \hat{u}_x^{(xr,n_2)}(n_2) & \hat{u}_x^{(\varphi r,n_2)}(n_2) & \cdots \\ 0 & 0 & 0 & \hat{u}_\varphi^{(rr,n_2)}(n_2) & \hat{u}_\varphi^{(xr,n_2)}(n_2) & \hat{u}_\varphi^{(\varphi r,n_2)}(n_2) & \cdots \\ \vdots & \vdots & \vdots & \vdots & \vdots & \vdots & \end{bmatrix} \tag{A.56}$$

A.8 Similarity measures

For the quantitative assessment of the verification example, an assessment of the similarity of vectors is necessary. In figure 6.3, the vertical displacement of the halfspace surface at the coordinate $x = 0$ and at time $t = t_{max}$ is depicted. A comparison of the depicted vectors using different similarity measures is performed in order to assess the sensitivity of the different measures. One of the possible similarity measures is the Pearson correlation coefficient (also named Q correlation coefficient). It is defined for comparing two vectors **a** and **b** with n elements as presented for example in [Backhaus et al 2011] by

$$d_{Pearson} = \frac{\sum\limits_{i=1}^{n} \left(a_i - \overline{a}\right)\left(b_i - \overline{b}\right)}{\sqrt{\sum\limits_{i=1}^{n} \left(a_i - \overline{a}\right)^2 \sum\limits_{i=1}^{n} \left(b_i - \overline{b}\right)^2}} \tag{A.57}$$

where the $\_$ symbol in equation (A.57) denotes the mean values of the vectors **a** and **b**. The Pearson correlation coefficient is appropriate if the similarity between vectors with respect to their similar behavior is to be evaluated. If the similarity of linearly dependent vectors is tested, the Pearson correlation coefficient yields a result of 1 which implies that no difference could be detected that is existing between linearly dependent vectors. Thus, this coefficient is not used in the further scope of this work.

Similarity between two vectors can also be assessed by calculating the cosine of the angle between the two vectors. Thus, the cosine coefficient can be calculated according to [Willet and Winterman 1986] for example as

$$d_{cos} = \frac{\sum\limits_{i=1}^{n} a_i b_i}{\sqrt{\sum\limits_{i=1}^{n} {a_i}^2 \sum\limits_{i=1}^{n} {b_i}^2}} \tag{A.58}$$

A quadratic form of the cosine coefficient, the modal assurance criterion (MAC) is evaluated according to [Allmang 2003] for example as

$$d_{MAC} = \frac{\left|\sum\limits_{i=1}^{n} a_i b_i\right|^2}{\sum\limits_{i=1}^{n} {a_i}^2 \sum\limits_{i=1}^{n} {b_i}^2} \tag{A.59}$$

Both coefficients are able to measure similarity of vectors quantitatively. But for vectors that possess the same phase information and different amplitudes ($\mathbf{b} = \lambda\mathbf{a}$), complete similarity is indicated which is not adequate for the verification example of chapter 6.

Another similarity measure is the Dice coefficient. It is defined, according to [Holliday et al 1995] for example as

$$D_{Dice} = \frac{2\sum\limits_{i=1}^{n} a_i b_i}{\sum\limits_{i=1}^{n} {a_i}^2 + \sum\limits_{i=1}^{n} {b_i}^2} \tag{A.60}$$

For identical vectors **a** and **b** its value reaches 1, for vectors with opposite sign the result of the Dice coefficient is -1. Analogously to [Schneider 2014] the sensitivities of the Dice and Tanimoto coefficients as introduced in section 6.2.2 are compared applying different modifications of a given, exponentially decaying function. As reference solution an exponentially decaying cosine function is defined by

$$y_{ref} = \cos\left(\frac{2\pi}{5}x\right) e^{-|0.2x|} \tag{A.61}$$

As comparison the following functions are chosen.

$$y_{c1} = \cos\left(\frac{2\pi}{5}x - \frac{2\pi}{5}0.1\,(n_1 - 1)\right) e^{-|0.2(x-0.1(n_1-1))|} \tag{A.62}$$

$$y_{c2} = (0.01n_2 - 0.01)\cos\left(\frac{2\pi}{5}x\right) e^{-|0.2x|} \tag{A.63}$$

$$y_{c3} = \begin{cases} \cos\left(\frac{2\pi}{5}x\right) e^{-|0.2x|} & \text{if } x \neq x_{max} \\ (1 + 0.01(n_3 - 1))\cos\left(\frac{2\pi}{5}x\right) e^{-|0.2x|} & \text{if } x = x_{max} \end{cases} \tag{A.64}$$

First, a phase shift is applied on the reference function y_{ref} thus leading to the comparison function y_{c1}. The value of the phase shift depends on the parameter n_1 that is evaluated for values between 1 and 51 which implies a phase shift between 0 and 2π applied in 50 steps.

In the second comparison function y_{c2}, the amplitude of the cosine function is changed depending on the parameter n_2. Values between 1 and 201 are assigned to the parameter n_2 which implies a change of the amplitude of the comparison function between 0 and 2 that is a doubling of the amplitude.

As third comparison function y_{c3}, individual values of the reference function are modified. The extrema of the cosine function are enlarged in a certain ratio defined via the parameter

n_3. n_3 ranges from 1 to 101 which means that the modified individual values change the amplitude of the extrema from a factor 0 to a factor 2.

In the following figures A.3, on the left hand side of each figure, the applied change is exemplarily depicted for one of the parameters n_i each. The right figure represents the respective Dice respectively Tanimoto coefficients.

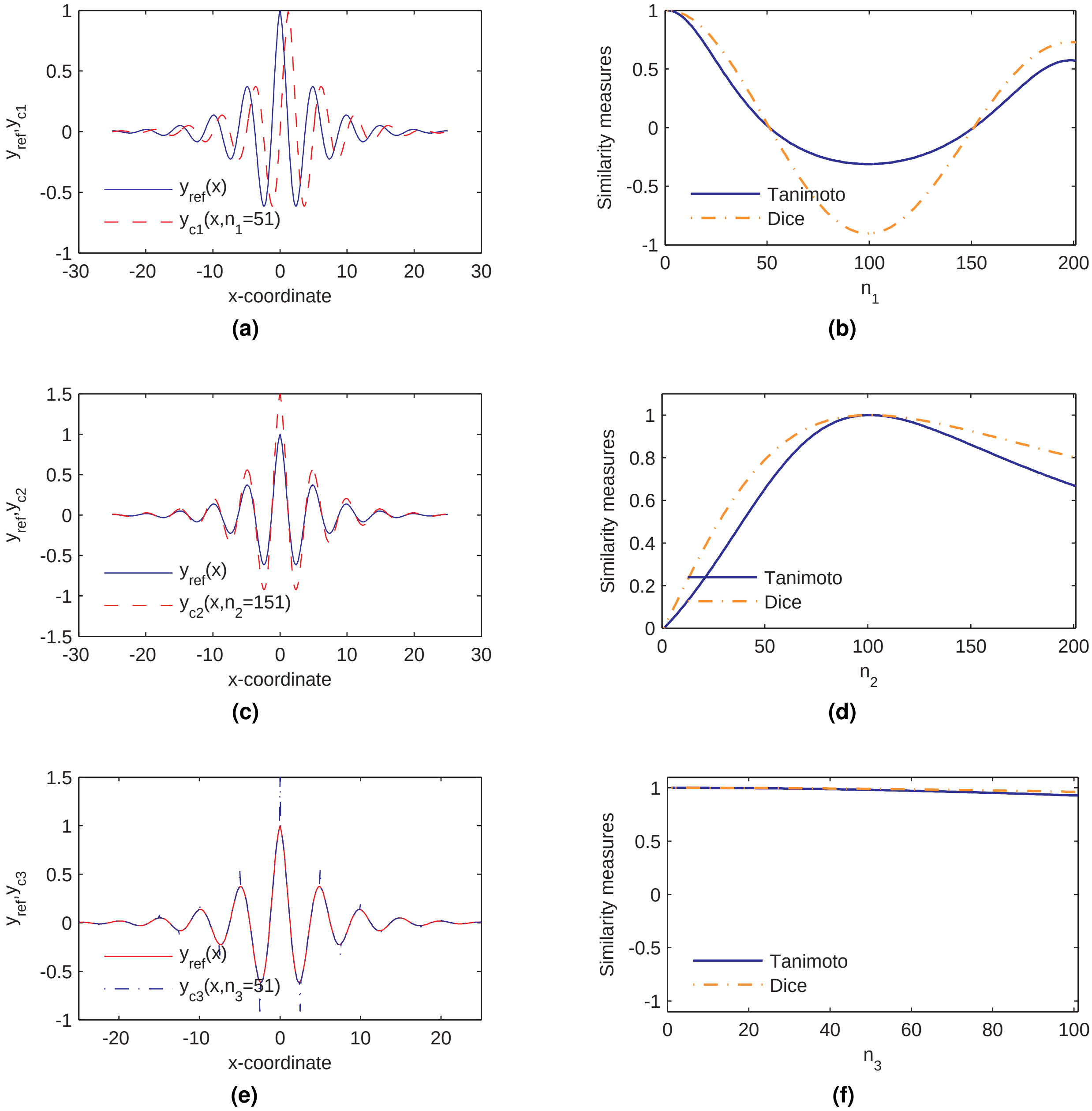

(a) (b) (c) (d) (e) (f)

Figure A.3: Comparison of the Dice and Tanimoto coefficients comparing a reference cosine function y_{ref} with a (A.3b) phase shifted comparison function y_{c1} as depicted in A.3a, with a (A.3d) comparison function y_{c2} with modified amplitude as depicted in A.3c and with a (A.3f) comparison function y_{c3} where the extrema of the cosine function are modified as depicted in A.3e

Comparing the results of the parameter study, it is visible that the Tanimoto coefficient reacts more sensitive if small changes are applied that disturb the similarity of the reference and comparison function. Therefore, the Tanimoto coefficient is chosen to quantify the similarity of the analytical solution and the coupled ITM-FEM solution in the verification example.

A.9 Derivation of the expression of a derived quantity Q as power product of the basic quantities

In equation (6.5) the statement is formulated that each quantity Q can be expressed by a power product of its basic quantities. This relationship is proved for example in [Bridgman and Holl 1932], the derivation shall be presented here for the basic quantities length L, mass M and time T.

Starting point is the description of the value Q_i of quantity Q as a function of the basic quantities L_i, M_i and T_i without further information about the form of this relationship.

$$Q_i = \mathrm{f}\left(L_i, M_i, T_i\right) \tag{A.65}$$

If the units of the basic quantities are multiplied with a constant factor, the values of the basic quantities are correspondingly changed. For example, if the unit of the basic quantity length is multiplied with a constant factor $\frac{1}{a}$, the value of the length is multiplied by a.

$$Q_i = \mathrm{f}\left(aL_i, M_i, T_i\right) \tag{A.66}$$

Now the ratio between two values of the derived function Q_1 and Q_2 shall be considered. This ratio between two values with the same dimension is independent on the dimension and thus independent on a change of the unit of a basic quantity. Therefore, it must be true that

$$\frac{\mathrm{f}\left(L_1, M_1, T_1\right)}{\mathrm{f}\left(L_2, M_2, T_2\right)} = \frac{\mathrm{f}\left(aL_1, M_1, T_1\right)}{\mathrm{f}\left(aL_2, M_2, T_2\right)} \tag{A.67}$$

Equation (A.67) can also be formulated as

$$\mathrm{f}\left(aL_1, M_1, T_1\right) = \mathrm{f}\left(aL_2, M_2, T_2\right) \frac{\mathrm{f}\left(L_1, M_1, T_1\right)}{\mathrm{f}\left(L_2, M_2, T_2\right)} \tag{A.68}$$

If equation (A.68) is derived with respect to a, the following equation is obtained.

$$L_1 \frac{\partial \mathrm{f}\left(aL_1, M_1, T_1\right)}{\partial \left(aL_1\right)} = L_2 \frac{\partial \mathrm{f}\left(aL_2, M_2, T_2\right)}{\partial \left(aL_2\right)} \frac{\mathrm{f}\left(L_1, M_1, T_1\right)}{\mathrm{f}\left(L_2, M_2, T_2\right)} \tag{A.69}$$

As the constant factor a is arbitrary, it is chosen to be equal to 1.

$$L_1 \frac{\partial \mathrm{f}\left(L_1, M_1, T_1\right)}{\partial L_1} = L_2 \frac{\partial \mathrm{f}\left(L_2, M_2, T_2\right)}{\partial L_2} \frac{\mathrm{f}\left(L_1, M_1, T_1\right)}{\mathrm{f}\left(L_2, M_2, T_2\right)} \tag{A.70}$$

Thus, a relationship between the functions f and their first derivatives with respect to the first basic quantity is obtained

$$L_1 \frac{\frac{\partial \mathrm{f}(L_1,M_1,T_1)}{\partial L_1}}{\mathrm{f}\left(L_1, M_1, T_1\right)} = L_2 \frac{\frac{\partial \mathrm{f}(L_2,M_2,T_2)}{\partial L_2}}{\mathrm{f}\left(L_2, M_2, T_2\right)} \tag{A.71}$$

which shall be valid for all values (L_i, M_i, T_i) of the function f. This is only possible if each side of equation (A.71) is a constant factor α' for all i.

$$L_i \frac{\frac{\partial \mathrm{f}(L_i,M_i,T_i)}{\partial L_i}}{\mathrm{f}\left(L_i, M_i, T_i\right)} = \alpha' \tag{A.72}$$

Equation (A.72) can also be formulated as

$$\frac{\mathrm{f}\left(L_i, M_i, T_i\right)}{\partial \,\mathrm{f}\left(L_i, M_i, T_i\right)} = \alpha \frac{L_i}{\partial L_i} \qquad \text{with } \alpha = \frac{1}{\alpha'} \tag{A.73}$$

Thus, function f can be expressed as the power of the basic quantity L_i multiplied with an integration constant C_L.

$$\mathrm{f}\left(L_i, M_i, T_i\right) = C_L L_i^{\alpha} \tag{A.74}$$

If this procedure is repeated for the basic quantities M_i and T_i, equation (6.5) is obtained.

$$Q_i = C\ {L_i}^{\alpha} {M_i}^{\beta} {T_i}^{\gamma} \tag{A.75}$$

Bibliography

[Abdel-Fattah et al 2000] Abdel-Fattah, T.T ; Hodhod, H.A ; Akl, A.Y: A novel formulation of infinite elements for static analysis. In: *Computers and Structures* Volume 77. 2000, p. 371–379

[Abramowitz and Stegun 1965] Abramowitz, M. ; Stegun, I. A.: *Handbook of mathematical functions: with formulas, graphs, and mathematical tables.* New York : Dover Publications, 1965

[Allmang 2003] Allmang, R. J.: The modal assurance criterion – Twenty years of use and abuse. In: *Journal of Sound and Vibration* Volume 37. 2003, p. 14–21

[Andersen and Nielsen 2003] Andersen, L. ; Nielsen, S. R. K.: Boundary element analysis of the steady-state response of an elastic half-space to a moving force on its surface. In: *Engineering Analysis with Boundary Elements* Volume 27. 2003, p. 23–38

[ANSYS 2012] ANSYS, Inc.: *ANSYS Mechanical user's guide: Documentation for ANSYS 14.* 2012

[Arens 2013] Arens, T.: *Mathematik.* 2. Auflage. Heidelberg : Spektrum Akad. Verl, 2013. – ISBN 978-3-8274-2347-4

[Arfken and Weber 1995] Arfken, G. B. ; Weber, H.-J.: *Mathematical methods for physicists.* 4. ed. San Diego : Acad. Press, 1995. – ISBN 0120598159

[Arias and Achenbach 2004] Arias, I. ; Achenbach, J. D.: Rayleigh wave correction for the BEM analysis of two-dimensional elastodynamic problems in a half-space. In: *International Journal for Numerical Methods in Engineering* Volume 60. 2004, p. 1–16

[Backhaus et al 2011] Backhaus, K. ; Erichson, B. ; Weiber, R.: *Fortgeschrittene multivariate Analysemethoden: Eine anwendungsorientierte Einführung: Erg. zu: Multivariate Analysemethoden. - Literaturangaben.* Berlin : Springer, 2011. – ISBN 9783642152481

[Baffet et al 2012] Baffet, D. ; Bielak, J. ; Givoli, D. ; Hagstrom, T. ; Rabinovich, D.: Long-time stable high-order absorbing boundary conditions for elastodynamics. In: *Computer Methods in Applied Mechanics and Engineering* Volume 241-244. 2012, p. 20–37

[Basu and Chopra 2003] Basu, U. ; Chopra, A. K.: Perfectly matched layers for time-harmonic elastodynamics of unbounded domains: theory and finite-element implementation. In: *Computer Methods in Applied Mechanics and Engineering* Volume 192. 2003, p. 1337–1375

[Bathe and Zimmermann 2002] Bathe, K.-J. ; Zimmermann, P.: *Finite-Elemente-Methoden.* 2., vollst. neu bearb. und erw. Aufl. Berlin : Springer, 2002. – ISBN 3-540-66806-3

[Bécache et al 2003] Bécache, E. ; Fauqueux, S. ; Joly, P.: Stability of perfectly matched layers, group velocities and anisotropic waves. In: *Journal of Computational Physics* Volume 188. 2003, p. 399–433

[Beer and Watson 1989] Beer, G. ; Watson, J. O.: Infinite boundary elements. In: *International Journal for Numerical Methods in Engineering* Volume 28. 1989, p. 1233–1247

[Ben-Israel and Greville 2003] Ben-Israel, A. ; Greville, T. N. E.: *Generalized inverses: Theory and applications.* Second Edition. New York, NY : Springer New York, 2003. – ISBN 0-387-00293-6

[Berenger 1994] Berenger, J-P.: A perfectly matched layer for the absorption of electromagnetic waves. In: *Journal of Computational Physics* Volume 114. 1994, p. 185–200

[Bettess 1977] Bettess, P.: Infinite elements. In: *International Journal for Numerical Methods in Engineering* Volume 11. 1977, p. 53–64

[Bettess and Bettess 1984] Bettess, P. ; Bettess, J. A.: Infinite elements for static problems. In: *Engineering Computations* Volume 1. 1984, p. 4–16

[Bettess and Bettess 1991] Bettess, P. ; Bettess, J. A.: Infinite elements for dynamic problems: Part 1 and Part 2. In: *Engineering Computations* Volume 8. 1991, p. 99–151

[Bock 1974] Bock, H. H.: *Automatische Klassifikation: Theoretische und praktische Methoden zur Gruppierung und Strukturierung von Daten ; (Cluster-Analyse).* Volume 24. Göttingen : Vandenhoeck & Ruprecht, 1974. – ISBN 3525401302

[Bonnet et al 1998] Bonnet, M. ; Maier, G. ; Polizzotto, C.: Symmetric Galerkin boundary element method. In: *Applied Mechanics Reviews* Volume 51. 1998, p. 669–704

[Bortz and Schuster 2010] Bortz, J. ; Schuster, C.: *Statistik für Human- und Sozialwissenschaftler.* 7., vollst. überarb. und erw. Aufl. Berlin : Springer, 2010. – ISBN 9783642127694

[Brebbia and Georgiou 1979] Brebbia, C. A. ; Georgiou, P.: Combination of boundary and finite elements in elastostatics. In: *Applied Mathematical Modelling* Volume 3. 1979, p. 212–220

[Bridgman and Holl 1932] Bridgman, P. W. ; Holl, H.: *Theorie der physikalischen Dimensionen: Ähnlichkeitsbetrachtungen in der Physik.* Leipzig und Berlin : Teubner, 1932

[Brigham 2010] Brigham, E. O.: *FFT-Anwendungen.* München : Oldenbourg, 2010. – ISBN 9783486215670

[Bronstein et al 2006] Bronstein, I. N. ; Semendjajev, K. A. ; Musiol, G. ; Mühlig, H.: *Taschenbuch der Mathematik*. Nachdr. der 6., vollst. überarb. und erg. Aufl. Frankfurt am Main : Deutsch, 2006. – ISBN 9783817120062

[Buchschmid 2002] Buchschmid, M.: *Geschlossene Lösung des Systems: Halbscheibe mit Loch*. Technische Universität München, Diplomarbeit, 2002

[Buckingham 1914] Buckingham, E.: On physically similar systems: Illustrations of the use of dimensional equations. In: *Physical Review* Volume 4. 1914, p. 345–376

[Carrer and Mansur 1996] Carrer, J. A. M. ; Mansur, W. J.: Time-domain BEM analysis for the 2D scalar wave equation: Initial conditions contributions to space and time derivatives. In: *International Journal for Numerical Methods in Engineering* Volume 39. 1996, p. 2169–2188

[Clayton and Engquist 1977] Clayton, R. ; Engquist, B.: Absorbing boundary conditions for acoustic and elastic wave equations. In: *Bulletin of the Seismological Society of America* Volume 67. 1977, p. 1529–1540

[Clouteau et al 2005] Clouteau, D. ; Arnst, M. ; Al-Hussaini, T. M. ; Degrande, G.: Freefield vibrations due to dynamic loading on a tunnel embedded in a stratified medium. In: *Journal of Sound and Vibration* Volume 283. 2005, p. 173–199

[Clouteau et al 2013] Clouteau, D. ; Cottereau, R. ; Lombaert, G.: Dynamics of structures coupled with elastic media - A review of numerical models and methods. In: *Journal of Sound and Vibration* Volume 332. 2013, p. 2415–2436

[Clouteau et al 2000] Clouteau, D. ; Elhabre, M. L. ; Aubry, D.: Periodic BEM and FEM-BEM coupling: Application to seismic behaviour of very long structures. In: *Computational Mechanics* Volume 25. 2000, p. 567–577

[Clouteau et al 2006] Clouteau, D. ; Othman, R. ; Arnst, M. ; Chebli, H. ; Degrande, G. ; Klein, R. ; Chatterjee, P. ; Janssens, B.: A numerical model for ground-borne vibrations from underground railway traffic based on a periodic FE-BE formulation. In: *Journal of Sound and Vibration* Volume 293. 2006, p. 645–666

[Collino 1993] Collino, F.: High order absorbing boundary conditions for wave propagation models: Straight line boundary and corner cases. In: *Mathematical and Numerical Aspects of Wave Propagation*. 1993, p. 161–171

[Coulier et al 2011] Coulier, P. ; Degrande, G. ; Dijckmans, A. ; Houbrechts, J. ; Lombaert, G. ; Rücker, W. ; Auersch, L. ; Rodríguez Plaza, M. ; Cuellar, V. ; Thompson, D. J. ; Ekblad, A. ; Smekal, A.: *Scope of the parametric study on mitigation measures on the transmission path: RIVAS Railway Induced Vibration Abatement Solutions Collaborative Project*. 2011

[Cruse 1968] Cruse, T. A.: A direct formulation and numerical solution of the general transient elastodynamic problem. II. In: *Journal of Mathematical Analysis and Applications* Volume 22. 1968, p. 341–355

[Cruse and Rizzo 1968] Cruse, T. A. ; Rizzo, F. J.: A direct formulation and numerical solution of the general transient elastodynamic problem. I. In: *Journal of Mathematical Analysis and Applications* Volume 22. 1968, p. 244–259

[De Oliveira Barbosa et al 2012] De Oliveira Barbosa, J. M. ; Park, J. ; Kausel, E.: Perfectly matched layers in the thin layer method. In: *Computer Methods in Applied Mechanics and Engineering* Volume 217-220. 2012, p. 262–274

[Dieterman and Metrikine 1996] Dieterman, H. A. ; Metrikine, A.: The equivalent stiffness of a half-space interacting with a beam. Critical velocities of a moving load long the beam. In: *European Journal of Mechanics - A/Solids* Volume 15. 1996, p. 67–90

[Dieterman and Metrikine 1997] Dieterman, H. A. ; Metrikine, A.: Critical velocities of a harmonic load moving uniformly along an elastic layer. In: *Journal of Applied Mechanics* Volume 64. 1997, p. 596–601

[Dolling 1969] Dolling, H.-J.: *Die Abschirmung von Erschütterungen durch Bodenschlitze*, Technische Universität Berlin, Ph.D. thesis, 1969

[Eringen and Suhubi 1975] Eringen, A. C. ; Suhubi, E. S.: *Elastodynamics: Linear theory.* New York : Acad. Pr., 1975. – ISBN 0122406028

[Fahrmeir et al 1996] Fahrmeir, L. (Editor.) ; Hamerle, A. (Editor.) ; Tutz, G. (Editor.): *Multivariate statistische Verfahren.* 2., überarb. Aufl. Berlin : de Gruyter, 1996. – ISBN 978-3-11-013806-1

[Fischer 2004] Fischer, M.: *The fast multipole boundary element method and its application to structure-acoustic field interaction.* Stuttgart, Universität Stuttgart, Ph.D. thesis, 2004

[Forrest and Hunt 2006] Forrest, J. A. ; Hunt, H. E. M.: A three-dimensional tunnel model for calculation of train-induced ground vibration. In: *Journal of Sound and Vibration* Volume 294. 2006, p. 678–705

[Freisinger 2016] Freisinger, J.: *Modellierung eines geschichteten Halbraums mit sphärischem Hohlraum*, Technische Universität München, Master thesis, 2016

[Frühe 2010] Frühe, G.: *Überlagerung von Grundlösungen in der Elastodynamik zur Behandlung der dynamischen Tunnel-Boden-Bauwerk-Interaktion*, Technische Universität München, Ph.D. thesis, 2010

[Gaul 1976] Gaul, L.: *Zur Berechnung der Vertikal- und Kippschwingungen eines starren Fundamentes auf viskoelastischem Halbraum.* Hannover, Technische Universität, Ph.D. thesis, 1976

[Gaul et al 2003] Gaul, L. ; Kögl, M. ; Wagner, M.: *Boundary element methods for engineers and scientists: Includes bibliographical references and index.* Berlin : Springer, 2003. – ISBN 3540004637

[Getzner Werkstoffe GmbH 2015] Getzner Werkstoffe GmbH ; Getzner Werkstoffe GmbH (Editor.): *Masse-Feder-Systeme*. 2015. – URL `https://www.getzner.com/uploads/media/04_Masse_Feder_System_01.pdf`

[Givoli 1991] Givoli, D.: Non-reflecting boundary conditions. In: *Journal of Computational Physics* Volume 94. 1991, p. 1–29

[Görtler 1975] Görtler, H.: *Dimensionsanalyse: Theorie der physikalischen Dimensionen mit Anwendungen*. Berlin u.a : Springer, 1975. – ISBN 3-540-06937-2

[Grote 2000] Grote, M. J.: *Nonreflecting boundary conditions for time dependent wave propagation: Research Report No. 2000-04: Seminar für Angewandte Mathematik*. 2000

[Grundmann and Müller 1988] Grundmann, H. ; Müller, G.: Schwingungen infolge zeitlich veränderlicher, bewegter Lasten im Untergrund. In: *Finite Elemente Anwendungen in der Baupraxis*. 1988, p. 177–187

[Gupta and Degrande 2010] Gupta, S. ; Degrande, G.: Modelling of continuous and discontinuous floating slab tracks in a tunnel using a periodic approach. In: *Journal of Sound and Vibration* Volume 329. 2010, p. 1101–1125

[Gupta et al 2007] Gupta, S. ; Hussein, M. F. M. ; Degrande, G. ; Hunt, H. E. M. ; Clouteau, D.: A comparison of two numerical models for the prediction of vibrations from underground railway traffic. In: *Soil Dynamics and Earthquake Engineering* Volume 27. 2007, p. 608–624

[Gupta et al 2009] Gupta, S. ; Stanus, Y. ; Lombaert, G. ; Degrande, G.: Influence of tunnel and soil parameters on vibrations from underground railways. In: *Journal of Sound and Vibration* Volume 217. 2009, p. 70–91

[Hardin and Drnevich 1972] Hardin, B. O. ; Drnevich, V. P.: Shear modulus and damping in soils, measurements and parameter effects. In: *Journal of Soil Mechanics and Foundations Division* Volume 98/6. 1972, p. 603–624

[Hastings et al 1996] Hastings, F. D. ; Schneider, J. B. ; Broschat, S. L.: Application of the perfectly matched layer (PML) absorbing boundary condition to elastic wave propagation. In: *Journal of the Acoustical Society of America* Volume 100. 1996, p. 3061–3069

[Haupt 1995] Haupt, W.: Wave propagation in the ground and isolation measures. In: *International Conferences on Recent Advances in Geotechnical Earthquake Engineering & Soil Dynamics*. 1995, p. 985–1016

[Holliday et al 1995] Holliday, J. D. ; Ranade, S. S. ; Willet, P.: A fast algorithm for selecting sets of dissimilar molecules from large chemical databases. In: *Quantitative Structure-Activity Relationships* Volume 14. 1995, p. 501–506

[Hughes 2000] Hughes, T. J. R.: *The finite element method: Linear static and dynamic finite element analysis*. Mineola, NY : Dover Publications, 2000. – ISBN 978-0-486-41181-1

[Hussein et al 2006] Hussein, M. F. M. ; Gupta, S. ; Hunt, H. E. M. ; Degrande, G. ; Talbot, J.: An efficient model for calculating vibration from a railway tunnel buried in a half-space. In: *Proceeding of the thirteenth International Congress on Sound and Vibration (ICSV13).* 2006

[Hussein et al 2008] Hussein, M. F. M. ; Hunt, H. E. M. ; Rikse, L. ; Gupta, S. ; Degrande, G. ; Talbot, J. ; Francois, S. ; Schevenels, M.: Using the PiP model for fast calculation of vibration from a railway tunnel in a multi-layered half-space:. In: *Noise and Vibration Mitigation for Rail transportation systems - Proceedings of the 9th International Workshop on Railway Noise Munich Germany 4 - 8 September 2007* Volume 99. Berlin and Heidelberg : Springer, 2008. – ISBN 978-3-540-74893-9

[Israil and Banerjee 1990] Israil, A. S. ; Banerjee, P. K.: Advanced development of time-domain BEM for two-dimensional scalar wave propagation. In: *International Journal for Numerical Methods in Engineering* Volume 29. 1990, p. 1003–1020

[Israil et al 1992] Israil, A. S. ; Banerjee, P. K. ; Wang, H. C.: Time-domain formulations of BEM for two-dimensional, axisymmetric and three-dimensional scalar wave propagation. In: Banerjee, P. K. (Editor.) ; Kobayashi, S. (Editor.): *Advanced dynamic analysis by boundary element methods* Volume 7. London : Elsevier, 1992, p. 75–113. – ISBN 1-85166-734-2

[Jaccard 1901] Jaccard, P.: Distribution de la flore alpine dans le Bassin des Dranses et dans quelques régions voisine. In: *Bulletin de la Société Vaudoise des Sciences Naturelles* Volume 37. 1901, p. 241–272

[Jaswon 1963] Jaswon, M. A.: Integral equation methods in potential theory I. In: *Proceedings of the Royal Society of London A* Volume 275. 1963, p. 23–32

[Johnson 2007] Johnson, S. G.: *Notes on perfectly matched layers (PMLs): Lecture Notes.* Massachusetts, Massachusetts Institute of Technology, Ph.D. thesis, 2007

[Jones and Hunt 2009] Jones, S. ; Hunt, H. E. M.: The effect of inclined soil layers on surface vibration from underground railways using a semi-analytical approach. In: *Journal of Physics: Conference Series* Volume 181. 2009

[Jones et al 2010] Jones, S. ; Hussein, M. F. M. ; Hunt, H. E. M.: Use of PiP to investigate the effect of a free surface on ground vibration due to underground railways. In: *Acoustics Australia* Volume 38. 2010

[Kammler 2008] Kammler, D. W.: *A first course in Fourier analysis.* 2. ed., rev. ed. Cambridge : Cambridge Univ. Press, 2008. – ISBN 9780521709798

[Kausel 1994] Kausel, E.: Thin-layer method: Formulation in the time domain. In: *International Journal for Numerical Methods in Engineering* Volume 37. 1994, p. 927–941

[Kausel 1999] Kausel, E.: Dynamic point sources in laminated media via the thin-layer method. In: *International Journal of Solids and Structures* Volume 36. 1999, p. 4725–4742

[Koecher 1997] KOECHER, M.: *Lineare Algebra und analytische Geometrie.* Vierte, ergänzte und aktualisierte Auflage. Berlin, Heidelberg : Springer Berlin Heidelberg, 1997. – ISBN 978-3-540-62903-0

[Konrad 1985] KONRAD, A.: *Der Zylinder, der zylindrische Hohlraum und die dickwandige Kreiszylinderschale unter beliebigen, ruhenden oder bewegten Lasten.* München, Technische Universität, Ph.D. thesis, 1985

[Krämer 1987] KRÄMER, E.: Dämpfung aus der Sicht der Ingenieure. In: *Dämpfung von Schwingungen bei Maschinen und Bauwerken.* 1987, p. 1–20

[Kreutz 2013] KREUTZ, J. H. G.: *Augmented beam elements using unit deflection shapes together with a Finite Element discretisation of the cross section*, Technische Universität München, Ph.D. thesis, 2013

[Krylov 1995] KRYLOV, V. V.: Generation of ground vibrations by superfast trains. In: *Applied Acoustics* Volume 44. 1995, p. 149–164

[Kuo et al 2011] KUO, K. A. ; HUNT, H. E. M. ; HUSSEIN, M. F. M.: The effect of a twin tunnel on the propagation of ground-borne vibration from an underground railway. In: *Journal of Sound and Vibration* Volume 330. 2011, p. 6203–6222

[Lenz 2003] LENZ, S.: *Nichtlineare Interaktion zwischen Fahrzeug und Untergrund unter Zuhilfenahme von Integraltransformationen*, Technische Universität München, Ph.D. thesis, 2003

[Lieb 1997] LIEB, M.: *Adaptive numerische Fouriertransformation in der Bodendynamik unter Verwendung einer Waveletzerlegung*, Technische Universität München, Ph.D. thesis, 1997

[Lombaert and Degrande 2009] LOMBAERT, G. ; DEGRANDE, G.: Ground-borne vibration due to static and dynamic axle loads of InterCity and high-speed trains. In: *Journal of Sound and Vibration* Volume 319. 2009, p. 1036–1066

[Lombaert et al 2006] LOMBAERT, G. ; DEGRANDE, G. ; KOGUT, J. ; FRANCOIS, S.: The experimental validation of a numerical model for the prediction of railway induced vibrations. In: *Journal of Sound and Vibration* Volume 297. 2006, p. 512–535

[Lombaert et al 2013] LOMBAERT, G. ; DIJCKMANS, A. ; COULIER, P. ; DEGRANDE, G. ; SMEKAL, A. ; EKBLAD, A. ; THOMPSON, D. J. ; JIANG, J. ; TOWARD, M. G. R. ; RÜCKER, W. ; KEIL, J. ; VUKOTIC, M. ; RODRÍGUEZ PLAZA, M. ; ANDRÉS, Á. ; CUELLAR, V. ; GARBURG, R. ; MÜLLER, R.: *Design guide and technology assessment of the transmission mitigation measures: RIVAS Railway Induced Vibration Abatement Solutions Collaborative Project.* 2013

[Long 1967] LONG, C. F.: On the completeness of the Lamé potential. In: *Acta Mechanica* Volume 3. 1967, p. 371–375

[Lysmer 1970] LYSMER, J.: Lumped mass method for Rayleigh waves. In: *Bulletin of the Seismological Society of America* Volume 60. 1970, p. 89–104

[Maharan 2004] MAHARAN, E.: *Finite-Infinite-Elemente-Modellierung zur Simulation der Boden-Bauwerk-Flüussigkeit-Interaktion unter dynamischer Anregung.* Wuppertal, Bergische Universität Wuppertal, Ph.D. thesis, 2004

[Manolis and Beskos 1988] MANOLIS, G. D. ; BESKOS, D. E.: *Boundary element methods in elastodynamics.* 1. publ. London u.a. : Unwin Hyman, 1988. – ISBN 0046200193

[Mansur and Brebbia 1982a] MANSUR, W. J. ; BREBBIA, C. A.: Formulation of the boundary element method for transient problems governed by the scalar wave equation. In: *Applied Mathematical Modelling* Volume 6. 1982, p. 307–311

[Mansur and Brebbia 1982b] MANSUR, W. J. ; BREBBIA, C. A.: Numerical implementation of the boundary element method for two dimensional transient scalar wave propagation problems. In: *Applied Mathematical Modelling* Volume 6. 1982, p. 299–306

[Meinhold and Miltzlaff 1978] MEINHOLD, P. ; MILTZLAFF, G.: *Feld- und Potentialtheorie.* Thun : Fachbuchverlag, 1978 (Mathematik für Ingenieure). – ISBN 3-87144-304-2

[Messner and Schanz 2010] MESSNER, M. ; SCHANZ, M.: An accelerated symmetric time-domain boundary element formulation for elasticity. In: *Engineering Analysis with Boundary Elements* Volume 34. 2010, p. 944–955

[Meyer 2009] MEYER, M.: *Signalverarbeitung: Analoge und digitale Signale Systeme und Filter.* 5. Aufl. Wiesbaden : Vieweg + Teubner, 2009. – ISBN 978-3-8348-0494-5

[Müller 1989] MÜLLER, G.: *Ein Verfahren zur Erfassung der Fundament-Boden Wechselwirkung unter Einwirkung periodischer Lasten*, Technische Universität München, Ph.D. thesis, 1989

[Müller 1993] MÜLLER, G.: *Ein Verfahren zur Kopplung der Randelementmethode mit analytischen Lösungsansätzen*, Technische Universität München, Ph.D. thesis, 1993

[Müller and Möser 2004] MÜLLER, G. ; MÖSER, M.: *Taschenbuch der Technischen Akustik.* Dritte, erweiterte und überarbeitete Auflage. Berlin, Heidelberg : Springer Berlin Heidelberg, 2004. – ISBN 978-3-642-62343-1

[Müller 2007] MÜLLER, K.: *Dreidimensionale dynamische Tunnel-Halbraum-Interaktion: Ein Verfahren auf der Grundlage einer Kopplung der Integraltransformationsmethode mit der Finite-Elemente-Methode*, Technische Universität München, Ph.D. thesis, 2007

[Müller et al 2008] MÜLLER, K. ; GRUNDMANN, H. ; LENZ, S.: Nonlinear interaction between a moving vehicle and a plate elastically mounted on a tunnel. In: *Journal of Sound and Vibration* Volume 310. 2008, p. 558–586

[Müller 2015] MÜLLER, P.: *Untersuchung der Effekte von Masse-Feder-Systemen auf Verformungen in einem Tunnel.* Technische Universität München, Bachelor thesis, 2015

[Park 2002] PARK, J.: *Wave motion in finite and infinite media using the thin-layer method.* Cambridge, Massachusetts Institute of Technology, Ph.D. thesis, 2002

[Park and Kausel 2003] Park, J. ; Kausel, E.: Numerical dispersion of SH waves. In: *Computational Fluid and Solid Mechanics.* 2003, p. 556–560

[Priestley 1981] Priestley, M. B.: *Spectral analysis and time series.* 1. London : Acad. Pr, 1981. – ISBN 0-12-564901-0

[Rabinovich et al 2011] Rabinovich, D. ; Givoli, D. ; Bielak, J. ; Hagstrom, T.: A finite element scheme with a high order absorbing boundary condition for elastodynamics. In: *Computer Methods in Applied Mechanics and Engineering* Volume 200. 2011, p. 2048–2066

[Rammerstorfer 2008] Rammerstorfer, F.: *Simulation von Wellenausbreitung unter Verwendung von Perfectly Matched Layers.* Technische Universität Graz, Diplomarbeit, 2008

[Rastandi 2003] Rastandi, J. I.: *Modelization of dynamic soil-structure interaction using integral transform-finite element coupling*, Technische Universität München, Ph.D. thesis, 2003

[Rathjens 2016] Rathjens, V.: *Modellierung eines geschichteten Halbraums mit zylindrischem Hohlraum*, Technische Universität München, Master thesis, 2016

[Rizzo 1967] Rizzo, F. J.: An integral equation approach to boundary value problems of classical elastostatics. In: *Quarterly of Applied Mathematics* Volume 25. 1967, p. 83–95

[Rogers and Tanimoto 1960] Rogers, D. J. ; Tanimoto, T. T.: A computer program for classifying plants. In: *Science* Volume 132. 1960, p. 1115–1118

[Rücker and Said 1994] Rücker, W. ; Said, S.: *Erschütterungsübertragung zwischen U-Bahn-Tunneln und dicht benachbarten Gebäuden.* Bremerhaven : Wirtschaftsverl. NW, Verl. für Neue Wiss., 1994. – ISBN 3-89429-422-1

[Savidis and Bergmann 2005] Savidis, S. A. ; Bergmann, S.: Slab track vibration and stress distribution induced by train passage. In: *Proceedings of the Sixth European Conference on Structural Dynamics.* 2005, p. 651–656

[Savidis and Bode 2002] Savidis, S. A. ; Bode, C.: Dynamic soil-track-interaction. In: *Proceedings of the Fifth European.* 2002, p. 153–163

[Schepers and Savidis 2009] Schepers, W. ; Savidis, S. A.: Kopplung von Finiten Elementen und Randelementen zur Lösung ausgedehnter dynamischer Boden-Bauwerk-Interaktionsprobleme im Frequenzbereich. In: *VDI Berichte.* 2009, p. 371–390

[Schneider 2014] Schneider, F.: *Parameterstudie zur Analyse des Anwendungsbereichs eines gekoppelten Verfahrens der Finite-Elemente-Methode mit Integraltransformationsmethode.* Technische Universität München, Bachelor thesis, 2014

[Schwarz 1991] Schwarz, H. R.: *Methode der finiten Elemente: Eine Einführung unter besonderer Berücksichtigung der Rechenpraxis.* Volume 47. 3., neubearb. Aufl. Stuttgart : Teubner, 1991. – ISBN 3-519-22349-X

[Sedov 1993] Sedov, L. I.: *Similarity and dimensional methods in mechanics.* 10. ed. Boca Raton u.a. : CRC Press, 1993. – ISBN 0849393086

[Sheng et al 1999] Sheng, X. ; Jones, C. J. C. ; Petyt, M.: Ground vibration generated by a load moving along a railway track. In: *Journal of Sound and Vibration* Volume 228(1). 1999, p. 129–156

[Sheng et al 2006] Sheng, X. ; Jones, C. J. C. ; Thompson, D. J.: Prediction of ground vibration from trains using the wavenumber finite and boundary element methods. In: *Journal of Sound and Vibration* Volume 293. 2006, p. 575–586

[Somigliana 1892] Somigliana, C.: Sulle espressioni analitiche generali dei movimenti oscillatori. In: *Tip. della R. Accademia dei Lincei.* 1892

[Sommerfeld 1949] Sommerfeld, A.: *Partial differential equations in physics.* Academic Press, 1949

[Stichlmair 1990] Stichlmair, J.: *Kennzahlen und Ähnlichkeitsgesetze im Ingenieurwesen.* Essen : Altos-Verlag Doris Stichlmair, 1990

[Symm 1963] Symm, G. T.: Integral equation methods in potential theory II. In: *Proceedings of the Royal Society of London A* Volume 275. 1963, p. 33–46

[Tadeu and Kausel 2000] Tadeu, A. ; Kausel, E.: Green's functions for two-and-a-half-dimensional elastodynamic problems. In: *Journal of Engineering Mechanics* Volume 126(10). 2000, p. 1093–1097

[Ullmann 2013] Ullmann, R.: *Modellierung des elastisch-isotropen Halbraums mittels Integraltransformationsmethoden und Prognose der dynamischen Systemantwort unter verschiedenen Lasten.* Technische Universität München, Bachelor thesis, 2013

[van Dalen and Metrikine 2008] van Dalen, K. N. ; Metrikine, A.: Transition radiation of elastic waves at the interface of two elastic half-planes. In: *Journal of Sound and Vibration* Volume 310. 2008, p. 702–717

[van Dalen et al 2015] van Dalen, K. N. ; Tsouvalas, A. ; Metrikine, A. ; Hoving, J. S.: Transition radiation excited by a surface load that moves over the interface of two elastic layers. In: *International Journal of Solids and Structures* Volume 73-74. 2015, p. 99–112

[VDI 2013] VDI: *VDI-Richtlinie 2038-2 Gebrauchstauglichkeit von Bauwerken bei dynamischen Einwirkungen.* 2013

[Viktorov 1967] Viktorov, I. A.: *Rayleigh and Lamb waves: Physical theory and applications.* New York : Plenum Pr. and Springer Verlag, 1967

[von Estorff and Prabucki 1990] von Estorff, O. ; Prabucki, M. J.: Dynamic response in the time domain by coupled boundary and finite elements. In: *Computational Mechanics* Volume 6. 1990, p. 35–46

[Waas 1972] Waas, G.: *Earth vibration effects and abatement for military facilities: Analysis method for footing vibrations through layered media.* 1972

[Werske 2013] Werske, A.: *Weltrekorde von Hochgeschwindigkeitszügen und Magnetschwebebahnen.* 2013. – URL `http://www.hochgeschwindigkeitszuege.com/news-und-infos/geschwindigkeits-rekorde.php`. – date visited: 05.12.2015

[Willet 1998] Willet, P.: Chemical similarity searching. In: *Journal of Chemical Information and Computer Sciences* Volume 38. 1998, p. 983–996

[Willet and Winterman 1986] Willet, P. ; Winterman, V.: A comparison of some measures for the determination of inter-molecular structural similarity measures of inter-molecular structural similarity. In: *Quantitative Structure-Activity Relationships* Volume 5. 1986, p. 18–25

[Wolf 1985] Wolf, J. P.: *Dynamic soil-structure interaction.* Englewood Cliffs : Prentice-Hall, 1985

[Wolf 2003] Wolf, J. P.: *The scaled boundary finite element method.* Chichester : Wiley Chichester and Wiley, 2003. – ISBN 978-0-471-48682-4

[Wolf and Song 2000] Wolf, J. P. ; Song, C.: The scaled boundary finite-element method - a primer: derivations. In: *Computers and Structures* Volume 78. 2000, p. 191–210

[Woods 1968] Woods, R. D.: Screening of surface waves in soils. In: *Journal of the Soil Mechanics and Foundations Division* Volume 94. 1968, p. 951–979

[Wu et al 1997] Wu, J. ; Kingsland, D. M. ; Lee, J.-F. ; Lee, R.: A comparison of anisotropic PML to Berenger's PML and its application to the finite-element method for EM scattering. In: *IEEE Transactions of Antennas and Propagation* Volume 45. 1997, p. 40–50

[Yang 1996] Yang, Y.-B.: Frequency-independent infinite elements for analysing semi-infinite problems. In: *International Journal for Numerical Methods in Engineering* Volume 39. 1996, p. 3553–3569

[Zeller 2012] Zeller, P.: *Handbuch Fahrzeugakustik: Grundlagen Auslegung Berechnung Versuch.* 2., überarbeitete Auflage. Wiesbaden : Vieweg+Teubner, 2012. – ISBN 978-3-8348-8657-6

[Zhang and Song 1991] Zhang, C. ; Song, C.: Infinite boundary elements for dynamic problems of 3-D half space. In: *International Journal for Numerical Methods in Engineering* Volume 31. 1991, p. 447–462

[Zienkiewicz et al 1983] Zienkiewicz, O. C. ; Emson, C. ; Bettess, P.: A novel boundary infinite element. In: *International Journal for Numerical Methods in Engineering* Volume 19. 1983, p. 393–404

[Zienkiewicz et al 1977] Zienkiewicz, O. C. ; Kelly, D. W. ; Bettess, P.: The coupling of the finite element method and boundary solution procedures. 1977, p. 355–375

[Zierep 1982] Zierep, J.: *Ähnlichkeitsgesetze und Modellregeln der Strömungslehre.* 2., überarb. Aufl. Karlsruhe : Braun, 1982. – ISBN 376502032X

[Zirwas 1996] Zirwas, G. F. A.: *Ein hybrides Verfahren zur Behandlung der Bauwerk-Boden-Wechselwirkung mit analytischen Integraltransformationen und numerischen Ansätzen*, Technische Universität München, Ph.D. thesis, 1996